

Molecular Magnetic Resonance Imaging for Tumour Targeting

Dr Gabriella Baio

A thesis submitted for the degree of
PhD by Publication

Candidate number 100269027

Norwich Medical School

University of East Anglia

Norwich, United Kingdom

June 2019

©This copy of the thesis has been supplied on condition that anyone who consults it is understood to recognise that its copyright rests with the author and that use of any information derived there from must be in accordance with current UK Copyright Law. In addition, any quotation or extract must include full attribution.

To my family

“I do not know what I may appear to the world, but to myself I seem to have been only like a boy playing on the seashore, and diverting myself in now and then finding a smoother pebble or a prettier shell than ordinary, whilst the great ocean of truth lay all undiscovered before me”.

Isaac Newton

Abstract

During my postgraduate training in Radiology at the University of Genoa, Italy, I developed research projects on the application of molecular magnetic resonance imaging for tumour targeting. Molecular imaging (MI) aims to provide “pictures of what is happening inside the body at molecular and cellular level”. Magnetic resonance imaging (MRI) has been applied to many aspects of MI. Although it offers better temporal and spatial resolution than other methodologies, it is less sensitive for molecular or cellular activities, and therefore there is a need to develop more efficient contrast agents. The publications included in this PhD thesis demonstrate the successful application of two classes of MRI contrast agents: ultrasmall superparamagnetic iron oxide nanoparticles (USPIO) and manganese (Mn^{2+}). Novel USPIO-antibody-conjugated probes for investigating lymphoma tumours were applied, and the potential of labelling natural killer cells by SPIO was demonstrated, offering a great opportunity for *in vivo* investigation of these lymphocytes that play an essential role in cell-based immune defence. The development of a birdcage prototype coil for a clinical 3T MR scanner with a commercial scientific collaboration was carried out. Research projects for investigating tumour calcium metabolism and risk of bone metastases were developed preclinically (by using Mn^{2+} in human preclinical cancer animal models) and clinically (by using *in vivo* proton magnetic resonance spectroscopy to investigate human breast cancer). An *in vivo* Manganese-enhanced-MRI (MEMRI) technique to visualise brown adipose tissue, its physiopathology, and its role in breast or prostate cancer progression, has been included as well. The last research projects carried out as the conclusion of this PhD were focused on: 1) the development of a novel USPIO-MR imaging approach to monitor chronic lymphocytic leukaemia (CLL), induced by interfering with both miR-15 and miR-16 expression; and

2) evaluating response to a potential treatment with the use of miRNA mimics or inhibitors.

Table of Contents

Abstract	4
List of Figures	11
Acknowledgements.....	14
Abbreviations Used in this Thesis	19
List of Papers: Impact factor and Role	23
Objective of this Thesis and Hypothesis.....	27
Chapter 1: Critical Analysis.....	28
1. Background and Introduction	28
1.1. Tumour targeting and cell labelling with MR.....	28
1.1.1. Tumour targeting by USPIO-antibody conjugates	28
1.1.2. Cell labelling by iron oxide nanoparticles.....	45
1.2. Investigation of tumour imaging by using MEMRI	47
1.3. Exploring a new role of MEMRI for visualising brown adipose tissue.....	57
1.4. Application of <i>in vivo</i> proton MR spectroscopy in breast cancer expressing different levels of calcium sensing receptors.....	62
1.5. A non-invasive approach to investigate chronic lymphocytic leukaemia by using iron oxide nanoparticles.....	69
Chapter 2: Original peer reviewed papers	83
2.1. Tumour targeting and cell labelling with MR.....	83
2.1.1. Tumour targeting by USPIO-conjugates	83
2.1.1.2. Title of paper	83
2.1.1.3. Objective of the study	83

2.1.1.4. What this study added to the literature.....	83
2.1.1.5. What changed as a result of the papers?	84
2.1.1.6. In retrospect, what should have been done differently in this study?.....	84
2.1.1.7. Future work as a result of this publication.....	85
2.1.1.8. Confirmation of authorship	85
2.1.1.9. External link to the papers on the journal website.....	85
2.1.2. Cell labelling by iron oxide nanoparticles.....	87
2.1.2.1. Title of paper	87
2.1.2.2. Objective of the study	87
2.1.2.3. What this study added to the literature.....	87
2.1.2.4. What changed as a result of the paper?.....	88
2.1.2.5. In retrospect, what should have been done differently in this study?.....	88
2.1.2.6. Future work as a result of this publication.....	89
2.1.2.7. Confirmation of authorship	89
2.1.2.7. External link to the paper on the journal website.....	89
2.2. Investigation of tumour imaging by using MEMRI	91
2.2.1. Title of paper	91
2.2.2. Objective of the study	91
2.2.3. What this study added to the literature.....	91
2.2.4. What changed as a result of the paper?.....	91
2.2.5. In retrospect, what should have been done differently in this study?.....	92

2.2.6. Future work as a result of this publication	92
2.2.7. Confirmation of authorship	92
2.2.8. External link to the paper on the journal website.....	92
2.2.1. Title of paper	94
2.2.2. Objective of the study	94
2.2.3. What this study added to the literature.....	94
2.2.4. What changed as a result of the paper?.....	94
2.2.5. In retrospect, what should have been done differently in this study?.....	94
2.2.6. Future work as a result of this publication	95
2.2.7. Confirmation of authorship	95
2.2.8. External link to the paper on the journal website.....	95
2.3 Exploring a new role of MEMRI to visualize Brown adipose tissue	97
2.3.1. Title of the abstract.....	97
2.3.2. Objective of the study	97
2.3.3. What this study added to the literature.....	97
2.3.4. In retrospect, what should have been done differently in this study?.....	97
2.3.5. Confirmation of authorship	97
2.3.6. External link to the paper on the journal website.....	98
2.4. Application of <i>in vivo</i> proton MR spectroscopy in breast cancer expressing different level of Calcium sensing receptors	100
2.4.1. Title of papers.....	100

2.4.2. Objective of the study	100
2.4.3. What this study added to the literature.....	100
2.4.4. What changed as a result of the paper?.....	101
2.4.5. In retrospect, what should have been done differently in this study?.....	101
2.4.6. Future work as a result of this publication.....	101
2.4.7. Confirmation of authorship.....	102
2.4.7. External link to the paper on the journal website.....	102
2.5. A non-invasive approach to investigate chronic lymphocytic Leukaemia by using iron oxide nanoparticles.....	104
2.5.1. Title of papers.....	104
2.5.2. Objectives of the studies	104
2.5.3. What these studies added to the literature.....	105
2.5.4. What changed as a result of the papers?	105
2.5.5. In retrospect, what should have been done differently in these studies?.....	105
2.5.6. Future work as a result of these publications.....	105
2.5.7. Confirmation of authorship.....	106
2.5.8. External link to the paper on the journal website.....	106
Discussion and Conclusion	108
Where are we now? Where are we going?	108
References	117

List of Figures

<i>Figure 1. Surface expression of CD20 antigen by D430B and Raji lymphoma cell lines by immunofluorescence and cytofluorimetric analysis.</i>	36
<i>Figure 2. Detection of anti-CD20-USPIO conjugates bound to the cell surface by cytofluorimetric analysis.</i>	36
<i>Figure 3. T2-weighted three-dimensional fast field echo images of D430B CD20 high tumour analysed before and after USPIO-anti-CD20 antibody administration.</i>	37
<i>Figure 4. T2-weighted three-dimensional fast field echo images of Raji CD20 low tumour analysed before and after USPIO-anti-CD20 antibody administration.</i>	38
<i>Figure 5. Representative MR Images of the control group injected with ferumoxides.</i>	38
<i>Figure 6. Immunofluorescence analysis of CD70 surface expression.</i>	40
<i>Figure 7. Coronal MR images of pseudo-metastatic lymphoma xenografts.</i>	42
<i>Figure 8. Experimental prototype birdcage coil for use with a clinical 3T MR scanner</i>	48
<i>Figure 9. Manganese enhanced MR imaging (MEMRI) of the orthotopic human breast cancer xenografts.</i>	52
<i>Figure 10. Immunohistochemical analysis of CaSR in human breast cancer MDA-MB-231 cells xenograft (a–c).</i>	53
<i>Figure 11. A, B Coronal MR images of the orthotopic human breast cancer xenograft in a verapamil-treated control.</i>	54
<i>Figure 12. Amount of internalized Mn²⁺ in B16F10 cells incubated with MnCl₂ and Mn-DO₂A for 1 and 7 h.</i>	56

<i>Figure 13. In vivo Non-invasive Detection of Brown adipose Tissue (BAT) through Manganese Enhanced Magnetic Resonance Imaging (MEMRI) in healthy controls.....</i>	<i>59</i>
<i>Figure 14. In vivo Non-invasive Detection of Brown adipose Tissue (BAT) through Manganese Enhanced Magnetic Resonance Imaging (MEMRI) in metastatic prostate and breast cancer animal models.....</i>	<i>60</i>
<i>Figure 15. In vivo Non-invasive Detection of Brown adipose Tissue (BAT) through Manganese Enhanced Magnetic Resonance Imaging (MEMRI) in orthotopic prostate and breast cancer animal models.....</i>	<i>61</i>
<i>Figure 16. Immunohistochemical analysis of CaSR expression in human breast cancers specimens (score 0-5)</i>	<i>65</i>
<i>Figure 17. Proton MR Spectroscopy choline peak and calcium sensing receptor (CaSR) correlation.....</i>	<i>66</i>
<i>Figure 18. Proton MR Spectroscopy choline peak and calcium sensing receptor (CaSR) correlation.</i>	<i>67</i>
<i>Figure 19. Representative slices of the sequence protocol used to measure the signal intensity (SI) in tissues of interest.</i>	<i>72</i>
<i>Figure 20. Magnetic resonance image signal determination and histological analysis in control (NSG-CTR) compared to engrafted (NSG-CLL) mice.</i>	<i>73</i>
<i>Figure 21. Comparison of magnetic resonance image signal intensity change in the spleen of control mice (NSG-CTR), mice engrafted (NSG-CLL) at 2 and 4 weeks, and non-engrafted (NSG-ne) mice.....</i>	<i>74</i>
<i>Figure 22. Representative experiment of treatment with rituximab.</i>	<i>76</i>
<i>Figure 23. Representative Immunohistochemistry and flow cytometry analysis of mouse spleens from a rituximab experiment.</i>	<i>77</i>
<i>Figure 24. CLL cell engraftment in NSG mice following in vitro transfection with miRNA mimics or inhibitors.....</i>	<i>80</i>

Acknowledgements

The bulk of the published work on which this thesis is based is my own. My contribution to each of the publications is stated per each paper discussed.

There are however notable contributions to the body of work from a number of friends and colleagues that I would like to acknowledge here.

When I started to develop my research projects, I was a radiology trainee at the University of Genoa, and the field of “Molecular Imaging”, at that time, was not well-known in the Italian scientific community. I have been asked several times by colleagues and friends, “how I could develop certain research ideas” and actually, I still have not a single answer. Looking back, I do believe that having started my graduation at University of Pisa in Biology (before my degree in Medicine), certainly contributed to my interest in the molecular and biology study of cancer. At the same time, having a family member, like my mum, affected by breast cancer, had a considerable contribution too. The knowledge of being doctor but “feeling useless” to someone you really love because of the lack of knowledge in detecting disease at very early stage, certainly, pushed my “imagination and will” in thinking “how as radiologist I could cover this gap”.

During my postgraduate training in radiology, I spent most of my “free time” in the laboratory of many colleagues and scientists. For this reason, I would like to thank all the colleagues from the Centre of Advanced Biotechnology (CBA- Centro di Biotecnologie Avanzate), at the National Italian Cancer Research Institute (IST-Istituto Nazionale per la Ricerca sul Cancro). Especially, Dr Marina Fabbi and Dr Silvano Ferrini at the Immunology Unit.

Marina and Silvano, provided me the great chance of learning several lab techniques in the field of Immunology. It has been one of my most exciting experiences learning basic science methods for supporting my molecular imaging study. Thanks to their extensive research knowledge I could also learn how to develop a full research project grant application and write a scientific paper for peer reviewed journals. Most of the pioneer work done by using iron oxide nanoparticles is the result of the collaboration with Marina and Silvano and I will always be thankful to their immense patience and availability at any time of the day and night, for performing all our experiments on MRI.

A special thanks to Mrs Anna Maria Cappelli and Mrs Laura Canton, the two MR radiographers, at IST. They both have been great in teaching me how to use a clinical MR scanner and how to apply all the clinical MR protocols to my preclinical studies. Their patience, support and friendship will always be part of my life.

I would like also to thank Dr Michele Cilli and Dr Laura Emionite, at the Animal Facility at CBA, IST, Genoa. They both have been great in teaching me all the techniques to develop cancer animal models and they have been constantly available in supporting “my risky research ideas”.

I am thankful to Dr Fabrizio Levrero, the MR physicist at IST, for supervising most of my technical MR measurements, especially in the work of USPIO-antibody-conjugates, which needed extensive MR studies for relaxivity measurements.

I have a special thanks to Dr Carlo Emanuele Neumaier, which was the head of the Radiology Department, at IST. Carlo has been not only my Radiology supervisor but also my research supervisor and a very good friend. We developed together the bulk of the work that is included in this thesis. Thanks to his support I could apply for several research project grant applications, first as Radiology trainee and later as consultant radiologist. One of these projects, allowed me to develop a scientific collaboration with General Electric (GE, Milwaukee, USA). Developing a new prototype MR coil together with Flick Engineering (Netherlands) and GE, has been an exciting experience. I certainly improved my MR physics and MR engineering knowledge, and I had the opportunity to experience how research is developed in a commercial environment too. For this reason, I would like here to mention Piero Ghedin and Sabina Prato from GE, for their substantial scientific support and collaboration.

I have been very lucky to collaborate with Prof Silvio Aime and Dr Eliana Gianolo, at the Molecular Imaging Center, at University of Turin. Silvio is one of the well-known pioneer scientists in the field of Molecular Imaging who has received during the World Molecular Imaging Conference 2013 the Gold Medal Award (“From Relaxation Enhancers to Frequency-Encoding Agents: How MRI Competes in the Molecular Imaging Arena”). He is a great Professor and, thanks to our collaboration, I not only improved the experiments on the application of manganese as MR tumour contrast agent, but I also found a fantastic team of scientists with whom I am still collaborating.

The last work developed on chronic lymphocytic leukaemia was done thanks to the collaboration with Prof Manlio Ferrarini and Dr Giovanna Cutrona. It

has been something very interesting and “out of my comfort zone as radiologist” developing a preclinical imaging method in the study of this disease treated with a very novel treatment such as miRNA mimics and miRNA inhibitors.

I would like to thank my PhD thesis supervisors, Dr Andoni Toms and Dr Donnie Cameron, for their great support and supervision. They are not only great colleagues and good friends, but thanks to their input and suggestions I had the opportunity to reflect a lot on the research developed all over these years, making myself more eager to improve in the Molecular Imaging field as Radiologist. A special thank also to Prof Alastair Forbes, for his advices and support during the writing of this thesis.

I thank all of my co-authors that I cannot list here, one by one, but without their collaboration and support I could not achieve any of the results that we obtained and, also all my radiology colleagues at the Norwich Nowrfolk University Hospital (NNUH), Norwich, for supporting and constantly motivating me, over these months.

I would like to dedicate a special thanks to Prof Chrit Moonen, at the University of Utrecht, for proof reading my PhD thesis. Chrit was the first scientist that I met during an International conference (ISMRM, Galveston, 2007) and he has been all over these twelve years, not only a very good scientific mentor, but also my best friend. I will never be thankful enough for his great support and friendship.

I take here also the opportunity to thank spider Greg for biting me during my University time and, transmitting his DNA: I am sure it gave me “the special power to become an insatiable researcher and doctor, too”.

Last but not least, I would like to express from the depth of my heart how grateful I am to my family, which provided, and still provides me, with their constant support and love every day of my life.

Norwich, 2019

Abbreviations Used in this Thesis

Ab - antibody

ATP - adenosine triphosphate

BRCA1 - breast cancer type 1 susceptibility protein

BREASE - single-voxel breast spectroscopy sequence

BAT - brown Adipose Tissue

CA - contrast agent

CAs - contrast agents

Ca²⁺ - calcium ions

CaSR - calcium sensing receptor

CaSRs - calcium sensing receptors

CDP - cytidine diphosphate

CDP - ethanolamine

CH-L - close homolog of L1 like protein

ChoK - choline kinase

CLL - chronic lymphocytic leukaemia

CT - computed tomography

DAG - diacylglycerol

DCE-MRI - dynamic contrast enhanced-magnetic resonance imaging

del(13)(q14) - deletion at 13q14.3

D430B and Raji - lymphoma cell lines

EANM - The European Association of Nuclear Medicine and Molecular Imaging and Society of Nuclear Medicine and Molecular Imaging joint

EBV - Epstein Barr virus

ESMI - European Molecular Imaging Society

FC - flow cytometry

¹⁸FDG-PET/CT - 2-deoxy-2-fluorine-18-fluoro-D-glucose-positron emission tomography/computed tomography

^{18}F -FACBC - anti-1-amino-3- ^{18}F -fluorocyclobutane-1-carboxylic acid
FISH - fluorescence in situ hybridization
GEP-NETs - gastroentero-pancreatic neuroendocrine tumors
 ^{68}Ga -PSMA - ^{68}Ga -prostate specific membrane antigen
 ^1H -MRS - ^1H -proton magnetic resonance spectroscopy
IHC - immunohistochemistry
IL-2 - interleukin 2
 ^{111}In -PSMA - ^{111}In -prostate specific membrane antigen
IST - National Italian Cancer Research Institute (Istituto Nazionale per la Ricerca sul Cancro)
 ^{177}Lu DOTA-TATE - ^{177}Lu -DOTATATE, DOTA-octreotate, oxodotreotide, DOTA-(Tyr3)-octreotate, and DOTA-0-Tyr3-Octreotate
mAb - monoclonal antibody
mAbs - monoclonal antibodies
MEMRI - manganese enhanced magnetic resonance Imaging
 Mg^{2+} - magnesium ions
MI - molecular imaging
MICAD - Molecular Imaging and Contrast Agent Database
MICoE - Molecular Imaging Center of Excellence
MIP - maximum intensity projection
miRNAs - microRNAs
 Mn^{2+} - manganese ions
 MnCl_2 – manganese chloride
MR - magnetic resonance
MRI - magnetic resonance imaging
NETTER-1 - phase 3 Neuroendocrine Tumors Therapy trial
NETPET - NeuroEndocrine Tumor Positron Emission Tomography grading system for NETs

NIH - National Institutes of Health
NHLs - non-Hodgkin lymphomas
NSG-CTR - NOD SCID gamma mouse control
NSG-CLL - NOD SCID gamma mouse chronic lymphocytic leukaemia
NSG-ne - non-engrafted mice
NK cells - natural killer cells
SD - standard deviation
SNR - signal-to-noise ratio
PBMC - peripheral blood mononuclear cell
PCho - phosphocholine
PET/CT - Positron emission tomography/Computed Tomography
PET/MR - Positron emission tomography/Magnetic Resonance
PROMISE - PROstate cancer Molecular Imaging Standardization
Evaluation
PtdCho - phosphatidylcholine
PtdEtn - phosphatidylethanolamine
PTH - parathyroid hormone
PTHrP - parathyroid hormone related protein
PSMA - prostate specific membrane antigen
R1 - longitudinal relaxivity
R2 - transverse relaxivity
ROI - region of interest
RS - Richter syndrome
SE - signal enhancement
SI - signal intensity
SPECT/CT - Single-photon emission computed tomography/Computed
Tomography
SPIO - superparamagnetic iron oxide nanoparticles

tCho - total choline-containing compounds
TNF – tumour necrosis factor
TRP – transient receptor potential channel
UCP1 - uncoupling protein one
USPIO – ultrasmall superparamagnetic iron oxide nanoparticles
USPIO-anti-CD20 - ultrasmall superparamagnetic iron oxide nanoparticles
antibody
3'-,UTR - 3'-un-translated region
VIBRANT - volume imaging for breast Assessment
VOI – volume of interest
WAT - white adipose tissue
WMIC - World Molecular Imaging Conference
 γ c - receptor gamma chain gene

List of Papers: Impact factor and Role

List of publications on which the thesis is based, including impact factor of the journal and my role to each of these studies.

- **Baio G**, Fabbi M, de Toterò D, Ferrini S, Cilli M, Derchi LE, Neumaier CE. Magnetic resonance imaging at 1.5 T with immunospecific contrast agent in vitro and in vivo in a xenotransplant model. *MAGMA*. 2006 Dec; 19(6):313-20. Epub 2006 Dec 12.

Impact Factor: 1.832

Cited by 23

Role: Principal investigator, conception and design, development of methodology, acquisition of data, analysis and interpretation of data, writing, review, and/or revision of the manuscript, study supervision.

- Neumaier CE, **Baio G**, Ferrini S, Corte G, Daga A. MR and iron magnetic nanoparticles. Imaging opportunities in preclinical and translational research. Review. *Tumori* 2008 Mar-Apr; 94(2):226-33.

Impact Factor: 1.304

Cited by 59

Role: Principal investigator, conception and design, development of methodology, acquisition of data, analysis and interpretation of data, writing, review, and/or revision of the manuscript, study supervision.

- **Baio G**, Fabbi M, Salvi S, de Toterò D, Truini M, Ferrini S, Neumaier CE. Two-step in vivo tumour targeting by biotin-conjugated antibodies and superparamagnetic nanoparticles assessed by magnetic resonance imaging at 1.5T. *Mol Imaging and Biol*. 2010 Jun; 12(3):305-15.

Impact Factor: 3.608

Cited by 25

Role: Principal investigator, conception and design, development of methodology, acquisition of data, analysis and interpretation of data, writing, review, and/or revision of the manuscript, study supervision.

- **Baio G**, Fabbi M, Emionite L, Cilli M, Salvi S, Ghedin P, Prato S, Carbotti G, Tagliafico A, Truini M, Neumaier CE. In vivo imaging of human breast cancer mouse model with high level expression of calcium sensing receptor at 3T. *Eur Radiol.* 2012 Mar; 22(3):551-8.

Impact Factor: 4.027

Cited by 16

Role: Principal investigator, conception and design, development of methodology, acquisition of data, analysis and interpretation of data, writing, review, and/or revision of the manuscript, study supervision.

- **Baio G**, Valdora F, Pace D, Salvi S, Villosio N, Truini M, Calabrese M and Neumaier CE. The key role of correlation between MR spectroscopy choline peak and calcium sensing receptor for breast cancer: Diagnosis by a 3T MR scanner. *Journal of Clinical Oncology.* ASCO 2013 Vol 31, No 15_suppl (May 20 Supplement).

Impact Factor: 26.303

Role: Principal investigator, conception and design, development of methodology, acquisition of data, analysis and interpretation of data, writing, review, and/or revision of the manuscript, study supervision.

- **Baio G**, Rescinito G, Rosa F, Pace D, Boccardo S, Basso L, Salvi S, Calabrese M, Truini M, Neumaier CE. Correlation between Choline Peak at MR Spectroscopy and Calcium-Sensing Receptor Expression Level in

Breast Cancer: A Preliminary Clinical Study. *Mol Imaging Biol.* 2015 Aug; 17(4):548-56.

Impact Factor: 3.608

Cited by 6

Role: Principal investigator, conception and design, development of methodology, acquisition of data, analysis and interpretation of data, writing, review, and/or revision of the manuscript, study supervision.

- Gianolio E, Arena F, Di Gregorio E, Pagliarin R, Delbianco M, **Baio G**, Aime S. MEMRI and Tumours: A method for the evaluation of the contribution of Mn(II) ions in the extra- cellular compartment. *NMR in Biomedicine.* 2015 Sep; 28(9):1104-10.

Impact Factor: 3.031

Cited by 7

Role: Co-investigator, conception and design, development of methodology, acquisition of data, analysis and interpretation of data, writing, review, and/or revision of the manuscript, study supervision.

- Valdora F, Cutrona G, Matis S, Morabito F, Massucco C, Emionite L, Boccardo S, Basso L, Recchia AG, Salvi S, Rosa F, Gentile M, Ravina M, Pace D, Castronovo A, Cilli M, Truini M, Calabrese M, Neri A, Neumaier CE, Fais F, **Baio G**, Ferrarini M. A non-invasive approach to monitor chronic lymphocytic leukaemia engraftment in a xenograft mouse model using ultra-small superparamagnetic iron oxide-magnetic resonance imaging (USPIO-MRI). *Clin Immunol.* 2016 Nov; 172:52-60.

Impact Factor: 3.557

Cited by 5

Role: Principal Investigator, conception and design, development of methodology, acquisition of data, analysis and interpretation of data, writing, review, and/or revision of the manuscript, study supervision.

- Cutrona G, Matis S, Colombo M, Massucco C, **Baio G**, Valdora F, Emionite L, Fabris S, Recchia AG, Gentile M, Neumaier CE, Reverberi D, Massara R, Boccardo S, Basso L, Salvi S, Rosa F, Cilli M, Zupo S, Truini M, Tassone P, Calabrese M, Negrini M, Neri A, Morabito F, Fais F, Ferrarini M. Effects of miRNA-15 and miRNA-16 expression replacement in chronic lymphocytic leukaemia: implication for therapy. *Leukaemia*. 2017 Feb 3 2017 Sep; 31(9):1894-1904.

Impact Factor: 10.023

Cited by 17

Role: Conception and design of the imaging methodology, development of imaging methodology, acquisition of data, analysis and interpretation of data, writing, review, and/or revision of the manuscript, imaging study supervision.

Conference Abstract

- Rosa F, Basso L, Pace D, Secondini L, Boccardo S, Neumaier CE, **Baio G**. In vivo Non-invasive Detection of Brown Adipose Tissue through Manganese Enhanced Magnetic Resonance Imaging (MEMRI). WMIC 2015. P688.

Role: Principal investigator, conception and design, development of methodology, acquisition of data, analysis and interpretation of data, writing, review, and/or revision of the manuscript, study supervision.

Objective of this Thesis and Hypothesis

Objective: to highlight some of the peer reviewed publications that I and my collaborators at the National Italian Cancer Research Institute (IST-Istituto Nazionale per la Ricerca sul Cancro) have written in the field of Molecular Imaging by using Magnetic Resonance Imaging, over the period 2006-2017.

Hypothesis: the research that we developed was part of a pioneering work started in 2005. We were the only two Italian groups working in the field of Molecular Imaging who were using Magnetic Resonance Imaging and new molecular imaging probes. The hypothesis of this PhD thesis is that the results of this work improved the knowledge in Molecular Imaging and the awareness of its potential, impacting positively on the scientific community. The scientific impact and novelty is highlighted and discussed for each publication in this thesis.

Chapter 1: Critical Analysis

1. Background and Introduction

This chapter provides an overview of the scientific background of the research that is part of this thesis. All the topics included in this thesis belong to a specific field of imaging called Molecular Imaging. Molecules and molecular processes have been made visible by nuclear medicine for decades and even the concept of molecular imaging is not new, it is only in 2000 that it became a “hot topic” in Radiology. During this period there has been a significant increase in the number of publications together with the release of several specialised journals and the foundation of several “Molecular Imaging Institutes” with the involvement of more radiologists [1]. This thesis is focused on the application of Magnetic Resonance Imaging (MRI) as a tool of Molecular Imaging (MI) to investigate “tumour targeting” (see below). Figures belonging to each paper have been included in the text, as published, in support of the critical analysis, without elaboration.

1.1. Tumour targeting and cell labelling with MR

1.1.1. Tumour targeting by USPIO-antibody conjugates

The concept of “tumour targeting” was first introduced in the imaging world in the 1950s when research led by Pressman *et al.* demonstrated for the first time that a radiolabelled antibody directed against a tissue antigen was able to perform selective tumour-targeted imaging [2,3]. Successively, between 1978 and 1987, Goldenberg *et al.* set an important imaging milestone in tumour targeting by demonstrating that a radiolabelled antibody directed against the tissue antigen was not only able to selectively target the antigen but could also be used for therapy, introducing for the first time the

concept of “theragnostic agents” [4-7]. In 1987, the investigation carried out on the strong affinity of the two molecules biotin and avidin (streptavidin) by Hnatowich *et al.* (biotin and avidin exhibit the highest known affinity in nature between a ligand and a protein; $K_a 10^{15}M^{-1}$) [7] enabled a form of imaging called “pretargeting”.

Pretargeting imaging was first conceived as a procedure to improve imaging by reducing background activity, thereby enhancing tumour/no tumour ratios. Thus, it is not surprising that in preclinical testing, pretargeting has provided an exceptional ability to detect small lesions in xenograft models. All tumour targeting studies were performed by the application of radiolabelled tracers detected by a gamma scintillation camera at various intervals after administration of the radioactive antibody. The application of MRI and a receptor-directed imaging probes was demonstrated later on, between 1990 and 1992 by *et al.* [8,9]. In these studies, a new contrast agent for magnetic resonance imaging, directed to a specific receptor on hepatocytes, was used for detecting liver cancer in rats.

To better understand the role of MRI in tumour targeting we need to consider the main physical properties of this technique. MRI is an imaging method able to produce high-resolution three-dimensional maps delineating morphological features of the tissue [10]. Differential contrast in soft tissues depends on, variously, endogenous differences in water content, relaxation times of water protons, and diffusion characteristics of the water in the tissue of interest. The specificity of MRI can be further increased using exogenous contrast agents (CAs) such as gadolinium chelates, iron oxide nanoparticles or manganese. The signal enhancement produced by MRI CAs (i.e., the efficiency of the CAs) depends on their longitudinal (r_1) and transverse (r_2) relaxivity (expressed in $mmol^{-1}s^{-1}$), which is defined as the increase of the

nuclear relaxation rate (the reciprocal of the relaxation time) of water protons produced by 1 mmol per litre of CA [11]. The paramagnetic CAs (most of them complexes of gadolinium but also manganese compounds) produce the so-called paramagnetic effect, which results in T1 shortening (and R1 enhancement) [11]. Organs taking up such agents will become hyperintense on T1-weighted MR images; these CAs are thus called positive contrast media. The CAs known as negative agents are generally composed of iron oxide nanoparticles (such as magnetite, Fe_3O_4 , maghemite, $\gamma\text{Fe}_2\text{O}_3$, or other ferrites). These CAs influence signal intensity mainly by shortening T2* and T2, making the contrast-enhanced tissue appear hypointense on T2 and T2*-weighted MR images, the so-called superparamagnetic effect [12,13].

The study carried out by Reimer *et al.* using iron oxide nanoparticles conjugated to an antibody for detecting liver cancer [8,9], introduced two novel assays in the application of MRI for tumour targeting: the relaxation time measurements of incubated human cell membrane solutions and the iron staining of biopsy samples. This study successfully indicated that *in vitro* imaging receptor assays were useful in predicting the affinity of a new receptor-directed MR imaging contrast agents in human tissue prior to clinical trials, opening new avenues in this field.

Development of targeted MR CA directed to specific molecular entities dramatically expanded the range of MR applications by combining the non-invasiveness and high spatial resolution of MRI with specific localisation of molecular targets. However, due to the intrinsically low sensitivity of MRI compared with nuclear imaging, high local concentrations of the CA at the target site are required to generate detectable MR contrast.

To meet these requirements, the MR-targeted CA should recognise targeted cells with high affinity and specificity. It should also have high relaxivity, which for a wide variety of CAs depends on the number of contrast-generating groups per single molecule of the agent. In order to improve CAs' affinity and specificity, important studies have been carried out by Artemov *et al.* to investigate the Her-2/neu receptor on breast cancer cells [14]. Breast cancer cells were imaged by MRI in the presence of a monoclonal antibody conjugated to iron oxide nanoparticles. This application of antibodies conjugated to iron oxide nanoparticles to target breast cancer cells was seen to be of great value for basic science studies in the laboratory, and showed tremendous potential for the clinic, offering new opportunities for diagnosing disease and guiding therapy, for example by providing information on the usefulness of the drug herceptin. The application of imaging technologies available for molecular imaging in the laboratory allowed the characterisation of a growing number of animal tumour models addressing important questions about tumorigenesis, and in development of new disease treatments. This study also served to decrease the number of animals to be sacrificed compared to when these techniques were not available [15,16].

In 2005, at the National Italian Cancer Research Institute (IST-Istituto Nazionale per la Ricerca sul Cancro), we were investigating the application of novel iron-oxide nanoparticle-antibody conjugates to target lymphoma tumours by a clinical MR human scanner [17].

Superparamagnetic iron oxide (SPIO) nanoparticles consist of iron oxides, magnetite (Fe_3O_4), maghemite (Fe_2O_3) or other ferrites, which are insoluble in water. SPIO nanoparticles are strong enhancers of proton relaxation, with

superior T2 (transverse relaxation) shortening effects, that can be used at a much lower concentration than paramagnetic agents. An important advantage of iron oxide nanoparticles is that they exhibit magnetic properties in the presence of an applied magnetic field, and they can form stable colloidal suspensions which can be crucial in biomedical fields, especially *in vivo*. Indeed, they can be directed to a desired site in the body, making them useful for controlled targeting in clinical and in pre-clinical studies [18].

The successful application of SPIOs is strongly dependent on the structural characteristics, such as the size, distribution, shape, and the ability to detect macromolecules. This opens up the possibility to engineer the surface of these particles, creating a polymeric or inorganic molecular shell surrounding the iron oxide cores, followed by the functionalisation with specific biomolecules on the outer shell layer.

Magnetic field gradients induced by superparamagnetic particles contribute to the dephasing of protons that move by diffusion in the vicinity of particles, resulting in significant T2/T2* relaxation. SPIOs are mostly used because of their negative enhancement effect on T2 and T2* weighted sequences. The predominant effect on the T2 relaxation time does not prevent the use of the properties of these agents on the T1 relaxation time when appropriate imaging sequences are chosen. The mean size of SPIOs ranges from approximately 60 to 250 nm, making them subject to phagocytosis by monocyte–macrophage system (i.e. Kupffer cells). Sequestered SPIO particles are metabolically biodegradable and bioavailable. They therefore exhibit a rapid turnover into the body iron stores and incorporate into erythrocyte haemoglobin. Depending on the iron oxide nanoparticle

composition and size, which influence their biodistribution, several pre-clinical applications (i.e., tumour targeting, cell labelling, immune cell trafficking) and clinical applications (i.e., detection of liver metastases, metastatic lymph nodes, inflammatory and/or degenerative diseases) are possible. SPIOs are also investigated as blood pool agents, in particular, ultrasmall superparamagnetic iron oxide particles (USPIO), which range from 10-40 nm in size, are used for their relaxivity properties, and applied for: angiography, tumour permeability and tumour blood volume using T1 weighted sequences; and steady-state cerebral blood volume and vessel size index measurements using T2* weighted sequences [18].

In order to provide different signal intensity from targeted and non-targeted tissue, SPIOs or USPIOs can be conjugated with different kinds of ligands (i.e. monoclonal antibodies, peptide, and oligonucleotides) [18]. The association of MRI with specific superparamagnetic tumour contrast agents offers increased accuracy and specificity of imaging [18]. In particular, monoclonal antibodies (mAbs) were an important emerging tool in cancer therapy at the time of this work, and the study of specific surface markers on tumour cells determined the feasibility of developing the monoclonal antibodies for using as targeted therapeutic agents. The main therapeutic effect of mAbs is due to the antigen-binding regions, which provide specificity to the tumour-killing effects. Therapeutic mAbs can also act by blocking the binding of growth factors, directly signalling arrest and apoptosis, or inducing elimination of mAb-decorated target cells via activation of host defence mechanisms [19]. The paucity of tumour specific antigens has led to the development of mAbs directed against receptors that are overexpressed in cancers compared with normal tissues (for example, trastuzumab for breast cancer). Alternatively, antibodies have been used to

target cell surface molecules characteristic of the lineage from which the malignant cells derive (for example, mAbs against CD20 (rituximab), CD52 (alemtuzumab), and CD33 (gemtuzumab ozogamicin)).

We focused our MI research on anaplastic large B-cell lymphoma, since our research group was very experienced in the investigation of this type of tumour and had previously established a CD30+ Epstein Barr virus (EBV)-infected B cell line that showed a B clonal rearrangement and strong CD30 antigen expression [20].

Anaplastic large B-cell lymphoma is the most common of the non-Hodgkin lymphomas (NHLs). The normal counterparts of these lymphomas are thought to be proliferating B cells (centroblasts or immunoblasts). As such, it is not surprising that, aside from pan-B markers such as CD19, CD20, and CD22, many NHLs express markers commonly associated with B-lymphocyte activation. Some of these activation markers could be viable alternative targets for antibody-based therapeutics. One such activation marker, CD70, is a member of the tumour necrosis factor (TNF) family whose expression is tightly regulated and only transiently induced on antigen-stimulated B and T cells. Of interest, CD70 is expressed by a variety of transformed cells of both hematopoietic and epithelial cell origin.

Our research team previously demonstrated the role of LD6 mAb (CD70 mAb) in recognising a novel non-lineage-specific activation antigen that was involved in the induction of the functional programme of long-term cultured T or natural killer cells [21,22]. Seventy one percent of diffuse large B-cell lymphomas, 33% of follicular lymphomas, 50% of B-cell lymphocytic leukaemia, 25% of Burkitt and mantle cell lymphomas, and

100% of Waldenström macroglobulinemia, as well as most Hodgkin disease Reed-Sternberg cells, express CD70 [23].

Following the identification of the tumour antigens that we aimed to target (CD20 and CD70), we then performed two imaging studies [17, 24] to image lymphoma tumour antigen expression by using mAbs conjugated to iron-oxide nanoparticles.

We applied two types of targeting approach: *direct tumour targeting* (where the primary antibody is directly conjugated to a specific tumour label) [17] and *indirect tumour targeting* (where the primary antibody is directly conjugated to a secondary non-specific tumour label) [24].

We applied a tumour mAb, USPIO-anti-CD20, specifically directed to CD20 lymphoma antigens for the *direct tumour targeting* experiment. Surface expression of CD20 antigen by D430B or Raji lymphoma cell lines and of anti-CD20-USPIO conjugates bound to the cell surface was performed by immunofluorescence and cytofluorimetric analysis (**Figure 1, 2**).

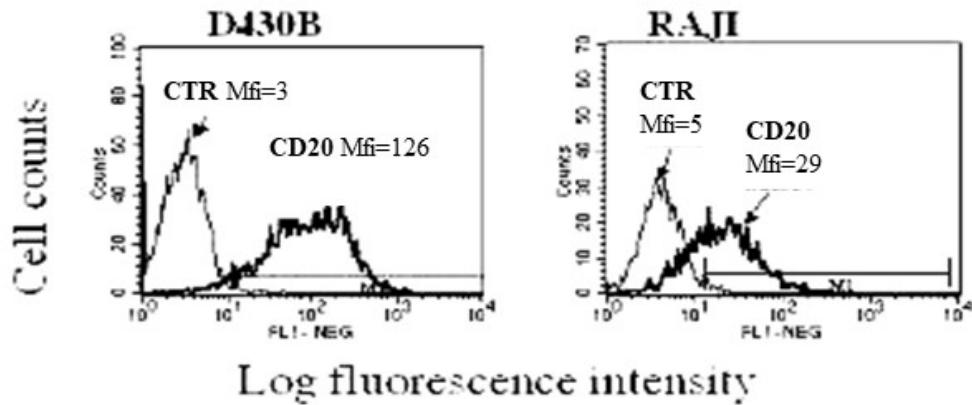


Figure 1. *Surface expression of CD20 antigen by D430B and Raji lymphoma cell lines by immunofluorescence and cytofluorimetric analysis. D430B cells display higher levels of Mfi (mean fluorescence intensity) than Raji cells. CTR= Control [17].*

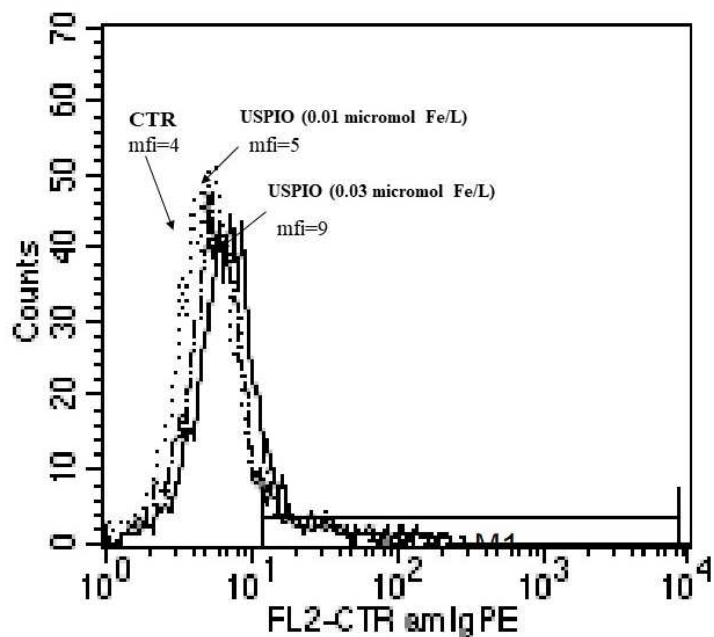


Figure 2. *Detection of anti-CD20-USPIO conjugates bound to the cell surface by cytofluorimetric analysis. Immunofluorescence profile of D430B control cells (CTR, dottedline) and of D430B USPIO-anti-CD20 cells stained with a phycoerythrin-labelled anti-mouse immunoglobulin antibody. With the increase of cell-bound USPIO-anti-CD20, higher fluorescence signal is detectable (continuous line). X axis: fluorescence intensity in log scale, Y axis: cell number [17].*

MRI at 1.5T allowed the detection of USPIO-antibody conjugates specifically bound to human tumour cells both *in vitro* and *in vivo* (**Figure 3, 4**) and, the MRI SI correlated with the concentration of USPIO-antibody used and with the antigen density at the cell surface. A control group injected with ferumoxides demonstrated that the decrease in SI was related to USPIO-antibody targeting (**Figure 5**).

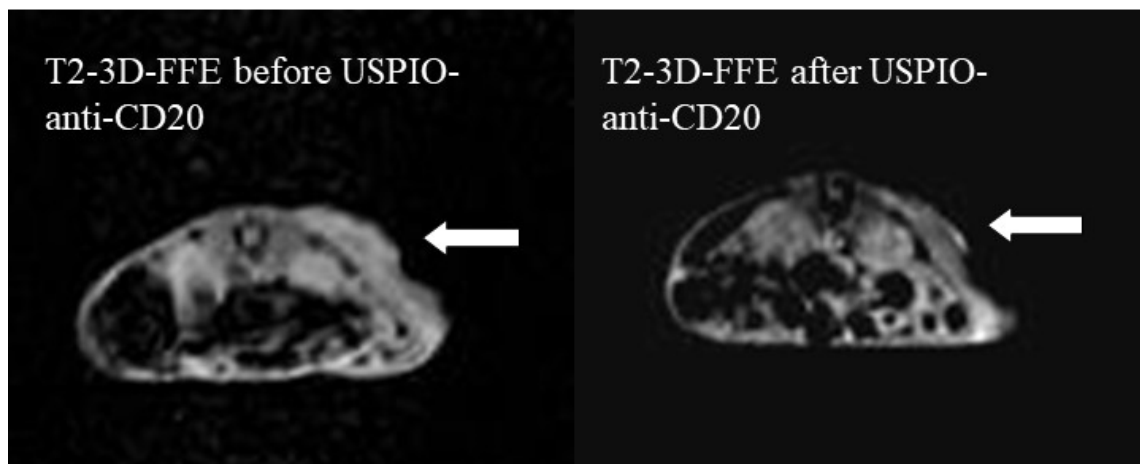


Figure 3. *T2-weighted three-dimensional fast field echo images of D430B CD20 high tumour analysed before and after USPIO-anti-CD20 antibody administration. On T2-weighted three-dimensional fast field echo images after USPIO-anti-CD20 antibody administration the CD20high D430B tumour showed an inhomogeneous decrease in signal intensity (arrows). T2-weighted three-dimensional fast field echo sequences=T2-3D-FFE (50/12/with flip angle7°). T1-weighted three-dimensional fast field echo sequences=T1-3D-FFE (17/4.6/with flip angle13°). USPIO ultrasmall superparamagnetic particle iron oxide, SI signal intensity [17].*

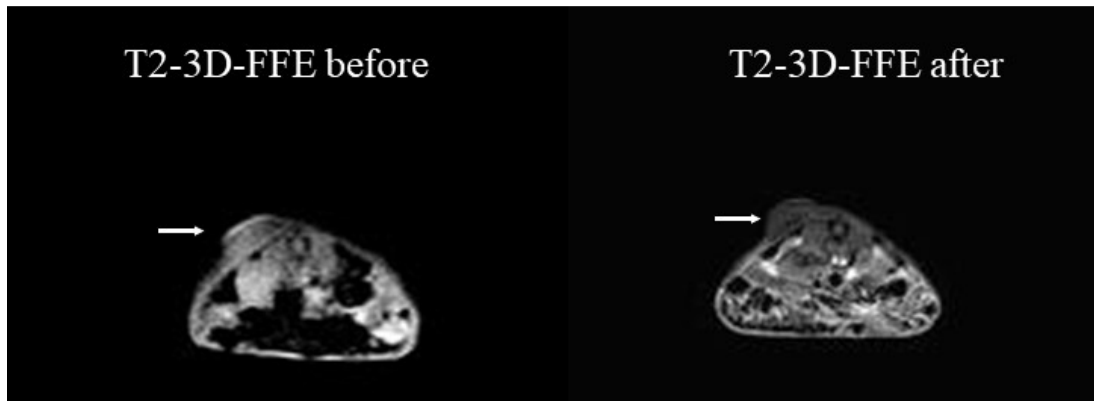
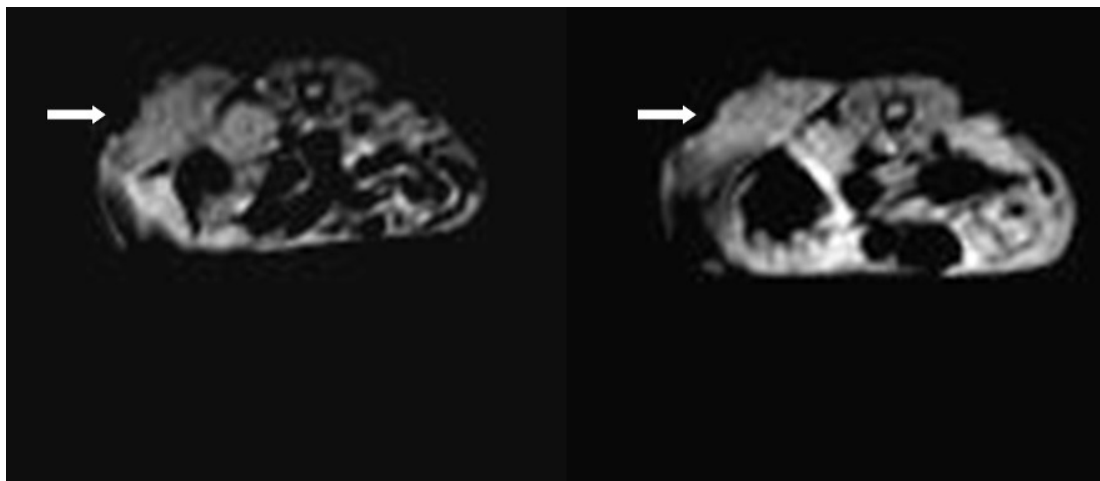


Figure 4. *T2-weighted three-dimensional fast field echo images of Raji CD20 low tumour analysed before and after USPIO-anti-CD20 antibody administration. On T2-weighted three-dimensional fast field echo images, the Raji CD20 low tumour analysed after USPIO-anti-CD20 antibody administration showed an inhomogeneous decrease in signal intensity (arrows). T2-weighted three-dimensional fast field echo sequences=T2-3D-FFE (50/12/with flip angle 7°); T1-weighted three-dimensional fast field echo sequences=T1-3DFFE (17/4.6/with flip angle 13°). USPIO ultrasmall superparamagnetic particle iron oxide, SI signal intensity [17].*



T2-3D-FFE before
ferumoxides administration

T2-3D-FFE after
ferumoxides administration

Figure 5. *Representative MR Images of the control group injected with ferumoxides. No changes of SI on T2-weighted three-dimensional fast field echo images before and after ferumoxides administration (arrows) were observed. T2-weighted three-*

dimensional fast field echo sequences=T2-3D-FFE (50/12/with flip angle7°). SI signal intensity [17].

Many antibodies directed to tumour antigens, potentially useful especially in experimental settings, are not available as USPIO conjugates. We therefore sought to evaluate whether an *indirect targeting* technique, which employs unlabelled mAbs followed by a common USPIO-conjugated secondary reagent, could provide an equally suitable contrast agent. The feasibility of targeting superparamagnetic particles to tumours by means of a two-step system based on the administration of tumour-specific biotin-conjugated antibodies followed by USPIO-anti-biotin, was assessed. We chose to target the human CD70 antigen, expressed by lymphoma cells and only transiently by normal activated lymphocytes, identified by the murine mAb LD6. Since LD6 does not react with murine cells, it seemed suitable for the monitoring of human lymphoma xenografts in mice. An isotype-matched murine mAb that does not react with human lymphoma cells, CH-L, was used as negative control. The two purified antibodies were both biotin-conjugated in-house and labelling was assessed by Western blot with streptavidin-HRPO and found to be equal (**Figure 6**). As common secondary reagent, commercially available USPIO particles conjugated with monoclonal anti-biotin were chosen since their physical characteristics matched those of the USPIO-anti-CD20 contrast agent successfully used in our previous experiment of the *direct tumour targeting*.

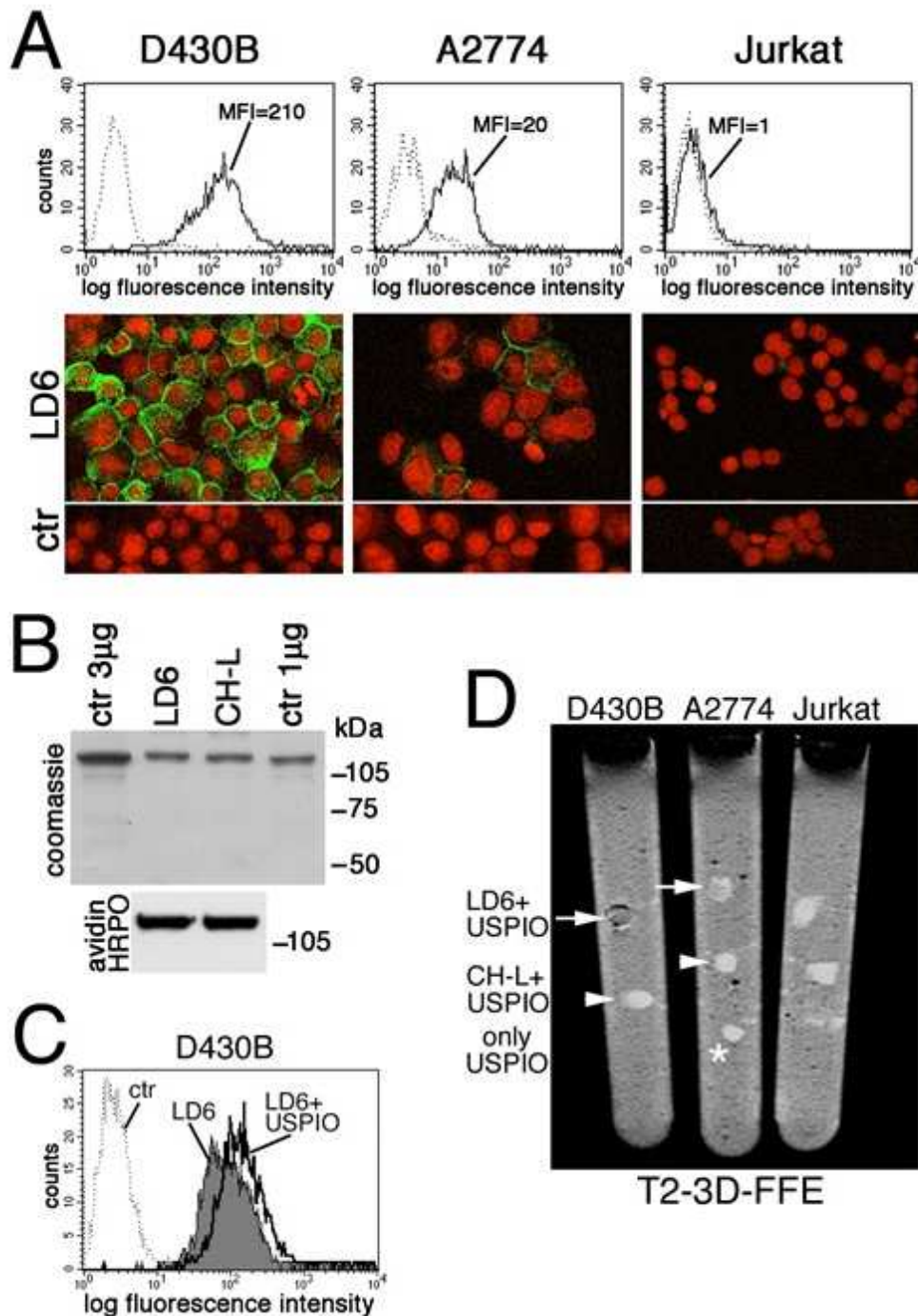


Figure 6. *Immunofluorescence analysis of CD70 surface expression.* (A) Surface expression of CD70 antigen by D430B lymphoma, A2774, ovarian carcinoma and Jurkat leukaemia cells as assessed by indirect immunofluorescence and cytofluorimetric analysis (upper panels) or confocal microscopy (lower panels). Immunofluorescence profiles of cells stained with biotin-conjugated anti-CD70 LD6 mAb (continuous line), or

with biotin-conjugated CH-L mAb as isotype matched negative control (dotted line), followed by FITC-Streptavidin. (B) Purity of LD6 and CH-L mAbs (1 μ g/lane) resolved by SDS-PAGE analysis under non-reducing conditions, as assessed by Coomassie blue staining of 8% polyacrylamide gels (upper panels). As standard 3 and 1 μ g of a commercially available IgG2b mAb were run in parallel lanes. (C) Immunofluorescence profile of D430B cells challenged with biotin-conjugated monoclonal antiCD70 (LD6) plus (continuous line) and minus (gray profile) USPIO-anti-biotin, followed by FITC-anti-mouse serum. (D) MRI analysis at 1.5 T of antibody+USPIO-treated cell pellets in test tubes. Only D430B cells treated with biotinylated LD6+USPIO-anti-biotin showed a clearly hypointense signal on T2-weighted threedimensional fast-field echo images [24].

LD6 and CH-L antibody display a similar degree of biotinylation as detected by western blot analysis of equimolar amounts of the two antibodies and staining with HRPO-streptavidin and revealed by chemoluminescence. Antibodies were resolved on 8% acrylamide gel under non-reducing conditions.

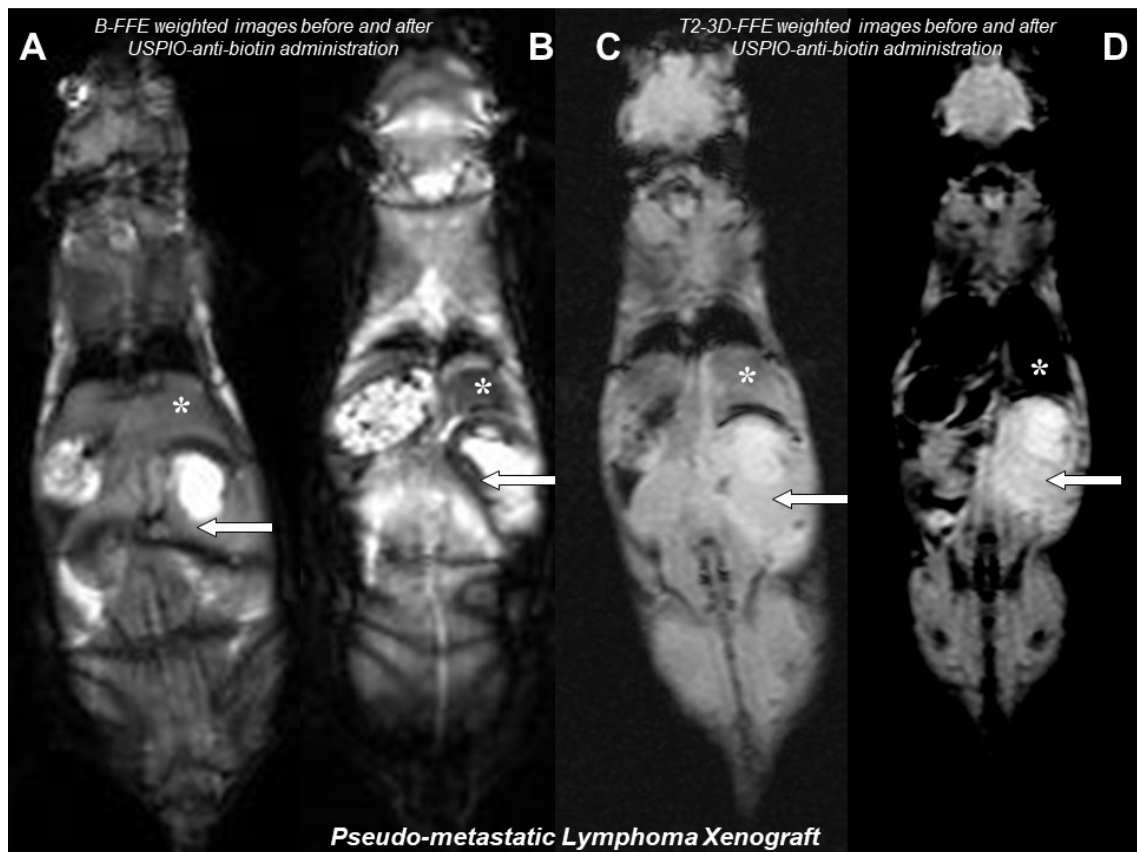


Figure 7. *Coronal MR images of pseudo-metastatic lymphoma xenografts. MRI images demonstrated the presence of tumour masses in the retroperitoneal space, in particular in the right kidney (arrow) with hydronephrosis (hyperintense signal area). On b-FFE weighted images, before (A) and 24 hours after (B) the administration of biotin-conjugated LD6 antibody plus USPIO-anti-biotin, tumours (arrows) and liver (*) showed an evident and homogeneous decrease in SI. On T2-weighted three-dimensional fast field echo images, before (C) and 24 hours after (D) the administration of biotin-conjugated LD6 antibody plus USPIO-anti-biotin, tumours (arrows) did not show decrease in SI whereas the liver showed a significant decrease in SI (*) [24].*

The novelty of these studies was in the application of USPIO-mAbs microbeads produced by a Biotech company (Miltenyi Biotec, Bergisch Gladbach, Germany) for *in vitro* cell separation as an MR contrast agent and the preclinical application of these microbeads using a clinical MR scanner. All previous studies applied high or ultra-high field MR scanners, up to 7T, which were dedicated for small animal models [25,26]. In our study, MR

imaging was performed on a clinical scanner at 1.5T, providing a good signal-to-noise ratio (SNR) for both tumour/no tumour. The use of a clinical MR scanner for preclinical studies in 2005 was novel, supporting the proof of concept that preclinical experiments could be carried out by using clinical tools, and thus the results obtained were more easily translatable into a clinical setting. The application of a molecular imaging platform such as USPIO-mAbs conjugates (specifically anti-CD20 mAb, rituximab or anti-CD70), once bound to the tumour antigen could also be applied as therapeutic tool, supporting once again the concept of imaging “theragnostic”.

The application of the USPIO-mAbs microbeads as MR probes was the first application in this type of experiment, as they had never been applied in an imaging study as contrast agents. With our experiments, MR imaging features of these microbeads were established for the first time. We measured the iron content of the USPIO-antibody core by inductively coupled plasma optical emission spectrometry with a Varian Vista Pro spectrometer (Varian Inc., Palo Alto, CA, USA) and calculated the specific MR Relaxivity features of the microbeads. The discovery of the MR microbeads’ features allowed us to apply this tool as an MR probe for *in vitro* and *in vivo* imaging studies.

Following our experiments, the Molecular Imaging and Contrast Agent Database (MICAD; <https://www.ncbi.nlm.nih.gov/books/NBK5330/>), a key component of the “Molecular Libraries and Imaging” programme of the National Institutes of Health (NIH) Common Fund (formerly NIH Roadmap), in Bethesda, Maryland, cited and officially included our

experiments as the first demonstration of the development of a new MI probe for MR imaging [27].

During this period, in 2005, in Europe, many scientific groups were developing research on MI and for this reason the European Molecular Imaging Society (ESMI- <http://www.e-smi.eu/index.php?id=1987>) was established; it became an independent structure in 2010. In the USA, the members of the Molecular Imaging Centre of Excellence (MICoE) agreed with respect to the important role of MI in Radiology and agreed world-wide with the official definition for “Molecular Imaging” and “molecular probes” [28]. All the studies that aimed to visualise, characterise, and measure biological processes at the molecular and cellular levels in humans and other living systems, were then officially termed “Molecular Imaging” and the endogenous or exogenous probes applied as imaging tools were defined as “Molecular Imaging probes”.

The improvement of these laboratory-based studies improved the potential of translating the basic science principles into the clinical environment. For this reason, we can consider MI as the interface between our growing understanding of the molecular basis of the disease and the translation of this knowledge to new treatments in the clinic and for a better selection of patients for specific therapies. With the opportunity of investigating the morphology plus function/metabolism, MI aims to increase both the specificity and sensitivity of tumour detection. The information coming out of genome sequencing can be used to develop imaging methods that are targeted at specific molecular features of the diseased tissue. In this view, imaging becomes a tool with tremendous potential for the early detection of

tumours, characterisation of the disease process, and understanding of the underlying biochemistry and evaluation of subsequent treatment.

1.1.2. Cell labelling by iron oxide nanoparticles

Following the MR tumour targeting investigation, we also explored the opportunity to target immune cells, such as Natural Killer (NK) cells: a subpopulation of lymphocytes that play an essential role in the cell-based immune defence against viruses and malignant cells. Various investigators have evaluated the antitumoural activity of NK cells, including mechanisms of immunosurveillance, escape strategies of the malignant cells, and risk of adverse reactions [29,30,31]. Previous cell labelling studies were performed with radioactive or fluorescent markers [30,31]. Labelling techniques with radioactive markers provide high sensitivity but limited spatial resolution and the risk of radiotoxic cell damage. Labelling techniques with fluorescent markers provide high sensitivity but are currently restricted to experimental applications at limited depth. Labelling with MR contrast agents have the advantage of being less toxic than radioactive markers and provide an anatomical resolution at the near microscopic level *in vivo*. However, MR cell tracking techniques are restricted by limited sensitivity, which require highly efficient labelling techniques in order to load up the investigated cells with high amounts of contrast agent particles. Such optimised labelling methods have been developed before for various haematopoietic cell populations, including lymphocytes, monocytes, and haematopoietic progenitor cells [30,31]. For non-phagocytic cell types, such labelling techniques required transfection, i.e., internalisation of contrast agents into the cells with the help of liposomes, proteins, or viral vectors. Genetically engineered lymphocytes already undergo a transfection process in order to shuttle new genetic information into the cells. A subsequent secondary

transfection, e.g., for purposes of contrast agent internalisation, has a known lower efficiency than the primary transfection. Therefore, cell labelling protocols for genetically engineered cells need to be tailored and optimised to these cells.

In our study, we aimed to demonstrate a non-invasive method to label NK lymphocytes. We applied a commercially available ferumoxides suspension (Endorem, Guerbet, Paris), combined either with protamine sulphate or with polylysine as transfection agents. For the assessment of labelling efficiency and to study the signal intensity we performed our experiments on a clinical MR scanner at 1.5 T and four groups were compared, respectively: unlabelled NK cells; NK-ferumoxides alone; NK-ferumoxides plus protamine (Pro); NK-ferumoxides plus polylysine (PLL). Significant decrease in SI on T2 MRI was achieved in human ferumoxides-PLL-NK-labeled cells (60%) compared with human ferumoxide-Pro-NK-labeled cells (30%) at concentrations that did not have deleterious effects on cellular viability or function. The detected contrast change lasted for at least 24 hours.

Our results raised the possibility that iron-oxide-nanoparticle-labelled lymphocytes could be used to track these cells in tumours and other tissues using high spatial resolution MRI. The optimisation of molecular-targeted contrast agents, MRI technology and the generation of new USPIO or SPIO antibodies, or other USPIO or SPIO ligands, may provide useful immunospecific-contrast agents for the diagnosis of tumours and for targeting cells for cell therapy. In this way, it promises to provide new methods for the early detection of cancer and support for personalised cancer therapy.

Our studies on the preclinical application of iron oxide nanoparticles, allowed us the opportunity to provide our contribution to a Molecular Imaging textbook, edited by Xiaoyuan Chen, with two chapters [18].

1.2. Investigation of tumour imaging by using MEMRI

The concept of using a clinical MR scanner for preclinical studies in order to easily translate results into a clinical setting, brought us to the development of a new prototype birdcage coil for animal models in conjunction with a clinical 3T MR scanner (**Figure 8**). This was the result of a scientific collaboration between me, General Electric Healthcare (GE, Milwaukee, USA), and Flick Engineering (The Netherlands).



Figure 8. *Experimental prototype birdcage coil for use with a clinical 3T MR scanner (Baio G & GE Healthcare & Flick Engineering-Department of Radiology, IRCCS AOU San Martino - IST - Genoa/IT).*

Some of the research produced using the new prototype birdcage coil is not part of this thesis; however, since this was an important part of my research career, I here cite a few works in which the new prototype birdcage coil was applied in small rodents for the first time [32,33]. The subsequent research project that we developed, using the new prototype birdcage coil for tumour targeting, aimed to investigate calcium metabolism in breast cancer animal models [34].

Changes in calcium metabolism can be a feature of cancer [35-39] and to better understand altered calcium metabolism *in vivo*, a non-invasive method such as imaging is of great value. To investigate calcium metabolism in tumours we used manganese as an MR contrast agent, because of the

interesting combined physical and biological properties of this contrast agent.

Manganese-enhanced-MRI (MEMRI) is a very old technique, and several imaging studies have been performed in order to target calcium ion metabolism. Manganese is a T1 contrast agent, which permits to combine anatomical with functional imaging in multiple systems. Furthermore, since it is an analogue of calcium ions, it can enter cells via the same transport systems as Ca^{2+} and can bind to several intracellular structures because of its high affinity for Ca^{2+} and Mg^{2+} binding sites on proteins and nucleic acids [40,41]. Several research studies applied manganese as an MR contrast agent to investigate the brain [42,43], heart [44,45], olfactory [46], visual [47,48] and somatosensory pathways of rats and mice [49-51]. Early investigation in the application of manganese to visualise breast cancer tumours was performed using a paramagnetic metalloporphyrin that chelates Mn^{2+} as an MR contrast agent in murine models [52,53].

In our experiments, we applied manganese to target breast cancer tumours with high level expression of Calcium Sensing Receptors (CaSRs) [34]. In the past decade the role of Ca^{2+} as the extracellular first messenger in causing or preventing cancer has been under active investigation [54] following the cloning of plasma membrane CaSR from the parathyroid gland [55]. CaSRs are seven-transmembrane G-protein-coupled receptors capable of sensing changes in extracellular calcium concentration, which inhibits secretion of parathyroid hormone (PTH) following binding with its physiological ligand Ca^{2+} [56]. CaSRs are expressed at different levels in normal human breast duct cells, in the duct cells of fibrocystic breast tissue, and in ductal carcinomas of the breast [57]. In addition, calcium ions play key roles not only in normal breast physiology but also in various

pathological conditions. *In vitro* studies have shown that increased Ca^{2+} levels induce terminal differentiation of normal human breast epithelial cells in culture [58]. Breast cancer has a marked tendency to spread to bone [59]. The observation that numerous cells within the bone marrow express CaSRs under normal circumstances [60], leads to the hypothesis that the presence of CaSRs on metastatic cells may contribute to their propensity to reside in bone, where locally high levels of Ca^{2+} are present during the resorption processes. The local Ca^{2+} level at resorption sites has been reported to rise as high as 40 mM [61]. Indeed, high Ca^{2+} levels (5, 7.5 and 10 mM) stimulate the secretion of parathyroid hormone related protein (PTHrP) in some breast cancer cell lines *in vitro*, presumably via a CaSR-mediated mechanism [62]. Excess PTHrP could contribute to the massive osteolysis caused by breast cancer bone metastases by promoting a feed-forward mechanism in which release of Ca^{2+} from the bone stimulates further PTHrP production and more bone resorption [63-65]. Interruption of this cycle by blockade of CaSR activity [66] could potentially offer substantial therapeutic benefit in this situation. Therefore, given the importance of Ca^{2+} in both the physiology and pathophysiology of the breast and bone, the CaSR could play different roles in these processes.

Moreover, the interest in CaSR has been refreshed by the finding that, in a selected group of patients with advanced breast cancer, CaSR expression assessed by immunohistochemistry is high, predominantly in tissue specimens from patients who developed bone metastases [67].

In our imaging study we addressed the possibility of using free MnCl_2 as a contrast agent in MRI of *in vivo* human breast cancer. This hypothesis was supported by previous observations showing that activation of CaSR by divalent cations such as Ca^{2+} and Mn^{2+} [68,69] triggers ion influx through

non-selective cation channels [38,70,71]. Therefore, we speculated that Mn^{2+} may accumulate in CaSR-positive breast cancer cells and allow their imaging. In addition, human breast cancer cell lines MDA-MB-231 and MCF-7, which give rise to tumours if transplanted in immunocompromised mice, express CaSR at different levels and secrete PTHrP upon stimulation [57,62,71,72].

Tumours formed by human breast cancer cells orthotopically implanted in the mammary fat pad of NOD/SCID mice maintain high CaSR expression and intravenous injection of $MnCl_2$ permits tumour imaging by a 3T MR scanner (**Figure 9, 10**).

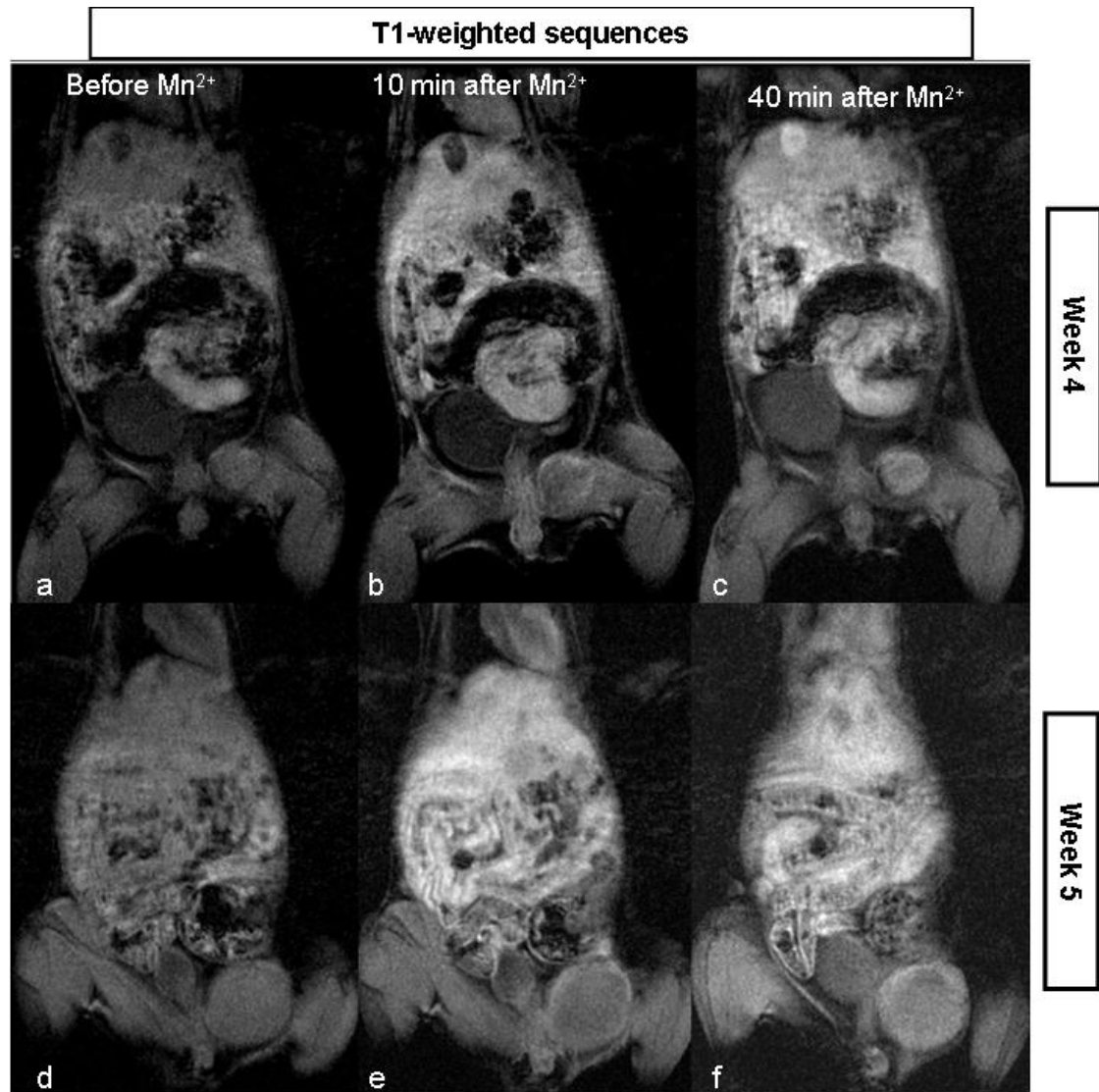


Figure 9. *Manganese enhanced MR imaging (MEMRI) of the orthotopic human breast cancer xenografts. a–f MRI of the same mouse at two different time points. The tumour dimension was 5 mm at the first determination and 10 mm the week after. On T1-weighted gradient echo images tumours showed a hyperintense area at their periphery (ring of manganese enhancement) 10 min after Mn^{2+} administration (b–e) and full contrast enhancement 40 min, with persistence of a brighter peripheral area (c–f) [34].*

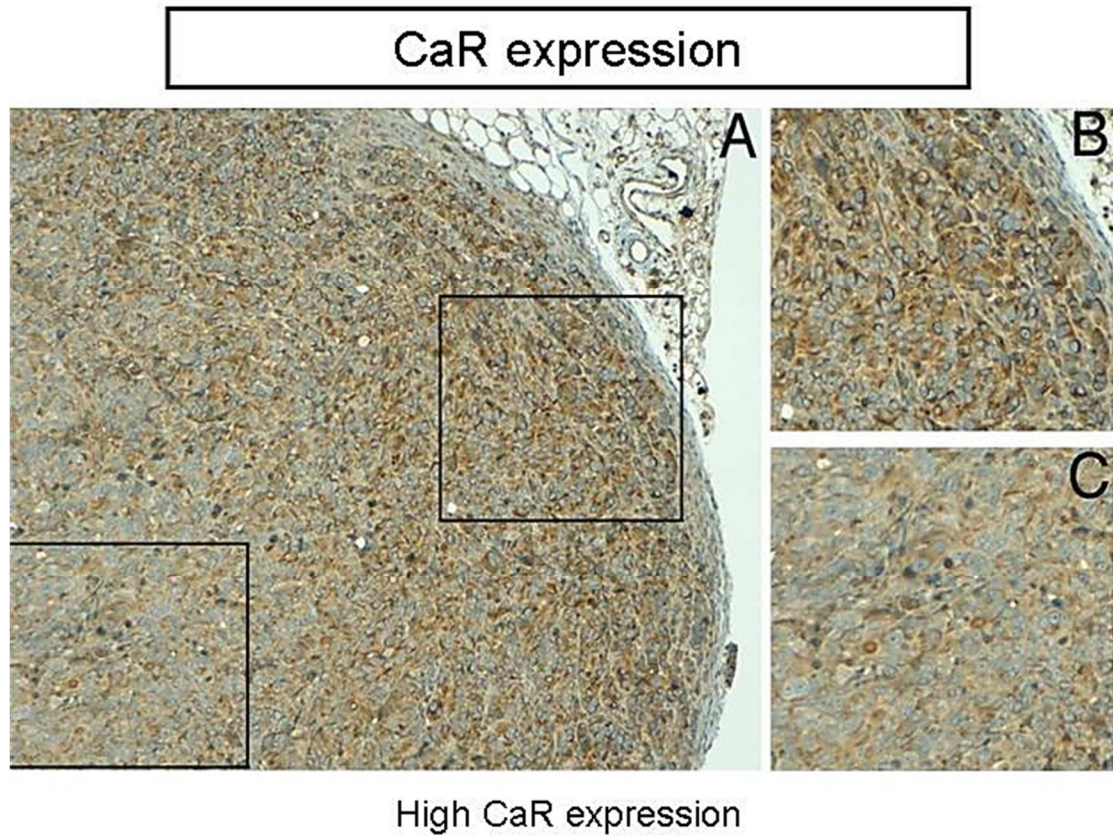


Figure 10. *Immunohistochemical analysis of CaSR in human breast cancer MDA-MB-231 cells xenograft (a–c). CaSR is detected in tumour cells (score 4–5) and displays more intense staining at the tumour periphery, as detailed in b and c. Original magnification 200× [34].*

The involvement of CaSR in MnCl_2 contrast enhancement was suggested by the study of its distribution in the tumour tissue and by blockade of MEMRI through the Ca^{2+} -antagonist drug verapamil (**Figure 11**).

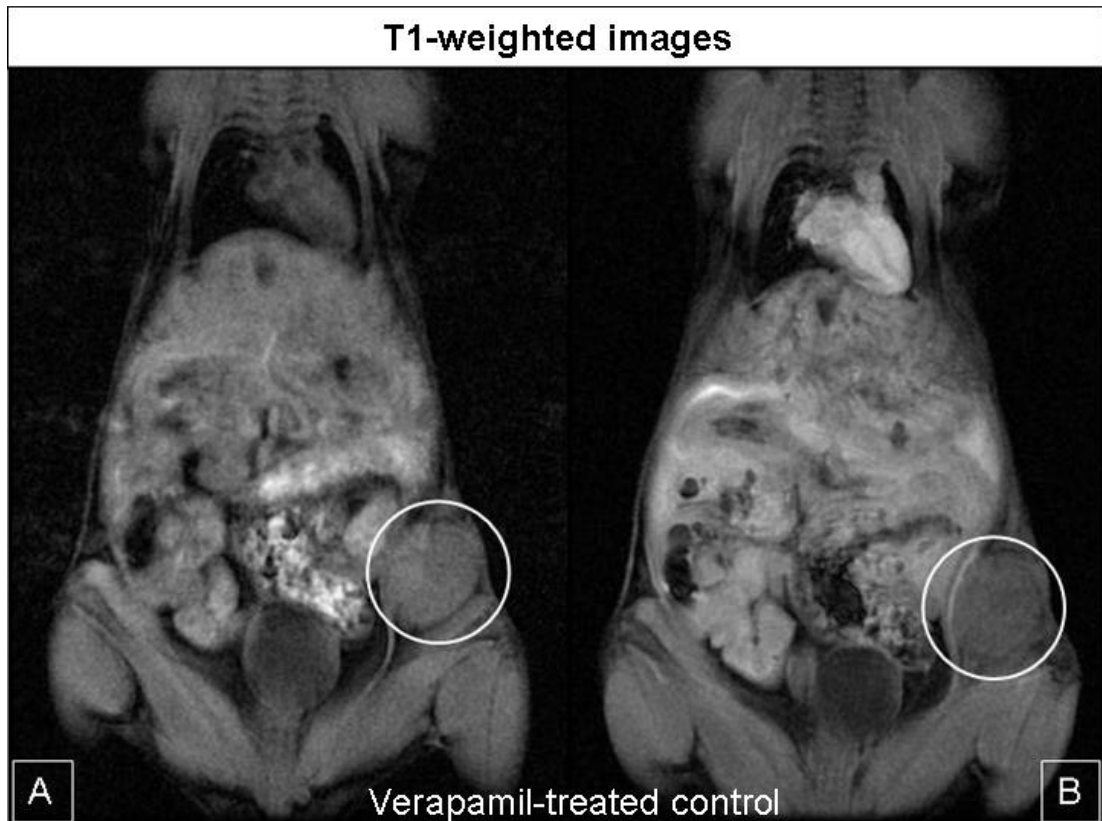


Figure 11. *A, B Coronal MR images of the orthotopic human breast cancer xenograft in a verapamil-treated control. MR images show no signal intensity increase after 40 minutes of Mn^{2+} administration (b) in the mouse treated with verapamil [34].*

A potential drawback to the use of Mn^{2+} as a contrast agent is its cellular toxicity, which limits the dose administered. It has been described that a dose of 30 mg/kg $MnCl_2 \cdot 4H_2O$ did not interfere with the animals' well-being [73]. Nevertheless, MR relaxation rates are proportional to the effective concentration of Mn^{2+} in tissue, thus significant amounts of Mn^{2+} are required to produce robust and detectable contrast. In our study, a single maximum dose of 8.5 mg/kg $MnCl_2$ was administered per mouse, well below the toxicity threshold described, and still permitted good SI in the MR images.

The goal of this study was to give proof of principle that Mn^{2+} could accumulate in breast cancer, possibly as result of CaSR expression *in vivo*. However, further studies to validate the role of manganese as tumour contrast agent were needed. Thus, we set up a method to evaluate the contribution of Mn^{2+} ions in the intra- and extracellular tumour compartments [74]. For imaging tumour detection and staging, it is relevant to assess whether the observed signal enhancement (SE) originates from the intracellular or the extracellular compartment. To tackle this task, we silenced the relaxation enhancement arising from Mn^{2+} in the extracellular space by using a sequestering agent which kept all the Mn^{2+} ions in the extracellular compartment in a highly stable chelate. The chelate was characterised by a low relaxivity (“MRI silent”). The comparison of the signal intensities of the region of interest (ROI) before and after the “sequestering” step allowed the identification of the relative contributions from intra- and extracellular tumour compartments in *in vitro* MEMRI experiment (**Figure 12**).

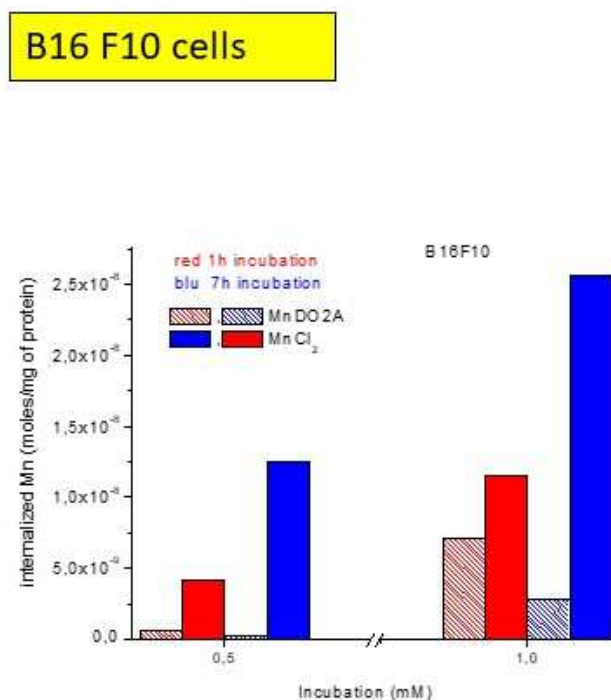


Figure 12. *Amount of internalized Mn²⁺ in B16F10 cells incubated with MnCl₂ and Mn-DO₂A for 1 and 7 h. (statistical analysis: $P < 0.01$; $P < 0.001$) [74].*

The interesting findings of this experiment underlined the different internalisation of Mn²⁺ ions also in *in vivo* experiments, between healthy and tumour tissues, since we found that in healthy tissue Mn²⁺ is mainly localised in the extracellular compartment while in the tumour tissues it is internalised in the intracellular compartment. The chemical composition of the extracellular microenvironment in healthy tissue may be very different from that present in tumours. Serum albumin could represent a reason why Mn²⁺ is temporarily sequestered. The main impact of this study was in providing a new insight in the investigation of Mn²⁺ as MR contrast agent to target tumours and thus strengthen the MEMRI approach for early detection and characterisation of tumours' calcium metabolism.

1.3. Exploring a new role of MEMRI for visualising brown adipose tissue.

The recent increased attention on the role of active BAT in adult humans, and its relationship with different pathological conditions, has opened new avenues, particularly in obesity research and treatment, diabetes, hypertension, and cancer cachexia. The study of BAT is interesting because, although the amount of this tissue is very small, it can have a pivotal role in the biology of energy balance. This tissue is found mainly in the neck, chest, around major blood vessels, muscles or white adipose tissue. High mitochondrial and capillary content, as well as the presence of uncoupling protein one (UCP1), are the main characteristics. Activation of UCP1 enables free-flow of protons across the mitochondrial membrane, resulting in rapid dissipation of chemical energy as heat. The primary energy source for this process comes from esterified fatty acids that are released from lipids at the same time as UCP1 is activated, usually through activation of the sympathetic nervous system.

Obesity and cancer cachexia are two conditions that result from an imbalance between energy intake and energy expenditure where the activation of BAT seems to play an important role. How cancer induces thermogenesis in brown fat cells and how this might relate to the wasting of fat and skeletal muscle is still unknown.

Clinical investigations on BAT's role and its activation in cancer are currently limited by the lack of non-invasive tools for measuring the mass and function of this tissue in humans. Currently, ¹⁸FDG-PET/CT (2-deoxy-2-fluorine-18-fluoro-D-glucose positron emission tomography/ computed Tomography) is considered the “gold-standard” method to identify BAT in humans [75], although BAT glucose metabolism does not accurately reflect

BAT thermogenic activity [76]. It is important to note that accurate quantification of total BAT volume of metabolic activity by the addition of numerous small regions of interest, typically less than 1 cm³ each, is very challenging with PET [76,77].

During the MEMRI experiments, we incidentally observed manganese uptake by Brown Adipose Tissue (BAT). We thus performed a new set of experiments to further investigate brown adipose tissue in both healthy controls and breast or prostate cancer animal models (orthotopic and pseudo-metastatic cancer animal models) using MEMRI [78]. We applied manganese as a contrast agent because of its accumulation in cells via calcium channels. Calcium ion influx has been linked with brown adipose tissue activation through adenosine triphosphate (ATP) [79,80] and we hypothesised that Mn²⁺, as a calcium surrogate, may accumulate in BAT through mitochondria and transient receptor potential channels (TRP), thus allowing its imaging.

MEMRI was able to visualise the activation and localisation of BAT vs white adipose tissue (WAT) in healthy controls (**Figure 13**) and in cancer animal models (**Figure 14, 15**).

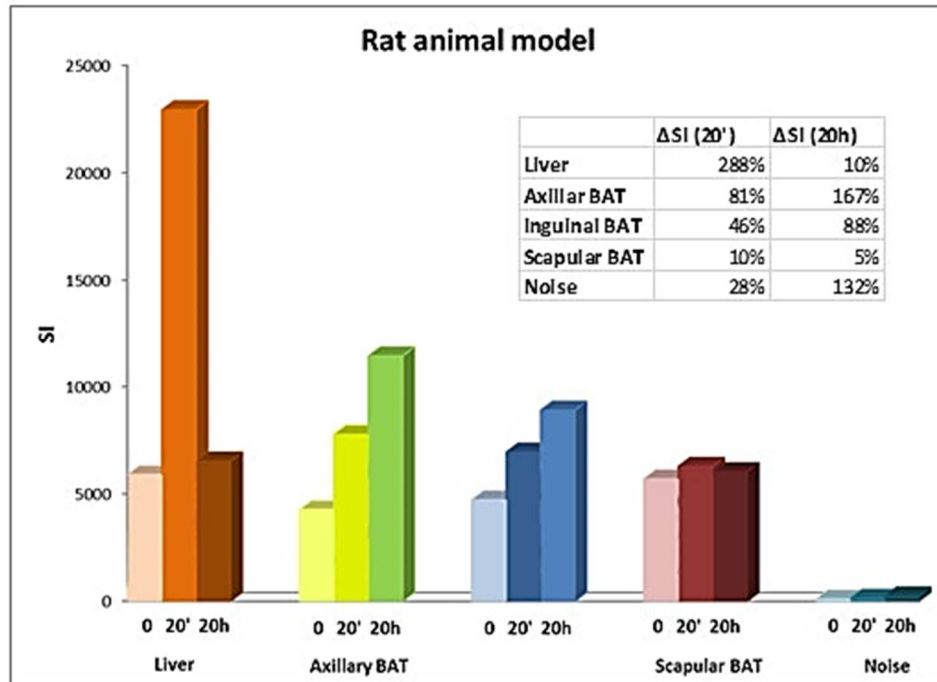


Figure 13. *In vivo Non-invasive Detection of Brown adipose Tissue (BAT) through Manganese Enhanced Magnetic Resonance Imaging (MEMRI) in healthy controls.* Signal intensity of liver, axillary, inguinal and scapular BAT, was calculated before and 20 minutes and 20 hours after $MnCl_2$ administration. $\Delta SI\%$ values are indicated in the table per each organ [78].

In cancer animal models BAT manganese uptake was independent from cold exposure or chemical drug activation. Especially, cancer animal models with advanced disease (pseudo-metastatic breast or prostate cancer animal models; **Fig. 14**) demonstrated a significant increase in BAT manganese uptake compared to localised tumour animal models (orthotopic breast or prostate cancer animal models; **Fig. 15**) ($P < 0.05$).

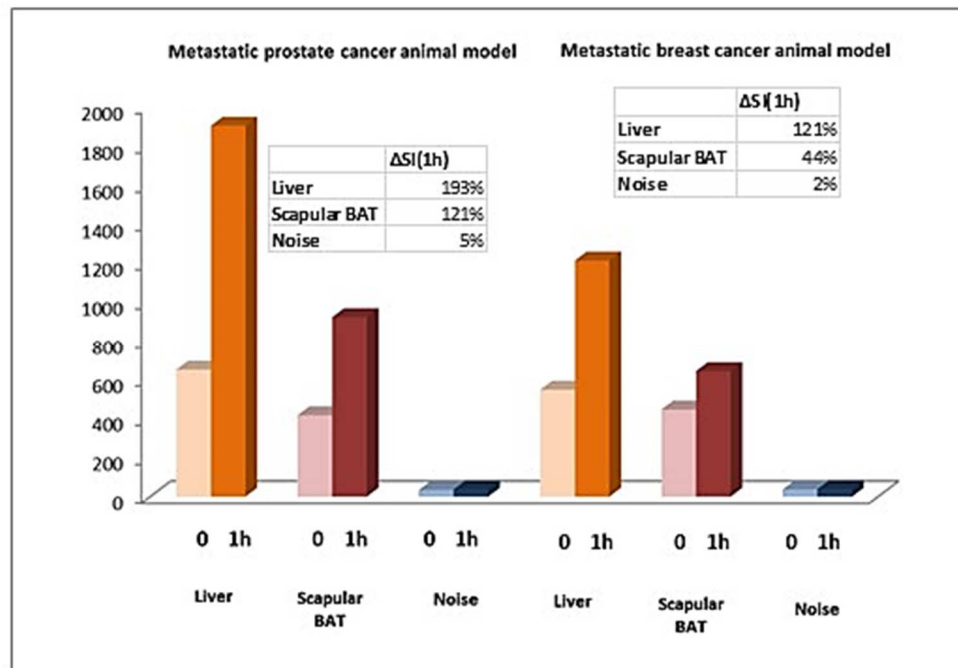


Figure 14. *In vivo Non-invasive Detection of Brown adipose Tissue (BAT) through Manganese Enhanced Magnetic Resonance Imaging (MEMRI) in metastatic prostate and breast cancer animal models. Signal intensity of liver and scapular BAT was calculated before and one hour after $MnCl_2$ administration. $\Delta SI\%$ values are indicated in the table per each organ [78].*

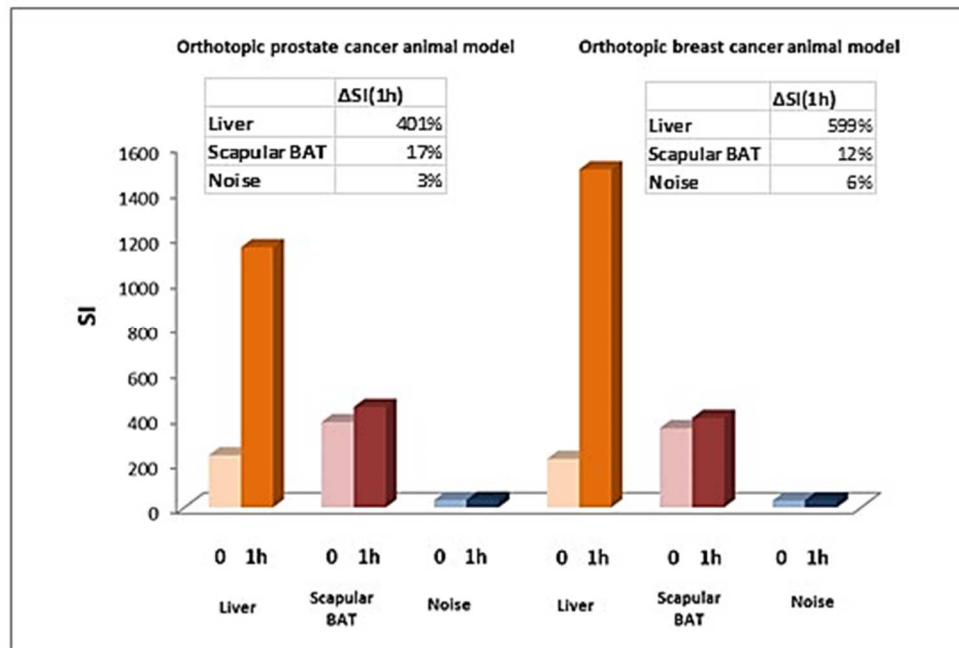


Figure 15. *In vivo Non-invasive Detection of Brown adipose Tissue (BAT) through Manganese Enhanced Magnetic Resonance Imaging (MEMRI) in orthotopic prostate and breast cancer animal models. Signal intensity of liver and scapular BAT was calculated before and one hour after $MnCl_2$ administration. $\Delta SI\%$ values are indicated in the table per each organ [78].*

The increased activity of BAT in the metastatic animal model (advanced disease) compared with the orthotopic model (localised disease) may suggest important implications of BAT in tumour progression and, thus, cancer cachexia. More studies in the molecular characterisation of the two different BATs are necessary to better understand the molecular process behind cancer progression and BAT activation.

Our findings opened important opportunities in the application of manganese as an MRI contrast agent to better understand BAT physiology and physiopathology *in vivo* and its role in cancer progression. The results of this research are not completely published yet, but they have been included in

this thesis because they were presented and awarded with a prize during the World Molecular Imaging Congress in 2015. This study was also selected as high impact research by Professor John C. Gore during his Highlighted Plenary Lecture (session 7- WMIC) [78].

1.4. Application of *in vivo* proton MR spectroscopy in breast cancer expressing different levels of calcium sensing receptors.

The main limitation of studies using Manganese as an MR contrast agent is that Manganese is not commercially available for application in the clinical setting, and thus can only be investigated in preclinical Molecular Imaging studies. To overcome this limitation and to further explore the role of CaSR in breast cancer tumours, we developed a prospective clinical MR investigation using *in vivo* proton magnetic resonance spectroscopy (^1H -MRS) in breast cancer patients [81].

Cancer cells have a multitude of redundant pathways and networks, and one of the hallmarks of cancer is the “cholinic phenotype” [82]. Activated cancer choline metabolism is characterised by increased phosphocholine (PCho) and total choline-containing compounds (tCho), which was discovered mostly via magnetic resonance spectroscopy (MRS) studies of tumours in the 1980s [83,84]. Initially, the increased PCho levels in cancer cells were considered as a significant indication of high rate of cancer cell proliferation [85]. Subsequent studies demonstrated that PCho and tCho levels in non-malignant breast or prostate epithelial cells identified malignant transformation, rather than just cell proliferation, as the cause of abnormal choline metabolism in cancers [86]. The search for biomarkers to detect cancer and to monitor non-invasively the response to treatment has led to

several clinical studies evaluating the non-invasive detection of tCho for these objectives.

Similar to studies in cancer cells [87], human tumour xenograft models [87], excised tumour tissue [88,89] and clinical studies have confirmed the activation of choline metabolism in human tumours *in vivo* [87,90]. Phosphocholine is both a precursor and a breakdown product of phosphatidylcholine (PtdCho), which, together with other phospholipids such as phosphatidylethanolamine (PtdEtn) and neutral lipids, forms the characteristic bilayer structure of cellular membranes and regulates membrane integrity [91]. The synthesis of PtdCho and PtdEtn, which are the most abundant phospholipids in the cell membrane, was first described by Kennedy and Weiss in 1956 [92] and this *de novo* biosynthesis of PtdCho and PtdEtn is termed the Kennedy pathway. The high-energy intermediates cytidine diphosphate (CDP)-choline and CDP-ethanolamine are required to synthesise PtdCho and PtdEtn. These two mirror pathways, one that uses choline and the other that uses ethanolamine, are called the CDP-choline and CDP-ethanolamine pathways, respectively. The biosynthesis and hydrolysis of PtdCho mediates mitogenic signal transduction events in cells, and products of choline phospholipid metabolism, such as PCho [93], diacylglycerol (DAG) [94,95], and arachidonic acid metabolites [94], may function as second messengers that are essential for this mitogenic activity. Growth factor stimulation [95], cytokines [96], oncogenes [86] or requirements for eicosanoid production [94] also regulate choline phospholipid metabolism. Underlying these phenotypic alterations in choline metabolism is a network of transporter systems and enzymes involved in choline phospholipid metabolism that are deregulated in cancer cells. The increased PCho and tCho levels that have been detected in human cancers are caused by interplay between multiple enzymes, which are at the

core of choline metabolism and which constitute the biosynthetic and catabolic pathways of PtdCho.

The understanding of the molecular mechanisms that regulate the production of PCho compound is very limited. *In vitro* studies on breast cancer cells demonstrated the important role of the CaSR in the pathway of choline kinase (ChoK) activity and PCho. Calcium ions induce a significant increase in extracellular PCho production in breast cancer cells primarily related to CaSR-induced ChoK activation and not from degradation of choline phospholipids [97]. Since a high level of CaSR expression induces a high concentration of calcium ions that activate ChoK in breast cancer cells, resulting in increased PCho production, we hypothesised that ¹H-MRS may detect elevated choline peak levels in breast cancer patients related to CaSR activity and expression levels demonstrated with immunohistochemistry analysis.

We prospectively correlated clinical results of breast MR spectroscopy obtained with a 3T MR scanner and CaSR-positive and negative breast specimens at immunohistochemistry analysis [81]. CaSR-expression-level quantification at immunohistochemistry analysis was also developed (**Figure 16**).

Immunohistochemistry of CaSR (score 0-5)

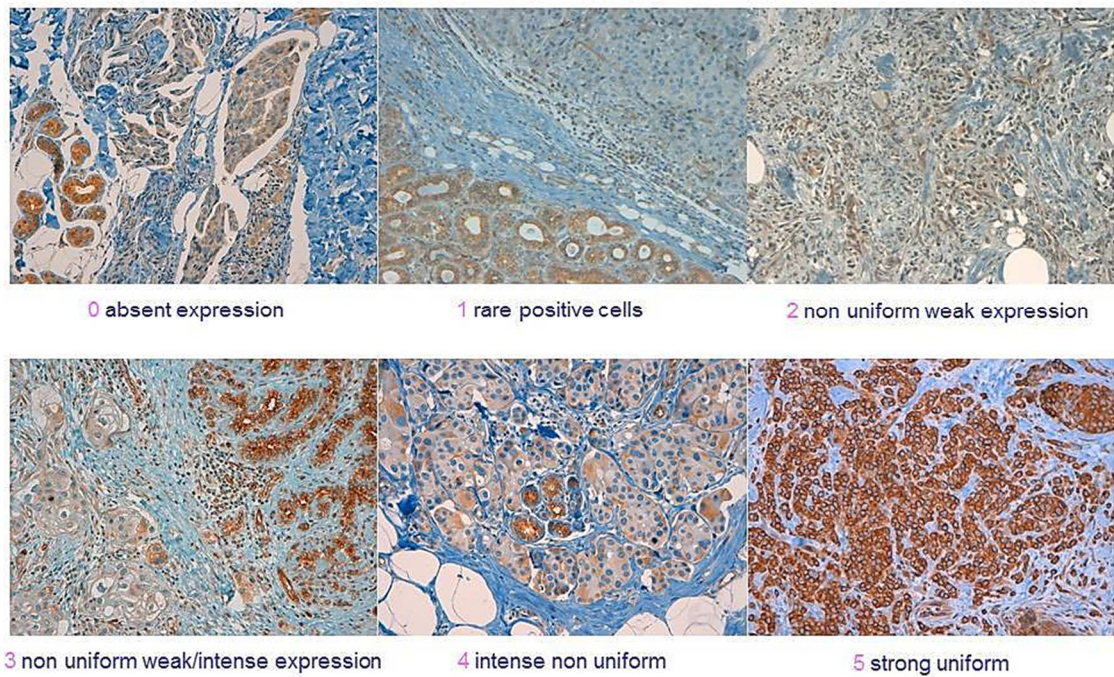


Figure 16. *Immunohistochemical analysis of CaSR expression in human breast cancers specimens (score 0-5) [81].*

The aim of this preliminary study was to evaluate a potential role of the CaSR in choline metabolism in breast lesion detected by ^1H -MRS. A total of 68% of the malignant lesions showed a positive choline peak (**Figure 17**), while 32% were negative (**Figure 18**). The combination of tCho measurement with DCE-MRI increases the specificity of malignancy up to 88% (100% after the inclusion of a single-slice T2* perfusion measurement) [98]; indeed, tCho is significantly higher in mass-type cancers compared to non-mass-type cancers [99]. In our study, 32% of breast cancers showed a negative tCho and in 91% of these lesions CaSR expression was low (score 1–2) (**Figure 18**). These results were supporting the correlation between the expression of this receptor in breast lesions and how this expression may influence the choline production within the tumour subsequently detected with ^1H -MRS.

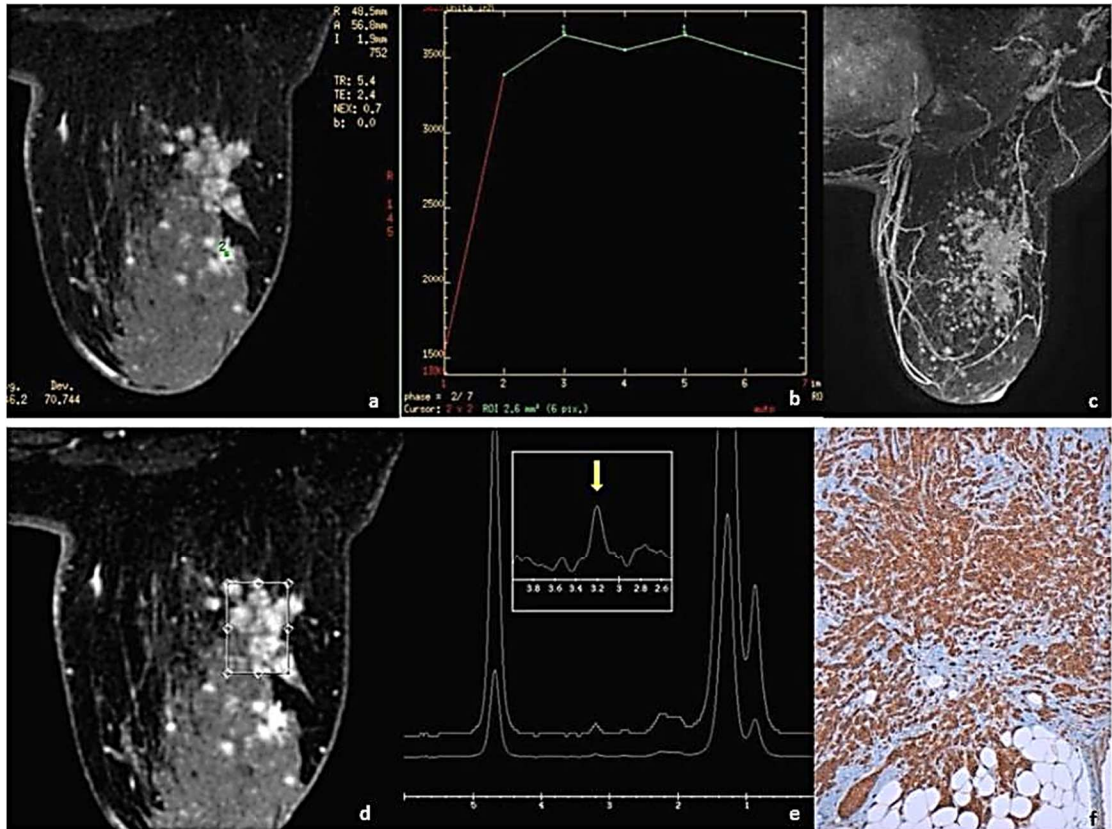


Figure 17. **Proton MR Spectroscopy choline peak and calcium sensing receptor (CaSR) correlation.** A 58-year-old woman with an invasive lobular carcinoma. a) Axial VIBRANT (Volume Imaging for BReast AssessmeNT) contrast-enhanced magnetic resonance (MR) image (repetition time/echo time [TR/TE] 5.3/2.4ms; 1.2mm slice thickness) shows an enhancing irregularly multifocal and multicentric lesion in the right breast. b) Malignant type kinetics intensity curve with rapid enhancement in the initial phase followed by a plateau in the late phase. c) MIP reconstruction image of the lesion in the right breast. d-e) Single-voxel MR spectroscopy (BREASE sequence): VOI localisation on the axial VIBRANT contrast-enhanced magnetic resonance MR image and the resonance peak of total composite choline compounds (tCho) that was evident at 3.2 ppm. f) Immunohistochemical analysis of CaSR expression in human breast cancer specimen (score 5) [81].

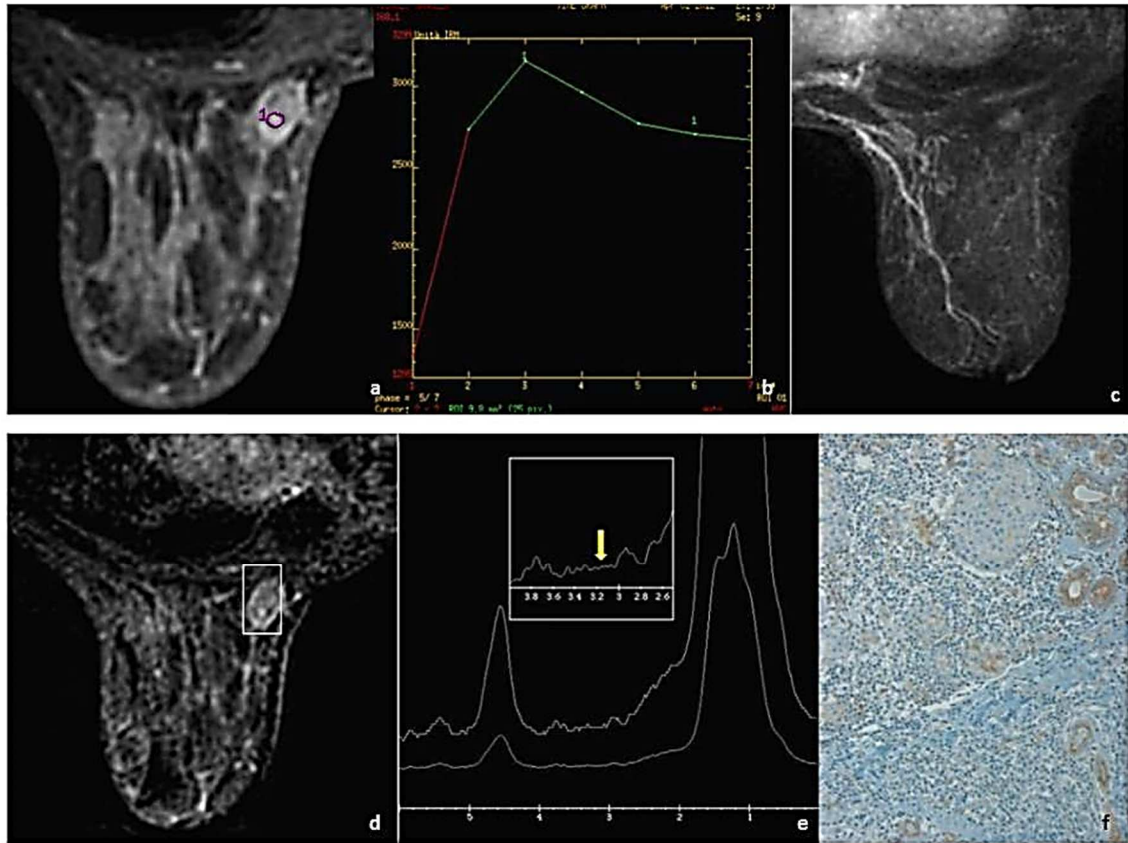


Figure 18. **Proton MR Spectroscopy choline peak and calcium sensing receptor (CaSR) correlation.** A 62-year-old woman with an invasive lobular carcinoma. a) Axial VIBRANT (Volume Imaging for BREast Assessment) contrast-enhanced magnetic resonance (MR) image (repetition time/echo time [TR/TE] 5.3/2.4ms; 1.2mm slice thickness) shows an enhancing nodule in the left breast. b) Malignant type kinetics intensity curve with rapid enhancement in the initial phase followed by washout. c) MIP reconstruction image of the lesion in the left breast. d-e) Single voxel MR spectroscopy (BREASE sequence): VOI localisation on the axial VIBRANT contrast enhanced magnetic resonance MR image and the resonance peak of total composite choline compounds (tCho) that was not evident at 3.2 ppm. f) Immunohistochemical analysis of CaSR expression in human breast cancer specimen (score 1) [81].

Benign lesions on DCE-MRI, diagnosed as papillary hyperplasia/apocrine metaplasia at the histology examination (“borderline benign lesions”), showed a consistent choline peak and CaSR with a high score (score 3). Although the sample size is insufficient in this group for clear conclusions, this result is consistent with the idea that this receptor is expressed and probably differently regulated in both benign and malignant conditions [100], thus influencing the ^1H -MRS results.

The physiological mechanism behind the CaSR-choline pathway confirms the importance of the role of this receptor in breast cancers. DCE-MRI plus ^1H -MRS could play an important role in the study of breast cancer and CaSR, allowing a “molecular imaging diagnosis” of this select group of patients with a high risk to develop bone metastases. Many clinical studies have already applied ^1H -MRS to monitor the response of locally advanced breast cancer, showing that the change in tCho concentration can serve as an indicator for predicting clinical response to therapy [101,102]. It would be challenging to investigate more how the receptor expression changes under chemotherapy and how this relates to the choline peak changes. Recent investigation of BRCA1 and CaSR showed how these two factors together suppress the expression of survivin and promote sensitivity to paclitaxel in human breast cancer cell [103]: this is another example of how CaSR could influence not only therapy response, but also the imaging results when using a technique such as ^1H -MRS (CaSR-choline production).

The future in biomarker research for the evaluation of treatment response will be the correlation of gene expression and MR imaging. Gene arrays and immunohistochemistry analysis of CaSR-Cho pathways could help to better

understand which gene expression is related to specific changes in the aggressiveness of the disease, as assessed by MRI.

The ongoing research and the development of new functional MR techniques applied in routine clinical care indicates that the prospects for substantial improvements in monitoring therapeutic response, as well as for early detection of breast cancer, are promising [104]. A key factor to success will depend on the reproducibility of the qualitative and quantitative measurements performed by imaging techniques such as MRI-¹H-MRS.

1.5. A non-invasive approach to investigate chronic lymphocytic leukaemia by using iron oxide nanoparticles.

Chronic lymphocytic leukaemia (CLL) is the most common form of adult leukaemia in Western countries. CLL is characterized by the clonal expansion of mature CD5+/CD23+ lymphocytes that can infiltrate multiple organs including lymph nodes, the bone marrow, spleen, and liver. CLL is heterogeneous in terms of therapy-free interval, response to treatment, and overall survival, ranging from rapid disease progression requiring early and frequent treatment, to survival for decades with minimal or no treatment. Computed tomography (CT) is used as the first-line modality for imaging of lymphoid malignancies [105]. The role of CT has not been clearly defined in CLL patients, although CT for routine disease monitoring of CLL has been largely discouraged [106-108]. CT scans are recommended for baseline and final assessment in clinical trials, but CT is not the method of choice for clinical staging [109,110]. On the other hand, FDG/PET, although not recommended on a routine basis, has proven useful in detecting the transformation of CLL into Richter Syndrome (RS) and for selecting the optimal site for performing a diagnostic biopsy [111-114]. Magnetic

resonance imaging (MRI) has been applied to investigate the involvement of the nervous system by CLL [115] or, for example, to diagnose bone marrow infiltration by CLL cells [116,117]. The interest for MRI relates to the intrinsic physical properties of this technique, which provides high sensitivity without the need for exposure to ionising radiation.

Several mouse models for the study of CLL development have been established. These encompass transgenic models in which key genes have been altered or xenograft models that use immunodeficient mice that are engrafted with human leukemic cells. In all instances, development of the CLL clone can be followed by monitoring peripheral blood for the presence of leukemic cells, but the evaluation of lymphoid tissues (i.e. the spleen in immunodeficient mice, as lymph nodes are mostly atrophic), where the leukemic cells have to seed to begin their proliferative phase, requires sacrificing the animals. Thus, sensitive and safe imaging techniques to monitor disease development may be useful in preclinical models and, more importantly based on the above considerations, may also find application in routine clinical practice. The sensitivity of MRI in *in vivo* preclinical studies can be improved by using a specific molecular imaging agent. With the help of efficient imaging agents, it is possible to detect early-stage disease precisely and to monitor the response to drug therapy. The efficacy of iron oxide nanoparticles used as specific contrast agents in MRI for liver, spleen, and lymph nodes has been demonstrated in experimental and clinical studies. Several studies have shown that these particles can significantly improve the detection and characterisation of focal lesions within these organs [119-121].

In our study [122], we aimed to establish a non-invasive specific MRI method to better visualise and quantify the presence of CLL disease by

USPIO within the spleen in a pre-clinical setting (**Figure 19, 20**). In particular, we used a mouse xenogeneic transplantation model, NOD/Shi-scid, γ cnnull (NSG) mice, a NOD/SCID-derived strain that lacks the IL-2 family common cytokine receptor gamma chain gene (γ c) [123,124]. A secondary goal of this study was to monitor CLL disease evolution using imaging strategies to reduce the overall number of mice needed to evaluate CLL cell engraftment over several time points, limiting their sacrifice and suffering during experimental protocols. We first observed that changes in spleen organisation could be identified four weeks after CLL cell inoculation using a 3T clinical scanner and USPIO nanoparticles (**Figure 21**). Histology of the spleens confirmed the presence of CD20+ nodular structures surrounded by CD3+ cells (**Figure 21**). In addition, Perls' Prussian blue staining demonstrated that iron particles were excluded from the nodular areas occupied by lymphoid cells, providing a rational explanation for the MRI signals observed (**Figure 21**). The combination of extracellular with intracellular iron oxide nanoparticle compartmentalisation within the CLL spleen affected iron oxide proton relaxivity, which sometimes resulted in an increase rather than the expected SI decrease. This high T2-USPIO effect has also been reported by Simon G.H. *et al.* [125]. Measuring circulating T and B cells can be employed to assess CLL engraftment in NSG mice by using flow cytometry (FC) analysis; however, this method may be misleading, as leukemic cells can be difficult to track due to their extremely low number in peripheral blood. In addition, when tracked, the leukemic cells may represent cells merely surviving after the injection. In contrast the application of USPIO enhanced MRI spleen analysis was able to assess the engraftment of CLL cells two weeks after their injection, as could also be confirmed by immunohistochemistry (IHC) evaluation.

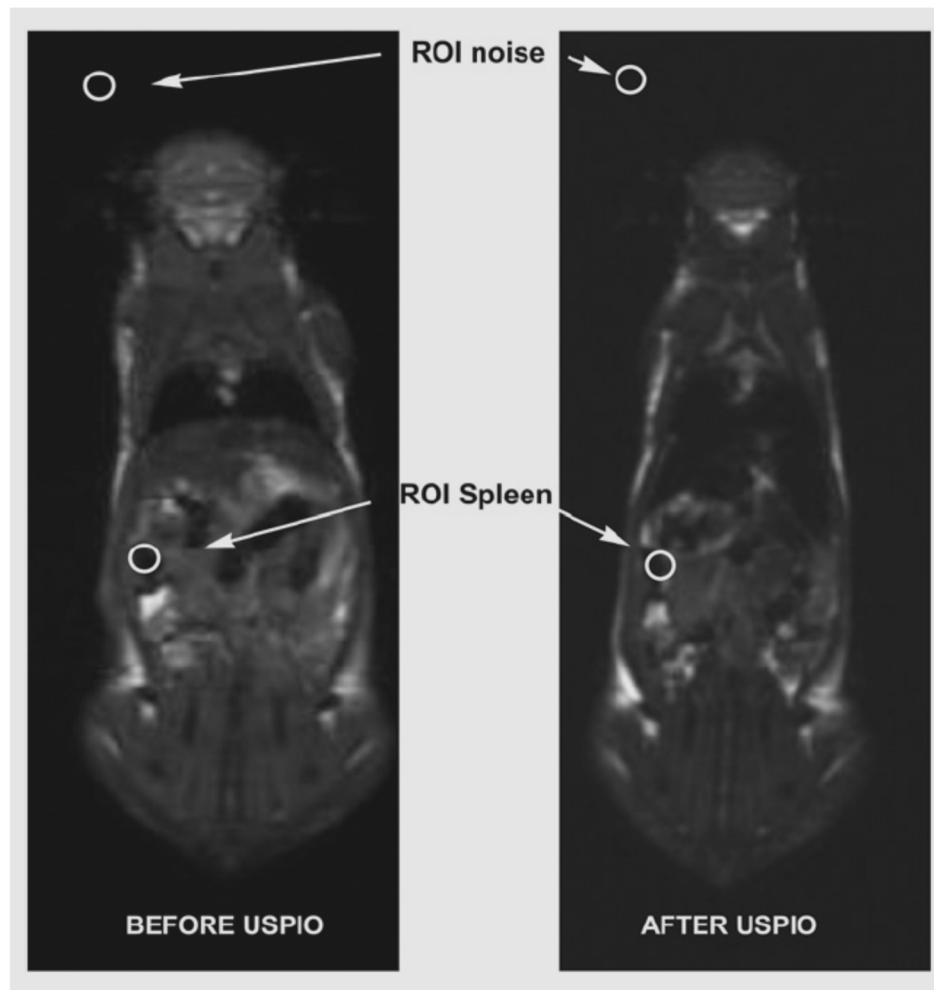


Figure 19. *Representative slices of the sequence protocol used to measure the signal intensity (SI) in tissues of interest. The regions of interest (ROIs, white circles) were drawn in the tissues of interest, spleen and in the region outside the anatomy of the mice (background noise) in order to measure the signal intensity (SI), as mean \pm standard deviation (SD) and to calculate the signal-to-noise ratio (SNR) [122].*

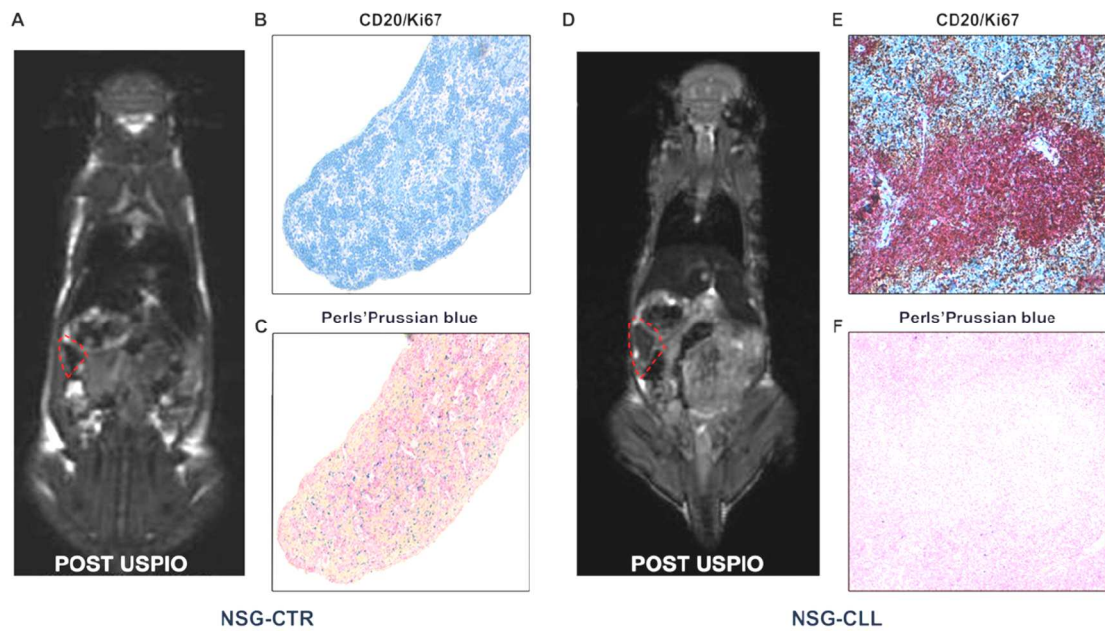


Figure 20. *Magnetic resonance image signal determination and histological analysis in control (NSG-CTR) compared to engrafted (NSG-CLL) mice. The figure shows representative in vivo USPIO magnetic resonance images (MRI) obtained after 24 h of USPIO administration in NSG-CTR (A) and NSG-CLL mouse (D). The position of the spleen is indicated by the red outline. Matched histology sections (magnification, 100 \times) show the absence (B) or the presence (E) of CD20 (red) and Ki67 (brown) positive cells; Perls' Prussian blue ferric iron staining (C and F) allows the detection of USPIO nanoparticles [122].*

A reliable assessment of CLL engraftment two weeks after leukemic clone inoculation is most advantageous given that this animal model does not allow long term persistence/expansion of the inoculated leukemic cells beyond six–to-eight weeks. Thereafter, mice can develop a graft-versus-host disease that may also cause the reduction and even disappearance of the leukemic cells [124]. In addition, leukemic cells can mature into plasmablasts/plasma cells [126]. The above limitations might confound the experimental data, particularly when drug treatments are evaluated, because this time-frame may not be sufficient to provide information on the long-term effect of drugs.

We also reported the possibility of identifying a cut-off value for $\Delta\text{SNR}\%$ able to discriminate NSG-CLL from NSG-CTR or NSG-ne mice.

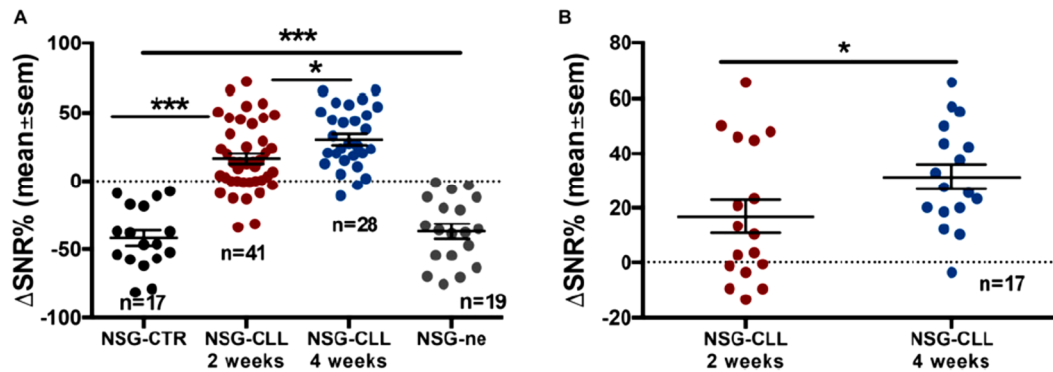


Figure 21. *Comparison of magnetic resonance image signal intensity change in the spleen of control mice (NSG-CTR), mice engrafted (NSG-CLL) at 2 and 4 weeks, and non-engrafted (NSG-ne) mice. (A) The scatter dot plot represents percentage signal-to-noise ratio change ($\Delta\text{SNR}\%$) of the MRI acquisition analysis comparing NSG-CLL mice at 2 weeks (red dots) and 4 weeks (blue dots) from peripheral blood mononuclear cell (PBMC) CLL injection, NSG-CTR mice (black dots) and NSG-ne (grey dots, evaluated at 4 weeks from PBMC CLL injection). Values of $\Delta\text{SNR}\%$ are expressed as mean \pm sd. NSG-CTR mice: -42.16 ± 5.6 ; NSG-CLL at 2 weeks: $+16.32 \pm 3.95$; NSG-CLL at 4 weeks: $+30.49 \pm 4.0$; NSG-CLL-ne mice: -37.21 ± 5.5 . Statistical comparisons were carried out using the Mann-Whitney U test. A P-value < 0.0001 is indicated by *** and $P = 0.017$ by *. (B) Comparison of MRI signals detected in the same mice 2 weeks (red dots) or 4 weeks (blue dots) from PBMC CLL injection ($P = 0.02$, Wilcoxon-matched pair test) [122].*

A similar cut-off value was used to identify the different disease extension at two and four weeks after inoculum in NSG-CLL mice. The identification of a relatively precise cut-off allows investigators to accurately define when a single mouse can be considered engrafted or not and make decisions regarding the subsequent experimental procedures. This analysis however requires standardisation of the instrument(s) used for the image acquisition.

USPIO-enhanced MRI was also able to detect CLL disease regression after rituximab treatment of engrafted mice. MRI images, acquired before and following treatment, detected definite changes with an inversion of the Δ SNR% value (**Figure 22**).

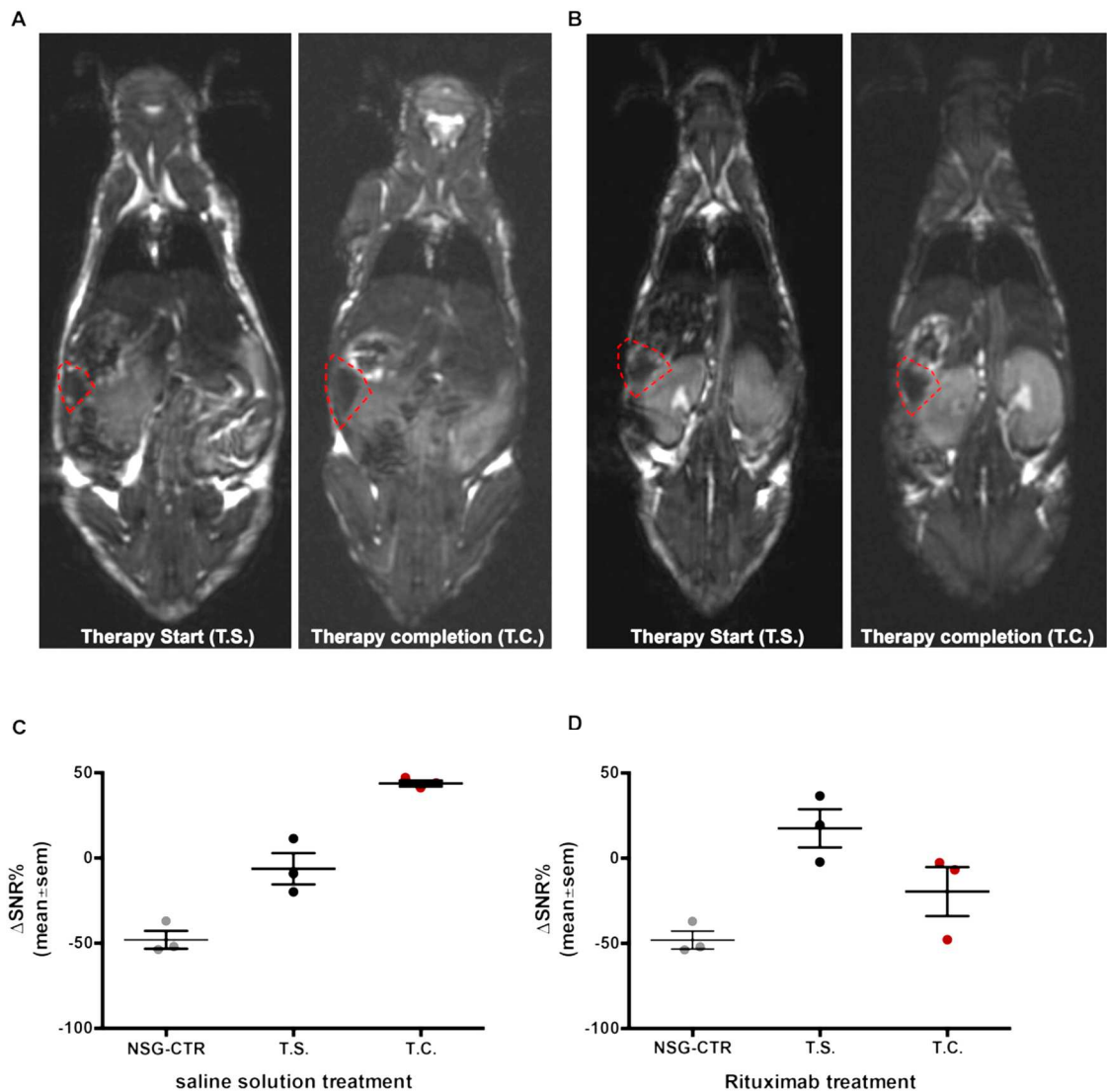


Figure 22. **Representative experiment of treatment with rituximab.** The figure shows a representative *in vivo* USPIO magnetic resonance image (MRI) obtained 24 h after USPIO administration in a NSG-CLL mouse treated with saline solution (A) and a NSG-CLL mouse treated with rituximab (B). The position of the spleen is indicated by the red outline. MRI images show acquisition at therapy start (T.S.) and at therapy completion (T.C.). The scatter dot plots (C) and (D) display data for each mouse and percentage signal-to-noise ratio change (Δ SNR %) mean values are calculated for each treatment-mice group ($n=3$) and the control NSG-CTR group [122].

Immunohistochemistry (IHC) showed a radical change in the architecture of the spleen of treated animals compared to controls. Following treatment,

lymphoid infiltrates were mainly represented by unorganised T lymphocytes with the loss of the typical CD20+ nodular areas. Tissue Perls' Prussian blue stain confirmed the diverse disposition of USPIO nanoparticles. Thus, this technique clearly distinguished between the different types of lymphoid infiltrates based on their organisation (**Figure 23**).

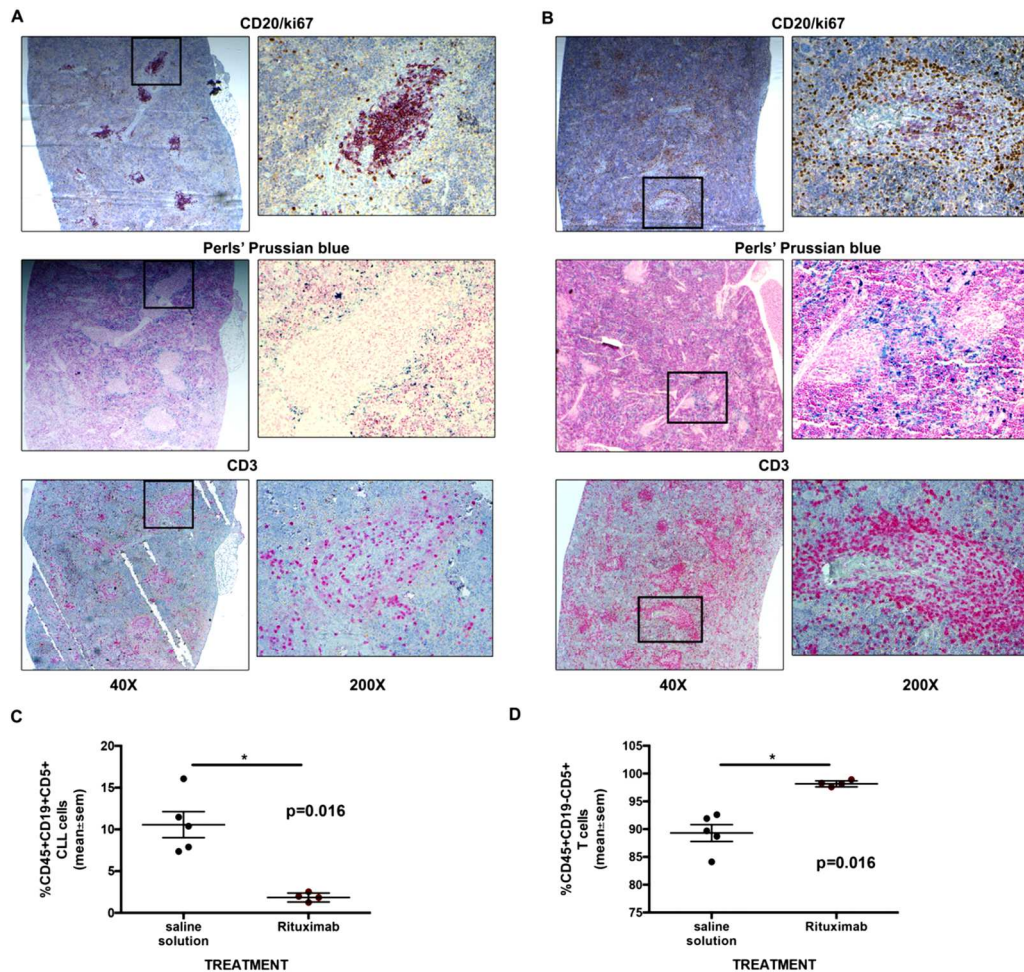


Figure 23. **Representative Immunohistochemistry and flow cytometry analysis of mouse spleens from a rituximab experiment.** The figure shows the histological analysis carried out for the presence of CLL cells (CD20, red), proliferating cells (Ki67, brown), T cells (CD3, red) and USPIO nanoparticles (Perls' Prussian blue) in the NSG-CLL mice treated with saline solution (A) and in NSG-CLL mice treated with rituximab (B). Magnification 40 \times (left panels) and 200 \times (right panels). In panels C and D, the scatter-plots show the presence of CLL cells and autologous T-cells, respectively, evaluated by flow cytometry (CD45+/CD19+/CD5+ or CD45+/CD19-/CD5+), indicating a significant decrease of

the percentage of CLL cells in the group of mice treated with rituximab (n = 4) compared to the control group treated with saline solution (n = 5). Statistical comparisons were carried out using a Wilcoxon test [122].

Another point that should be underlined is that the use of this technique limits the number of animals to be tested and sacrificed. This is important for several reasons: first, it requires fewer leukemic cells for injection, thus sparing other cells for additional experimental procedures. Although many CLL cells can generally be recovered from CLL patients, a typical experiment may require more than half a billion cells, a quantity often obtained from selected patients only. Second, this approach facilitates clearance of animal experimentation protocols by ethics committees. Currently, animal testing regulations pay increasing attention to the procedures and the experimental settings applied, encouraging the use of methods that limit animal sacrifice and, ultimately, the suffering of animals. A related point is the control of experimental variability, as only animals with evidence of disease are used to complete the experimental procedures with no additional trauma.

The results of this research were published in a special issue of *Clinical Immunology* to commemorate Dr Henry G. Kunkel, father of both clinical and basic immunology [127].

The established USPIO-MRI imaging approach to investigating CLL has been applied successively in new set of experiments [128]. In lymphoproliferative disorders, chromosomal abnormalities, including deletions, translocations or duplications, have traditionally led to the identification of genes that frequently have a pivotal role in disease pathogenesis [129]. Specifically, the deletion at 13q14.3 [del(13)(q14)] is

observed in approximately 50% of CLL cases, either in a mono- or biallelic form, and is also present in the early disease stages [130,131], including monoclonal B cell lymphocytosis [132,133], suggesting a likely pathogenetic role. The search for the gene(s) involved in the deletion was complex and unfruitful for a long time until the identification of the DLEU2 gene: a DNA segment that carries the locus of two microRNAs (miRNAs), called miR-15a and miR-16-1 (miR-15 and miR-16, respectively), located in the fourth intronic region [135-139]. miRNAs are single stranded, non-coding RNA, which are evolutionarily conserved and capable of regulating the expression of several genes concomitantly [140]. The regulation of gene expression occurs mainly through the specific binding of miRNAs to the 3'-un-translated region (3'-UTR) of the messenger RNA of the target gene via a RNA-induced silencing complex (RISC) [141], although additional mechanisms have been described [142].

In this study [129], we investigated the possibility of interfering with both miR-15 and miR-16 expression by CLL cells, both in *in vivo* and *in vitro* experiments. Collectively, the data indicate that control of target genes by miR-15 and miR-16 is still functional in full-blown leukaemia, since the transfection of miR-15 or miR-16 mimics in CLL cells, with del(13)(q14), results in diminished survival *in vitro* and impaired growth in NSG mice. In contrast, inhibition of miR-15 or miR-16 expression by specific inhibitors in CLL cells lacking del(13)(q14) favours cell survival *in vitro* and cell engraftment and expansion in NSG mice. This experimental approach also provides a model for investigating the potential treatment of CLL with the use of miRNA mimics or inhibitors. The effects of *in vitro* transfection with miRNA-15 or miRNA-16 mimics/inhibitors on the growth of CLL cells in NSG mice and the inhibition of CLL cell expansion in NSG mice by

treatment with miR-15 and miR-16 mimics have been monitored using MRI and iron oxide nanoparticles (**Figure 24**).

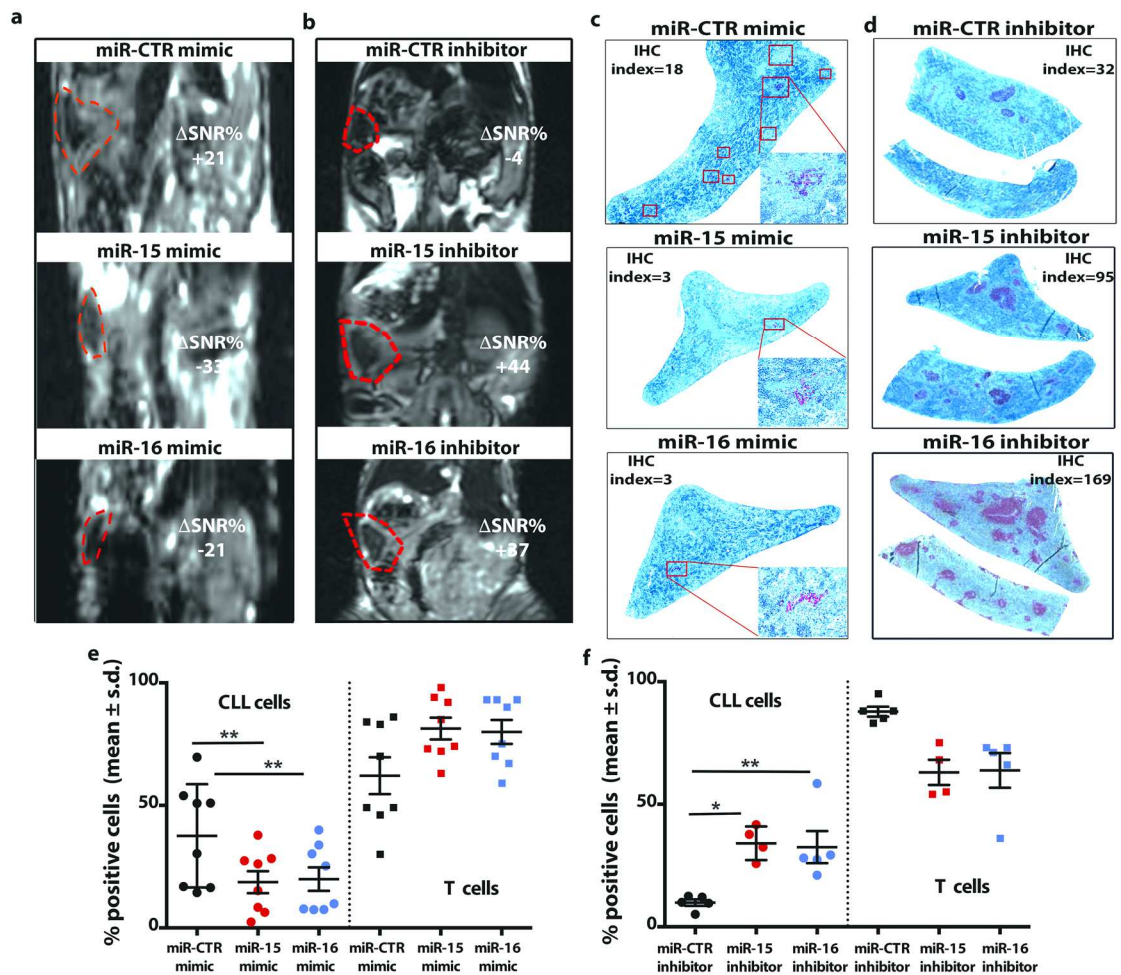


Figure 24. *CLL cell engraftment in NSG mice following in vitro transfection with miRNA mimics or inhibitors. Representative tests on mice engrafted with CLL cells pre-treated in vitro with miRNA mimics (CLL CD0310), miRNA inhibitors (CLL PM0608), or miRNA-CTR. (a-b) the figure shows the MRI images 24h after USPIO administration. The position of the spleen is indicated by the dotted red outline. Δ SNR% values also are indicated. The spleens with superior iron uptake and consequent lower Δ SNR% values, appear darker and less nodular. Conversely, spleens with lower iron uptake and higher Δ SNR% values are not so dark and show a nodular structure possibly related to the presence of follicles. (c-d) α -CD20 Ab staining (red) of paraffin tissue embedded spleen samples following injection of CLL cells pre-treated with the indicated miRNA (d). The CD20+ follicle-like structures are highlighted by red squares in (c) (magnification 40x).*

*The 400x magnification of a representative follicle for each panel is shown. IHC index is indicated in each panel. (e-f) Flow-cytometry analysis of cells from of the same spleens used for the IHC analyses shown in (c) and (d). (e) Pooled flow-cytometry data obtained from 4 CLL cases with biallelic del(13)(q14) pre-treated with miRNA mimics in vitro before injection into mice (n=8 mice for each treatment group). The cells, harvested from mice at the end of tests, were stained and counted. Statistical comparisons were carried out using Wilcoxon-matched pair test. A P value=0.0078 is indicated by **. (f) Pooled flow-cytometry data on cells from 2 CLL cases with normal FISH pre-treated in vitro with miRNA inhibitors prior to injection into mice (n=5 mice for miR-CTR, n=4 for miR-15 and n=5 for miR-16 inhibitors). * and ** indicate P=0.016 and P=0.007 P-values respectively (Mann-Whitney U test). In (e-f) values are expressed as mean \pm s.d [129].*

This study provides a proof of principle supporting the potential use of miRNA mimics to block CLL clonal expansion. Notably, additional miRNA other than miR-15 or miR-16 may become suitable therapeutic targets, since several studies have demonstrated anomalous expression of various miRNAs in CLL cells compared to normal cells [135,136,143]. Moreover, when certain miRNAs are excessively expressed, specific miRNA inhibitors can be employed. In connection with this, it is of note that Ibrutinib, which is effective in reducing CLL clonal expansion, causes significant down-regulation of some miRNAs [144]. Several anomalies in miRNA expression have prognostic/predictive value for disease course and outcome, indicating a potential mechanistic role in the disease pathogenesis/progression [143,145]. Thus, the miRNA approach, especially if multiple miRNA mimics and inhibitors can be targeted, either alone or in combination with other drugs, may represent an additional tool for therapy of a disease that so far has escaped attempts towards a radical cure.

Chapter 2: Original peer reviewed papers

2.1. Tumour targeting and cell labelling with MR

2.1.1. Tumour targeting by USPIO-conjugates

2.1.1.2. Title of paper

- **Baio G**, Fabbi M, de Toterò D, Ferrini S, Cilli M, Derchi LE, Neumaier CE. Magnetic resonance imaging at 1.5 T with immunospecific contrast agent *in vitro* and *in vivo* in a xenotransplant model. *MAGMA* 2006 Dec; 19:313-20.
- **Baio G**, Fabbi M, Salvi S, de Toterò D, Truini M, Ferrini S, Neumaier CE. Two-step *in vivo* tumour targeting by biotin-conjugated antibodies and superparamagnetic nanoparticles assessed by magnetic resonance imaging at 1.5T. *Mol Imaging and Biol*, 2010 Jun; 12(3):305-15.

2.1.1.3. Objective of the study

To demonstrate that MRI at 1.5T allows the detection of USPIO-antibody conjugates specifically bound to human tumour cells *in vitro* and *in vivo*, and that the MRI signal intensity (SI) correlates with the concentration of USPIO-antibody used and with the antigen density at the cell surface.

2.1.1.4. What this study added to the literature

The magnetic nanoparticles used in these experiments are a well-known tool for immunomagnetic cell separation. In our experiments, these microbeads were tested and characterised as MR contrast agents for tumour targeting. The Molecular Imaging and Contrast Agent Database (MICAD), a key component of the “Molecular Libraries and Imaging” program of the National Institutes of Health (NIH) Common Fund (formerly NIH

Roadmap), in Bethesda, Maryland, cited and officially included our experiments as the first demonstration for the development of new Molecular Imaging probes for MR imaging [27].

2.1.1.5. What changed as a result of the papers?

The mAbs-USPIO-based MR molecular imaging probe is still not used in the clinical setting. However, our experiments had a commercial impact, since in 2010, the Biotech Company that was producing these microbeads (Miltenyi Biotec, Germany, <https://www.miltenyibiotec.com/GB-en/>) together with Nano-PET Pharma (Germany, <http://www.nanopet-pharma.com/company/about-us/>) developed a new Preclinical section (Viscover™ Imaging Agents; <https://www.miltenyibiotec.com/GB-en/products/macs-imaging-and-microscopy/viscover-imaging.html>) and a new marketing section for the production of preclinical MR contrast agents.

2.1.1.6. In retrospect, what should have been done differently in this study?

Looking back at this work, we had relatively few mice tested, and even though we had sufficient numbers to show statistical significance in terms of MR signal intensity, a larger number would have made the argument stronger. However, the application of an imaging tool such as MR, especially a clinical human MR scanner, to basic science research, was something very novel and most of the scientific studies published over this period in the scientific community used a small number of animals too. For this reason, our results are still considered consistent. As a control group, we applied unconjugated iron oxide nanoparticles; however, the possibility to compare an alternative MR CA, such a MAb conjugated-gadolinium compound could have possibly decreased the non-specific uptake of Kupffer cells that we instead observed with iron oxide nanoparticles. Another possibility could have been to, first, block the tumour antigen expressed by cells and then

administer the USPIO-mAb conjugates, in order to demonstrate that the decrease in SI observed was due to the specificity of this compound in lymphoma tumour targeting.

2.1.1.7. Future work as a result of this publication

Following the preclinical application of mAbs-USPIO beads for MR tumour targeting we developed new research with the application of USPIO nanoparticles to label cells for *in vivo* MR tumour immunotherapy.

2.1.1.8. Confirmation of authorship

This is shown at the end of Chapter 2.

2.1.1.9. External link to the papers on the journal website

<https://www.ncbi.nlm.nih.gov/pubmed/17160691>

<https://www.ncbi.nlm.nih.gov/pubmed/19806404>

G. Baio
M. Fabbi
D. de Totero
S. Ferrini
M. Cilli
L.E. Derchi
C.E. Neumaier

Magnetic resonance imaging at 1.5 T with immunospecific contrast agent in vitro and in vivo in a xenotransplant model

Received: 21 June 2006
Revised: 27 October 2006
Accepted: 30 October 2006
Published online: 12 December 2006
© ESMRMB 2006

G. Baio · L.E. Derchi
DICMI – Radiologia,
University of Genova,
Largo Rosanna Benzi 8,
16100 Genoa, Italy

M. Fabbi · D. de Totero · S. Ferrini
Laboratory of Immunological Therapy,
IST, National Cancer Institute,
Largo Rosanna Benzi 10,
16100 Genoa, Italy

M. Cilli
Animal Facility, IST,
National Cancer Institute,
Largo Rosanna Benzi 10,
16100 Genoa, Italy

C.E. Neumaier (✉)
Department of Diagnostic Imaging, IST,
National Cancer Institute,
Largo Rosanna Benzi 10,
16100 Genoa, Italy
E-mail: carlo.neumaier@istge.it
Tel.: +39-010-5600872
Fax: +39-010-511014

Abstract *Object:* Demonstrating the feasibility of magnetic resonance imaging (MRI) at 1.5 T of ultrasmall particle iron oxide (USPIO)-antibody bound to tumor cells in vitro and in a murine xenotransplant model.

Methods: Human D430B cells or Raji Burkitt lymphoma cells were incubated in vitro with different amounts of commercially available USPIO-anti-CD20 antibodies and cell pellets were stratified in a test tube. For in vivo studies, D430B cells and Raji lymphoma cells were inoculated subcutaneously in immunodeficient mice. MRI at 1.5 T was performed with T1-weighted three-dimensional fast field echo sequences (17/4.6/13°) and T2-weighted three-dimensional fast-field echo sequences (50/12/7°). For in vivo studies MRI was performed before and 24 h after USPIO-anti-CD20 administration.

Results: USPIO-anti-CD20-treated D430B cells, showed a dose-dependent decrease in signal intensity (SI) on T2*-weighted images and SI enhancement on T1-weighted images in vitro. Raji cells showed lower SI changes, in accordance to the fivefold lower expression of CD20 on Raji with respect to D430B cells. In vivo 24 h after USPIO-anti-CD20 administration, both tumors showed an inhomogeneous decrease of SI on T2*-weighted images and SI enhancement on T1-weighted images.

Conclusions: MRI at 1.5 T is able to detect USPIO-antibody conjugates targeting a tumor-associated antigen in vitro and in vivo.

Keywords Iron oxide particle · Cell-specific MRI · In vivo small animal MRI · Targeted contrast material · Lymphoma

Introduction

In the last few years molecular imaging has emerged as a new way to perform diagnostic imaging. Advances in molecular and cell biology, and genetics have provided a new set of tumor-associated targets suitable for the development of imaging technologies in oncology. In particular, magnetic resonance imaging (MRI) with

specific probes is an important area under development. Many promising probes are being, or will be, applied to the diagnosis of cancer and may also facilitate cancer therapies. Furthermore a growing number of antibodies specifically directed to tumor-associated antigens are available for clinical use [1]. MRI is a non-invasive and reproducible technique with high spatial and contrast resolution. Ultrasmall superparamagnetic particle iron oxide (USPIO) may represent a suitable tool for labelling molec-

ular probes targeting specific tumor-associated markers for in vitro and in vivo detection by MRI. An important property of USPIO is the strong T2 relaxivity that produces a decrease in signal intensity (SI) on T2-weighted images [2, 3] and also a high T1 relaxivity with an increase of SI on T1-weighted images [4, 5]. The association of MRI with specific superparamagnetic tumor contrast agents is able to increase the accuracy and the specificity of imaging [1].

Previous studies were often performed with MRI systems with high field strength up to 7T [6, 7].

In the present study we demonstrate that MRI at 1.5 T allows the detection of USPIO-antibody conjugates specifically bound to human tumor cells in vitro, and that the MRI SI correlates with the concentration of USPIO-antibody used and with the antigen density at the cell surface.

We also studied the possible use of these conjugated monoclonal antibodies as contrast agents for in vivo labeling of human tumor cells. CD20+ B cell lymphomas [8, 9] were used as suitable models for targeting by commercially available USPIO-anti-CD20 conjugates.

Methods

Contrast agent

Superparamagnetic antibodies

We used commercially available USPIO bound to an anti-CD20 monoclonal antibody (IgG1-murine) and stabilized with sodium citrate (Miltenyi Biotec, Germany). The overall mean particle diameter is approximately 50 nm: assuming a diameter of 30 nm for the magnetic bead there are typically 10–200 antibody molecules/particle. Particles are composed of a biodegradable, non-toxic ferromagnetic matrix (dextran) [10].

The r_1 and r_2 relaxivities were 30 and 60 $L s^{-1} mmol^{-1}$, respectively [measured at 37°C in vitro at 1.5 T (Philips Gyroscan NT-Intera)].

Ferumoxides

For in vivo studies in a murine model, we used commercially available ferumoxides non targeted by CD20-antibody as reference product for our control group (Endorem, Laboratoire Guerbet, Aulnay-sous-Bois, France). This contrast is made of colloid-based superparamagnetic iron oxide (SPIO) particles with a diameter of 120–180 nm.

The r_1 and r_2 relaxivities are 40 and 160 $L s^{-1} mmol^{-1}$ [11, 12].

Ferumoxides particles consist of magnetic cores, which are covered with a dextran T-10 layer [11, 13]. Ferumoxides, instead of Ferumoxtran (Sinerem, Laboratoire Guerbet), is approved in

Italy as a MR contrast agent specific for the reticulum-endothelial system.

USPIO-antibody binding to cells in vitro

Five million human D430B cells (anaplastic large cell lymphoma B cell line) [8] and Raji Burkitt lymphoma cells (ICLC, Interlab Cell Line Collection) were incubated with different amounts (0.001, 0.005, 0.01 and 0.03 $\mu mol Fe/L$) of anti-CD20 monoclonal antibody USPIO conjugates, for 15 min both on ice and at 37°C (in order to operate in the same condition as in vivo). Unbound beads were then removed by centrifugation and cells were subsequently included in a matrigel sponge (BD Biosciences, Italy). The D430B cell pellets and Raji cell pellets were then stratified in two test-tubes with 2.5% agarose. Lymphoma cell pellets without USPIO-anti-CD20 were also prepared. As a control, another test tube containing different amounts of USPIO-anti-CD20 (0.005, 0.01 and 0.03 $\mu mol Fe/L$) included in matrigel sponges was made.

Immunofluorescence analysis

Expression of surface antigens by D430B and Raji cell lines was analyzed by immunofluorescence using commercially available fluorescein isothiocyanate (FITC)-conjugated antibodies to CD20 antigen (Caltag, CA, USA) or isotype-matched control antibodies. The presence of USPIO-antibody bound to the cells was verified by staining with a phycoerythrin-labelled anti-mouse immunoglobulin antibody (Southern Biotec Inc., USA). All samples were analyzed by cytofluorimetric analysis on a FACScan (BD Biosciences, Italy).

Animal model

Experiments were performed on ten mice, were approved by the Institutional Review Committee of the National Cancer Institute (IST), and were performed in accordance to the National Regulation on Animal Research Resources. Six-week old female NOD-SCID mice were obtained from a colony bred under sterile conditions in the animal facility of the house. Mice were injected s.c. with 2×10^7 cells of the human D430B cell line or with 2×10^6 cells of the Raji Burkitt lymphoma cell line. Two to three weeks following cell inoculation, mice developed palpable masses of 0.5–1 cm^2 with a superficial ulceration characteristic of the subcutaneous growth of these lymphomas. The superparamagnetic antibodies were injected through the tail vein at a dose of 8 $\mu mol Fe/Kg$ per mouse 24 h before MRI. We performed the same experiments in the control group injecting ferumoxides in the tail vein at the dose of 17 $\mu mol Fe/Kg$ per mouse 24 h before MRI.

Magnetic resonance imaging

MRI was performed with a clinical 1.5 T MR system (Philips Gyroscan NT-Intera).

For in vitro studies Test-tubes were placed in a surface coil and were analyzed by MR using a coronal plane on their longitudinal

axis. The temperature during the experiment was 28°C and the mean acquisition time was 30 min per experiment.

For in vivo studies The animals were anaesthetized by intraperitoneal injection of a mixture of xylazine and ketamine and were placed on a surface coil in prone position, on a support filled with water at 37°C to preserve their body temperature. Images were obtained on coronal and axial planes perpendicular to the vertebral column of the animal. MRI was performed before and 24 h after USPIO-anti-CD20 monoclonal antibody administration. The temperature during the experiment was 28°C. The mean acquisition time was 30 min for each experiment.

For in vitro and in vivo studies, we performed the following sequences T1-weighted three-dimensional fast-field echo sequences (repetition time in ms/echo time in ms/flip angle/number of acquisitions/17/4.6/13°/10) and T2-weighted three-dimensional fast-field echo sequences (repetition time in ms/echo time in ms/flip angle/number of acquisitions/ 50/12/7°/2) were performed with a field of view of 100 × 100 mm, a matrix of 256 × 256 pixels and a slice thickness of 2 mm. In addition, T1-weighted TSE sequences (450/20/90°/2), T2-weighted TSE sequences (3111/130/90°/2), were performed with a field of view of 100 × 100 mm, a matrix of 256 × 256 pixels and a slice thickness of 2 mm. PDW-weighted TSE sequences (1500/9.8/90°/2) were performed only for in vivo experiments, with a field of view of 100 × 100 mm, a matrix of 256 × 256 pixels and a slice thickness of 2 mm.

Data analysis

Qualitative visual analysis and quantitative SI measurements were performed. Qualitative analyses, for both experiments, were performed by two radiologists (C.E.N.; G.B.) on a commercially available workstation (DICOMed Review, EbitAET, 3Mpixel, Barco Monitor). Both observers were blinded. They selected the imaging sequences and parameters providing optimal SI and contrast in relationship with the superparamagnetic properties of USPIO for each pellet and in vivo before and after USPIO administration.

For in vitro studies SI was measured in the middle section of the pellets for each test-tube by one investigator using defined region of interest (ROI) on T1- and T2*-weighted images. The size of the ROI was as small as possible (0.22 mm²). We measured SI of each matrigel pellet containing only USPIO-anti-CD20 at different doses, and of the pellets containing non labelled lymphoma cells; the same analysis was performed on the pellets containing D430B cells with different doses of USPIO-anti-CD20 (0.001, 0.005, 0.01 and 0.03 μmol Fe/L), and for the pellets containing Raji cells with USPIO-anti-CD20 at different doses (0.001, 0.005, 0.01 and 0.03 μmol Fe/L).

For in vivo studies PDW-weighted TSE sequences were used to get an anatomical image of the mouse and for tumor detection. The SI of the lesion was measured in the middle section of the tumor by one investigator using a defined region of interest (ROI) on T1- and T2*-weighted images. The size of the region of interest depended on the diameter of the tumor, with a minimum of 4.43 mm². We performed this analysis also in the control group.

For in vitro and in vivo studies the SI data were divided by the background noise to yield the signal-to-noise ratio (SNR). SNR = SI/noise [14].

The difference in SI (Δ SI) was calculated, for D430B cells-USPIO-anti-CD20 and Raji cells-USPIO-anti-CD20, as follows:

$$\Delta SI = (SI_{\text{non labelled cells}} - SI_{\text{cells-USPIO-antiCD20}}) / \text{noise.}$$

The difference in SI (Δ SI) for the in vivo studies was calculated comparing SI before and after USPIO-anti-CD20 administration, as follows:

$$\Delta SI = (SI_{\text{before-microbeads}} - SI_{\text{after-microbeads}}) / \text{noise.}$$

Results

Detection of USPIO-antibody conjugates binding to human lymphoma cells in vitro by MRI at 1.5 T

Immunofluorescence analysis showed that the D430B cell line expressed the CD20 molecule at levels approximately fivefold higher than the Raji lymphoma cell line: 126 versus 29 in terms of mean fluorescence intensity by immunofluorescence and cytofluorimetric analysis (Fig. 1a).

We then analyzed cell pellets containing D430B cells and Raji cells, which were allowed to react with different amounts of USPIO-anti-CD20 conjugates (0.001, 0.005, 0.01 and 0.03 μmol Fe/L).

Immunofluorescence analysis, using a phycoerythrin-labelled anti-mouse immunoglobulin, showed that USPIO-antibody conjugates bind to the cell surface, as indicated by a dose-dependent shift in the mean fluorescence intensity values with respect to controls in the absence of USPIO (Fig. 1b).

D430B cells-USPIO-anti-CD20 showed an important decrease in SI on T2*-weighted images and SI enhancement on T1-weighted images, which is more evident in the pellet treated with 0.03 μmol Fe/L of USPIO-anti-CD20. Raji cells-USPIO-anti-CD20 showed a slight hypointensity on T2-weighted images and an inhomogeneous hyperintensity on T1-weighted images. On T1- and T2*-weighted images there were no differences in SI between the pellet with only cells and the pellet with 0.001 μmol Fe/L of beads; only an inhomogeneous decrease in SI in the pellets with 0.005 and 0.01 μmol Fe/L of beads was observed (Fig. 2).

The analysis of matrigel pellets containing USPIO-anti-CD20 conjugates (0.005, 0.01, 0.03 μmol Fe/L) used as control was performed to detect the SI of only USPIO-antiCD20. Pellets showed a decrease in SI on T2-weighted three-dimensional fast field echo images (T2*), whereas SI enhancement was observed on T1-weighted three-dimensional fast field echo images (Fig. 3). The observed changes in SI are in accordance with the typical properties of ultrasmall superparamagnetic particle iron oxide: strong T2 relaxivity

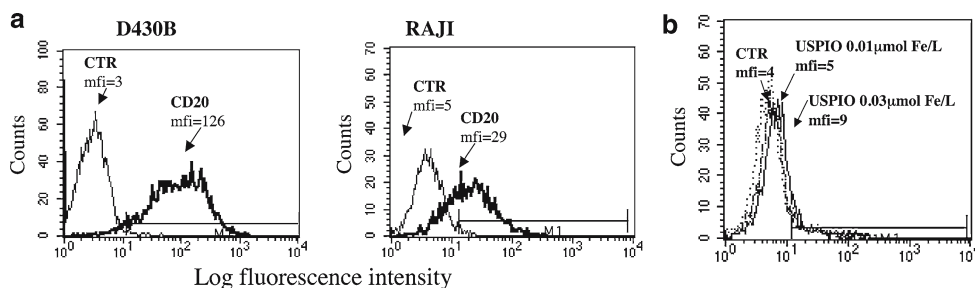


Fig. 1 **a** Surface expression of CD20 antigen by D430B and Raji lymphoma cell lines by immunofluorescence and cytofluorimetric analysis. D430B cells display higher levels of Mfi than Raji cells. Mfi mean fluorescence intensity. **b** Detection of anti-CD20-USPIO conjugates bound to the cell surface by cytofluorimetric analysis. Immunofluorescence profile of D430B control cells (CTR, dotted line) and of D430B-USPIO-anti-CD20 cells stained with a phycoerythrin-labelled anti-mouse immunoglobulin antibody. With the increase of cell-bound USPIO-anti-CD20, higher fluorescence signal is detectable (continuous line). X axis: fluorescence intensity in log scale, Y axis: cell number. Mfi mean fluorescence intensity

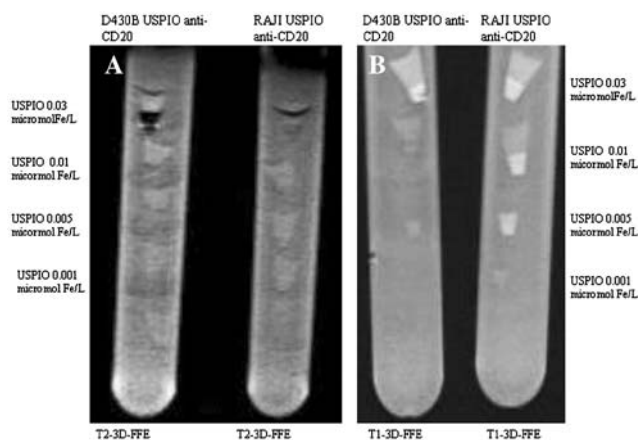


Fig. 2 Representative MR images of cell pellets in test-tubes. Each pellet contains 5×10^6 D430B lymphoma cells (**a**) and 5×10^6 Raji lymphoma cells (**b**), with of USPIO-anti-CD20 respectively. **a** D430B cells-USPIO-anti-CD20 showed an important decrease in SI on T2-weighted three-dimensional fast field echo images that was more evident in the pellet treated with $0.03 \mu\text{mol Fe/L}$ of USPIO-anti-CD20, while Raji cells-USPIO-anti-CD20 showed a slight hypointensity in the same sequences. **b** D430B cells-USPIO-anti-CD20 showed a SI enhancement on T1-weighted three-dimensional fast field echo images and Raji cells-USPIO-anti-CD20 an inhomogeneous hyperintensity on T1-weighted three-dimensional fast field echo sequences = T2-3D-FFE (50/12 with flip angle 7°); T1-weighted three-dimensional fast field echo sequences = T1-3D-FFE (17/4.6 with flip angle 13°). USPIO ultrasmall superparamagnetic particle iron oxide, SI signal intensity

on T2-weighted images and high T1 relaxivity on T1-weighted images.

At the quantitative analysis, the values of decrease in ΔSI on T2*-weighted images of the D430B-pellet with $0.03 \mu\text{mol Fe/L}$ of USPIO-anti-CD20 were threefold higher than the values of the pellet with $0.01 \mu\text{mol Fe/L}$, and sixfold higher than the values of the pellet with $0.005 \mu\text{mol Fe/L}$. The same results were observed for the ΔSI on T1-weighted images (Table 1). When Raji lymphoma cells were used as target cells, the proportional differences of ΔSI , observed at different USPIO doses, were less evident than those found for D430B, in accordance with the differential expression of the CD20 antigen by the two cell lines (Table 2).

Table 1 ΔSI values of D430B cells with different doses of USPIO-anti-CD20 on T1- and T2-weighted 3D-FFE images calculated on the pellets

	ΔSI	
	T1-3D-FFE	T2-3D-FFE
D430B-USPIO-anti-CD20 $3 \mu\text{L}$	-36.6	~73
D430B-USPIO-anti-CD20 $1 \mu\text{L}$	-12.4	~24
D430B-USPIO-anti-CD20 $0.5 \mu\text{L}$	-6.2	~12

$\Delta\text{SI} = (\text{SI}_{\text{D430B non labelled}} - \text{SI}_{\text{D430B-USPIO-antiCD20}}) / \text{noise}$, T1-3D-FFE = T1 three-dimensional fast field echo sequences, T2-3D-FFE = T2 three-dimensional fast field echo sequences

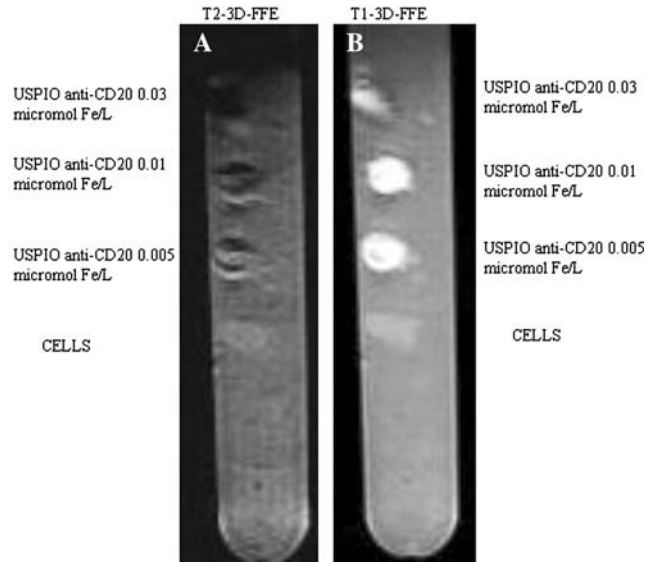


Fig. 3 Representative MR images of USPIO-anti-CD20 conjugated without cells in a test-tube. Each pellet contains 0.005, 0.01 and 0.03 $\mu\text{mol Fe/L}$ of USPIO-anti-CD20 without cells. One pellet contains only 5×10^6 lymphoma cells. On T2-weighted three-dimensional fast field echo images note **a** the decrease in SI of USPIO at different dose. On T1-weighted three-dimensional fast field echo images **b** note the increase of SI of USPIO-anti-CD20 at different dose. T2-weighted three-dimensional fast field echo sequences = T2-3D-FFE (50/12/with flip angle 7°); T1-weighted three-dimensional fast field echo sequences = T1-3D-FFE (17/4.6 with flip angle 13°). USPIO ultrasmall superparamagnetic particle iron oxide, SI signal intensity

Table 2 ΔSI values of Raji cells with different doses of USPIO-anti-CD20 on T1- and T2-weighted 3D-FFE images calculated on the pellets

	ΔSI	
	T1-3D-FFE	T2-3D-FFE
Raji-USPIO-anti-CD20 3 μL	-25	~ 43
Raji-USPIO-anti-CD20 1 μL	-9	~ 17.7
Raji-USPIO-anti-CD20 0.5 μL	-6	~ 12

$\Delta\text{SI} = (\text{SI}_{\text{Raji-non-labelled}} - \text{SI}_{\text{Raji-USPIO-anti-CD20}}) / \text{noise}$, T1-3D-FFE = T1 three-dimensional fast field echo sequences, T2-3D-FFE = T2 three-dimensional fast field echo sequences

Therefore, the magnitude of ΔSI observed was related both to the CD20 expression level and to the dose of USPIO-CD20 used.

In vivo MRI of human lymphoma xenografts using USPIO-anti-CD20 contrast agent

PDW-weighted TSE-sequences gave an anatomical image of the mouse and were used for tumor detection. Subsequently, we acquired T1- and T2*-weighted images from D430B and Raji xenotransplanted lymphomas before and 24 h after USPIO-anti-CD20 i.v. injection.

The D430B tumor showed an inhomogeneous decrease in SI on T2*-weighted images and a slight SI enhancement on T1-weighted images (Fig. 4).

Under the same experimental conditions, the Raji tumor showed slight inhomogeneous hypointensity and hyperintensity, respectively, on T2*- and T1-weighted images, at the visual analysis (Fig. 5).

For quantitative analysis we positioned the ROI on the tumor of each mouse before (mean \pm SD; $1,665 \pm 190$) and after (mean \pm SD; $1,000 \pm 200$) beads administration. Mean values and standard deviations have been calculated in all ten mice: the SNR (signal-to-noise ratio) of D430B tumor after USPIO-anti-CD20 administration showed an important decrease on T2*-weighted sequences (mean $\text{SNR}_{\text{before}} \pm \text{SD} / \text{meanSNR}_{\text{after}} \pm \text{SD}$; $82 \pm 9 / 57 \pm 11$). For the Raji tumor, the decrease of SNR on T2*-weighted sequences after the USPIO-antibody administration was less important (mean $\text{SNR}_{\text{before}} \pm \text{SD} / \text{mean SNR}_{\text{after}}$, $\pm \text{SD}$; $47 \pm 10 / 40 \pm 13$).

The different values of ΔSI in D430B tumor ($35\% \pm 7$) and in Raji tumor ($15\% \pm 8$) were consistent with the different expression of CD20 obtained at immunofluorescence analysis, with a major accumulation of the USPIO-anti-CD20 antibody 24 h after administration at the CD20^{high} D430B tumor site and a minor accumulation at the CD20^{low} Raji tumor site (detected on both tumors by a decrease in SI on T2*-weighted images).

In the control group injected with ferumoxides at the visual analysis there were not appreciable differences in the SI (Fig. 6). These results were confirmed at the quantitative analysis setting ROIs on tumors before (mean \pm SD: $1,392 \pm 86$) and after (mean \pm SD:

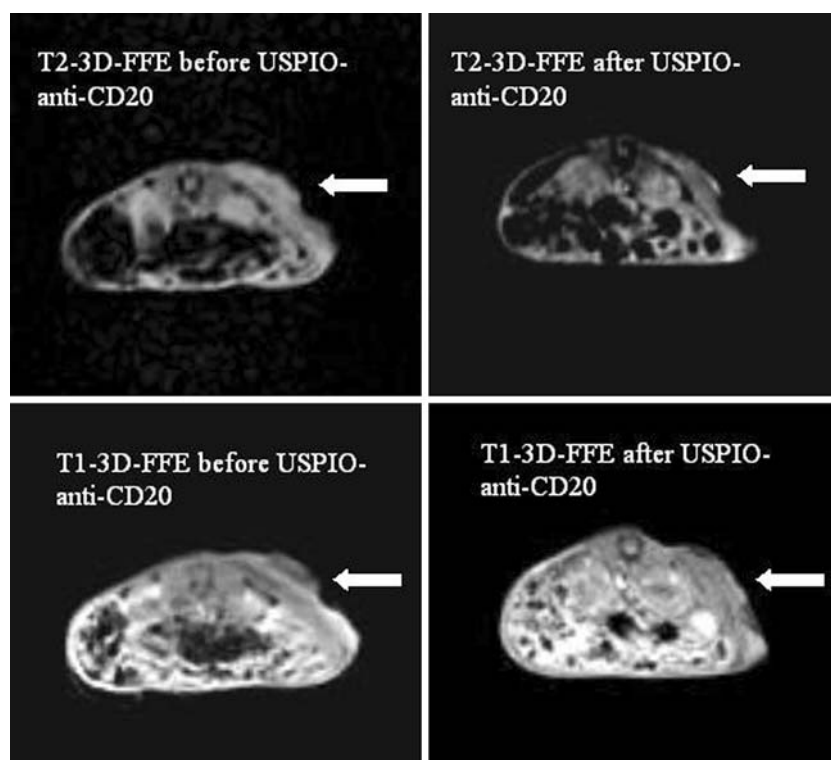


Fig. 4 On T2-weighted three-dimensional fast field echo images after USPIO-anti-CD20 antibody administration the CD20high D430B tumor showed an inhomogeneous decrease in signal intensity (*arrows*). On T1-weighted three-dimensional fast field echo images obtained after USPIO-anti-CD20 antibody administration, the CD20high D430B tumor showed an inhomogeneous SI enhancement (*arrows*). T2-weighted three-dimensional fast field echo sequences = T2-3D-FFE (50/12/with flip angle7°). T1-weighted three-dimensional fast field echo sequences = T1-3D-FFE (17/4.6/with flip angle13°). USPIO ultrasmall superparamagnetic particle iron oxide, SI signal intensity

$1,322 \pm 80$) ferumoxides administration. A ΔSI not statistically significant ($5\% \pm 6$) was observed.

Discussion

A wide set of commercially available USPIO-antibody conjugates used for cells separation techniques are available and some of them are also developed as clinical grade reagents [1].

Our in vitro study was designed to assess the feasibility of the use of MR equipment at 1.5 T to detect USPIO-antibodies bound to tumor cells at doses potentially suitable for small animal models in a pre-clinical setting.

In this study we demonstrate that commercially available USPIO-antibody conjugates specific for a B cell lymphoma-associated antigen binding to the human D430B cells or to the Raji Burkitt lymphoma cell line can be visualized on MRI at 1.5 T.

We also demonstrate by in vitro assays that there is a dose-response relationship between the different amounts of USPIO-anti-CD20 bound to the cells and the ΔSI (Table 1) on T2*-weighted images. This effect is more

evident on cells expressing high levels of the target antigen (D430B) with respect to cells with lower expression (Raji), indicating that the magnitude of ΔSI observed depends both on the dose of the immunospecific contrast agent and on the target antigen expression levels of the cells.

On the basis of our in vitro assays, we estimated that the minimal dose providing a detectable signal by MRI in vitro ($0.005\text{--}0.01 \mu\text{mol Fe/L}$) is largely compatible with the amount of USPIO injectable into living mice without toxic effects ($8 \mu\text{mol Fe/kg}$) as reported by previous studies [6, 7], and that accumulation of less than 5% of the injected dose at the tumor site in vivo in the mouse would provide a detectable signal. All MR signal findings observed correlate with the known T2* and T1 relaxation properties of USPIO.

Indeed, in vivo experiments indicated that the intravenous administration of a single dose of USPIO-anti-CD20 antibody conjugates, 18–24 h before performing MRI at 1.5 T is sufficient to induce detectable changes of SI, in a reproducible fashion ($35\% \pm 7$).

The control group was injected with ferumoxides, in the in vivo studies, to investigate the possible role of the non-specific distribution of USPIO in the tumor.

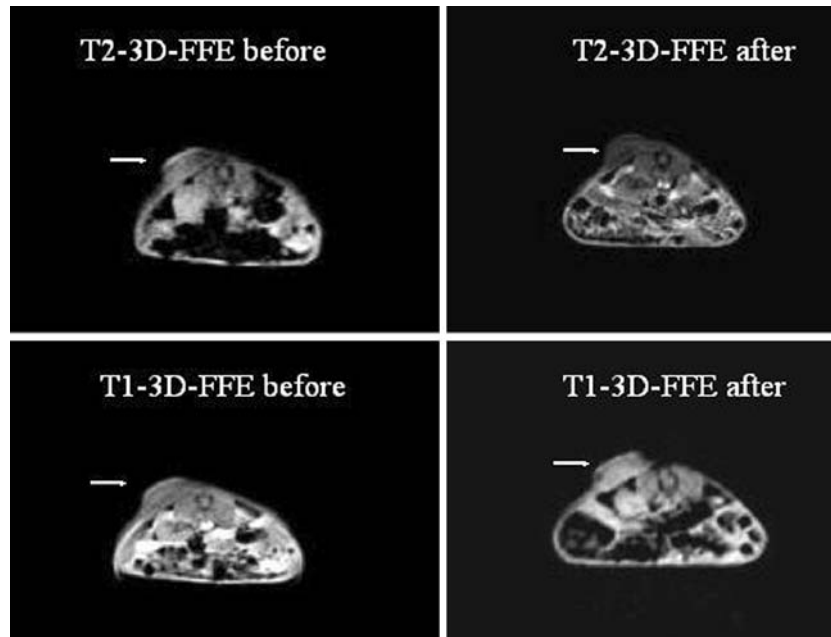


Fig. 5 On T2-weighted three-dimensional fast field echo images, the Raji CD20low tumor analysed after USPIO-anti-CD20 antibody administration showed an inhomogeneous decrease in signal intensity (*arrows*). On T1-weighted three-dimensional fast field echo images obtained after USPIO-anti-CD20 antibody administration the tumor showed a slight SI enhancement (*arrows*). T2-weighted three-dimensional fast field echo sequences = T2-3D-FFE (50/12/with flip angle7°); T1-weighted three-dimensional fast field echo sequences = T1-3D-FFE (17/4.6/with flip angle13°). *USPIO* ultrasmall superparamagnetic particle iron oxide, *SI* signal intensity

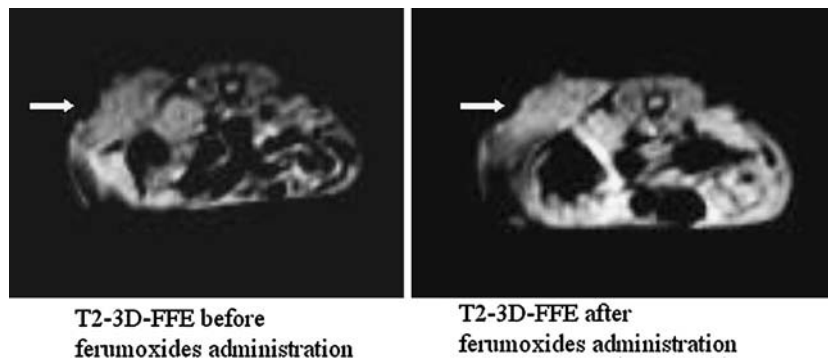


Fig. 6 Representative MR images of the control group injected with ferumoxides. No changes of SI on T2-weighted three-dimensional fast field echo images before and after ferumoxides administration (*arrows*) were observed. T2-weighted three-dimensional fast field echo sequences = T2-3D-FFE (50/12/with flip angle7°). *SI* signal intensity

The results obtained in this control group suggested that non-specific localization is low in this type of tumor, indicating that the higher ΔSI of the USPIO-anti-CD20 conjugate is related to the specific ability of the conjugated antibodies to target the tumor-associated antigen *in vivo*.

The bigger size of the ferumoxides that we have used in the control group (120–180 nm) compared to the size of USPIO-anti-CD20 (50 nm), probably represents a potential limitation of our study. Actually, unconjugated USPIO from Miltenyi are not commercially available. In

addition, another type of USPIO (Sinerem, Guerbet, Paris, France) whose size (30–50 nm) is more comparable to the particles we used (50 nm), is still not commercially available in Italy. For these reasons we have used Endorem as a reference product for our control group.

Our results are consistent with those obtained in previous studies using similar USPIO contrast agents to visualize inflammatory cell infiltrating the brain in a murine model of autoimmune encephalomyelitis [6]. However, these previous studies used a 3.5–7T MRI equipment, while in the present investigation the high antigen expres-

sion by a homogeneous population of tumor cells allowed the detection of cell-bound USPIO by a 1.5 T standard equipment. The ΔSI observed in specific ROIs indicates that this strategy is certainly suitable for highly expressed antigens.

The potential limitation of the present study may relate to the relatively low iron concentration in the commercially available USPIO-antibody conjugate in comparison to the clinically available non-targeted MRI contrast agents, which are non-specifically internalized by the reticulum-endothelial cells. Thus the development of similar USPIO-targeted antibodies with high iron-oxide content may allow to enhance the sensitivity of detection, in order to permit the MRI of tumors with small diameters or with lower target antigen density. Another possible application of antibody targeted MRI technology is related to in vivo tracking of cells that had been labelled by MRI contrast agents in vitro after manipulations and then transferred into a recipient host. Previous studies showed that in vitro cell

labelling by MRI contrast agents can be performed by either non-targeted nano-particles which enter the cell in a non-specific fashion or by specific USPIO-antibody conjugates that specifically bind to a cell surface antigen and can be then eventually internalized [15,16].

We believe that optimizing molecular targeted contrast agents, MRI technology and the generation of new USPIO-antibodies or other USPIO-ligands, specifically able to bind to tumor-associated markers, may provide useful immunospecific contrast agents for the diagnosis of tumors and for targeting therapies of cancer.

Conclusion

MRI at 1.5 T provides a simple method of molecular imaging using commercially available antibodies specific for human targets, opening the possibility for cell tracking in vitro and in vivo. The development of new tumor specific contrast agents may further improve this technology.

References

- Kellogg GJ, Krohn KA, Larson SM, Weissleder R, Mankoff DA, Hoffman JM, Link JM, Guyton KZ, Eckelman WC, Scher HI, O'Shaughnessy J, Chenson BD, Sigman CC, Tatum JL, Mills GQ, Sullivan DC, Woodcock J (2005) The progress and promise of molecular imaging probes in oncologic drug development. *Clin Cancer Res* 11(22):7967–7985
- Tanimoto A, Oshio K, Suematsu M, Pouliquen D, Stark DD (2001) Relaxation effects of clustered particles. *J Magn Reson Imaging* 14:72–77
- Ferrucci JT, Stark DD (1990) Iron oxide-enhanced MR imaging of the liver and spleen: review of the first 5 years. *AJR Am J Roentgenol* 155:943–950
- Small WC, Nelson RC, Bernardino ME (1993) Dual contrast enhancement of both T1- and T2-weighted sequences using ultrasmall superparamagnetic iron-oxide. *Magn Reson Imaging* 11:645–654
- Li W, Tutton S, Vu AT, Pierchala L, Li BS, Lewis JM, Prasad PV, Edelman RR (2005) First-pass contrast-enhanced magnetic resonance angiography in humans using ferumoxytol, a novel ultrasmall superparamagnetic iron oxide (USPIO)-based blood pool agent. *J Magn Reson Imaging* 21(1): 46–52
- Pirko I, Johnson A, Ciric B, Gamez J, Macura SI, Pease LR, Rodriguez M (2003) In vivo magnetic resonance imaging of immune cells in the central nervous system with superparamagnetic antibodies. *FASEB J* 10.1096/fj.02-1124fje
- Pirko I, Ciric B, Gamez J, Bieber AJ, Warrington AE, Johnson AJ, Hanson DP, Pease LR, Macura SI, Rodriguez M (2004) A human antibody that promotes remyelination enters the CNS and decreases lesion load as detected by T2-weighted spinal cord MRI in a virus-induced murine model of MS. *FASEB J* 10.1096/fj.04-2026fje
- Tazzari PL, de Toter D, Bolognesi A, Testoni N, Pileri S, Roncella S, Reato G, Stein H, Gobbi M, Stirpe F (1999) An Epstein-Barr virus-infected lymphoblastoid cell line (D430B) that grows in SCID-mice with the morphologic features of a CD30+ anaplastic large cell lymphoma, and is sensitive to anti-CD30 immunotoxins. *Haematologica* 84:988–995
- Buske C, Weigert O, Dreyling M, Unterhalt M, Hiddemann W (2006) Current status and perspective of antibody therapy in follicular lymphoma. *Haematologica* 91(1):104–112
- Recktenwald D, Radbruch A (1998) Cell Separation methods and applications. Marcel Dekker, New York
- Weissleder R, Elizondo G, Wittemberg J, Rabito C, Bengel H, Josephson L (1990) Ultrasmall superparamagnetic iron oxide: characterization of a new class of contrast agents for MR imaging. *Radiology* 175:489–493
- Weissleder R (1994) Liver MR imaging with iron oxides: toward consensus and clinical practice. *Radiology* 193:593–595
- Jung CW (1995) Surface properties of superparamagnetic iron oxide MR contrast agents: ferumoxides, ferumoxtran, ferumoxsil. *Magn Reson Imaging* 13:675–691
- Wolff SD, Balaban RS (1997) Assessing contrast on MR images. *Radiology* 202:25–29
- Jendelová P, Herynek V, Urdziková L, Glogarová K, Kroupová J, Andersson B, Bryja V, Burian M, Hájek M, Syková E (2004) Magnetic resonance tracking of transplanted bone marrow and embryonic stem cells labeled by iron oxide nanoparticles in rat brain and spinal cord. *J Neurosci Res* 76:232–243
- Jendelová P, Herynek V, Urdziková L, Glogarová K, Rahmatová S, Fales I, Andersson B, Procházka P, Zamecnik, Eckschlanger T, Kobyłka P, Hájek M, Syková E (2005) Magnetic Resonance tracking of human CD34⁺ progenitor cells separated by means of immunomagnetic selection and transplanted into injured rat brain. *Cell Transplant* 14:173–182

RESEARCH ARTICLE

Two-Step *In Vivo* Tumor Targeting by Biotin-Conjugated Antibodies and Superparamagnetic Nanoparticles Assessed by Magnetic Resonance Imaging at 1.5 T

Gabriella Baio,¹ Marina Fabbi,² Sandra Salvi,³ Daniela de Totero,² Mauro Truini,³ Silvano Ferrini,² Carlo Emanuele Neumaier¹

¹Department of Diagnostic Imaging, IST, National Cancer Institute, Largo Rosanna Benzi 10, 16132, Genoa, Italy

²Unit of Immunological Therapy, IST, National Cancer Institute, Largo Rosanna Benzi 10, 16132, Genoa, Italy

³Department of Pathology, IST, National Cancer Institute, Largo Rosanna Benzi 10, 16132, Genoa, Italy

Abstract

Purpose: The purpose of this study was to assess two-step *in vivo* tumor targeting by specific biotin-conjugated antibodies and ultrasmall superparamagnetic iron oxide (USPIO)-anti-biotin nanoparticles as contrast agents for magnetic resonance imaging (MRI) at 1.5 T.

Procedures: D430B human lymphoma cells, expressing the CD70 surface antigen, were injected either s.c. or i.v. to induce pseudo-metastases in NOD/SCID mice. Thirty micrograms of biotin-conjugated monoclonal anti-CD70 was injected i.v., followed 4 h later by 8 $\mu\text{mol Fe/Kg}$ USPIO-anti-biotin. After 24 h, MRI was performed on T2* and b-FFE sequences. Signal intensity (SI) was calculated before and after USPIO-anti-biotin administration.

Results: Subcutaneous xenografts showed a dishomogeneous 30% decrease in SI on T2* with anti-CD70+USPIO-anti-biotin treatment. Pseudo-metastatic xenografts showed a slight reduction in SI on T2*, but a 60% decrease in SI on b-FFE-weighted sequences. Prussian blue staining confirmed the presence of iron nanoparticles in the excised tumors.

Conclusion: MRI at 1.5 T can detect tumors by a two-step *in vivo* biotin-based protocol, which may allow the targeting of any cell surface antigen.

Key words: Magnetic resonance imaging, Iron oxide particles, *In vivo* small animal MRI, Targeted contrast agent, Antibody

Introduction

The selection of monoclonal antibodies (mAbs) directed to surface antigens expressed by tumor cells has

Significance Biotin-labeled tumor-specific antibodies followed by a common USPIO-conjugated secondary reagent represent a suitable contrast agent for the diagnosis and monitoring of tumors by MR using balanced fast-field echo sequences.

Correspondence to: Carlo Emanuele Neumaier; e-mail: carlo.neumaier@istge.it

increasingly enabled the development of new reagents for diagnostic purposes or for targeted therapies. Therapeutic mAbs can act in a variety of ways, such as by blocking growth factors, by signaling arrest and apoptosis, or by eliminating mAb-decorated target cells through the activation of host effector mechanisms. The antigen-binding regions of these antibodies provide specificity to the tumor-killing effects, whereas the Fc portion of the mAbs is involved in complement activation and antibody-dependent cellular cytotoxicity mediated by specific Fc receptors on NK cells [1]. In hematological malignancies, mAbs directed

against lineage-specific markers are used to target neoplastic cell populations which express such markers similarly to the normal cellular lineage from which they derive. In the case of B cell lymphomas or leukemias, mAbs directed against CD20 (rituximab) are currently used in combination with chemotherapy. Nonetheless, because CD20 is expressed by all mature B cells, monoclonal anti-CD20 therapy also affects the normal B cell population. The normal counterpart of non-Hodgkin's lymphomas (NHLs) is represented in most instances by proliferating B cells (centroblasts or immunoblasts). Therefore, NHLs frequently express B lymphocyte activation markers in addition to B cell lineage markers such as CD19, CD20, and CD22. Some activation markers may represent good alternative targets for antibody-based therapeutics for NHLs since targeting of such activation antigens would spare the normal resting B cell population. CD70, a member of the TNF family of ligands, is an activation marker that is transiently expressed on antigen-stimulated B and T cells. Furthermore, CD70 is expressed by thymic stromal cells and by mature dendritic cells, but not by other normal tissues. During the immune response, CD70 interacts with its specific receptor CD27, a member of the TNF receptor family. The CD27/CD70 interaction regulates the expansion and differentiation of effector and memory T cell populations, B cell expansion, germinal center formation, and plasma cell differentiation. CD70 is found on 70% of diffuse large B cell lymphomas, 33% of follicular lymphomas, 50% of B cell lymphocytic leukemias, 25% of Burkitt's and mantle cell lymphomas, and 100% of Waldenström macroglobulinemia, as well as the majority of Reed–Sternberg cells. CD70 has also been detected on nasopharyngeal carcinoma, thymic carcinoma, astrocytoma, glioblastoma, and renal cell carcinoma [2].

Beyond their use as therapeutic agents, mAbs can also be used as specific probes for the molecular imaging of tumors [3]. In particular, magnetic resonance imaging (MRI) can be effectively applied to molecular imaging approaches in view of its reproducibility and of its high spatial and contrast resolution. Ultrasmall superparamagnetic iron oxide (USPIO) nanoparticles may represent suitable tools for labeling molecular probes which target specific tumor-associated markers for *in vitro* and *in vivo* detection by MRI. Important properties of USPIO are the strong T2 relaxivity that produces a decrease in signal intensity (SI) on T2-weighted images [4, 5] and high T1 relaxivity that causes an increase in SI on T1-weighted images [6, 7]. The association of MRI with specific superparamagnetic tumor contrast agents is able to increase the accuracy and the specificity of imaging [8]. Molecular imaging is often performed with MR scanners which operate at field strengths up to 7 T [9–12].

In the present study, we demonstrate that MRI at 1.5 T allows the detection of USPIO-antibody conjugates specifically bound to human tumor cells by means of a two-step procedure. The possible use of specific biotin-labeled antibodies combined with the USPIO-anti-biotin as contrast

agents for *in vivo* labeling of human tumor cells is explored in a xenotransplantation model.

Material and Methods

Cells and Antibodies

Human D430B anaplastic large B cell lymphoma [13], A2774 ovarian carcinoma (from J. Bénard, Institut Gustave Roussy, Paris, France), and Jurkat T cell leukemia cell lines (American Type Culture Collection) were cultured in RPMI 1640 (Cambrex, Verviers, Belgium), supplemented with L-glutamine, 10% heat-inactivated fetal calf serum (FCS; BioWhittaker Cambrex), and antibiotics at 37°C in a 5% CO₂ incubator. Monoclonal anti-human CD70, murine IgG2a clone LD6 [14, 15], was purified from serum-free culture medium by affinity chromatography on Sepharose-Protein A (GE Healthcare®, Little Chalfont, UK) and subsequently conjugated with EZ-Link Sulfo-NHS-LC-biotin (Pierce®, Rockford, IL, USA) according to the manufacturer's instructions. As isotype-matched negative control, murine mAb CH-L, directed against the CD158b antigen [16], which is not expressed by D430B cells, was similarly prepared. The concentration of the purified mAbs was determined by measuring the optical density at 280 nm and by the Lowry protein assay [17]. Purity of the antibodies was checked by resolving them by sodium dodecyl sulfate–polyacrylamide gel electrophoresis (SDS-PAGE) under non-reducing conditions on an 8% acrylamide gel followed by Coomassie blue staining [17]. The degree of mAb biotinylation was assessed with the Biotin Quantitation Kit (Pierce®).

Contrast Agent

Commercially available (Miltenyi Biotech, Bergisch Gladbach, Germany) USPIO nanoparticles coated with a monoclonal anti-biotin (murine IgG1), stabilized with sodium citrate, and approved for clinical use in humans as magnetic cell separators were used. Particles were composed of a biodegradable, non-toxic ferromagnetic matrix (dextran-based), and their overall mean diameter was approximately 50 nm. Assuming a diameter of 30 nm for the magnetic core, there were typically 10–200 antibody molecules per particle [18]. The iron content of the USPIO-anti-biotin core was measured by inductively coupled plasma optical emission spectrometry with a Varian Vista Pro spectrometer (Varian Inc., Palo Alto, CA, USA) and found to be 20 mM/L. The r1 and r2 relaxivities were 30 and 60 L s⁻¹ mmol⁻¹, respectively, as assessed at 1.5 T (Philips Gyroscan NT-Intera, Philips, Best, The Netherlands) by measuring particles *in vitro* at 37°C [19].

Immunofluorescence Analysis

Surface expression of the CD70 antigen by the cell lines was analyzed by immunofluorescence and flow cytometry. Immunofluorescence was performed by incubating 10⁵ viable cells with 2 µg/mL biotin-conjugated monoclonal anti-CD70 (clone LD6) or isotype control (clone CH-L) for 30 min on ice. The cells were then washed twice with phosphate-buffered saline (PBS) 2% FCS and incubated with fluorescein isothiocyanate (FITC)-conjugated streptavidin (Caltag Laboratories, Burlingame, CA, USA) as secondary reagent. After washes, cells were analyzed on a FACScan (Becton Dickinson, Mountain View, CA, USA).

In addition, the localization of CD70 antigen was studied by immunofluorescence and confocal microscopy analysis. Cell suspensions were stained with 2 $\mu\text{g}/\text{mL}$ LD6 or CH-L followed by Alexa488-conjugated (Fab)₂ goat anti-mouse Ig as secondary reagent. Cells were then fixed (1% paraformaldehyde in PBS), permeabilized (0.2% Triton-X-100 in PBS), and cell nuclei were counterstained with propidium iodide. Mowiol-mounted slides were analyzed by confocal fluorescence microscopy using an Olympus (Olympus Optical, Tokyo, Japan) laser scanning microscope FV500 equipped with an Olympus IX81 inverted microscope.

To detect the binding of USPIO-anti-biotin to the biotin-conjugated antibodies, D430B cells were incubated with biotin-LD6 and biotin-CH-L as above. After washes, cells were challenged with 10 μL of the USPIO-anti-biotin suspension for 20 min on ice. D430B cells were then washed again, and the presence of USPIO-anti-biotin bound to the cells carrying biotin-conjugated monoclonal anti-CD70 was verified by staining with FITC-labeled anti-mouse immunoglobulin goat serum (Caltag) followed by flow cytometry analysis.

USPIO-antibody Binding to Cells In Vitro

Two million human D430B, A2774, or Jurkat cells were incubated with biotin-conjugated LD6 or CH-L mAb or with PBS for 30 min on ice, washed, and further incubated with 10 μL of the USPIO-anti-biotin suspension for 15 min on ice. Unbound beads were then removed by centrifugation and cells were subsequently included in a matrigel sponge. The cell pellets were then stratified in test tubes with 2.5% agarose as described [19] and analyzed by MRI.

Animal Experiments

In vivo experiments were approved by the Institutional Review Board of the National Cancer Institute (IST) and were performed in accordance with the national (Italian) regulations on Animal Research Resources. Six-week-old female NOD/SCID mice were obtained from a colony bred in-house under sterile conditions. Mice were injected subcutaneously with 2×10^7 human D430B cells. Two to 3 weeks later, they developed palpable masses of 0.5 to 0.8 cm^3 .

In a second set of experiments, 2×10^7 D430B cells per mouse were injected into the tail vein to induce pseudo-metastases. Mice were monitored for weight loss every other day and by MRI starting 3 weeks after inoculum.

To target tumor-expressed human CD70 antigen, 30 μg per mouse of biotin-labeled LD6 mAb was administered into the tail vein in 100- μL volume, and MRI was performed immediately. Four hours after administration of the biotin-labeled antibody, 8 μmol Fe/Kg per mouse of USPIO-anti-biotin was injected in the tail vein in 100- μL volume. MRI was performed again 24 h later. As negative control, groups of mice were similarly injected with biotin-conjugated CH-L mAb or with PBS prior to USPIO-anti-biotin.

Magnetic Resonance Imaging

MRI was performed with a clinical 1.5 T MR system (Philips, Gyroscan NT-Intera).

Test tubes were placed on a surface coil in a prone position and were analyzed by MR using a coronal plane on their longitudinal axis.

Mice were anesthetized by intraperitoneal injection of a mixture of xylazine and ketamine and were placed on a surface coil in a prone position on a support filled with water at 37°C to preserve body temperature. Imaging was performed before and 24 h after administration of USPIO-anti-biotin.

The temperature during experiments was 28°C, and the mean acquisition time was 30 min for each experiment. Images were obtained on coronal and axial planes.

The following sequences were applied: T1-weighted three-dimensional fast-field echo sequences (repetition time in milliseconds/echo time in milliseconds/flip angle/17/4.6/13°) and T2-weighted three-dimensional fast-field echo sequences (repetition time in milliseconds/echo time in milliseconds/flip angle/50/12/7°) were performed with a field of view of 100×100 mm, a matrix of 256×256 pixels, and a slice thickness of 2 mm. Three-dimensional balanced gradient echo (3D-b-FFE) sequences (repetition time in milliseconds/echo time in milliseconds/flip angle/11/4.1/45°) were performed with a field of view of 150×150 mm, a matrix of 256×256 pixels, and a slice thickness of 1 mm. In addition, T1-weighted turbo spin-echo sequences (450/20/90°) and T2-weighted turbo spin-echo sequences (3111/130/90°) were performed with a field of view of 100×100 mm, a matrix of 256×256 pixels, and a slice thickness of 2 mm.

Ex Vivo MRI and Histopathological Analysis

Mice were euthanized by CO₂ method immediately after the *in vivo* MRI session. Tumors and liver were excised and fixed in 4% buffered formalin. *Ex vivo* MRI was subsequently performed.

Specimens were then paraffin-embedded and processed for histological analysis according to standard techniques. The presence of iron was detected by Pearl Prussian blue staining and was qualitatively assessed by an experienced pathologist (M.T.) with an Olympus BX41 microscope by estimating iron-positive cells.

Statistical Analysis

Both qualitative and quantitative analyses were performed. Qualitative visual analyses were performed by two radiologists (C.E.N. and G.B.) on a commercially available workstation (DICOMED Review, EbitAET, 3Mpixel, Barco Monitor). Both observers were blinded. They selected the imaging sequences and parameters which provided optimal SI and contrast relative to the USPIO superparamagnetic properties.

Quantitative analyses were expressed as mean SI \pm standard deviation with SI being measured in tumor and liver by one investigator using a defined region of interest (ROI) on T2*- and b-FFE-weighted images. The size of the region of interest depended on the diameter of the tumor. The same analysis was performed in the control group.

The SI values were divided by the background noise to yield the signal-to-noise ratio (SNR) according to the formula $\text{SNR} = \text{SI}/\text{noise}$ [20].

The difference in SI (ΔSI) was calculated by comparing SI before and after the administration of USPIO-anti-biotin, as follows:

$$\Delta\text{SI} = (\text{SI}_{\text{before-microbeads}} - \text{SI}_{\text{after-microbeads}}) / \text{noise}.$$

Results

Immunofluorescence Analysis of Biotin-Conjugated Antibodies and USPIO-Anti-biotin with Human Lymphoma Cells

Biotin-conjugated monoclonal anti-CD70 (LD6) and an irrelevant mAb (CH-L) were tested for reactivity with D430B lymphoma, A2774 ovarian carcinoma, and Jurkat leukemia cells by immunofluorescence analysis using streptavidin-FITC as secondary reagent. As shown in Fig. 1a, mAb LD6 (continuous line) reacted strongly with D430B cells, weakly (ten times lower in terms of fluorescence intensity) with A2774 cells, and showed no reactivity with Jurkat cells. The isotype-matched mAb CH-L (dotted line) did not bind to any cell line, showing background fluorescence equal to streptavidin-FITC without antibody (not shown). Confocal microscopy confirmed the strong membrane staining of the monoclonal anti-CD70 on D430B and the low staining on A2774 cells (Fig. 1b, lower panels).

Purity of antibody preparation was assessed by SDS-PAGE analysis under non-reducing conditions and Coomassie blue staining, which showed a single band of approximately 150 kDa (Fig. 1b, upper panel). The degree of biotinylation was similar in the two mAbs since Western blot analysis of the two biotin-conjugated mAbs, run in equimolar amounts in parallel lanes, revealed a similar intensity of the antibody bands on avidin-peroxidase staining (Fig. 1b, lower panel). The two mAbs showed a comparable level of biotinylation (3 and 3.4 biotin per antibody molecule for CH-L and LD6, respectively) also by the use of a biotin quantitation kit.

The suitability of mAbs conjugated in house with Sulfo-NHS-LC-biotin as a target for USPIO-anti-biotin was then verified. Figure 1c shows the immunofluorescence profile of D430B cells challenged with biotin-conjugated monoclonal anti-CD70 (LD6) plus (continuous line) and minus (gray profile) USPIO-anti-biotin, followed by FITC-anti-mouse serum. In the presence of USPIO-anti-biotin bound to biotin-LD6 mAb, a higher fluorescence signal was detectable due to the additional murine monoclonal anti-biotin carried by the magnetic particles.

In Vitro MRI Detection of Biotin-Labeled Monoclonal Anti-CD70 and USPIO-Anti-biotin Conjugates Bound to the Cells

Prior to conducting the *in vivo* experiments, the ability of MRI at 1.5 T to detect *in vitro* binding of USPIO-anti-biotin to cells expressing CD70 at high (D430B) and low (A2774) levels was investigated. D430B cells challenged with biotin-labeled mAb LD6 plus USPIO-anti-biotin showed an evident hypointense signal on T2*-weighted images, whereas no changes in SI were observed with biotin-CH-L mAb, as shown in Fig. 1d. A2774 cells treated with biotin-LD6 plus USPIO-anti-biotin showed only a slightly hypointense signal, and no appreciable signal changes were

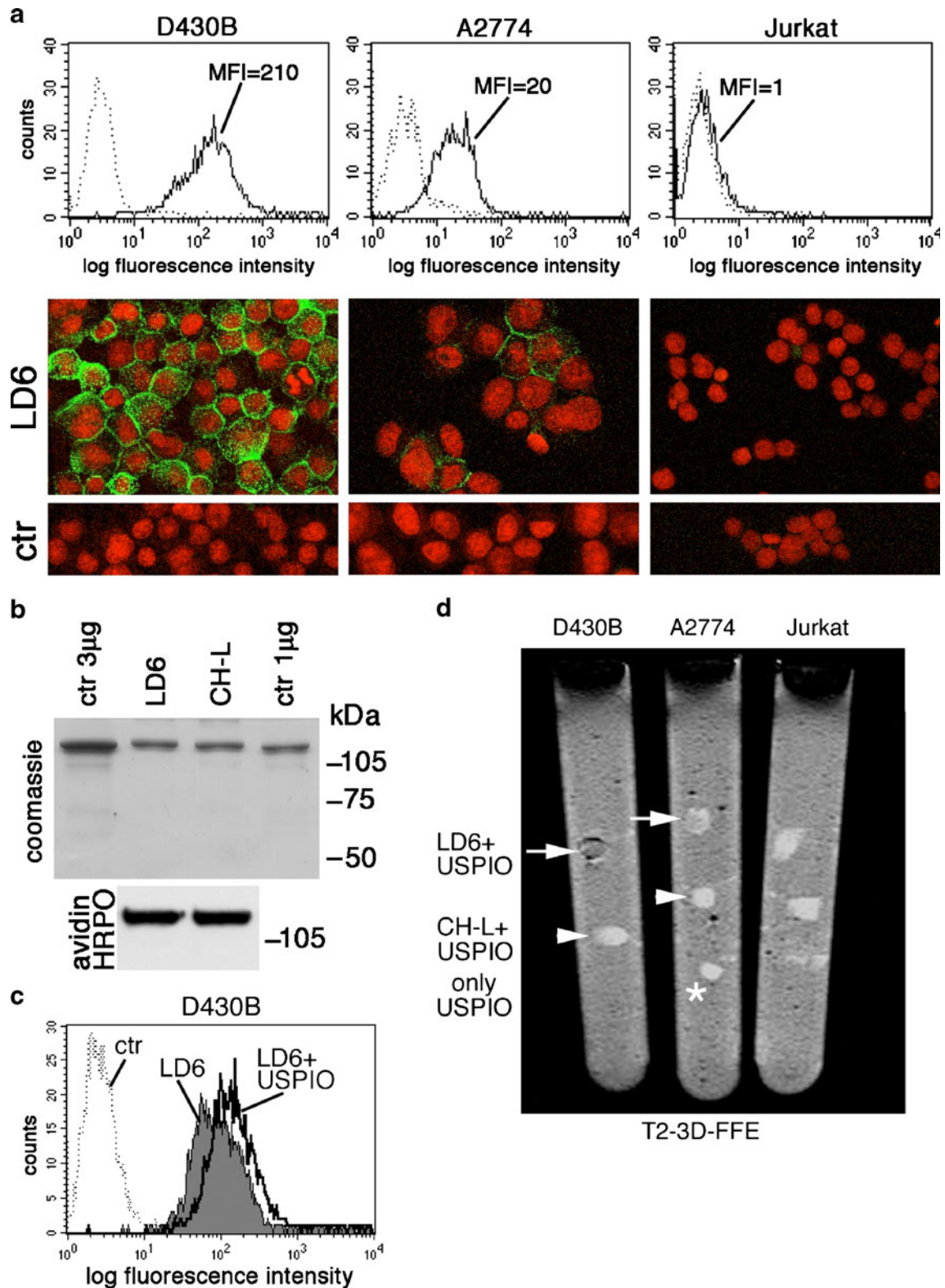
observed by treatment with biotin-labeled mAb CH-L and USPIO-anti-biotin alone (Fig. 1d). As expected, the CD70-negative Jurkat cell pellets showed no changes in SI under the same conditions (Fig. 1d). The barely detectable changes in SI induced by the LD6/USPIO complex on CD70-low cells suggest that the biotinylated mAb LD6 is suitable only for the *in vivo* detection by MRI at 1.5 T of tumors with a CD70-bright phenotype.

Fig. 1. Immunofluorescence analysis of CD70 surface expression and detection of biotin-labeled monoclonal anti-CD70 and USPIO-anti-biotin conjugates bound to the cell surface. **a** Surface expression of CD70 antigen by D430B lymphoma, A2774 ovarian carcinoma, and Jurkat leukemia cells as assessed by indirect immunofluorescence and cytofluorimetric analysis (*upper panels*) or confocal microscopy (*lower panels*). Immunofluorescence profiles of cells stained with biotin-conjugated monoclonal anti-CD70 (LD6, *continuous line*) or with biotin-conjugated mAb CH-L as isotype-matched negative control (*dotted line, ctr*), followed by FITC-streptavidin. *MFI* mean fluorescence intensity. **b** Purity of LD6 and CH-L mAbs (1 µg/lane) resolved by SDS-PAGE analysis under non-reducing conditions as assessed by Coomassie blue staining of 8% polyacrylamide gels (*upper panels*). As standards, 3 and 1 µg of a commercially available IgG2b mAb (*ctr*) were run in parallel lanes. Antibodies LD6 and CH-L display a similar degree of biotinylation as detected by Western blot analysis of equimolar amounts and staining with HRPO-streptavidin followed by chemiluminescence. Antibodies were resolved on an 8% acrylamide gel under non-reducing conditions. *Numbers* indicate molecular weight markers. **c** Immunofluorescence profile of D430B cells challenged with biotin-conjugated monoclonal anti-CD70 (LD6) plus (*continuous line*) and minus (*gray profile*) USPIO-anti-biotin, followed by FITC-anti-mouse serum. In the presence of USPIO-anti-biotin bound to biotin-LD6 mAb, higher fluorescence signal is detectable due to the additional murine mAb carried by the magnetic particles. Profile of negative control without primary antibody and with USPIO-anti-biotin (*dotted line, ctr*) is shown. Samples were analyzed on a FACscan flow cytometer. *X-axis* fluorescence intensity in log scale, *Y-axis* cell number. **d** MRI analysis at 1.5 T of antibody+USPIO-treated cell pellets in test tubes. Each pellet contained 2×10^6 D430B lymphoma, A2774, or Jurkat cells that had been stained by either biotinylated LD6+USPIO-anti-biotin (*arrows*), biotinylated CH-L+USPIO-anti-biotin (*arrowhead*), or USPIO-anti-biotin alone (*asterisk*). Only D430B cells treated with biotinylated LD6+USPIO-anti-biotin showed a clearly hypointense signal on T2-weighted three-dimensional fast-field echo images.

observed by treatment with biotin-labeled mAb CH-L and USPIO-anti-biotin alone (Fig. 1d). As expected, the CD70-negative Jurkat cell pellets showed no changes in SI under the same conditions (Fig. 1d). The barely detectable changes in SI induced by the LD6/USPIO complex on CD70-low cells suggest that the biotinylated mAb LD6 is suitable only for the *in vivo* detection by MRI at 1.5 T of tumors with a CD70-bright phenotype.

In Vivo MRI of Human Lymphoma Subcutaneous Xenografts

To assess if the monoclonal anti-CD70 could specifically target human lymphoma cells *in vivo* and be detected by MRI, human D430B cells were subcutaneously injected in NOD/SCID mice and allowed to grow up to a tumor mass of



0.5 cm³. Mice then underwent an MRI session to collect images before treatment and immediately thereafter were injected i.v. with either biotin-conjugated mAb LD6 or CH-L followed 4 h later by USPIO-anti-biotin.

The following day, MRI was repeated. As shown in Fig. 2, 24 h after the administration of biotin-conjugated

monoclonal anti-CD70 (LD6) plus USPIO-anti-biotin, subcutaneous tumors showed a slight and inhomogeneous decrease in SI on T2*-weighted images (Fig. 2a, b).

Regions of interest were defined and signal intensity calculated on the tumor of each mouse before (mean \pm SD, 1,894 \pm 170) and after (mean \pm SD, 1,350 \pm 160) USPIO

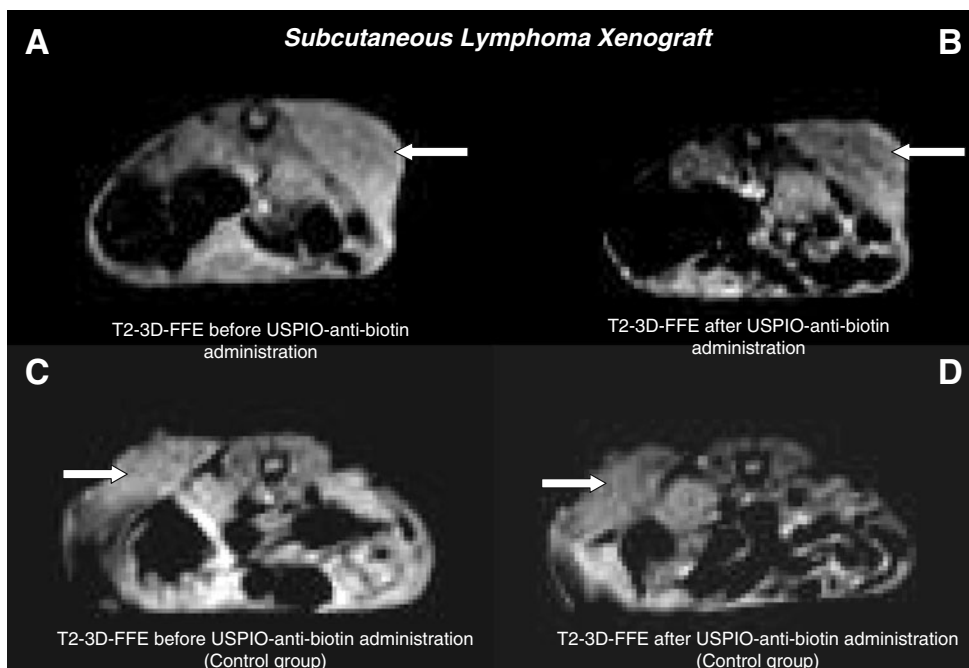


Fig. 2. Axial MR images of subcutaneous lymphoma xenografts. On T2-weighted three-dimensional fast-field echo images before (a) and 24 h after (b) the administration of biotin-conjugated monoclonal anti-CD70 (LD6) plus USPIO-anti-biotin, subcutaneous tumors showed a slight and dishomogeneous decrease in SI (arrows). In control groups (c, d) injected with the biotin-conjugated antibody CH-L plus USPIO-anti-biotin or with USPIO-anti-biotin alone, no appreciable differences in SI of the tumor were observed (arrows) before (c) and 24 h after (d) administration of the contrast agent.

administration. Mean values and standard deviations were calculated in all mice. The SNR of D430B tumor after USPIO-anti-biotin administration showed a decrease in SI on T2*-weighted sequences (mean SNR_{before} ± SD/meanSNR_{after} ± SD, 38 ± 3/27 ± 3). Analyses of images confirmed a decrease of about 30% in SI measured after USPIO-anti-biotin administration. Results are the mean of three independent experiments.

In control groups injected with the biotin-conjugated CH-L antibody plus USPIO-anti-biotin or with USPIO-anti-biotin alone, no appreciable differences in SI of the tumor were observed (Fig. 2c, d). These results were confirmed and quantified by setting ROIs on tumors before (mean ± SD, 1,494 ± 76) and after (mean ± SD, 1,420 ± 68) USPIO administration. A non-significant ΔSI (around 5% difference) was indeed observed. Results are the mean of three experiments.

In Vivo MRI of Human Pseudo-metastatic Lymphoma Xenografts

A pseudo-metastatic animal model was then set up by i.v. injection of human lymphoma cells in NOD/SCID mice. As soon as weight loss, a sign of tumor take, was detected, mice underwent MRI to collect images before treatment, which demonstrated the presence of tumor masses in the retroperitoneal space, in particular in the kidney.

After MRI mice were injected i.v. with either biotin-conjugated antibody, LD6 or CH-L followed 4 h later by USPIO-anti-biotin. The following day, MRI was repeated. Twenty-four hours after the administration of biotin-conjugated

monoclonal anti-CD70 plus USPIO-anti-biotin, tumors showed a slight decrease in SI when T2-weighted sequences were applied, but a significant decrease in SI when b-FFE-weighted sequences were applied (Fig. 3).

Quantitative analysis was then performed by setting ROIs on b-FFE-weighted images and measuring SI on the tumor of each mouse before (mean ± SD, 1,303 ± 635) and after (mean ± SD, 499 ± 235) USPIO administration. The SNR of D430B tumor after USPIO administration showed a clear-cut decrease (mean SNR_{before} ± SD/meanSNR_{after} ± SD, 141 ± 159/60 ± 57). Analyses of images confirmed a decrease of about 60% in SI after USPIO-anti-biotin administration.

In control groups injected with the biotin-conjugated CH-L antibody plus USPIO-anti-biotin, no appreciable differences in SI of the tumor were observed. Quantitative analysis performed by setting ROIs on tumors and measuring SI before (mean ± SD, 230 ± 34) and after (mean ± SD, 257 ± 63) USPIO-anti-biotin administration confirmed the visual analysis. Also, in this case, a non-significant ΔSI was observed.

It is noteworthy that 24 h after the administration of biotin-conjugated LD6 antibody plus USPIO-anti-biotin, the liver showed a decrease in SI on T2*- and, in particular, on b-FFE-weighted sequences (Fig. 3).

Quantitative analyses were performed on b-FFE-weighted images of the liver of each treated mouse by setting ROIs and measuring SI before (mean ± SD, 1115 ± 66) and after (mean ± SD, 349 ± 31) USPIO administration. Mean values and standard deviations were calculated in all mice: the SNR of liver after USPIO-anti-biotin administration confirmed a

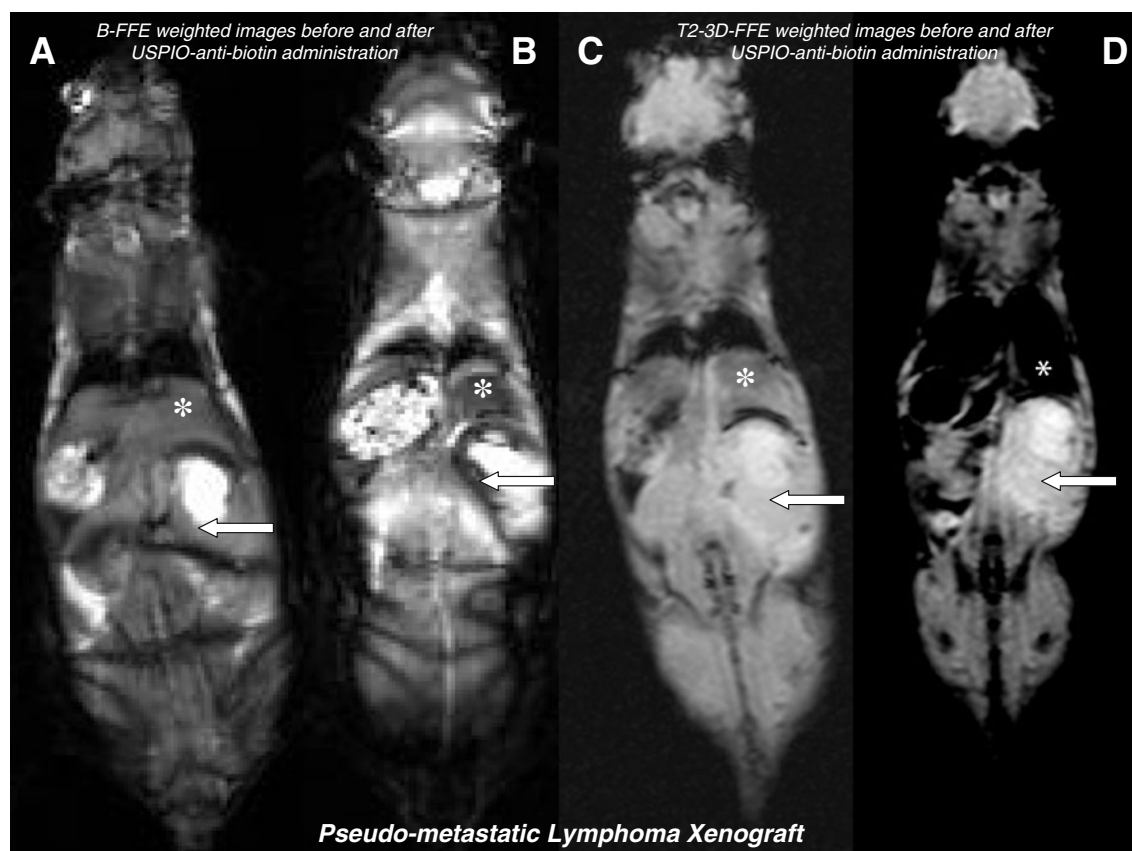


Fig. 3. Coronal MR images of pseudo-metastatic lymphoma xenografts. MRI images demonstrated the presence of tumor masses in the retroperitoneal space, in particular in the right kidney (*arrow*) with hydronephrosis (hyperintense signal area). On b-FFE weighted images, before (**a**) and 24 h after (**b**) the administration of biotin-conjugated LD6 plus USPIO-anti-biotin, tumors (*arrows*) and liver (*asterisk*) showed an evident and homogeneous decrease in SI. On T2-weighted three-dimensional fast-field echo images before (**c**) and 24 h after (**d**) administration of biotin-conjugated LD6 plus USPIO-anti-biotin, tumors (*arrows*) showed a less or not significant decrease in SI, whereas the liver showed a significant decrease in SI (*asterisk*).

significant decrease in SI on b-FFE-weighted sequences (mean $\text{SNR}_{\text{before}} \pm \text{SD} / \text{meanSNR}_{\text{after}} \pm \text{SD}$, $120 \pm 16 / 43 \pm 7$).

Quantitative analyses of the liver of control mice inoculated with biotin-conjugated CH-L plus USPIO-anti-biotin showed a significant ΔSI before (mean $\pm \text{SD}$, 214 ± 25) and after (mean $\pm \text{SD}$, 54 ± 12) USPIO administration.

Ex Vivo MR Imaging and Detection of Iron Oxide-Labeled Cells in Human Lymphoma Xenografts

Since subcutaneous tumors showed a decrease in SI on T2*-weighted images that was less evident in pseudo-metastatic tumors, the same T2* sequences to the excised pseudo-metastatic tumor were applied. *Ex vivo* MR images of the pseudo-metastatic tumor showed a higher decrease in SI on T2*-weighted images (Fig. 4) compared to T2*-weighted images obtained *in vivo* (Fig. 3c, d), while this difference was not evident in the liver which already showed a strong ΔSI *in vivo*.

To verify if iron particles had been actually delivered to the tumors, histopathological analysis by Pearl Prussian blue staining was performed on subcutaneous and pseudo-metastatic tumors that had been excised from mice after MRI.

Microscope examination showed iron nanoparticles bound to the reactive tissue and to the tumor cells in the case of subcutaneous tumors (data not shown). In addition, as shown in Fig. 5a, iron bound to tumor cells (approximately 10–15%) was detected also in the case of pseudo-metastatic tumors in mice that had received treatment with biotin-conjugated monoclonal anti-CD70 plus USPIO-anti-biotin. No Prussian blue staining was detectable in the case of treatment with the isotype-matched negative control (CH-L) plus USPIO-anti-biotin (Fig. 5b) or USPIO-anti-biotin alone (Fig. 5c). As expected on the basis of MRI data, Pearl Prussian blue staining was observed in the liver of mice receiving either LD6 or the irrelevant control antibody (Fig. 5d) or only the USPIO-anti-biotin, thereby indicating non-specific uptake by the reticulum–endothelial system in the liver (Fig. 5e).

Discussion

Magnetic nanoparticles formed by iron oxide/dextran complexes are a promising tool for several *in vitro* and *in vivo* applications. Because their unique magnetic features can be applied to special medical techniques, they can be used as a

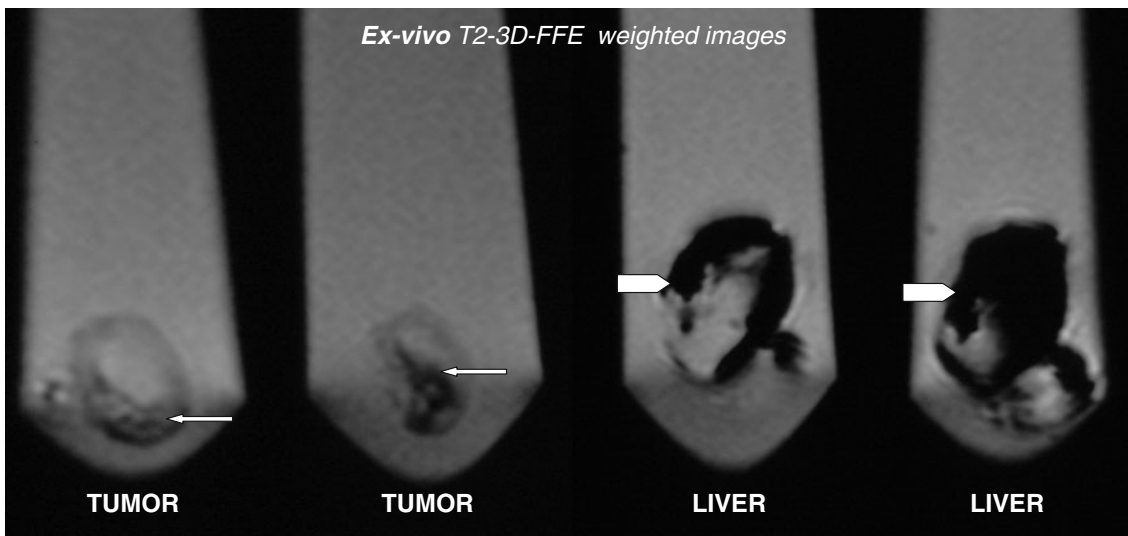


Fig. 4. *Ex vivo* MR images of pseudo-metastatic lymphoma xenografts. Tumor (arrows) and liver (arrowheads) specimens fixed in 4% buffered formalin showed a clear decrease in SI (arrows) on T2*-weighted images.

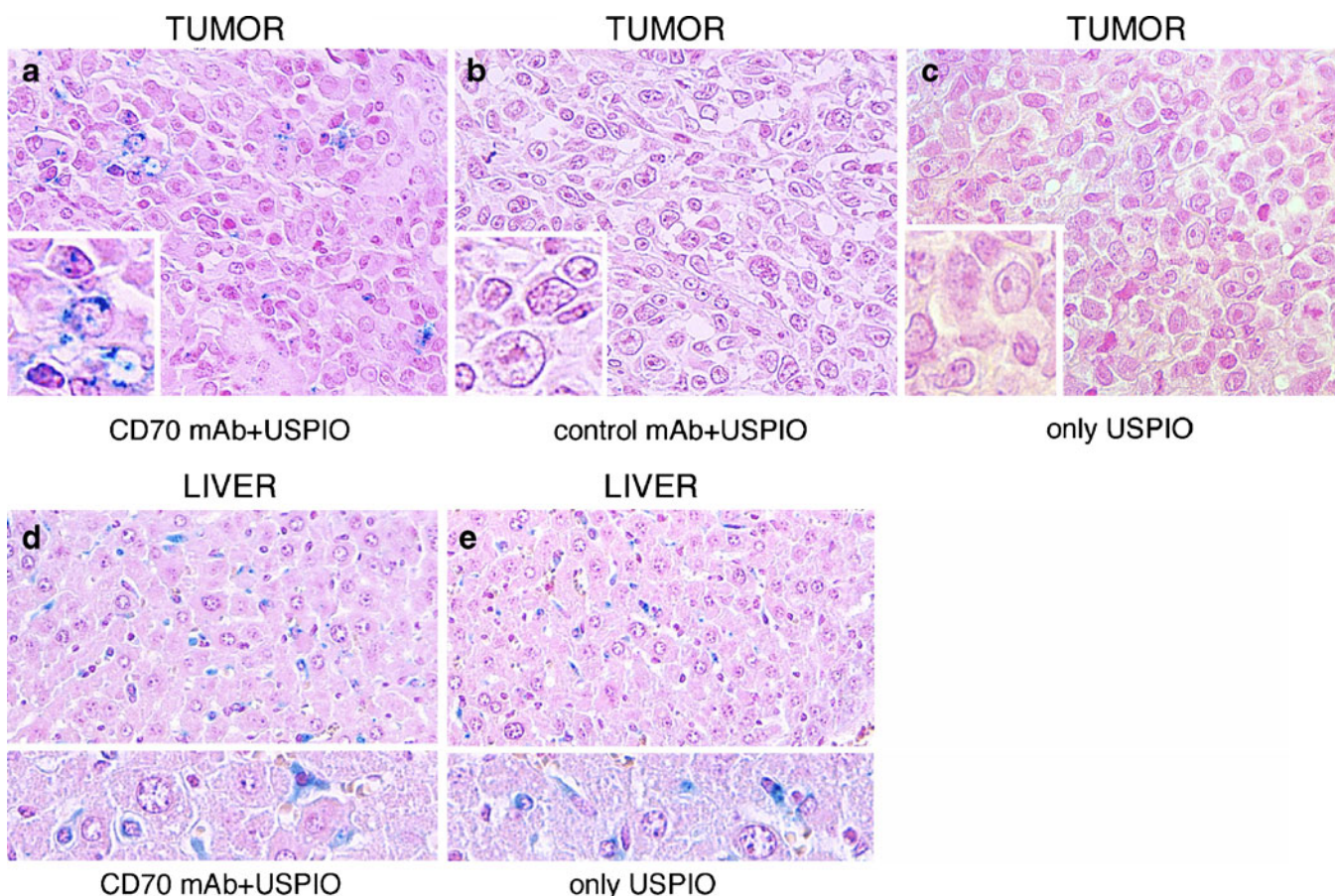


Fig. 5. Histochemical detection of iron nanoparticles in pseudo-metastatic tumor xenografts (a–c) and in the liver (d, e). In a and d, the monoclonal anti-CD70 LD6 was used as primary antibody, while in b, the isotype-matched control antibody CH-L was used. In c and e, only USPIO-anti-biotin was administered to mice. Iron bound to tumor cells was detected (a). No Prussian blue staining was detectable in the case of treatment with the isotype-matched negative control (b) or with USPIO-anti-biotin alone (c). As expected on the basis of MRI data, Prussian blue staining was observed in the liver (d) of mice receiving LD6 or only USPIO (e), indicating non-specific uptake by the reticulum–endothelial system. Tissue sections were stained with the Prussian Blue method and images were taken using an Olympus BX41 Microscope equipped with Olympus Camedia C-7070 camera (original magnification $\times 200$ or $\times 400$).

flexible, fast, and simple magnetic sorting system for the separation of large numbers of cells according to specific cell surface markers [21].

Moreover, these particles are completely biodegradable and show no toxic effects or incompatibility with biological organisms, thereby substantiating their use as contrast agents for MRI and as carrier systems for therapy [21].

We previously demonstrated that USPIO-anti-CD20 conjugates were able to bind to neoplastic B cells *in vivo* and were detectable by MRI at 1.5 T, indicating that they could be used to monitor the disease [19, 22]. However, many antibodies directed to tumor antigens, potentially useful especially in experimental settings, are not available as USPIO conjugates. We therefore sought to evaluate whether an “indirect” targeting technique, which employs unlabeled mAbs followed by a common USPIO-conjugated secondary reagent, could provide an equally suitable contrast agent.

In this study, we assessed the feasibility of targeting superparamagnetic particles to tumors by means of a two-step system based on the administration of tumor-specific biotin-conjugated antibodies followed by USPIO-anti-biotin. For this purpose, we chose to target the human CD70 antigen, expressed by lymphoma cells and only transiently by normal activated lymphocytes, identified by the murine mAb LD6 [14, 15]. Since LD6 does not react with murine cells, it seemed suitable for the monitoring of human lymphoma xenografts in mice. An isotype-matched murine mAb that does not react with human lymphoma cells, CH-L, was used as negative control. The two purified antibodies were both biotin-conjugated in-house, and labeling was assessed by Western blot with streptavidin-HRP and found to be equal. As common secondary reagent, commercially available USPIO particles conjugated with monoclonal anti-biotin were chosen since their physical characteristics matched those of the USPIO-anti-CD20 contrast agent successfully used in our previous work [19]. Before *in vivo* experiments, the reactivity of USPIO-anti-biotin toward the biotin-labeled monoclonal anti-CD70 bound to the lymphoma cell surface was checked *in vitro* by immunofluorescence.

We initially assessed the combination of biotin-labeled antibodies with USPIO-anti-biotin in human lymphoma xenografts induced subcutaneously in immunodeficient mice. In this set of experiments, visual analysis showed a slight and dishomogeneous decrease in SI on T2*-weighted images.

Quantitative analysis confirmed a 30% decrease in SI at the tumor site. Histopathological analysis with Pearl Prussian blue staining demonstrated that iron nanoparticles were indeed present, in keeping with the MRI results. The control group was injected with only USPIO-anti-biotin or with isotype control CH-L mAb and USPIO-anti-biotin to investigate the possible role of the non-specific distribution of USPIO in the tumor. The results obtained suggest that non-specific localization is low in this type of tumor, indicating that the MR signal

obtained is related to the specific ability of the conjugated antibodies to target the tumor-associated antigen *in vivo*. We also observed an evident localization of iron in the liver regardless of the primary antibody used for treatment. This finding may be due to the aspecific phagocytosis of nanoparticles by liver reticulum-endothelial cells and to interaction of the Fc component of the antibodies with surface Fc receptors. The subcutaneous xenograft animal model was chosen because tumor growth can be easily monitored.

In a second set of experiments, we developed a pseudo-metastatic lymphoma model by injecting mice with tumor cells in the tail vein. *In vivo* MRI demonstrated a decrease in SI especially on b-FFE-weighted sequences compared to T2*-weighted sequences. In *ex vivo* MR images, tumor specimens showed a higher decrease in SI on T2*-weighted images compared to *in vivo* MR examination.

The magnetic susceptibility of iron nanoparticles produces magnetic field dishomogeneities that are known to affect regions in MR images over a far greater area than the actual particle distribution. Cell-bound large iron nanoparticles can influence magnetic resonance SI many pixels away and produce an effect described as “blooming artifact,” the size of which is pulse-sequence- and field-strength-dependent. To maximize the ability to visualize this effect, most imaging studies have used T2- or T2*-weighted spin-echo and gradient echo sequences and high magnetic field strengths. The region of signal void in these images is consequentially larger than the actual area occupied by the iron-targeted tumor cells.

Our *in vivo* images of mouse kidneys were acquired with T2*-weighted and b-FFE-weighted sequences. We observed that b-FFE-weighted gradient echo sequences displayed high sensitivity also to small numbers of iron nanoparticles, in particular in the case of intracellular iron localization. Indeed, b-FFE-weighted gradient echo imaging sequences have a number of advantages over other imaging sequences, above all for cellular imaging fields.

As demonstrated in another study performed with a different MR instrument at 1.5 T [23], the high sensitivity to off-resonance effects, which was originally considered a negative aspect of this imaging sequence, showed that it was instead very effective for cellular imaging with iron oxide nanoparticles. Indeed, it was recently demonstrated for the first time that individual SPIO-labeled cells can be detected *in vivo* using this specialized microimaging approach [24].

While maintaining the sensitivity to iron oxide-labeled cells intrinsic to gradient echo sequences, balanced gradient echo-weighted sequence exhibits blooming artifact suppression traits intrinsic to spin-echo sequences. In addition, the b-FFE-weighted gradient echo sequence provides substantially enhanced SNR compared to spin-echo and gradient echo sequences. This improvement in SNR allows microimaging at lower field strengths and acquisition of images at high spatial resolution with reasonable scan times. These

two factors were key to visualizing small numbers of iron-targeted tumor cells.

Our results reflect those obtained in previous studies which used similar USPIO contrast agents to visualize inflammatory cell infiltration of the brain in a murine model of autoimmune encephalomyelitis [11]. However, these studies used 3.5- to 7-T MRI equipment, while in the present investigation, the high antigen expression by a homogeneous population of tumor cells allowed the detection of cell-bound USPIO by 1.5-T standard equipment.

Our present *in vitro* data using an anti-CD70 suggest that MRI at 1.5 T can detect tumor cells and eventually identify metastases that express the relevant target antigens at high levels, whereas tumors with low CD70 antigen expression may not be detected. Thus, the monoclonal anti-CD70 may represent an additional and molecularly specific contrast agent in the diagnosis and follow-up of CD70-expressing tumors. In addition, MRI detection at 1.5 T of lymphoma masses by monoclonal anti-CD70 *in vivo* may be suggestive of a strong antigenic expression and of a good tumor localization of the CD70 mAb, thus allowing the selection of those patients that could benefit from CD70 mAb-based immunotherapy. Indeed, previous data indicate that therapy with the mAb LD6 inhibits the growth of CD70-expressing tumors grown as xenografts in immunodeficient mice [2].

One potential limit of the present study may be the iron concentration in the commercially available USPIO-antibody conjugate used (20 mM/L) which, compared to concentrations in clinically available non-targeted MRI contrast agents that are non-specifically internalized by reticulum-endothelial cells, was low. The development of similar USPIO-targeted antibodies with high iron oxide content may thus allow improvements in the sensitivity of detection in order to permit the MR imaging of tumors with small diameters or with lower target antigen density.

A possible application of superparamagnetic antibody-targeted MRI technology is the *in vivo* tracking of cells. Indeed, previous studies have shown that *in vitro* cell labeling by MRI contrast agents can be performed by either non-targeted nanoparticles, which enter the cell in a non-specific fashion, or by specific USPIO-antibody conjugates that specifically bind to a cell surface antigen and can then eventually be internalized [25, 26].

Conclusion

In this study, we report that a two-step technique based on tumor-specific biotin-conjugated primary antibodies and commercially available USPIO-anti-biotin provides a simple method of molecular imaging using MRI at 1.5 T. Moreover, this approach contributes to efforts focusing on cell labeling *in vitro* and *in vivo*. The development of new tumor-specific contrast agents may further improve this technology and provide a new tool for the diagnosis of tumors and for cancer-targeting therapies.

Acknowledgments. This work was supported by the Italian Association for Cancer Research (AIRC), the Regione Liguria, and the Italian Ministry of Health. We thank Mr. T. Wiley for language revision.

References

- McEarchern JA, Oflazoglu E, Francisco L et al (2007) Engineered anti-CD70 antibody with multiple effector functions exhibits *in vitro* and *in vivo* antitumor activities. *Blood* 109(3):1185–1192
- Israel BF, Gulley M, Elmore S et al (2005) Anti-CD70 antibodies: a potential treatment for EBV+ CD70-expressing lymphomas. *Mol Cancer Ther* 4(12):2037–2044
- Massoud TF, Paulmurugan R, Gambhir SS (2004) Molecular imaging of homodimeric protein-protein interactions in living subjects. *FASEB J* 18(10):1105–1107
- Tanimoto A, Oshio K, Suematsu M et al (2001) Relaxation effects of clustered particles. *J Magn Reson Imaging* 14:72–77
- Ferrucci JT, Stark DD (1990) Iron oxide-enhanced MR imaging of the liver and spleen: review of the first 5 years. *AJR Am J Roentgenol* 155:943–950
- Small WC, Nelson RC, Bernardino ME (1993) Dual contrast enhancement of both T1- and T2-weighted sequences using ultrasmall superparamagnetic iron-oxide. *Magn Reson Imaging* 11:645–654
- Li W, Tutton S, Vu AT et al (2005) First-pass contrast-enhanced magnetic resonance angiography in humans using ferumoxytol, a novel ultrasmall superparamagnetic iron oxide (USPIO)-based blood pool agent. *J Magn Reson Imaging* 21(1):46–52
- Kelloff GJ, Krohn KA, Larson SM et al (2005) The progress and promise of molecular imaging probes in oncologic drug development. *Clin Cancer Res* 11(22):7967–7985
- Reynolds PR, Larkman DJ, Haskard DO et al (2006) Detection of vascular expression of E-selectin *in vivo* with MR imaging. *Radiology* 241(2):469–476
- Kang HW, Torres D, Wald L et al (2006) Targeted imaging of human endothelial-specific marker in a model of adoptive cell transfer. *Lab Invest* 86(6):599–609
- Pirko I, Johnson A, Ciric B et al (2003) *In vivo* magnetic resonance imaging of immune cells in the central nervous system with superparamagnetic antibodies. *FASEB J*. doi:10.1096/fj.02-1124fje
- Pirko I, Ciric B, Gamez J et al (2004) A human antibody that promotes remyelination enters the CNS and decreases lesion load as detected by T2-weighted spinal cord MRI in a virus-induced murine model of MS. *FASEB J*. doi:10.1096/fj.04-2026fje
- Tazzari PL, de Toter D, Bolognesi A et al (1999) An Epstein-Barr virus-infected lymphoblastoid cell line (D430B) that grows in SCID-mice with the morphologic features of a CD30+ anaplastic large cell lymphoma, and is sensitive to anti-CD30 immunotoxins. *Haematologica* 84:988–995
- Ferrini S, Cantoni C, Ciccone E et al (1991) A novel surface molecule expressed by long-term cultured T and natural killer cells is involved in cell activation. *Eur J Immunol* 21(9):1981–1987
- Orengo AM, Cantoni C, Neglia F et al (1997) Reciprocal expression of CD70 and of its receptor, CD27, in human long term-activated T and natural killer (NK) cells: inverse regulation by cytokines and role in induction of cytotoxicity. *Clin Exp Immunol* 107(3):608–613
- Cauda R, Goletti D, Lucia MB et al (1994) Analysis of natural killer (NK) cell subsets defined by the expression of two novel surface antigens (EB6 and GL183) in AIDS and AIDS-related conditions. *Clin Immunol Immunopathol* 70(3):198–210
- Harlow E, Lane D (1988) Storing and purifying antibodies. In: Harlow E, Lane D (eds) *Antibodies: a laboratory manual*. Cold Spring Harbor Laboratory, Cold Spring Harbor, pp 283–312
- Gee PA (1998) Immunomagnetic cell separation using antibodies and superparamagnetic microspheres. In: Recktenwald D, Radbruch A (eds) *Cell separation methods and applications*. Marcel Dekker, New York, pp 175–208
- Baio G, Fabbi M, de Toter D et al (2006) Magnetic resonance imaging at 1.5 T with immunospecific contrast agent *in vitro* and *in vivo* in a xenotransplant model. *MAGMA* 19(6):313–320
- Wolff SD, Balaban RS (1997) Assessing contrast on MR images. *Radiology* 202:25–29
- Ito A, Shinkai M, Honda H et al (2005) Medical application of functionalized magnetic nanoparticles. *J Biosci Bioeng* 100(1):1–11

22. Neumaier CE, Baio G, Ferrini S et al (2008) MR and iron magnetic nanoparticles. Imaging opportunities in preclinical and translational research. *Tumori* 94(2):226–233
23. Tai JH, Foster P, Rosales A et al (2006) Imaging islets labeled with magnetic nanoparticles at 1.5 Tesla. *Diabetes* 55(11):2931–2938
24. Heyn C, Ronald JA, Mackenzie LT et al (2006) *In vivo* magnetic resonance imaging of single cells in mouse brain with optical validation. *Magn Reson Med* 55:23–29
25. Jendelová P, Herynek V, Urdziková L et al (2004) Magnetic resonance tracking of transplanted bone marrow and embryonic stem cells labeled by iron oxide nanoparticles in rat brain and spinal cord. *J Neurosci Res* 76:232–243
26. Jendelová P, Herynek V, Urdziková L et al (2005) Magnetic resonance tracking of human CD34+ progenitors cells separated by means of immunomagnetic selection and transplanted into injured rat brain. *Cell Transplant* 14:173–182

2.1.2. Cell labelling by iron oxide nanoparticles

2.1.2.1. Title of paper

- Neumaier CE, **Baio G**, Ferrini S, Corte G, Daga A. MR and iron magnetic nanoparticles. Imaging opportunities in preclinical and translational research. Review Tumori 2008 Mar-Apr; 94:226-33.
- **Baio G**, Daga A, Cappelli AM, Derchi LE, Corte G, Neumaier CE. “Targeting dei Linfociti NK con ferumoxides mediante una Risonanza Magnetica ad 1.5T”. SIRM Rome 2008. Magna cum Laude. P1500.

2.1.2.2. Objective of the study

To noninvasively label NK cell lymphocytes by using two types of superparamagnetic contrast agents (USPIO and SPIO) and different types of transfection agents.

2.1.2.3. What this study added to the literature

Several attempts to image NK cells have been made by different groups using direct labelling strategies that involve purifying cells from peripheral blood, radiolabelling with ^{111}In -oxine, and re-administering to patients. This approach has limitations such as cell manipulation in culture and cell-function impairment after ex-vivo labelling. Several studies reported the high toxicity of ^{111}In -oxine to cells, leading to improper migration into target organs. *In vitro* labelling with unmodified USPIO applied at high concentration proved its effectiveness on cells such as monocytes, glioma cells, macrophages, or oligodendrocytes. In contrast, the *in vitro* spontaneous endocytosis of dextran-coated particles with non-phagocytic cells remains insufficient to allow most applications in cellular MR imaging. There are many problems associated with the low endocytosis capacity of some

“candidate” cells like lymphocytes. Moreover, cellular toxicity studies conducted with high iron concentrations in the labelling medium (e.g., 2mg Fe per ml of culture medium) led to the conclusion that free radicals could be generated, leading to reduced cell multiplication and even cellular death [146]. To improve the endocytosis internalisation of nanoparticles by non-phagocytic cells, different systems were proposed, such as coupling particles to a transfection agent or the modification of their external structure. However, these studies are often reserved to the specialised laboratories that developed them, and/or represent difficulties for non-specialists. An interesting alternative was proposed by our study, by using marketed (U)SPIO-like Feridex[®] or Sinerem[®]. In the presence of these agents, (U)SPIO were internalised in cells via the formation of endosomes. The transfection agents involve polycationic dendrimers such as Superfect[®], poly-L-lysine, or FuGENE[®]. Given its low price and wide availability, poly-L-lysine became the transfection agent of choice, as several studies reflect. The results of this piece of research were presented during the SIRM 2008 and awarded with a Magna cum Laude.

2.1.2.4. What changed as a result of the paper?

The past several years has seen tremendous advances in the engineering of immune effector cells as therapy for cancer. Despite this improvement in basic science, labelled NK cells are still not applied in the clinical environment. Several labelling studies have been carried out on stem cells as a novel therapeutic option for cell-death-related diseases, such as myocardial infarction by using iron oxide nanoparticles, but most of these are still preclinical.

2.1.2.5. In retrospect, what should have been done differently in this study?

Looking back at this work, we could have performed the preclinical *in vivo* MR imaging study of (U)SPIO-labelled NK cells in healthy controls and in cancer animal models. This set of experiments would have made our cell labelling MR protocol stronger.

2.1.2.6. Future work as a result of this publication

For the development of NK cell-based immunotherapies in solid tumors, the ability to accurately and quantitatively assess tumor homing and biodistribution by molecular imaging is the key. Imaging of NK cell-based therapies allows for an immediate assessment of therapeutic efficacy, off-target effects, severity of the immunosuppressive microenvironment, and quantification of NK cell expansion. Following the research studies on preclinical MR application of iron oxide nanoparticles, I was invited to write two chapters for one of the first Molecular Imaging books on Probes for Cancer research (“Molecular Imaging probes for cancer research”, edited by Professor Xiaoyuan Chen, Laboratory of Molecular Imaging and Nanomedicine (LOMIN), at NIH Bethesda, USA).

2.1.2.7. Confirmation of authorship

This is shown at the end of Chapter 2.

2.1.2.7. External link to the paper on the journal website

<https://www.ncbi.nlm.nih.gov/pubmed/18564611>

Tumori, 94: 226-233, 2008

MR and iron magnetic nanoparticles. Imaging opportunities in preclinical and translational research

Carlo Emanuele Neumaier¹, Gabriella Baio¹, Silvano Ferrini², Giorgio Corte³,
and Antonio Daga³

¹Department of Diagnostic Imaging, ²Laboratory of Immunological Therapy, ³Translational Oncology,
Istituto Nazionale per la Ricerca sul Cancro, IST, Genoa, Italy

ABSTRACT

Ultrasmall superparamagnetic iron oxide nanoparticles and magnetic resonance imaging provide a non-invasive method to detect and label tumor cells. These nanoparticles exhibit unique properties of superparamagnetism and can be utilized as excellent probes for magnetic resonance imaging. Most work has been performed using a magnetic resonance scanner with high field strength up to 7 T. Ultrasmall superparamagnetic iron oxide nanoparticles may represent a suitable tool for labeling molecular probes that target specific tumor-associated markers for *in vitro* and *in vivo* detection by magnetic resonance imaging.

In our study, we demonstrated that magnetic resonance imaging at 1.5 T allows the detection of ultrasmall superparamagnetic iron oxide nanoparticle conjugated antibody specifically bound to human tumor cells *in vitro* and *in vivo*, and that the magnetic resonance signal intensity correlates with the concentration of ultrasmall superparamagnetic iron oxide nanoparticle antibody used and with the antigen density at the cell surface. The experiments were performed using two different means of targeting: direct and indirect magnetic tumor targeting. The imaging of tumor antigens using immunospecific contrast agents is a rapidly evolving field, which can potentially aid in early disease detection, monitoring of treatment efficacy, and drug development. Cell labeling by iron oxide nanoparticles has emerged as a potentially powerful tool to monitor trafficking of a large number of cells in the cell therapy field. We also studied the labeling of natural killer cells with iron nanoparticles to a level that would allow the detection of their signal intensity with a clinical magnetic resonance scanner at 1.5 T.

Magnetic resonance imaging and iron magnetic nanoparticles are able to increase the accuracy and the specificity of imaging and represent new imaging opportunities in preclinical and translational research.

Introduction

Magnetic resonance imaging (MRI) offers a non-invasive technique to obtain anatomic and metabolic/functional information with high spatial and temporal resolution. It has two particular advantages over techniques that involve the use of radionuclides or optical probes: higher spatial resolution, and physiological, molecular and anatomical information can be extracted simultaneously. For specific detection of macromolecules using MRI, i.e., molecular imaging, ligands need to be conjugated to MR contrast agents in order to induce a different signal intensity (SI) from the non-targeted tissue. Similarly, for MRI detection of the cell populations of interest, i.e., cellular imaging, cells need to be labeled with MR contrast agents in order to make them stand out from the surrounding tissues. For both applications, gadolinium chelates may be used, but they have low relaxivity values, which further decrease upon cellu-

Key words: iron oxide nanoparticle, magnetic resonance, targeted contrast material, *in vivo* small animal magnetic resonance imaging, cell-specific magnetic resonance imaging.

Correspondence to: Carlo E Neumaier, Department of Diagnostic Imaging, IST, Istituto Nazionale per la Ricerca sul Cancro, Largo Rosanna Benzi 10, 16100 Genoa, Italy.
Tel +39-010-5600872;
fax +39-010-511014;
e-mail carlo.neumaier@istge.it

lar internalization, are not biocompatible, and very little is known about their potential toxicity following cellular dechelation over time.

Superparamagnetic iron oxide particles (SPIO), which were introduced as contrast agents shortly after the use of gadolinium chelates¹⁻³, currently appear to be the preferred material. In particular, ultrasmall superparamagnetic iron oxide particles (USPIO) may represent a suitable tool for labeling molecular probes that target specific tumor-associated markers for *in vitro* and *in vivo* detection by MRI. An important property of USPIO is the strong T2 relaxivity that produces a decrease in SI on T2-weighted images^{4,5} and also a high T1 relaxivity with an increase in SI on T1-weighted images^{6,7}. The association of MRI with specific tumor iron oxide nanoparticles is able to increase the accuracy and the specificity of imaging⁸.

Monoclonal antibodies (mAbs) represent an important emerging tool in cancer therapy, and the study of specific surface markers on tumor cells has determined an important development of mAbs for use as targeted therapeutic agents. Therapeutic mAbs can act by blocking growth factors, directly signaling arrest and apoptosis, or inducing elimination of mAb-decorated target cells via activation of host defense mechanisms⁹.

The preparation and use of magnetically labeled mAbs seemed to be an extension of the earlier work in nuclear medicine carried out using radiolabeled antibodies. In this way, the detailed anatomic information on the MR images can be specifically marked in order to detect a disease in its earliest stages, particularly tumors. Immunoglobulins can be covalently linked to the dextran polysaccharide coat of the iron oxide using an established method^{10,11}. Iron oxide nanoparticles have been conjugated to polyclonal immunoglobulin G for the detection of induced inflammation¹², to mAb fragments for the specific visualization of myocardial infarction¹³, to intact mAbs for immunospecific detection of intracranial small cell lung carcinoma¹⁴, intracellular adhesion molecule-1 gene expression on transfected cell lines¹⁵ and oligodendrocyte progenitors¹⁶, and to synaptotagmin I for detection of apoptotic tumor cells¹⁷. Alternative ways of attaching mAbs to magnetic nanoparticles include glutaraldehyde cross-linking¹⁸, complexing through ultrasonication^{19,20}, using the biotin-streptavidin system^{21,22} and amine-sulfhydryl group linkage^{23,24}. The aforementioned studies provide examples of cases where molecular MRI using iron oxides has proven to be successful. Moreover, most work has been performed using an MR scanner with high field strength up to 7 T.

However, cellular imaging aims to visualize cells. It is a non-invasive method to study cellular processes which entails proper labeling of cells with appropriate MR contrast agents²⁵. Cell labeling by SPIO has emerged as a potentially powerful tool to monitor trafficking of transplanted cells by magnetic resonance, e.g. in studies

for tissue repair, but it has also become increasingly important in the development of oncologic cell therapies.

We report our experience in tumor and cell labeling. For tumor targeting, we used two different approaches: direct magnetic tumor targeting by a USPIO conjugated antibody specifically bound to human tumor cells *in vitro* and *in vivo*, and indirect magnetic tumor targeting based on a bridge of tumor-specific biotin-conjugated antibodies *in vivo*. We demonstrated that the MRI SI correlates with the concentration of USPIO antibody used and with the antigen density at the cell surface. We also studied the possible use of these conjugated monoclonal antibodies as contrast agents for *in vivo* labeling of human tumor cells.

For cell labeling, we investigated the possibility of labeling human natural killer (NK) T cells with iron nanoparticles and different types of transfection agents. We tested these types of targeting at a level that would allow their SI with a clinical MR scanner at 1.5 T.

Iron oxide nanoparticles

The *in vitro* magnetic properties of USPIO are reported to be a T₁ relaxivity (r₁) of 21.6 (mmol/liter-sec)⁻¹ and a T₂ relaxivity (r₂) of 44.1 (mmol/liter-sec)⁻¹ at 37 °C and 0.47 tesla (T), where mmol/liter is the concentration of iron oxide. Conventional, water-soluble, paramagnetic contrast agents are generally metal chelates with unpaired electrons, and they work by shortening both T₁ and T₂ relaxation times of surrounding water protons to produce a signal-enhancing effect²⁶. They distribute in the extracellular fluid and do not cross the intact blood-brain barrier²⁷. Another approach is the development of water-insoluble SPIO nanoparticles that comprise iron oxides such as magnetite (Fe₃O₄), maghemite (γ-Fe₂O₃), or other ferrites^{28,29}. Ferromagnetic crystals are composed of magnetized domains the size of a micron. Superparamagnetism occurs when the size of the crystals is smaller than the ferromagnetic domain (~30 nm). SPIO agents typically consist of an iron oxide core and a hydrophilic coating³⁰. They have very high relaxivities (R₁ and R₂), and the significant capacity of these particles to increase the susceptibility effect of the measured spin-spin relaxation time (T₂^{*}) is especially useful in MRI. This large T₂^{*} effect is the result of the non-homogeneous distribution of these superparamagnetic particles, which accelerates the loss of phase coherence of the spins contributing to the MRI signal. Clinically, SPIO are predominantly used for their negative enhancement effect on T₂- and T₂^{*}-weighted sequences. This class of MRI agents includes large oral SPIO (300-3500 nm) agents, standard SPIO (60-150 nm) agents, USPIO (10-40 nm) agents, monocrystalline iron oxide (10-30 nm) nanoparticle agents, and cross-linked iron oxide agents (a form of monocrystalline iron oxide nanoparticles with a cross-linked dextran coating)³¹. Both the size and

the surface properties of SPIO particles affect their pharmacokinetics, organ distribution, and intracellular uptake³². Biologically, SPIO particles are usually taken up by the reticuloendothelial system and phagocytic cells. USPIO particles are less prone to liver uptake and are small enough to migrate across the capillary wall of tumors³³.

Tumor targeting

Direct tumor magnetic labeling

We used commercially available USPIO bound to an anti-CD20 monoclonal antibody (immunoglobulin G1-murine) and stabilized with sodium citrate (Miltenyi Biotec, Bergisch Gladbach, Germany). USPIO-anti-CD20 mAb is a molecular imaging agent developed for MRI of CD20 antigen-positive B cell lymphomas. The particles were composed of a biodegradable, non-toxic, ferromagnetic matrix (dextran). The overall mean particle diameter was ~30-50 nm. There were typically 10-200 antibody molecules/particle (30 nm in diameter). The *in vitro* R_1 and R_2 relaxivities measured at 37 °C and 1.5 T were 30 and 60 liter·s⁻¹·mmol⁻¹, respectively³⁴. The CD20 antigen is a 35-kDa, cell-surface non-glycosylated, hydrophobic phosphoprotein expressed on normal and malignant B cells, and it does not shed, modulate, or internalize^{35,36}. It is present on ~9% of the peripheral blood mononuclear cell (PBMC) fraction and >90% of B cells from blood and lymphoid organs. Lymphoma cells from >90% of patients with B-cell non-Hodgkin lymphoma express this antigen. Despite the presence of CD20 on normal B cells, it is a good tumor target for molecular targeting with antibodies for the management of non-Hodgkin lymphoma.

As cell lines, D430B and Raji cells (anaplastic large B-cell lymphoma) were used. The expression of surface antigens by D430B and Raji cell lines was analyzed by immunofluorescence. The presence of USPIO antibody bound to the cells was verified by staining with a phycoerythrin-labeled anti-mouse immunoglobulin antibody (Southern Biotec Inc., Birmingham, AL, USA). All samples were analyzed by cytofluorimetric analysis on a FACScan (BD Biosciences, Franklin Lakes, NJ, USA).

In vitro study. We incubated five million human D430B cells³⁷ and Raji Burkitt lymphoma cells (ICLC, Interlab Cell Line Collection) with different amounts of anti-CD20 monoclonal antibody USPIO conjugates. After incubation with the USPIO-mAb conjugates, unbound conjugates were removed and cells were included in a matrigel sponge for MRI imaging with a 1.5-T MR system (Philips Gyroscan NT-Intera). Immunofluorescence analysis showed that USPIO-anti-CD20 mAb bound to the cell surface and the D430B cells expressed five times more CD20 molecules than the Raji Burkitt cells. USPIO anti-CD20 mAb on D430B cells showed a

decrease in SI on T2*-weighted images and SI enhancement on T1-weighted images (Figure 1). In comparison, USPIO anti-CD20 mAb on Raji Burkitt cells only showed a slight hypointensity on T2-weighted images and a non-homogeneous hyperintensity on T1-weighted images (Figure 1). Quantitative analysis showed that the changes in T1 SI ($\Delta SI = SI_{\text{non-labeled}} - SI_{\text{USPIO anti-CD20 mAb}} / \text{noise}$) values from the three-dimensional fast-field echo sequences at 1.5 T for the USPIO anti-CD20 mAb on D430B cells were -36.6, -12.4, and -6.2 for 0.03 μmol iron (Fe)/liter, 0.01 μmol Fe/liter, and 0.005 μmol Fe/liter USPIO anti-CD20 mAb, respectively. The T2 ΔSI values were -73, -24, and -12 for 0.03 μmol Fe/liter, 0.01 μmol Fe/liter, and 0.005 μmol Fe/liter USPIO anti-CD20 mAb, respectively. In comparison, the T1 ΔSI values of the USPIO anti-CD20 mAb on Raji Burkitt cells were -25, -9, and -6 for 0.03 μmol Fe/liter, 0.01 μmol Fe/liter, and 0.005 μmol Fe/liter USPIO anti-CD20 mAb, respectively. The T2 ΔSI values were -43, -17.7, and -12 for 0.03 μmol Fe/liter, 0.01 μmol Fe/liter, and 0.005 μmol Fe/liter USPIO anti-CD20 mAb, respectively.

In vivo study. Experiments were approved by the Institutional Review Committee of the National Cancer Institute and were performed in accordance with the National Regulations on Animal Research Resources. MRI

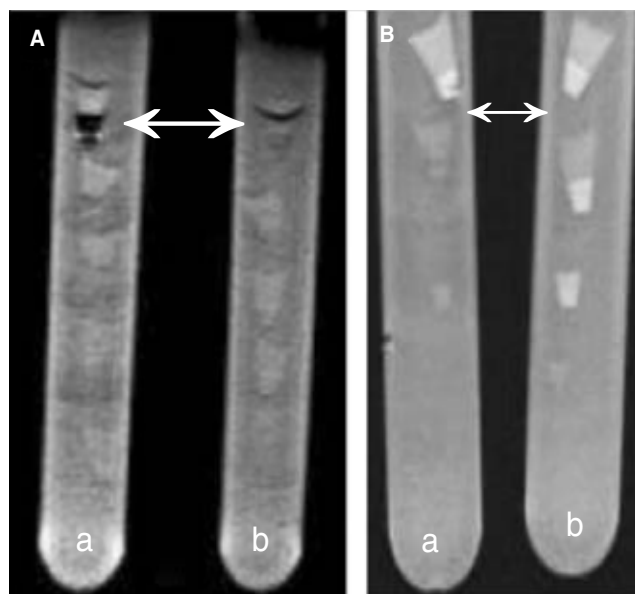


Figure 1 - Representative MR images of cell pellets in test-tubes. Each pellet contains 5×10^6 D430B lymphoma cells and 5×10^6 Raji lymphoma cells on T2*-weighted images (A) and on T1-weighted images (B), with of USPIO-anti-CD20, respectively. A) D430B cells-USPIO-anti-CD20 showed an important decrease of SI on T2*-weighted images that is more evident in the pellet treated with 0.03 μmol Fe/l of USPIO-anti-CD20, whereas Raji cells-USPIO-anti-CD20 showed a slight hypointensity in the same sequences (double arrow). B) D430B cells-USPIO-anti-CD20 showed a SI enhancement on T1-weighted images and Raji cells-USPIO-anti-CD20 an inhomogeneous hyperintensity on T1-weighted three-dimensional fast field echo images (double arrow).

studies were performed in NOD-SCID mice bearing s.c. D430B or the Raji Burkitt tumors (0.5-1 cm²). Each mouse received an i.v. dose of 8 µmol Fe/kg 24 h before imaging with a 1.5 T-MR system³⁴.

The D430B tumors showed a non-homogeneous SI decrease on T2*-weighted images (Figure 2) and a slight SI enhancement on T1-weighted images. In comparison, the Raji Burkitt tumors showed slight non-homogeneous hypointensity on T2*-weighted images and slight nonhomogeneous hypertensity on T1-weighted images. Quantitative analysis studies were conducted with the region-of-interest technique to obtain the signal/noise (SNR) ratios. The T2*-weighted Δ SI value ($\text{SNR}_{\text{before}}/\text{SNR}_{\text{after}}$) of the D403B tumor ($n = 5$) was $35 \pm 7\%$ ($82 \pm 9\%/57 \pm 11\%$), whereas the T2*-weighted Δ SI value of the Raji Burkitt tumor was $15 \pm 8\%$ ($47 \pm 10\%/40 \pm 13\%$). In comparison, tumors in mice injected with a non-specific standard SPIO agent ferumoxide (17 µmol Fe/kg) showed a T2*-weighted Δ SI value of $5 \pm 6\%$ ($1,392 \pm 86\%/1,322 \pm 80\%$).

Indirect tumor magnetic labeling

We used commercially available USPIO bound to an anti-biotin monoclonal antibody (immunoglobulin G1-murine) and stabilized with sodium citrate (Miltenyi Biotec). The r_1 and r_2 relaxivities were 30 L·sec⁻¹·mmol⁻¹ and 60 L·sec⁻¹·mmol⁻¹, respectively³⁴. Anti-CD70 murine mAb, clone LD6, was purified from culture medium by affinity chromatography on Sepharose-Protein A (GE Healthcare, Chalfont, St Giles, UK) and subsequently conjugated with EZ-Link Sulfo-NHS-LC-biotin (Pierce®, Rockford, IL) according to the manufacturer's instructions^{38,39}. Surface expression of the CD70 antigen by the D430B line was analyzed by immunofluorescence and flow cytometry. To detect the binding of USPIO anti-biotin to the biotin-conjugated antibodies, D430 B cells were incubated with biotin-LD6 and biotin-CH-Leo. After washes, cells were challenged with 10 ml of the USPIO anti-biotin suspension, and the presence of USPIO-anti-biotin bound to the cells carry-

ing biotin-conjugated anti-CD70 mAb was verified by staining with a FITC-labeled anti-mouse immunoglobulin antibody (Caltag) followed by flow cytometric analysis. Mice were injected s.c. with 2×10^7 human D430B cells (palpable masses of 0.5 to 1 cm²). In a second set of experiments, 2×10^7 D430B cells per mouse were injected into the tail vein to induce pseudo-metastases, in particular localized in kidney and retroperitoneum. To target tumor-expressed human CD70 antigen, 30 µg per mouse of biotin-labeled LD6 mAb was administered via the tail vein and MRI was performed with an MR scanner at 1.5 T. Four hours after administration of the biotin-labeled antibody, 16 µmol Fe/kg per mouse of USPIO anti-biotin was injected in the tail vein. MRI was performed again 24 h later. As negative control, a group of mice was similarly inoculated with biotin-conjugated CH-Leo mAb. We performed the histological analysis according to standard techniques. Iron oxide-labeled cells were stained with Perl's Prussian blue stain. The D430B s.c. tumors showed a nonhomogeneous SI decrease on T2- and T2*-weighted images 24 h after USPIO anti-biotin administration (Figure 3); the D430B pseudo-metastases showed an important decrease in SI on T2* (Figure 4) and on balanced fast-field, echo-weighted images. Histopathological analysis using the Prussian blue stain demonstrated a significant iron localization in the D430B pseudo-metastases in comparison to s.c. D430B tumor.

Cell labeling

NK cells were generated from PBMC obtained from healthy donors. The PBMC were enriched for NK cell populations by negative depletion using immunomagnetic beads (NK cell isolation kit II; Miltenyi Biotec). PBMC were incubated with a biotin-conjugated antibody mix containing anti-CD3, anti-CD4, anti-CD14, anti-CD15, anti-CD19, anti-CD36, anti-CD123 and anti-235a (glycophorin A). Cells were washed and cen-

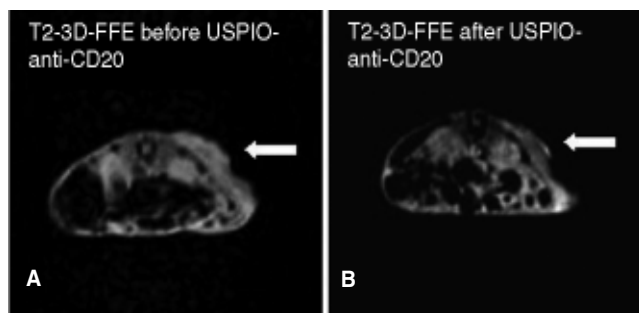


Figure 2 - Direct magnetic tumor targeting *in vivo*. On T2*-weighted images before (A) and after (B) USPIO-anti-CD20 antibody administration. The CD20 high D430B tumor showed a non-homogeneous decrease of signal.

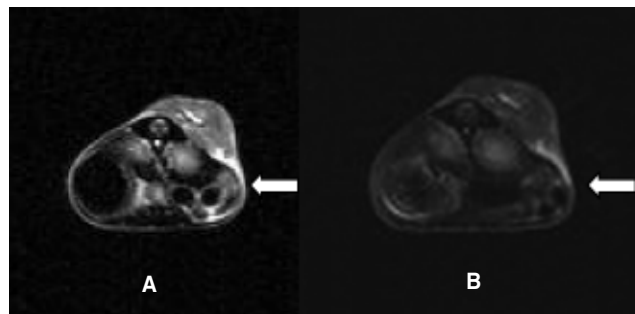


Figure 3 - Indirect tumor targeting in D430B subcutaneous lymphoma. On T2-weighted images, before (A) and after (B) USPIO-anti-biotin administration. There was a nonhomogeneous decrease in signal.

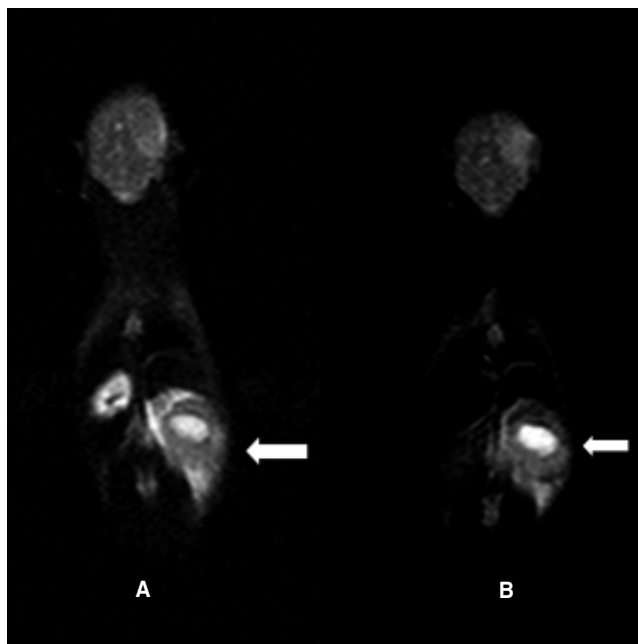


Figure 4 - Indirect tumor targeting in D430B pseudo-metastases lymphoma. On T2-weighted images, before (A) and after (B) USPIO-anti-biotin administration. There was a decrease in signal intensity in D430B.

trifuged. The supernatant was discarded and the cell pellet was resuspended in 0.1% phosphate-buffered saline human AB serum and incubated at 4 °C for 10 min after the addition of depletion anti-biotin microbeads. The cell suspension was loaded on a column in the magnetic field of a magnetic-activated cell sorter. NK cell purity was determined by flow cytometry. Enriched NK cells were expanded as bulk NK cell populations in RPMI containing 10% heat-inactivated fetal calf serum and 500 IU/ml of interleukin-2.

As a targeted contrast agent, we used a commercially available ferumoxide suspension (Endorem, Guerbet, Paris), which has a total iron content of 11.2 and 28 mg/ml, respectively. As a transfection agent, protamine sulfate (Pro, 6 mg/ml) or polylysine (PLL, 1.5 mg/ml) was added. The final FE-Pro or FE-PLL suspensions were added directly to the cells and incubated overnight. For the assessment of labeling efficiency and to study the SI on an MR scanner at 1.5 T, four groups were compared: unlabelled cells; NK-ferumoxides alone; NK-ferumoxides plus protamine; NK-ferumoxides plus PLL (Figure 5). Cell viability was measured in single cell suspensions by trypan blue exclusion. Perl's Prussian blue stain was performed to show iron localization in NK cells. On T2-weighted images, we observed a decrease in SI in all three groups due to iron in NK cells (Figure 5), but in the quantitative analysis, we calculated a significant decrease in SI in human ferumoxides-PLL-NK-labeled cells (60%) compared with human ferumoxide-Pro-NK-labeled cells (30%). Perl's Prussian blue stain demonstrated that the hypointensi-

ty on MRI was due to ferumoxides in NK cells. Moreover, there were no toxic effects after labeling cells, and with our doses no apoptosis or necrosis was observed.

Discussion

SPIO particles appear to be the preferred material for the targeting of tumor and cells. The popularity of SPIO particle labeling is mainly because: 1) they provide a strong change in signal (hypointensity) per unit of metal (on T2*-weighted images), 2) they are composed of biodegradable iron (biocompatible and can be recycled by cells using biochemical pathways for iron metabolism), 3) their surface coating (dextran) allows chemical linkage of functional groups and ligands, 4) they can be easily detected by light and electron microscopy, and 5) they can be manipulated and change their magnetic properties according to size. Iron nanoparticles can be conjugated to specific mAbs in order to label tumor and cells. These "molecular probes" are able to induce a different SI in tumor tissue compared to normal tissue. Many promising probes are being, or will be, applied to the diagnosis of cancer and may also facilitate cancer therapy. Furthermore, many antibodies directed to tumor-associated antigens are available for clinical use. A wide spectrum of commercially available SPIO antibodies used for cell-separation techniques is available, and some of them are also available as clinical-grade reagents⁸. They may be a promising tool for several *in vitro* and *in vivo* applications.

In our studies, we demonstrated the successful use of a commercially available USPIO antibody conjugate for MRI *in vitro* and in a murine model. In medicine, many

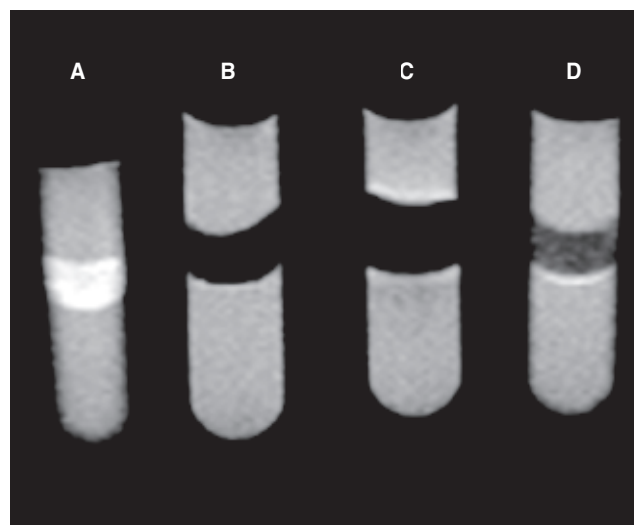


Figure 5 - T2-weighted images of USPIO natural killer labeled cells and natural killer cells. A) Unlabelled natural killer cells. B) Ferumoxides Pro-NK-labeled cells. C) Ferumoxides PLL-NK-labeled cells. D) NK-ferumoxides

approaches have been investigated for diagnosis and therapy and have offered a large variety of applications: magnetic cell separation, MRI, magnetic targeted drug delivery, and magnetically induced hyperthermia. Such particles do not have any toxic effect or incompatibility with biological organisms, therefore they have a potential use as contrast agents for MRI and as a carrier system for drugs⁴⁰.

Our *in vitro* study was designed to assess the feasibility of the use of an MR scanner at 1.5 T to detect USPIO antibodies bound to tumor cells at potentially suitable doses for small animal models in a pre-clinical setting. We demonstrated that commercially available USPIO antibody conjugates specific for a B-cell lymphoma-associated antigen binding to the human D430B cells or to the Raji Burkitt lymphoma cell line can be visualized on MRI at 1.5 T. We also demonstrated through *in vitro* assays that there is a dose-response relationship between the different amounts of USPIO anti-CD20 bound to the cells and the DSI on T2*-weighted images. This effect is more evident on cells expressing high levels of the target antigen (D430B) than on cells with a lower expression (Raji), indicating that the magnitude of DSI observed depends on the dose of the immunospecific contrast agent and on the target antigen expression of the cells. Indeed, *in vivo* experiments indicated that the intravenous administration of a single dose of USPIO anti-CD20 antibody conjugate 24 h before performing MRI at 1.5 T is sufficient to induce detectable changes of SI in a reproducible fashion ($35\% \pm 7$). Our results are consistent with those obtained in previous studies using similar USPIO contrast agents to visualize inflammatory cells infiltrating the brain in a murine model of autoimmune encephalomyelitis⁴¹. However, these previous studies used a 3.5-7 T MR scanner, whereas in the present investigation the high antigen expression by a homogeneous population of tumor cells allowed the detection of cell-bound USPIO by a 1.5 T standard scanner. With indirect magnetic tumor targeting, we assessed the feasibility of targeting superparamagnetic particles to tumors by a bridge of tumor-specific biotin-conjugated antibodies. We demonstrated that the combination of specific biotin-labeled antibodies with the USPIO anti-biotin as the common secondary reagent was able to target two types of murine models: the xenotransplant (s.c.) and the pseudo-metastases lymphoma tumors. In particular, the D430B pseudo-metastasis was localized in the kidney and retroperitoneum. These tumor sites are more vascularized than s.c. tumors. In fact, the decrease in SI at MRI visualization was more evident in D430B pseudo-metastases, and Perl's Prussian blue staining demonstrated a significant iron concentration in this type of tumor model.

A potential limitation of these molecular probes may be related to the relatively low iron concentration compared with the clinically available non-targeted MRI contrast agents, which are non-specifically internalized

by the reticular-endothelial cells. Thus the development of similar USPIO-targeted antibodies with high iron oxide content may enhance the sensitivity of detection, in order to allow MRI of tumors with small diameters or with lower target antigen density. We believe that this indirect method opens the possibility to target any cell surface antigen, thus becoming a useful tool in MRI.

Another possible application of iron nanoparticles and MRI is to label cells. In our cell labeling experiments, we illustrated the possibility to label NK cells with ferumoxides and different kinds of transfection agents. NK cells are a subpopulation of lytic effector lymphocytes that represents the first line of defense against tumor progression and metastasis. More studies were performed with stem cells, which have a significant phagocytic activity. This characteristic is less evident in NK cells. For this reason, we used different kinds of transfection agents. The complex ferumoxides-PLL-NK cells showed a substantial decrease in SI on T2*-weighted images, and Perl's Prussian blue staining confirmed the presence of ferumoxides in NK cells, thus proving that PLL is more efficient than Pro as a transfection agent for the internalization of ferumoxides by NK cells.

We have shown that significant changes in T2-weighted MRI SI can be achieved in human NK lymphocytes with a short incubation of iron oxide nanoparticles at concentrations that do not have deleterious effects on cellular viability or function. The detected contrast change lasted for at least 24 h and raises the possibility that iron oxide nanoparticle labeling of lymphocytes could be used to track these cells in tumors and other tissues using high spatial resolution MRI. Iron nanoparticles might be a type of targeting to study *in vivo* NK cell migration at a level that would allow the detection of their SI with a clinical MR scanner at 1.5 T. We believe that by optimizing molecular-targeted contrast agents, MRI technology and the generation of new USPIO or SPIO antibodies, or other USPIO or SPIO ligands, may provide useful immunospecific contrast agents for the diagnosis of tumors and for targeting cells for cell therapy. In this way, it promises to provide new methods for the early detection of cancer and support for personalized cancer therapy. Nevertheless, there has been sufficient experience with specifically targeted contrast agents and high-resolution techniques for MRI and other modalities that we must begin moving these new technologies from the laboratory to the clinic.

Conclusions

MRI combined with iron oxide contrast agents is able to increase the accuracy and specificity of imaging and represents a new imaging opportunity in preclinical and translational research.

References

- Mendonca Dias MH, Lauterbur PC: Ferromagnetic particles as contrast agents for magnetic resonance imaging of liver and spleen. *Magn Reson Med*, 3: 328-330, 1986.
- Olsson M, Persson B, Salford L, Schroder U: Ferromagnetic particles as contrast agents in T2 NMR imaging. *Magn Reson Imaging*, 4: 437-440, 1986.
- Renshaw PF, Owen CS, McLaughlin AC, Frey TG, Leight JS Jr: Ferromagnetic contrast agents: a new approach. *Magn. Reson. Med*, 3: 217-225, 1986.
- Tanimoto A, Oshio K, Suematsu M, Pouliquen D, Stark DD: Relaxation effects of clustered particles. *J Magn Reson Imaging*, 14: 72-77, 2001.
- Ferrucci JT, Stark DD: Iron oxide-enhanced MR imaging of the liver and spleen: review of the first 5 years. *AJR Am J Roentgenol*, 155: 943-950, 1990.
- Small WC, Nelson RC, Bernardino ME: Dual contrast enhancement of both T1- and T2-weighted sequences using ultrasmall superparamagnetic iron oxide. *Magn Reson Imaging*, 11: 645-654, 1993.
- Li W, Tutton S, Vu AT, Pierchala L, Li BS, Lewis JM, Prasad PV, Edelman RR: First-pass contrast-enhanced magnetic resonance angiography in humans using ferumoxytol, a novel ultrasmall superparamagnetic iron oxide (USPIO)-based blood pool agent. *J Magn Reson Imaging*, 21(1): 46-52, 2005.
- Kelloff GJ, Krohn KA, Larson SM, Weissleder R, Mankoff DA, Hoffman JM, Link JM, Guyton KZ, Eckelman WC, Scher HI, O'Shaughnessy J, Chenson BD, Sigman CC, Tatum JL, Mills GQ, Sullivan DC, Woodcock J: The progress and promise of molecular imaging probes in oncologic drug development. *Clin Cancer Research*, 11: 7967-7985, 2005.
- McEarchern JA, Oflazoglu E, Francisco L, McDonagh CE, Gordon KA, Stone I, Klussman K, Turcott E, van Rooijen N, Carter P, Grewal IS, Wahl AF, Lav CE: Engineered anti-CD70 antibody with multiple effector functions exhibits in vitro and in vivo antitumor activities. *Blood*, 109: 1185-1192, 2007.
- Dutton AH, Tokuyasu KT, Singer SJ: Iron-dextran antibody conjugates: general method for simultaneous staining of two components in high-resolution immunoelectron microscopy. *Proc Natl Acad Sci USA*, 76: 3392-3396, 1979.
- Sanderson CJ, Wilson DV: A simple method for coupling proteins to insoluble polysaccharides. *Immunology*, 20: 1061-1065, 1971.
- Weissleder R, Lee AS, Fischman AJ, Reimer P, Shen T, Wilkinson R, Callahan RJ, Brady TJ: Polyclonal human immunoglobulin G labeled with polymeric iron oxide: antibody MR imaging. *Radiology*, 181: 245-249, 1991.
- Weissleder R, Lee AS, Khaw BA, Shen T, Brady TJ: Antimyosin-labeled monocrySTALLINE iron oxide allows detection of myocardial infarct: MR antibody imaging. *Radiology*, 182: 381-385, 1992.
- Remsen LG, McCormick CI, Roman-Goldstein S, Nilaver G, Weissleder R, Bogdanov A, Hellstrom I, Kroll RA, Neuwelt EA: MR of carcinoma-specific monoclonal antibody conjugated to monocrySTALLINE iron oxide nanoparticles: the potential for noninvasive diagnosis. *Am J Neuroradiol*, 17: 411-418, 1996.
- Bulte JWM, Verkuyl JM, Herynek V, Katsanis E, Brocke S, Holla M, Frank JA: Magnetoimmunodetection of (transfected) ICAM-1 gene expression. *Proc Int Soc Magn Reson Med*, 6: 307, 1998.
- Bulte JWM, Zhang S, van Gelderen P, Herynek V, Jordan EK, Duncan ID, Frank JA: Neurotransplantation of magnetically labeled oligodendrocyte progenitors: magnetic resonance tracking of cell migration and myelination. *Proc Natl Acad Sci USA*, 96: 15256-15261, 1999.
- Zhao M, Beauregard DA, Loizou L, Davletov B, Brindle KM: Non-invasive detection of apoptosis using magnetic resonance imaging and a targeted contrast agent. *Nat Med*, 7: 1241-1244, 2001.
- Renshaw PF, Owen CS, Evans AE, Leigh JS Jr: Immunospecific NMR contrast agents. *Magn Reson Imag*, 4: 351-357, 1986.
- Cerdan S, Lotscher HR, Kunnecke B, Seelig J: Monoclonal antibody-coated magnetite particles as contrast agents in magnetic resonance imaging of tumours. *Magn Reson Med*, 12: 151-163, 1989.
- Suwa T, Ozawa S, Ueda M, Ando N, Kitajima M: Magnetic resonance imaging of esophageal squamous cell carcinoma using magnetite particles coated with anti-epidermal growth factor receptor antibody. *Int J Cancer*, 75: 626-634, 1998.
- Artemov D, Mori N, Ravi R, Bhujwala ZM: Magnetic resonance molecular imaging of the HER-2/neu receptor. *Cancer Res*, 63: 2723-2727, 2003.
- Bulte JW, Hoekstra Y, Kamman RL, Magin RL, de Leij L, Webb AG, Briggs RW, Go KG, Hulstaert CE, Miltenyi S, The TH: Specific MR imaging of human lymphocytes by monoclonal antibody-guided dextran-magnetite particles. *Magn Reson Med*, 25: 148-157, 1992.
- Tiefenauer LX, Kuhne G, Andres RY: Antibody-magnetite nanoparticles: in vitro characterization of a potential tumour-specific contrast agent for magnetic resonance imaging. *Bioconj Chem*, 4: 347-352, 1993.
- Tiefenauer LX, Tschirky A, Kuhne G, Andres RY: In vivo evaluation of magnetite nanoparticles for use as a tumour contrast agent in MRI. *Magn Reson Imaging*, 14: 391-402, 1996.
- Modo, M, Hoehn, M, Bulte, JW: Cellular MR imaging. *Mol Imaging*, 4: 143-164, 2005.
- Weissleder R, Elizondo G, Wittenberg J, Rabito CA, Bengel HH, Josephson L: Ultrasmall superparamagnetic iron oxide: characterization of a new class of contrast agents for MR imaging. *Radiology*, 175: 489-493, 1990.
- Runge VM, Kirsch JE, Wells JW, Awh MH, Bittner DF, Woolfolk CE: Enhanced liver MR: Contrast agents and imaging strategy. *Crit Rev Diagn Imaging*, 34: 1-3, 1993.
- Corot C, Robert P, Idee JM, Port M: Recent advances in iron oxide nanocrystal technology for medical imaging. *Adv Drug Deliv Rev*, 58: 1471-1504, 2006.
- Bulte JW, Kraitchman DL: Iron oxide MR contrast agents for molecular and cellular imaging *NMR Biomed*, 17: 484-499, 2004.
- Thorek DL, Chen AK, Czupryna J, Tsourkas A: Superparamagnetic iron oxide nanoparticle probes for molecular imaging. *Ann Biomed Eng*, 34: 23-38, 2006.
- Wang YX, Hussain SM, Krestin GP: Superparamagnetic iron oxide contrast agents: physicochemical characteristics and applications in MR imaging. *Eur Radiol*, 11: 2319-2331, 2001.
- Fleige G, Seeberger F, Laux D, Kresse M, Taupitz M, Pilgrimm H, Zimmer C: In vitro characterization of two different ultrasmall iron oxide particles for magnetic resonance cell tracking. *Invest Radiol*, 37: 482-488, 2002.
- Sun R, Dittrich J, Le-Huu M, Mueller MM, Bedke J, Kartenbeck J, Lehmann WD, Krueger R, Bock M, Huss R, Seliger C, Gröne HJ, Misselwitz B, Semmler W, Kiessling F: Physical and biological characterization of superparamagnetic iron oxide- and ultrasmall superparamagnetic iron oxide-labeled cells: a comparison. *Invest Radiol*, 40: 504-513, 2005.
- Baio G, Fabbi M, de Toterò D, Ferrini S, Cilli M, Derchi LE, Neumaier CE: Magnetic resonance imaging at 1.5 T with immunospecific contrast agent in vitro and in vivo in a xenotransplant model. *Magma*, 19: 313-320, 2006.
- Hainsworth JD: Monoclonal antibody therapy in lymphoid malignancies. *Oncologist*, 5: 376-384, 2000.
- Tobinai K: Rituximab and other emerging antibodies as molecular target-based therapy of lymphoma. *Int J Clin Oncol*, 8: 212-223, 2003.

37. Tazzari PL, de Toterò D, Bolognesi A, Testoni N, Pileri S, Roncella S, Reato G, Stein H, Gobbi M, Stirpe F: An Epstein-Barr virus-infected lymphoblastoid cell line (D430B) that grows in SCID-mice with the morphologic features of a CD30+ anaplastic large cell lymphoma, and is sensitive to anti-CD30 immunotoxins. *Haematologica*, 84: 988-995, 1999.
38. Ferrini S, Cantoni C, Ciccone E, Biassoni R, Prigione I, Bottino C, Venzano P, Moretta L: A novel surface molecule expressed by long-term cultured T and natural killer cells is involved in cell activation. *Eur J Immunol*, 21: 1981-1987, 1991.
39. Orengo AM, Cantoni C, Neglia F, Biassoni R, Ferrini S: Reciprocal expression of CD70 and of its receptor, CD27, in human long term-activated T and natural killer (NK) cells: inverse regulation by cytokines and role in induction of cytotoxicity. *Clin Exp Immunol*, 107: 608-613, 1999.
40. Ito A, Shinkai M, Honda H, Takeshi K: Medical application of functionalized magnetic nanoparticles. *J Biosci Bioeng*, 100: 1-11, 2005.
41. Pirko I, Johnson A, Ciric B, Gamez J, Macura SI, Pease LR, Rodriguez M: In vivo magnetic resonance imaging of immune cells in the central nervous system with superparamagnetic antibodies. *FASEB J*, 18: 179-182, 2004.

2.2. Investigation of tumour imaging by using MEMRI

2.2.1. Title of paper

- **Baio G**, Fabbi M, Emionite L, Cilli M, Salvi S, Ghedin P, Prato S, Carbotti G, Tagliafico A, Truini M, Neumaier CE. In vivo imaging of human breast cancer mouse model with high level expression of calcium sensing receptor at 3T. *Eur Radiol.* 2012 Mar; 22(3):551-8.

2.2.2. Objective of the study

To demonstrate that MEMRI can be applied to visualise human breast CaSR-expressing cancer cells using a prototype birdcage with a clinical 3T human scanner.

2.2.3. What this study added to the literature

Most of the studies published during this period applied MEMRI to investigate overexpressed manganese-superoxide dismutase tumours. Our aim was to target tumours with high CaSR expression levels and to find the best MR contrast agents to target this type of tumour. This was a novel application certainly of value for the scientific literature. The application of a clinical human scanner with a prototype birdcage coil was something novel too, since all previous studies used ultra-high field MR preclinical scanners.

2.2.4. What changed as a result of the paper?

Manganese is not commercially available as an MR contrast agent, thus clinical applications cannot be explored. However, several preclinical imaging studies extensively demonstrated the interesting role of this ion combined with MR imaging, which could find a new interesting application and potentially come back into the clinical market soon.

2.2.5. In retrospect, what should have been done differently in this study?

Looking back to this work, silencing CaSR expression in the breast cancer cell lines would have strengthened the link between CaSR expression levels and manganese uptake at MRI. The application of Verapamil as Calcium antagonist is not specific for CaSR and any calcium receptors/channels could participate to the manganese uptake that we observe at MRI.

2.2.6. Future work as a result of this publication

Following this paper, we further explored the role of manganese as a contrast agent to investigate tumour calcium metabolism. We investigated if the manganese uptake we had observed on MRI was due to extracellular or intracellular internalisation of manganese. The results of this experiment are discussed in the following section. However, we also performed further research exploring different calcium receptors (CaSR and TRPV6) in different types of cancer animal models (breast and prostate), which is not included in this thesis because it has recently been submitted to a journal for review, and is not published as yet.

2.2.7. Confirmation of authorship

This is shown at the end of Chapter 2.

2.2.8. External link to the paper on the journal website

<https://www.ncbi.nlm.nih.gov/pubmed/21947485>

In vivo imaging of human breast cancer mouse model with high level expression of calcium sensing receptor at 3T

Gabriella Baio · Marina Fabbi · Laura Emionite · Michele Cilli · Sandra Salvi · Piero Ghedin · Sabina Prato · Grazia Carbotti · Alberto Tagliafico · Mauro Truini · Carlo Emanuele Neumaier

Received: 24 May 2011 / Revised: 22 August 2011 / Accepted: 9 September 2011 / Published online: 24 September 2011
© European Society of Radiology 2011

Abstract

Objectives To demonstrate that manganese can visualise calcium sensing receptor (CaSR)-expressing cells in a human breast cancer murine model, as assessed by clinical 3T magnetic resonance (MR).

Methods Human MDA-MB-231-Luc or MCF7-Luc breast cancer cells were orthotopically grown in NOD/SCID mice to a minimum mass of 5 mm. Mice were evaluated on T1-weighted sequences before and after intravenous injection of $MnCl_2$. To block the CaSR-activated Ca^{2+} channels, verapamil was injected at the tumour site 5 min before Mn^{2+} administration. CaSR expression in vivo was studied by immunohistochemistry.

Results Contrast enhancement was observed at the tumour periphery 10 min after Mn^{2+} administration, and further increased up to 40 min. In verapamil-treated mice, no contrast enhancement was observed. CaSR was strongly expressed at the tumour periphery.

Conclusion Manganese enhanced magnetic resonance imaging can visualise CaSR-expressing breast cancer cells in vivo, opening up possibilities for a new MR contrast agent.

Key Points

- Manganese contrast agents helped demonstrate breast cancer cells in an animal model.
- Enhancement was most marked in cells with high calcium sensing receptor expression.
- Manganese uptake was related to the distribution of CaSR within the tumour.
- Manganese MRI may become useful to investigate human breast cancer.

G. Baio (✉) · A. Tagliafico · C. E. Neumaier
Department of Diagnostic Imaging, IST, National Cancer Institute,
Largo Rosanna Benzi 10,
16132 Genoa, Italy
e-mail: gabriella.baio@istge.it

M. Fabbi · G. Carbotti
Unit of Immunological Therapy, IST, National Cancer Institute,
Largo Rosanna Benzi 10,
16132 Genoa, Italy

L. Emionite · M. Cilli
Animal Facility, IST, National Cancer Institute,
Largo Rosanna Benzi 10,
16132 Genoa, Italy

S. Salvi · M. Truini
Department of Pathology, IST, National Cancer Institute,
Largo Rosanna Benzi 10,
16132 Genoa, Italy

P. Ghedin · S. Prato
General Electric, GE,
Milano, Italy

Keywords Magnetic Resonance Imaging · Manganese chloride · Breast cancer · Calcium receptor · In vivo small animal MRI

Introduction

Calcium (Ca^{2+}) ion is required to maintain normal structure and function in all living cells [1, 2] and occupies a prominent position in the signal transduction system of the cell, participating in a variety of physiological and biological events such as proliferation, apoptosis [3, 4] and differentiation [5]. The role of Ca^{2+} as a second messenger has received great attention, as a multitude of growth factors and cytokines signal through this ubiquitous molecule [6]. Moreover, in the past decade the role of Ca^{2+} as extracellular first messenger in causing or preventing

cancer has been under active investigation [7] since the cloning of plasma membrane calcium-sensing receptor (CaSR) from the parathyroid gland [8]. CaSR is a seven-transmembrane G-protein-coupled receptor [7], capable of sensing changes in extracellular calcium concentration, which inhibits secretion of parathyroid hormone (PTH) following binding with its physiological ligand Ca^{2+} [9]. The CaSR is expressed at different levels in normal human breast duct cells, in the duct cells of fibrocystic breast tissue, and also in ductal carcinomas of the breast [10]. In addition, calcium ions play key roles not only in normal breast physiology but also in various pathological conditions. For instance, Ca^{2+} is an important constituent of milk, which has a Ca^{2+} content of 200 mg/litre [11]. Furthermore, a diagnostically important characteristic of breast cancers, that can be very useful during mammographic screening, is their tendency to form microcalcification within ducts [12]. In vitro studies have shown that increased Ca^{2+} levels induce terminal differentiation of normal human breast epithelial cells in culture [13].

Breast cancer has a marked tendency to spread to bone [14]. The observation that numerous cells within the bone marrow express the CaSR under normal circumstance [15], leads to hypothesise that the presence of CaSRs on metastatic cells may contribute to their propensity to reside in bones, where locally high levels of Ca^{2+} are present during resorption processes. The local Ca^{2+} level at resorption sites has been reported to rise as high as 40 mM [16].

Indeed, high Ca^{2+} levels (5, 7.5 and 10 mM) stimulate the secretion of parathyroid hormone related protein (PTHrP) in some breast cancer cell lines in vitro, presumably via a CaSR-mediated mechanism [17]. Excess PTHrP could contribute to the massive osteolysis caused by breast cancers' bone metastases by promoting a feed-forward mechanism in which release of Ca^{2+} from the bone, stimulates further PTHrP production and more bone resorption [18–20]. Interruption of this cycle by blockade of CaSR activity [21] could potentially offer substantial therapeutic benefit in this situation. Therefore, given the importance of Ca^{2+} in both the physiology and pathophysiology of the breast and bone, the CaSR could play different roles in these processes.

Moreover, the interest in CaSR has been refreshed by the finding that in a selected group of patients with advanced breast cancer, CaSR expression assessed by immunohistochemistry is high, predominantly in tissue specimen from patients who developed bone metastases [22].

Clinically useful MR contrast agents are generally gadolinium based, however, there has been a renewed interest in combining the strong magnetic resonance (MR) relaxation effects of manganese ions (Mn^{2+}), to develop imaging techniques sensitive to specific molecular processes,

such as Ca^{2+} mobilisation. Indeed, Mn^{2+} can enter cells via the same transport systems in the same way as Ca^{2+} and can bind to a number of intracellular structures because of its high affinity for Ca^{2+} and Mg^{2+} binding sites on proteins and nucleic acids [23, 24]. Mn^{2+} ion is increasingly used for MRI in animals and it has been found to be a good contrast medium for MRI of the brain [25, 26] and the heart [27, 28]. Finally, the olfactory [29], visual [30, 31], and somatosensory pathways of rat and mouse brain have been visualised in detail after direct injection of MnCl_2 into a specific brain region [32–34].

Manganese-enhanced (ME)-MRI is developed with the aim to achieve unique tissue contrast, assess tissue viability, find a surrogate marker of Ca^{2+} influx into cells and trace neuronal connections [35]. Previous reports explored the use of a paramagnetic metalloporphyrin that chelates Mn^{2+} as MR contrast agent in murine models of breast cancer [36, 37].

Here, we address the possibility of using free MnCl_2 as a contrast agent in MRI of in vivo human breast cancer. This hypothesis is supported by previous observations showing that activation of CaSR by divalent cations such as Ca^{2+} and Mn^{2+} [38, 39] triggers ion influx through non-selective cation channels [4, 40, 41]. Therefore, we speculated that Mn^{2+} may accumulate in CaSR-positive breast cancer cells and allow their imaging.

In addition, human breast cancer cell lines MDA-MB-231 and MCF-7, which give rise to tumours if transplanted in immunocompromised mice, express CaSR at different levels and secrete PTHrP upon stimulation [10, 42, 43].

Here we show that tumours formed by human breast cancer cells orthotopically implanted in the mammary fat pad of NOD/SCID mice maintain high CaSR expression and that intravenous injection of MnCl_2 allows tumour imaging by a 3T MR scanner. The involvement of CaSR in MnCl_2 contrast enhancement was suggested by the study of its distribution in the tumour tissue and by blockade of ME-MRI through the Ca^{2+} -antagonist drug verapamil.

Materials and methods

Animal models and contrast agents

In vivo experiments were approved by the Institutional Review Committee of the National Cancer Institute (IST), and were performed in accordance to the National Regulation on Animal Research Resources (D.L. 116/92).

Six-week old female NOD/SCID mice ($n=6$) were obtained from a colony bred in house under sterile conditions in the animal facility. Mice were injected in the lower left mammary fat pad with 2×10^6 luciferase-transduced human breast cancer MDA-MB-231-luc-D3H1

or MCF-7-luc-F5 cells (Xenogen Corporation). When the tumour mass diameter was approximately 5 mm, as assessed by palpation and measurement with a caliper, mice were subjected to MR examination. The pre-clinical MR imaging protocol was developed for an experimental mouse-dedicated volume coil with a diameter of 55 mm applied within a commercially available 3T clinical system (Signa EXCITE®HDxT, GE, Milwaukee, USA). A solution of 5 mM MnCl₂·4H₂O (Sigma Chemical Co., St. Louis, MO, USA) in 0.9% NaCl, was prepared and 180 µL were injected intravenously per mouse (i.e. a dose range between 7.4 mg/kg in a 24 g mouse and 8.5 mg/kg in a 21 g mouse).

In a control group ($n=2$), in order to block the CaSR-activated Ca²⁺ channels, 0.3 mg/kg of verapamil solution (Isoptin, Abbott, Italy) was injected subcutaneously at the tumour side, 5 min before MnCl₂ administration, and MRI carried out as described above.

Magnetic resonance imaging and mouse dedicated coil

Magnetic resonance imaging was performed with a clinical 3T MR system (Signa EXCITE®HDxT, GE, Milwaukee, USA). Mice were anaesthetised by intraperitoneal injection of xylazine (30 mg/kg) and ketamine (100 mg/kg) and were positioned in a prototype coil (birdcage linear coil, transmit/receive coil, 100 mm long, 55 mm diameter, tuned at 127.6 MHz, GE, Milwaukee, USA) placed on a support filled with warm water to preserve mice from hypothermia. The room temperature during experiments was 23°C, and the mean acquisition time was limited to 50 min, by the spontaneous awakening of mice. The imaging parameters are listed in Table 1.

Both qualitative and quantitative analyses were performed on T1-gradient-echo weighted images. Qualitative visual analyses were performed by two radiologists (A.T. and G.B.) on a commercially available workstation (AW Volume Share 2, ADW 4.4, GE, Milan, Italy). Both observers were blinded. They selected the imaging sequences and parameters, which provided optimal signal intensity (SI) and contrast relative to the manganese properties.

Quantitative analyses were expressed as SI±standard deviation of each mouse, with SI being measured in tumour and muscle of contralateral leg by one investigator using a defined region of interest (ROI). The size of the region of

interest depended on the diameter of the tumour (8 mm). The same analysis was performed in the control group. We also performed a ROI only on the ring of contrast enhancement at the tumour periphery at 10 and 40 min of manganese administration.

The SI values were divided by the background noise to yield the signal-to-noise ratio (SNR) according to the formula [44]:

$$\text{SNR} = \text{SI}/\text{noise}$$

The difference in SI (ΔSI) before and 40 min after MnCl₂ administration, was calculated as follows:

$$\Delta\text{SI}_{\text{tumour}} = \text{SI}_{\text{tumour after Mn}^{2+}} - \text{SI}_{\text{tumour before Mn}^{2+}}/\text{noise}$$

$$\Delta\text{SI}_{\text{muscle}} = \text{SI}_{\text{muscle after Mn}^{2+}} - \text{SI}_{\text{muscle before Mn}^{2+}}/\text{noise}$$

Histopathological analysis

Mice were euthanised using the carbon dioxide method shortly after the MRI session, always before the onset of signs of distress and when the tumour reached the maximum diameter of 1 cm. Breast tumours were excised and fixed in 10% buffered formalin. Specimens were then paraffin-embedded and processed for histological analysis according to standard techniques. The specimen sections, which were best representative of tumour areas, were identified through Hematoxylin-Eosin staining. The sections (3 µm) were immunostained using a BenchMark XT automated immunostainer (Ventana Medical Systems, Strasbourg, France). Briefly, the sections were deparaffined, antigen-retrieval was performed with high pH citrate buffer for 30 min and samples were challenged with a 1:200 dilution of the anti-calcium sensing receptor polyclonal rabbit antibody (code PA1-934A, AffinityBioReagents, Golden, CO, USA) or with buffer only, as negative control, for 30 min at 37°C. Parathyroid cancer specimens were used as positive staining control. The antibody complex was revealed with the Polymeric System UltraView DAB Detection kit (Ventana Medical Systems). The sections were then counterstained with modified Gill's hematoxylin, mounted in Eukitt (Bio-Optica, Milano, Italy) and observed with a light microscope (Olympus, Tokyo, Japan) using 10X, 20X, 40X and 63X objectives.

Table 1 Parameters utilised for MRI at 3T with a 55 mm birdcage linear coil

	Plane	TR (ms)	TE (ms)	FA	Bandwidth	FoV (mm)	Frequency	Phase	Thickness (mm)
T1-GRE	Coronal	13.4	3.6	15°	19.23	60	288	288	1.20
T1-3D-GRE	Coronal	7.3	2.5	20°	50	100	320	320	1.00
T2-TSE	Coronal	4000	85	90°	31.25	100	320	320	1.00

T1-GRE T1-weighted gradient-echo sequences; *T1-3D-GRE* T1-weighted three dimensional gradient-echo sequences; *T2-TSE*, T2-weighted turbo-spin-echo sequences; *TR (ms)* repetition time in milliseconds; *TE (ms)* echo time in milliseconds; *FA* flip angle; *FoV* field of view

The immunohistochemical results were qualitatively classified according to intensity and pattern of the staining by two experienced pathologists (S.S. and M.T.), blind to the *in vivo* imaging results. A 6-point scale was used to score the intensity of the CaSR staining, going from score 0 (absent expression) to score 5 (intense, widespread expression), as described in the literature [22].

Results

Manganese-enhanced MRI at 3T of breast cancer *in vivo*

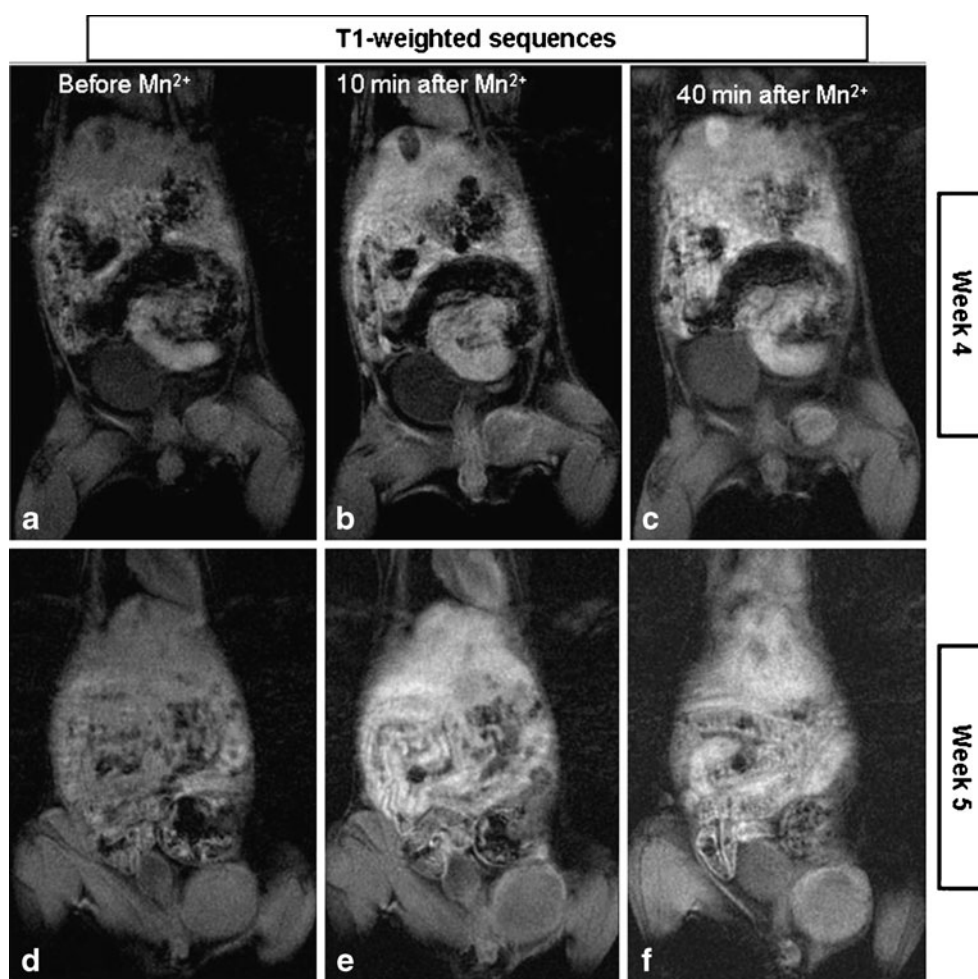
When tumour xenotransplants reached a diameter of approximately 5 mm, mice ($n=6$) were examined by MRI following injection *i.v.* with $MnCl_2$ as contrast agent. Ten minutes after $MnCl_2$ administration, a ring of contrast enhancement on T1-weighted images, was observed at the tumour periphery (Fig. 1b–e). Full contrast enhancement at the tumour site was reached around 40 min after $MnCl_2$ injection, with persistence of a brighter peripheral area (Fig. 1c–f). Similar results were

obtained in all mice, independently of the xenografted breast cancer cell line.

To evaluate the relationship between manganese-driven SI increase and divalent cations channels' activity, two mice, which had shown good manganese-enhanced imaging of their tumours few days before, were inoculated with the calcium-antagonist drug verapamil at the tumour site 10 min before the *i.v.* administration of $MnCl_2$. As shown in Fig. 2, blockade of divalent cations dynamics prevented manganese-enhanced imaging of tumours, supporting a key role for CaSR and the functionally related non-selective cation channels in $MnCl_2$ -mediated tumour imaging.

Quantitative analysis was then performed by setting ROIs on T1-gradient-echo-weighted images of each mouse and measuring SI on the tumour before and 40 min after manganese administration. The same sampling was performed on the muscle of the contralateral leg before and 40 min after manganese administration. Data, expressed as SNR and ΔSI , are listed in Table 2. Paired student's *t*-test analysis of SNR values before and 40 min after Mn^{2+} administration yielded a significant P value for tumour ($P <$

Fig. 1 Manganese enhanced MR imaging (MEMRI) of the orthotopic human breast cancer xenografts. **a–f** MRI of the same mouse at two different time points. The tumour dimension was 5 mm at the first determination and 10 mm the week after. On T1-weighted gradient echo images recorded before and after Mn^{2+} administration, tumours showed a hyperintense area at their periphery (ring of manganese enhancement) 10 min after Mn^{2+} administration (**b–e**) and full contrast enhancement 40 min, with persistence of a brighter peripheral area (**c–f**)



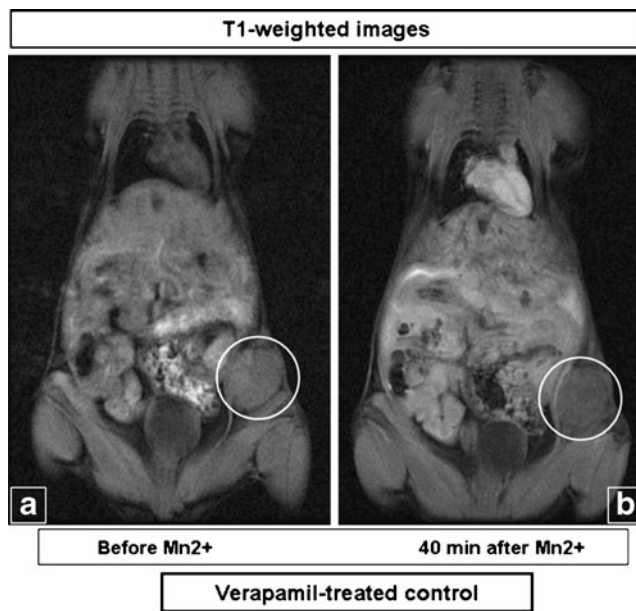


Fig. 2 **a, b** Coronal MR images of the orthotopic human breast cancer xenograft in a verapamil-treated control. MR images show no signal intensity increase after Mn^{2+} administration in the mouse treated with verapamil

0.05) but not for muscle ($P=0.2$). Analysis of images confirmed an increase of 23% of ΔSI in the tumour after manganese administration, whereas the muscle showed only a 4% increase. In control groups treated with verapamil, no appreciable differences in ΔSI of the tumour were observed.

When quantitative analysis was performed by setting ROIs only on the ring of contrast enhancement, visible at the tumour periphery both 10 and 40 min after injection of manganese on T1-GRE-weighted images, the ΔSI showed an average increase of 50% (mean of six independent experiments).

Table 2 Quantitative analysis of each tumour before and 40 min after $MnCl_2$ i.v. injection correlated with the signal intensity of muscle of the contralateral leg at the same time points. Signal intensity values are calculated on T1-gradient echo weighted images

Mouse	Tumour before ^a SNR ^c	Tumour after ^b SNR	ΔSI^d	Muscle before SNR	Muscle after SNR	ΔSI
1	7.2	10.4	3.2	7.2	8.4	1.2
2	6.9	8.8	1.9	7.1	7.2	0.1
3	7.8	8.8	1.0	6.1	6.7	0.6
4	7.4	8.9	1.5	8.1	8.9	0.8
5	6.4	7.1	0.7	6.8	6.1	-0.7
6	6.9	8.6	1.7	7.5	7.6	0.1

^a Before $MnCl_2$ administration

^b 40 min after $MnCl_2$ administration

^c SNR SI/noise; SI signal intensity

^d $\Delta SI_{tumour} = SI_{tumour\ 40\ min\ after\ Mn^{2+}} - SI_{tumour\ before\ Mn^{2+}/noise}$, $\Delta SI_{muscle} = SI_{muscle\ 40\ min\ after\ Mn^{2+}} - SI_{muscle\ before\ Mn^{2+}/noise}$

Immunohistochemical analysis of CaSR

To correlate manganese-enhanced MR images with CaSR expression by tumour cells in vivo, mice were euthanised after the MRI session, and tumours were excised, fixed and paraffin embedded for subsequent immunohistochemical analysis. CaSR was expressed at very high levels (staining score 4–5) in all tumour xenografts grown from both MDA-MB-231-luc (Fig. 3) and MCF-7-luc (not shown). The highest expression of CaSR molecules was found at the periphery of the tumour mass (Fig. 3a, b), consistently with the ring of contrast enhancement observed in MRI short time after $MnCl_2$ administration. These data suggest that manganese as contrast agent could be useful in detecting tumours with high expression of CaSR, which seems an indicator of bone metastasis potential [22].

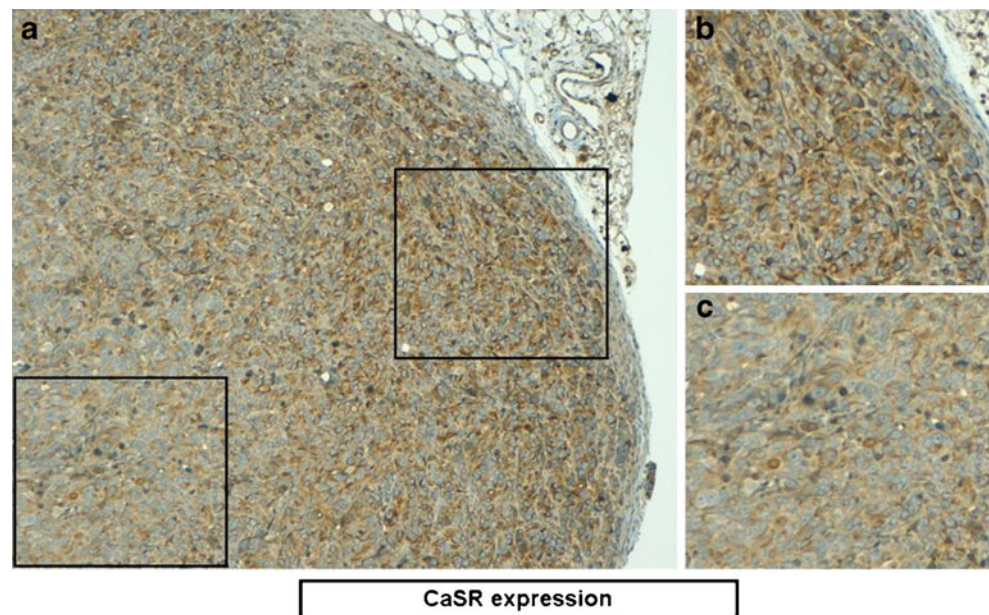
Discussion

The biology of Mn^{2+} ion combined with its ability to act as an MR contrast agent opens the possibility of using manganese-enhanced MR imaging (MEMRI) to visualise tissue function. Manganese can enter cells via a number of transport systems, which can be regulated by the plasma membrane calcium sensing receptor (CaSR).

We therefore set up an animal model to assess whether it is possible to visualise human breast cancer cells with high expression levels of CaSR in vivo, using Mn^{2+} as a contrast agent and a 3T clinical MR scanner equipped with an experimental birdcage linear coil with a diameter of 55 mm. In vivo MRI was performed on mice carrying a few mm tumour masses.

In all mice tested, T1-weighted MR images showed a characteristic ring of manganese enhancement in the tumour 10 min after the injection of $MnCl_2$. The full

Fig. 3 Immunohistochemical analysis of CaSR in human breast cancer MDA-MB-231 cells xenograft (a–c). A CaSR is detected in tumour cells (score 4–5) and displays more intense staining at the tumour periphery, as detailed in b and c. Original magnification 200×



manganese contrast enhancement was observed approximately 40 min after $MnCl_2$ injection with persistence of a brighter peripheral area. We considered the possibility that the early appearance of a ring of contrast enhancement could relate to the presence of a neoangiogenic rim at the tumour periphery. However, this hypothesis seems unlikely, because we did not observe a ring of contrast enhancement during the vascular phase occurring within the first min from injection. In addition, the observation that verapamil pre-treatment abolished the formation of the ring, rather supports a role for CaSR-mediated activation of cation channels leading to Mn^{2+} intracellular influx.

Moreover, the possibility that the body temperature could alter the pharmacokinetics of the contrast agent has to be taken into account. However, a slight hypothermia was reached only toward the end of the MRI session.

When tumour sampling was performed by setting a ROI only on the ring of contrast enhancement at the tumour periphery, a 50% increase in ΔSI , both 10 and 40 min after manganese administration, was reached. Immunohistochemistry showed a higher CaSR molecule expression at the periphery of the tumour than in its centre. The lower CaSR density at the tumour centre may therefore be responsible for the lower increase of ΔSI (average 23%), when the whole tumour was analysed 40 min after manganese administration on T1-gradient-echo-weighted images. We do not know whether the particular distribution of CaSR within the tumour is related to the tumour invasive front or it is specifically related to the human-murine front line in xenotransplants, and whether it is peculiar to this cancer model or shared by others.

We chose to correlate the MRI results with the signal intensity obtained in the muscle because of the presence of the calcium channels that allow the manganese uptake in such

tissue. Nonetheless, we did not observe an important change in signal intensity in the muscle after manganese administration.

These differences may be due to the previously reported interaction of CaSRs with the transient cation channels (TRPC) in breast cancer cell lines, where the high expression levels of CaSRs determine a higher calcium influx by such cation channels [45, 46].

To further correlate manganese contrast enhancement of the tumour mass with divalent cations receptor and channel activity, the calcium antagonist drug verapamil was injected next to the tumour site 5 min before $MnCl_2$ administration. As no contrast enhancement (see Fig. 2), and no quantitative changes in SI, were observed in the tumours of verapamil pre-treated mice, it is likely that the manganese enhancement of the tumour was due to activation of divalent cations' dynamics triggered by Mn^{2+} interaction with CaSR. Verapamil was injected at the tumour side to achieve high local concentration without systemic toxic effects.

A potential drawback to the use of Mn^{2+} as a contrast agent is its cellular toxicity, which limits the dose administered. Recently it was described that a dose of 30 mg/kg $MnCl_2 \cdot 4H_2O$ did not interfere with the animals' well-being [47]. Nevertheless, MR relaxation rates are proportional to the effective concentration of Mn^{2+} in tissue, thus significant amounts of Mn^{2+} are required to produce robust and detectable contrast.

In our study, a single maximum dose of 8.5 mg/kg $MnCl_2$ was administered per mouse, well below the toxicity threshold described, and still allowed to achieve good signal intensity in the MR images.

The goal of this study was to give a proof of principle that Mn^{2+} could accumulate in breast cancer, possibly as result of CaSR expression in vivo. Of course, CaSR is

expressed in many different tissues, as described by the literature and a subcutaneous murine model represented an ideal situation, with little interference from normal tissue. However, a recent study reports that CaSR expression levels, are higher in human breast cancer cell lines than in normal breast cells, and that such higher levels are associated to an higher concentration of Ca^{2+} in the extracellular space [48]. On these bases, we hypothesised that breast cancer cells could accumulate Mn^{2+} more efficiently than normal breast cells. Moreover, we could expect that human breast cancers expressing high levels of CaSR (score 5) take up manganese more efficiently than the ones expressing low CaSRs levels (score 0–1). Further studies with CaSR-specific inhibitors in animal models where larger amounts of normal tissue surround tumour cells, will be required to fully address this point.

We also considered that the expression of CaSR in other tissues could determine a high background and a decrease in contrast noise ratio (CNR), and thus represent a potential limit for a possible future application of Mn^{2+} to MR imaging. However, several studies indicate that Mn^{2+} uptake is related to the specific function of CaSR in a given tissue [25–34]. This implies that manganese-enhanced magnetic resonance imaging (MEMRI) of human breast cancer, could take advantage from a careful, tissue-specific timing of MRI acquisition and from improved post-processing of images.

In summary, this preliminary investigation reports that MEMRI at 3T can visualise CaSR-expressing human breast cancer xenotransplants in vivo, opening the exploration of a potential MR contrast agent to study human breast cancer into clinic.

Acknowledgments The authors thank Dr. Silvano Ferrini for his helpful discussions and revision of the manuscript.

This study was supported by the Italian Ministry of Health ‘Progetto oncologico di Medicina Molecolare: i tumori femminili’.

References

- Barrett PQ, Kojima I, Kojima K et al (1986) Short term memory in the calcium messenger system. Evidence for a sustained activation of protein kinase C in adrenal glomerulosa cells. *Biochem J* 238:905–912
- Rasmussen H (1986) The calcium messenger system (1). *N Engl J Med* 314:1094–1101
- Capiod T, Shuba Y, Skryma R et al (2007) Calcium signalling and cancer cell growth. *Subcell Biochem* 45:405–427
- Brown EM, MacLeod RJ (2001) Extracellular calcium sensing and extracellular calcium signaling. *Physiol Rev* 81:239–297
- Bikle DD, Oda Y, Xie Z (2004) Calcium and 1,25(OH)₂D: interacting drivers of epidermal differentiation. *J Steroid Biochem Mol Biol* 89–90:355–360
- Heaney RP (2006) Calcium intake and disease prevention. *Arq Bras Endocrinol Metabol* 50:685–693
- Brown EM (2000) G protein-coupled, extracellular Ca^{2+} (Ca^{2+} -(o))-sensing receptor enables Ca^{2+} -(o) to function as a versatile extracellular first messenger. *Cell Biochem Biophys* 33:63–95
- Garrett JE, Capuano IV, Hammerland LG et al (1995) Molecular cloning and functional expression of human parathyroid calcium receptor cDNAs. *J Biol Chem* 270:12919–12925
- Fukumoto S (2008) Basic and clinical aspects of calcimimetics. Structure and function of calcium-sensing receptor. *Clin Calcium* 18:32–36
- Cheng I, Klingensmith ME, Chattopadhyay N et al (1998) Identification and localization of the extracellular calcium-sensing receptor in human breast. *J Clin Endocrinol Metab* 83:703–707
- Prentice A, Jarjou LMA, Cole TJ et al (1995) Calcium requirements of lactating Gambian mothers, effects of a calcium supplement on breast-milk calcium concentration, maternal bone mineral content and urinary calcium excretion. *Am J Clin Nutr* 62:58–67
- Galkin BM, Feig SA, Patchefsky AS et al (1977) Ultrastructure and microanalysis of “benign” and “malignant” breast calcifications. *Radiology* 124:245–249
- McGrath CM, Soule HD (1984) Calcium regulation of normal human mammary epithelial cell growth in culture. *In Vitro* 20:652–662
- Percival RC, Yates AJ, Gray RE et al (1985) Mechanism of malignant hypercalcemia in carcinoma of the breast. *Br Med J Clin Res* 291:776–779
- House MG, Kohlmeier L, Chattopadhyay N et al (1997) Expression of an extracellular calcium-sensing receptor in human and mouse bone marrow cells. *J Bone Miner Res* 12:1959–1970
- Silver IA, Murrills RJ, Etherington DJ (1988) Microelectrode studies on the acid microenvironment beneath adherent macrophages and osteoclasts. *Exp Cell Res* 175:266–276
- Sanders JL, Chattopadhyay N, Kifor O et al (2000) Extracellular calcium-sensing receptor expression and its potential role in regulating parathyroid hormone-related peptide secretion in human breast cancer cell lines. *Endocrinology* 141:4357–4364
- Coleman RE (1997) Skeletal complications of malignancy. *Cancer* 80:1588–1594
- Guisse TA, Mundy GR (1998) Cancer and bone. *Endocr Rev* 19:18–54
- Guisse TA, Yin JJ, Taylor SD et al (1996) Evidence for a causal role of parathyroid hormone-related protein in the pathogenesis of human breast cancer-mediated osteolysis. *J Clin Invest* 98:1544–1549
- Nemeth EF, Fox J, Delmar EG et al (1998) Stimulation of parathyroid hormone secretion by a small molecule antagonist of the calcium receptor (Abstract). *J Bone Miner Res* 23:S156
- Mihai R, Stevens J, McKinney C et al (2006) Expression of the calcium receptor in human breast cancer—a potential new marker predicting the risk of bone metastases. *Eur J Surg Oncol* 32:511–515
- Drapeau P, Nachsen DA (1984) Manganese fluxes and manganese-dependent neurotransmitter release in presynaptic nerve endings isolated from rat brain. *J Physiol* 348:493–510
- Narita K, Kawaski F, Kita H (1990) Mn and Mg influxes through Ca channels of motor nerve terminals are prevented by verapamil in frogs. *Brain Res* 510:289–295
- Lin YJ, Koretsky AP (1997) Manganese ion enhances T1-weighted MRI during brain activation: an approach to direct imaging of brain function. *Magn Reson Med* 38:378–388
- Duong TQ, Silva AC, Lee SP et al (2000) Functional MRI of calcium-dependent synaptic activity: cross correlation with CBF and BOLD measurements. *Magn Reson* 43:383–392
- Hu TC, Pautler RG, MacGowan GA et al (2001) Manganese enhanced MRI of mouse heart during changes in inotropy. *Magn Reson Med* 46:884–890

28. Krombach GA, Saeed M, Higgins CB et al (2004) Contrast-enhanced MR delineation of stunned myocardium with administration of MnCl₂ in rats. *Radiology* 230:183–190
29. Pautler RG, Silva AC, Koretsky AP (1998) In vivo neuronal tract tracing using manganese-enhanced magnetic resonance imaging. *Magn Reson Med* 40:740–748
30. Watanabe T, Michaelis T, Frahm J (2001) Mapping of retinal projections in the living rat using high-resolution 3D gradient-echo MRI with Mn²⁺-induced contrast. *Magn Reson Med* 46:424–429
31. Lin CP, Tseng WY, Cheng HC et al (2001) Validation of diffusion tensor magnetic resonance axonal fiber imaging with registered manganese-enhanced optic tracts. *NeuroImage* 14:1035–1047
32. Allegrini PR, Wiessner C (2003) Three-dimensional MRI of cerebral projections in rat brain in vivo after intracortical injection of MnCl₂. *NMR Biomed* 16:252–256
33. Lin Y (1997) MRI of the rat and mouse brain after systemic administration of MnCl₂. Thesis, Carnegie Mellon University, Pittsburgh, PA
34. Watanabe T, Natt O, Boretius S et al (2002) In vivo 3D MRI staining of mouse brain after subcutaneous application of MnCl₂. *Magn Reson Med* 48:852–859
35. Lee JH, Koretsky AP (2004) Manganese enhanced magnetic resonance imaging. *Curr Pharm Biotechnol* 5:529–537
36. Ogan MD, Revel D, Brasch RC (1987) Metalloporphyrin contrast enhancement of tumours in magnetic resonance imaging. A study of human carcinoma, lymphoma, and fibrosarcoma in mice. *Invest Radiol* 22:822–828
37. van Zijl PC, Place DA, Cohen JS et al (1990) Metalloporphyrin magnetic resonance contrast agents. Feasibility of tumour-specific magnetic resonance imaging. *Acta Radiol* 374:75–79
38. Remy C, Kirchhoff P, Hafner P et al (2007) Stimulatory pathways of the Calcium-sensing receptor on acid secretion in freshly isolated human gastric glands. *Cell Physiol Biochem* 19:33–42
39. Günzel D, Amasheh S, Pfaffenbach S et al (2009) Claudin-16 affects transcellular Cl⁻ secretion in MDCK cells. *J Physiol* 587:3777–3793
40. Ye C, Rogers K, Bai M et al (1996) Agonists of the Ca²⁺-sensing receptor (CaR) activate nonselective cation channels in HEK293 cells stably transfected with the human CaR. *Biochem Biophys Res Commun* 226:572–579
41. Tsien RW, Hess P, McCleskey EW et al (1987) Calcium channels: mechanisms of selectivity, permeation, and block. *Annu Rev Biophys Chem* 16:265–290
42. Sanders JL, Chattopadhyay N, Kifor O et al (2000) Extracellular calcium-sensing receptor expression and its potential role in regulating parathyroid hormone-related peptide secretion in human breast cancer cell lines. *Endocrinology* 141:4357–4363
43. VanHouten J, Dann P, McGeoch G et al (2004) The calcium-sensing receptor regulates mammary gland parathyroid hormone-related protein production and calcium transport. *J Clin Invest* 113:598–608
44. Wolff SD, Balaban RS (1997) Assessing contrast on MR images. *Radiology* 202:25–29
45. El Hiani Y, Ahidouch Lehen'kyi V, Hague F et al (2009) Extracellular signal-regulated kinases 1 and 2 and TRPC1 channels are required for calcium-sensing receptor-stimulated MCF-7 breast cancer cell proliferation. *Cell Physiol Biochem* 23:335–346
46. Aydar E, Yeo S, Djamgoz M, Palmer C (2009) Abnormal expression, localization and interaction of canonical transient receptor potential ion channels in human breast cancer cell lines and tissues: a potential target for breast cancer diagnosis and therapy. *Cancer Cell Int* 18:9–23
47. Grünecker B, Kaltwasser SF, Peterse Y, Sämann PG et al (2010) Fractionated manganese injections: effects on MRI contrast enhancement and physiological measures in C57BL/6 mice. *NMR Biomed* 23:913–921
48. Huang C, Hydo LM, Liu S, Miller RT (2009) Activation of choline kinase by extracellular Ca²⁺ is Ca²⁺-sensing receptor, Galphai2 and Rho-dependent in breast cancer cells. *Cell Signal* 21:1894–1900

2.2.1. Title of paper

- Gianolio E, Arena F, Di Gregorio E, Pagliarin R, Delbianco M, **Baio G**, Aime S. MEMRI and tumours: a method for the evaluation of the contribution of Mn(II) ions in the extracellular compartment. *NMR Biomed.* 2015 Sep; 28(9):1104-10.

2.2.2. Objective of the study

To set-up a simple method to evaluate the contribution of Mn²⁺ ions in the intra- and extracellular tumour compartments in a MEMRI experiment.

2.2.3. What this study added to the literature

This work provided interesting information regarding manganese ion distribution not only in tumours but also in healthy organs, such as liver, kidneys, and muscles, and how this can affect MR imaging analysis and interpretation, especially in experiments that aim to demonstrate calcium metabolism in tumours.

2.2.4. What changed as a result of the paper?

As stated above, manganese is not commercially available as MR contrast agent, thus clinical applications cannot be explored. However, the publications and preclinical experimental studies with manganese are overall increasing in the scientific community, exploring new interesting applications for this contrast agent which could come back into the clinical market soon.

2.2.5. In retrospect, what should have been done differently in this study?

Looking back to our experiments, we could have explored the calcium receptors expression level on a different type of cancer cell line (such as B16F10 murine melanoma cells) to strengthen our previous *in vivo* studies performed on breast cancer cell lines, and thus explore a further role of CaSR in a different type of tumour, such as melanoma by MEMRI.

2.2.6. Future work as a result of this publication

Following this work, we developed a new set of preclinical investigations on the application of MEMRI in cancer animal models and brown adipose tissue. The results of this work are discussed in the next chapter.

2.2.7. Confirmation of authorship

This is shown at the end of Chapter 2.

2.2.8. External link to the paper on the journal website

<https://www.ncbi.nlm.nih.gov/pubmed/26174622>

MEMRI and tumors: a method for the evaluation of the contribution of Mn(II) ions in the extracellular compartment

Eliana Gianolio^a, Francesca Arena^a, Enza Di Gregorio^a, Roberto Pagliarin^b, Martina Delbianco^b, Gabriella Baio^{c,d} and Silvio Aime^{a*}



The purpose of the work was to set-up a simple method to evaluate the contribution of Mn²⁺ ions in the intra- and extracellular tumor compartments in a MEMRI experiment. This task has been tackled by “silencing” the relaxation enhancement arising from Mn²⁺ ions in the extracellular space. *In vitro* relaxometric measurements allowed assessment of the sequestering activity of DO2A (1,4,7,10-tetraazacyclododecane-1,7-diacetic acid) towards Mn²⁺ ions, as the addition of Ca-DO2A to a solution of MnCl₂ causes a drop of relaxivity upon the formation of the highly stable and low-relaxivity Mn-DO2A. It has been proved that the sequestering ability of DO2A towards Mn²⁺ ions is also fully effective in the presence of serum albumin. Moreover, it has been shown that Mn-DO2A does not enter cell membranes, nor does the presence of Ca-DO2A in the extracellular space prompt migration of Mn ions from the intracellular compartment.

On this basis the *in vivo*, instantaneous, drop in SE% (percent signal enhancement) in T₁-weighted images is taken as evidence of the sequestration of extracellular Mn²⁺ ions upon addition of Ca-DO2A. By applying the method to B16F10 tumor bearing mice, T₁ decrease is readily detected in the tumor region, whereas a negligible change in SE% is observed in kidneys, liver and muscle. The relaxometric MRI results have been validated by ICP-MS measurements. Copyright © 2015 John Wiley & Sons, Ltd.

Additional supporting information may be found in the online version of this article at the publisher's web site.

Keywords: MEMRI; cellular and molecular cancer imaging; molecular and cellular probes; DO2A; calcium receptors; relaxivity

INTRODUCTION

Mn²⁺ ions are used as positive contrast agents in manganese-enhanced MRI (MEMRI) to mimic Ca²⁺ transport in biological systems. Although MEMRI has been proposed for tracing neuronal connections, recently it has also been considered useful for tumor detection, as uptake of Mn²⁺ ions may be up-regulated in cancer cells (1–8). Upon i.v. administration of MnCl₂, the detection of hyperintense regions in T₁-weighted MR images allows us to trace the distribution of the paramagnetic metal ions, as Mn²⁺ ions markedly affect the relaxation times of water protons. Unfortunately, it is not straightforward to relate signal enhancement (SE) to the local concentration of the metal ions, as the relaxivity of Mn²⁺ containing species may cover a very wide range of values.

Mn²⁺ is an endogenous metal ion, and it can be coordinated by a number of naturally occurring molecules to form small or large complexes, each characterized by its own relaxivity. Among the small complexes that can be formed in biological fluids, one may list the following: [Mn(hydrogen-carbonate)]⁺, [Mn(citrate)]⁻, [Mn(carbonate)] and [Mn(oxalate)] (9). Their relaxivities are, in general, low, both because of their small size and because of the small number of water molecules in the inner coordination sphere of the paramagnetic metal ion. In contrast, binding to macromolecules may generate very high relaxivities at the imaging fields. For instance, Mn²⁺ bound to human serum albumin has been reported to have a relaxivity of 97.2/(mM s) at 0.47 T, 25 °C and pH 7 (10). On

this basis, whereas it appears very difficult, if not impossible, to extract precise information on the actual speciation of Mn²⁺ ions in living systems, the occurrence of high SE can be taken as an indication of coordination to macromolecular systems.

Moreover, we deemed it interesting to seek a method that provides information on the relative distribution of Mn²⁺ ions

* Correspondence to: Silvio Aime, Department of Molecular Biotechnologies and Health Sciences & Molecular Imaging Center, University of Torino, Torino, Italy. E-mail: silvio.aime@unito.it

a E. Gianolio, F. Arena, E. Di Gregorio, S. Aime
Department of Molecular Biotechnologies and Health Sciences & Molecular Imaging Center, University of Torino, Torino, Italy

b R. Pagliarin, M. Delbianco
Department of Chemistry, University of Milano, Milano, Italy

c G. Baio
Diagnostic Imaging and Senology Unit, National Cancer Institute – IST, Azienda Ospedaliera Universitaria San Martino – IRCCS, Genova, Italy

d G. Baio
Aberdeen Biomedical Imaging Centre, University of Aberdeen, Aberdeen, UK

Abbreviations used: MEMRI, manganese-enhanced magnetic resonance imaging; DO2A, 1,4,7,10-tetraazacyclododecane-1,7-diacetic acid; EDTA, ethylene diamine tetraacetic acid; SE, signal enhancement; BSA, bovine serum albumin; DMEM, Dulbecco's modified Eagle's medium; PBS, phosphate-buffered saline; ROI, region of interest.

in the intracellular and in the extracellular compartment. In the context of tumor detection and staging, it is relevant to assess whether the observed SE has to be assigned to the intracellular or the extracellular compartment. To tackle this task, a procedure was set up based on sequestering all the Mn²⁺ ions in the extracellular compartment into a highly stable chelate characterized by a low relaxivity ("MRI silent", Fig. 1). Then, the comparison of the signal intensities of the region of interest (ROI) before and after the "sequestering" step allows the identification of the relative contributions from intra- and extracellular compartments in a MEMRI experiment.

EXPERIMENT

Relaxometric characterization

The longitudinal water proton relaxation rate was measured at 0.47 T (20 MHz proton Larmor frequency) by a Stelar SPINMASTER (Stelar, Mede, Pavia, Italy) spectrometer using the standard inversion-recovery technique. The temperature was controlled with a Stelar VTC-91 air-flow heater equipped with a copper-constantan thermocouple (uncertainty 0.1 °C). Relaxivities were measured at both 25 °C and 37 °C in water and in serum, respectively.

In vitro cellular uptake

B16F10 murine melanoma cells and MDA-MB-231 and MCF7 human breast cancer cells were cultured in 75 cm² flasks in a humidified incubator at 37 °C and in CO₂/air (5:95 v/v) in Dulbecco's modified Eagle's medium (DMEM) containing 10% fetal bovine serum, 100 U/ml penicillin and 100 mg/ml streptomycin. About 8 × 10⁵ cells were seeded in 6 cm Petri dishes. Twenty-four hours after seeding, cells were washed and incubated with different concentrations (0.5 or 1 mM) of MnCl₂ and Mn-DO2A (1,4,7,10-tetraazacyclododecane-1,7-diacetic acid) for 1 h or 7 h at 37 °C in a CO₂ incubator. After this incubation time, the cells were washed three times with 5 ml ice-cold phosphate-buffered saline (PBS), detached with trypsin-EDTA (ethylene diamine tetraacetic acid), and, for the acquisition of MR images, collected in 50 µL of PBS and transferred into glass capillaries, that were centrifuged at 1500 g for 5 min. The resulting cellular pellets were placed in an agar phantom and underwent MRI acquisition. After imaging, the labeled cells were suspended in 200 µL PBS and sonicated to obtain cell lysates. Mn content was measured by ICP-MS analysis (Element-2; Thermo-Finnigan, Rodano, Italy). The preparation of the samples for ICP-MS analysis was carried out as follows: (i) 150 µL of each cell lysate was mineralized with 1 ml of concentrated HNO₃ (65%) under microwave heating at 160 °C for 40 min (Milestone

MicroSYNTH microwave lab station equipped with an optical fiber temperature control and HPR-1000/6M six-position high-pressure reactor, Bergamo, Italy); (ii) after mineralization, the volume of each sample was brought to 2 ml with ultrapure water and the sample was analyzed by ICP-MS. The calibration curve was obtained using four manganese absorption standard solutions (Sigma-Aldrich) in the range 0.005–0.2 µg/ml.

The protein content of cells lysates was determined by the Bradford method using bovine serum albumin (BSA) as standard.

A specific experiment has been carried out in order to assess whether the presence of Ca-DO2A in the extracellular compartment could drive the delivery of Mn²⁺ ions from the intracellular space. After the incubation (1 h) of B16F10 cells with MnCl₂ (1 mM), cells were washed twice with PBS and re-incubated for increasing times (30 min, 1 h, 2 h, 4 h) with fresh culture medium containing Ca-DO2A (1 mM). The control experiment was carried out re-incubating the labelled cells with culture medium without Ca-DO2A. Mn content was measured by ICP-MS analysis as reported above.

MRI in vitro

The MR images were acquired with a standard T₁-weighted spin-echo sequence and recorded on a Bruker Avance 300 spectrometer operating at 7.1 T equipped with a micro-imaging probe (T_R/T_E/N_{EX} 250/3.9/8, FOV 1 cm, one slice, 1 mm).

MRI in vivo

Tumor bearing mice were prepared by inoculating subcutaneously about 1 × 10⁶ B16F10 cells into the flank of 10 weeks old female C57B1/6 mice of about 25 g. The mice underwent MRI analysis 7–10 days after cell inoculation. All tumors were approximately the same size at the time of image acquisition (250 ± 50 mm³). Tumor development was followed by palpation and caliper measurement. Tumor volume was calculated according to the formula (L × W²)/2, where L and W are the maximum length and width of the tumor. The investigation complied with national legislation about the care and use of laboratory animals.

Mice were divided into three groups (n = 3 each) and each group was treated i.v. with one of the following solutions:

- (1) MnCl₂ (0.058 mmol/kg) + Ca-DO2A (0.116 mmol/kg)
- (2) MnCl₂ (0.058 mmol/kg)
- (3) Mn-DO2A (0.058 mmol/kg).

In the first group, Ca-DO2A was injected i.v. 30 min after the administration of MnCl₂.

MR images were acquired on the Aspect M2 scanner (Aspect Imaging, Shoham, Israel) operating at 1 T equipped with a horizontal bore MRI magnet using a standard T₁-weighted multislice spin echo sequence (T_R = 250 ms, T_E = 7.0 ms, N_{EX} = 10, FOV = 3.5 cm, six slices, 1 mm). During the experiments, animals were anaesthetized with isoflurane gas (0.5–2%) in O₂; anesthesia was maintained by adjustment of gas level as a function of breath rate, kept close to 70 breaths/min. For the measure of SE%, ROIs were selected on different slices of the investigated organs throughout the organ's volume. ROIs were selected to include the tumor margins as defined in T_{2W} images. SE of each organ was calculated as percentage signal increase with respect to the image acquired before the administration of MnCl₂. Intensity normalization was achieved by using an external reference (ProHance® 0.5 mM).

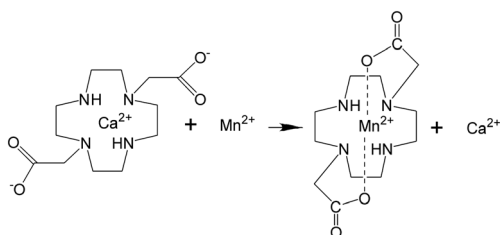


Figure 1. Schematic representation of the formation of Mn-DO2A complex.

Determination of manganese content in tissues

Mn content was measured by ICP-MS analysis. The preparation of the samples for ICP-MS analysis was carried out as follows: (i) tissue samples were freeze-dried, weighed and digested with 1.5 ml (kidneys, tumor and muscle) or 3 ml (liver) of concentrated HNO₃ (65%) for 24 h; (ii) 1 ml of digested tissues were mineralized under microwave heating at 160 °C for 40 min; (iii) after mineralization, the volume of each sample was brought to 3 ml with ultrapure water and the sample was analyzed by ICP-MS. Data are presented as mg of Mn per gram of dry tissue.

RESULTS

The “sequestering agent”

The relaxivity (defined as the paramagnetic contribution to the observed proton relaxation rate of a solution in which the paramagnetic agent is present at 1 mM concentration) of MnCl₂ and Mn-DO2A was measured at 25 °C and 37 °C in water and in serum at the magnetic field strength of 0.47 T. The obtained values are reported in Table 1. Thanks to the six coordinated water molecules around the Mn(II) ion, MnCl₂ is endowed with a relatively high water relaxivity. A further remarkable increase in relaxivity is achieved in serum, as a consequence of the formation of an adduct with albumin (10). In contrast, Mn-DO2A is endowed with very low relaxivity values both in water and in serum (Table 1).

Figure 2(A) reports the relaxivity changes observed upon addition of aliquots of Ca-DO2A to a solution of MnCl₂ (1 mM) in the presence and in the absence of BSA. For both systems,

the addition of Ca-DO2A quickly leads to the asymptotic value, corresponding to the relaxivity of Mn-DO2A. To get more insight into the relationship between the stability of Mn-DO2A and the release of Mn²⁺ to endogenous macromolecules, we investigated the titration of a Mn-DO2A solution (0.58 mM) with BSA. The titration has been followed by ¹H-relaxometry by measuring the observed proton relaxation rate (*R*_{1obs}) at 0.47 T as a function of the BSA concentration (Fig. 2(B)). At each data point the measured *R*_{1obs} value is given by

$$R_{1obs} = R_1^0 + r_{1p}^{MnDO2A} \chi^{MnDO2A} + r_{1p}^{MnBSA} \chi^{MnBSA} \quad [1]$$

and

$$\chi^{MnDO2A} + \chi^{MnBSA} = 1 \quad [2]$$

where χ^{MnDO2A} and χ^{MnBSA} are the molar fractions of Mn bound to DO2A and to BSA respectively, r_{1p}^{MnDO2A} and r_{1p}^{MnBSA} are the relaxivities of Mn-DO2A and Mn-BSA at 0.47 T and 25 °C reported in Table 1 (1.8 and 72.5/(mM s), respectively) and R_1^0 is the diamagnetic contribution measured for the BSA-containing solutions in the absence of Mn-DO2A.

Equations [1] and [2] allow us to calculate, for each experimental data point, the percentage of Mn that has been transferred to BSA (Fig. 2(B)). Even with a large excess of BSA the amount of Mn bound to the protein remains very low.

Uptake studies of MnCl₂ and Mn-DO2A in tumor cells

About 1 × 10⁶ B16F10, MDA-MB-231 and MCF7 cells were incubated in DMEM medium containing 0.5 or 1 mM MnCl₂ or Mn-DO2A, respectively. At the end of the incubation period (1 h or 7 h), cells were extensively washed and the obtained cellular pellets underwent the determination of Mn content and MR image acquisition. The amounts of internalized Mn, assessed by ICP-MS, are reported in Fig. 3(A) for B16F10 cells, and in Fig. S1 for MDA-MB-231 and MCF7 cells. The reported data have been obtained by subtracting the naturally occurring Mn content measured for the same number of unlabeled cells.

In Fig. 3(B) the MR images of pellets of labelled B16F10 cells, recorded at 7.1 T, are reported. The amount of internalized metal is much higher (6–10-fold depending on the incubation time) in the case of cells incubated in the presence of MnCl₂ with respect to those incubated with Mn-DO2A. Similar results were obtained

	Relaxivity /(mM s) at 0.47 T			
	Water		Serum	
	25 °C	37 °C	25 °C	37 °C
MnCl ₂	7.8 ± 0.11	6.5 ± 0.21	72.5 ± 0.35	55.2 ± 0.23
Mn-DO2A	1.5 ± 0.13	1.3 ± 0.11	1.8 ± 0.15	1.5 ± 0.12

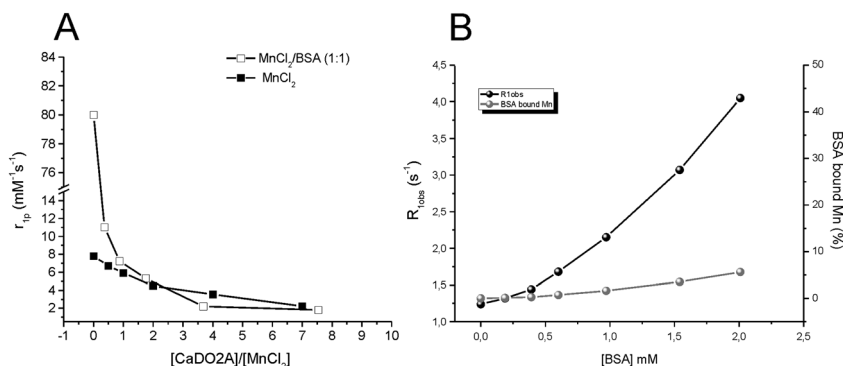


Figure 2. (A) Variation of the relaxivity of a solution of MnCl₂ as a function of the addition of increasing concentrations of Ca-DO2A in water and in the presence of BSA. (B) Variation of the observed proton relaxation rate of a solution of Mn-DO2A (0.58 mM) as a function of the addition of increasing concentrations of BSA in PBS. On the same graph the percentages of BSA-bound manganese calculated from *R*_{1obs} values are also reported as a function of BSA concentration. Measurements were made at 25 °C, 20 MHz and neutral pH.

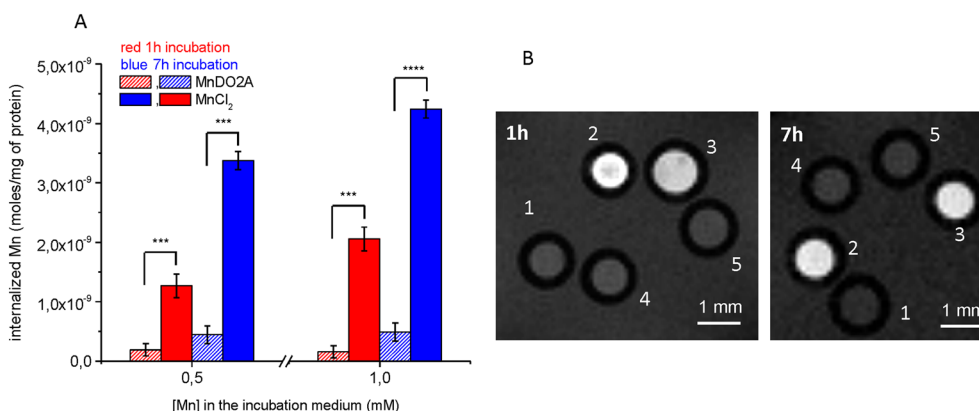


Figure 3. (A) Amount of internalized Mn^{2+} in B16F10 cells incubated with $MnCl_2$ and Mn-DO2A for 1 and 7 h. Error bars represent standard deviations (statistical analysis: *** $P < 0.01$; **** $P < 0.001$). (B) MR images at 7.1 T of pellets of B16F10 cells labelled as follows: (1) control; (2, 3) $MnCl_2$ 1 mM and 0.5 mM respectively; (4, 5) Mn-DO2A 1 mM and 0.5 mM respectively.

for MCF7 cells, whereas MDA-MB-231 turned out to be even more effective in the Mn^{2+} uptake (Fig. S1).

Figure 3(B) reports the MR images obtained from pellets of B16F10 cells labelled with $MnCl_2$ (3,4) and with Mn-DO2A (4,5). In the case of $MnCl_2$ labeling the pellets are highly hyperintense, whereas the pellets of cells labelled with Mn-DO2A are not distinguishable from control cells (1).

In order to assess whether the presence of an excess of Ca-DO2A in the extracellular compartment may enhance the efflux of manganese from the intracellular space, B16F10 cells previously labelled with $MnCl_2$ were re-incubated, for increasingly longer intervals, in culture media containing Ca-DO2A (1 mM) or not, and the amount of intracellular Mn determined by ICP-MS. The data, reported in Fig. 4, reveal that the presence of Ca-DO2A in the culture medium does not affect the decrease of the intracellular Mn concentration with time with respect to the control experiment. Apparently there is a slow efflux of Mn ions from the cellular cytoplasmic compartment that is independent of the presence or absence of Ca-DO2A in the cell suspension medium.

In vivo MRI experiments on B16F10 tumor bearing mice

In vivo MRI experiments were carried out at 1 T. Mice were divided into three groups and each group was treated i.v. with $MnCl_2$ + Ca-DO2A, $MnCl_2$ or Mn-DO2A.

In the first group, the dose of Ca-DO2A was injected i.v. 30 min after the administration of $MnCl_2$. In analogy to what is seen *in vitro*, the added Ca-DO2A undergoes a transmetallation reaction with Mn^{2+} ions present in the vascular and extracellular compartments, leading to a steady SE% (Fig. 5(A)). In the tumor region, the formation of Mn-DO2A corresponds to a net decrease of SE (Figs. 5(B) and 6). In kidneys, liver and muscle no significant change in the signal intensity occurs (Fig. 5(A) and Fig. S2). In the group administered with Mn-DO2A, the tumor SE remained low ($24.2 \pm 2.4\%$) for the two hours of the study (Fig. 5(B)). Conversely, the administration of $MnCl_2$ yielded to a strong tumor SE that steadily decreased during the first hour to reach a value (70%) that is about three times the enhancement observed for Mn-DO2A. The difference in SE% observed in the MR images of mice administered with $MnCl_2$, before and after Ca-DO2A injection, indicates that the contribution arising from Mn^{2+} in the extracellular compartment is important only in the tumor region ($25 \pm 5\%$).

After 2 h from the administration of the $MnCl_2$ or Mn-DO2A solutions, the animals were sacrificed and the Mn content in

liver, kidney, muscle and tumor tissues was determined by ICP-MS. Figure 7 compares the SE% values (taken immediately before sacrifices) and the Mn content determined by ICP-MS. From these data it is evident that most of the administered manganese can be found in kidneys and liver. Upon comparing ICP and MRI SE% values measured in experiments with either $MnCl_2$ or ($MnCl_2$ + Ca-DO2A), one can conclude that the relaxation enhancement observed in tumors appears significantly high with respect to the amount of Mn found in the analytical determination.

DISCUSSION

Mn^{2+} ion is known to form highly stable complexes with hexacoordinating ligands, e.g. EDTA, whose Mn^{2+} complex is characterized by a K_f value of 7.94×10^{13} (11). Interestingly, EDTA does not wrap perfectly around the metal ion and leaves room for the coordination of one water molecule (12). This causes the relaxivity of Mn-EDTA to be rather high ($r_{1p} = 2.9/(\text{mM s})$) at 0.47 T and 35 °C (13). Therefore, EDTA has not been considered suitable as sequestering agent for the intended aim of the project. Conversely, DO2A (Fig. 1) appears to be a good candidate for this application. It forms a highly stable complex with Mn^{2+} ions ($K_f = 1.35 \times 10^{16}$) (14) whose water relaxivity, at 0.47 T and 25 °C, is $1.5/(\text{mM s})$ (Table 1). In fact DO2A wraps perfectly around the Mn^{2+} ion, yielding an octahedral geometry by using the six available donor atoms (four nitrogens and two oxygens) (Fig. 1) with no inner-sphere water molecule.

The observed relaxivity arises from the outer sphere contribution due to water molecules diffusing at the surface of the paramagnetic complex. For our purpose Mn-DO2A complex can be considered "MRI silent". In order to be minimally invasive it was deemed useful to use the Ca^{2+} complex of DO2A rather than the sodium salt or the free acid. The equilibrium reaction depicted in Fig. 1 was first followed *in vitro* through relaxometric measurements. Thanks to the difference in relaxivity between $MnCl_2$ and Mn-DO2A, it is possible to follow the exchange reaction through the relaxometric measurement of a solution of $MnCl_2$ titrated with Ca-DO2A (Fig. 2(A)).

When Ca-DO2A is added to a solution of $MnCl_2$, Mn^{2+} ions are readily sequestered by the DO2A ligand to form the highly stable Mn-DO2A, as the latter complex is much more stable than Ca-DO2A ($\log K_f = 7.16$) (15).

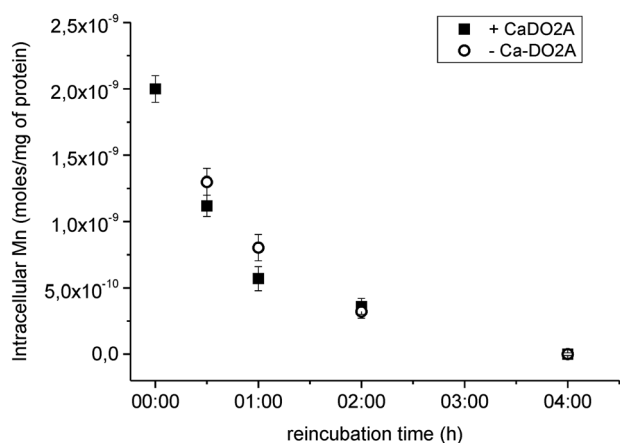


Figure 4. Amount of internalized Mn^{2+} in B16F10 cells labelled with $MnCl_2$ as a function of the re-incubation time with fresh medium containing (■) or not (○) 1 mM Ca-DO2A.

Both when Mn^{2+} ions are dissolved in pure water and when they are bound to serum albumin, the addition of Ca-DO2A leads to a marked and sudden decrease in the observed relaxivity due to the formation of the almost “silent” Mn-DO2A complex. It is worth noting that, in the presence of high concentrations of albumin, as it might be the case of the extracellular tumor matrix, the amount of Mn which is transferred from Mn-DO2A to the protein remains quite low (Fig. 2(B)). On this basis it is evident that in blood (albumin concentration 0.6 mM), at a dose of 0.058 mmol/kg (0.58 mM, considering an average mouse weight of 20 g and a blood volume of 2 ml) the amount of Mn that has been transferred to albumin from Mn-DO2A is only 0.7%. However, the high relaxivity of the Mn–albumin system strongly amplifies this contribution in the observed SE%. Moreover, in the tumor extracellular matrix, due to the extravasation through the hyper-permeable tumor vessels, the local concentration of Albumin is markedly higher than in the blood thus further enhancing the attainable SE%.

In order to assess the differences in the biodistribution of Mn^{2+} ions and Mn-DO2A complexes, it has been deemed useful to investigate the uptake of these species in tumor cells. First, B16F10 cells were considered, and the data reported in Fig. 3 clearly allow us to draw the conclusion that, while $MnCl_2$ enters cells, likely

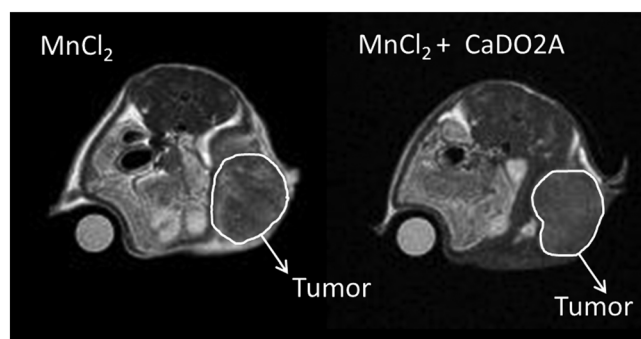


Figure 6. T1 MR images of B16F10 tumor bearing mice administered with $MnCl_2$ before (left) and after (right) the administration of Ca-DO2A. The tumor region is circled in white.

through calcium channels and calcium receptors, Mn-DO2A does not appear to have any active pathway to enter cells (16).

The B16F10 tumor cell line was not selected for a specific ability to take up Mn^{2+} ions, but for the ease of obtaining an *in vivo* subcutaneous tumor model. Actually, we compared the uptake efficiency of $MnCl_2$ and Mn-DO2A in B16F10 cells with that in MCF7 and MDA-MB-231 (both human breast cancer cell lines), which are frequently used in MEMRI of tumor cells (Fig. S1) (3,4,6,7). The ability of B16F10 cells to take up Mn was only slightly lower than that of MCF7 cells, while in the highly metastatic MDA-MB-231 cells the amount of accumulated Mn was doubled. The amount of Mn accumulated by B16F10 cells is well above the threshold for MRI visualization, and these cells were chosen to obtain the subcutaneous tumors for the *in vivo* experiments. The *in vivo* tumor model was easily obtained in C57B1/6 mice, while expensive nude mice would have been required in the case of use of MCF7 or MDA-MB-231 human cancer cells.

The very low internalization efficiency shown by Mn-DO2A is crucial for the intended aim of the work, as it demonstrates that Mn^{2+} ions, once sequestered by DO2A ligand, will not be able to be taken up by tumor cells. Moreover, the addition of Ca-DO2A to Mn-labelled cells does not influence the efflux of Mn ions from the intracellular compartment.

The method was validated *in vivo* through the acquisition of MR images of mice sequentially administered with $MnCl_2$ and Ca-DO2A. Control experiments were carried out on mice administered with $MnCl_2$ or Mn-DO2A. As can be noticed in

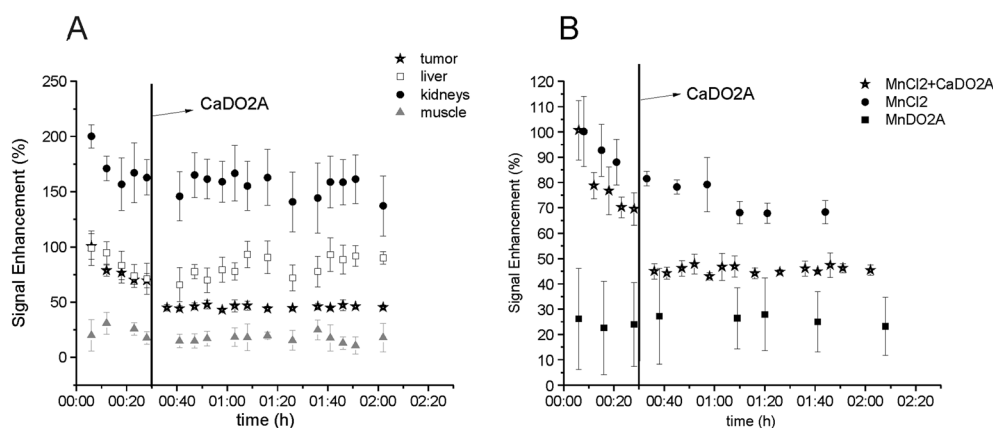


Figure 5. (A) T1 MR SE in liver, kidney, muscle and tumor of B16F10 tumor bearing mice administered with $MnCl_2$ and, after 30 min, with Ca-DO2A. (B) Tumor SE in mice administered with $MnCl_2$ + Ca-DO2A compared with that obtained in mice administered with $MnCl_2$ or Mn-DO2A only. Error bars represent standard deviations. The vertical black line on the graph represents the time point at which Ca-DO2A was administered.

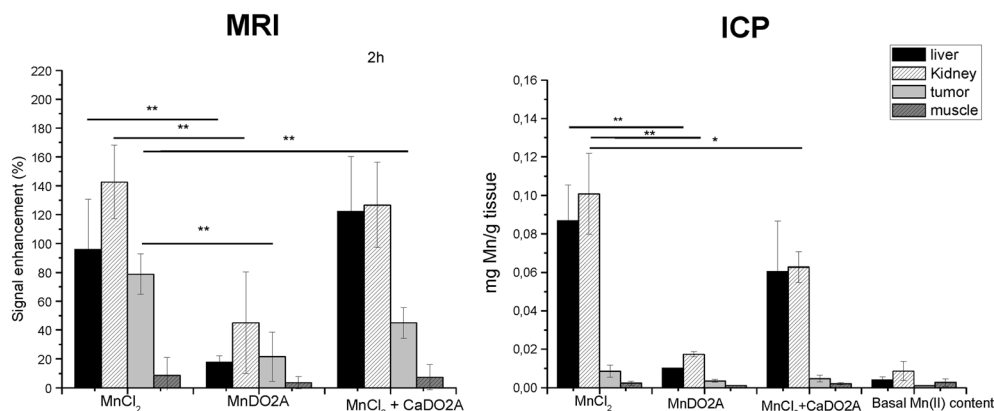


Figure 7. 1 T MRI SE and manganese content determined through ICP-MS analysis in tissues of mice administered with MnCl₂, Mn-DO₂A or MnCl₂ + Ca-DO₂A, 2 h after the administration. Error bars represent standard deviations (statistical analysis: *** $P < 0.01$; **** $P < 0.001$).

Fig. 5(B) and 6, in the tumor region, the arrival of Ca-DO₂A corresponds to a net and sudden decrease of signal intensity, indicating that a significant number of the administered Mn²⁺ ions were coordinated to biomolecules in the extracellular matrix. Conversely, the i.v. administration of Ca-DO₂A has a low effect on SE% in the kidney region, and it is negligible in the muscle tissue. In the liver it appears to cause a slight increase of the observed SE%, likely reflecting an increase in the hepatobiliary excretion route of Mn-DO₂A. The peculiar behavior observed in the tumor region may be accounted for by the presence of a relatively large extracellular region (17–19) where an important fraction of the Mn(II) ions finds suitable coordination to the endogeneous biomolecules during the MEMRI experiment. Interestingly, 45% of SE in the tumor region is still maintained up to 2 h after the administration of Ca-DO₂A. This contribution is ascribable to the Mn²⁺ ions, which have already been internalized by tumor cells in the first 30 min. This finding appears in contrast with the *in vitro* results reported in Fig. 4 that suggest a steady efflux of Mn²⁺ ions from the labeled cells. Likely, the *in vivo* conditions maintain a higher level of integrity of the cellular membranes.

Other considerations may also be made comparing the results obtained upon the administration of MnCl₂ and of Mn-DO₂A. Two hours after the administration (Fig. 5(B)), the values of SE% in the tumor region correspond to 70% in the case of administration of MnCl₂ (intra- + extracellular contributions) and 24% for Mn-DO₂A (extracellular contribution), respectively. The three sets of experimental data, with an estimation that 30% of the MRI signal is lost for the clearance of the paramagnetic manganese ions (either free or as Mn-DO₂A), allow us to establish that 45% and 25% of the observed SE are respectively due to the intra- and extracellular contributions in B16F10 xenografted tumors. Considering that only 70% of SE is maintained after 2 h, due to clearance of the probe, these values were recalculated to be 64% and 36%, respectively for the intra- and extracellular contributions. These values appear to be coherent with the intra- and extracellular volume fractions reported for tumor tissues (Table 2). This analysis was restricted to the tumor region because in the other investigated organs the addition of Ca-DO₂A had almost no effect on SE%. Even considering that healthy organs are characterized by a reduced extracellular volume fraction (Table 2) with respect to tumor, the behavior observed for kidney, liver and

Table 2. Intra- and extracellular contributions to MR signal (measured as SE%) upon MnCl₂ administration compared with intra- and extracellular volume fractions estimated by other methods

		Intracellular	Extracellular	Reference
Tumor	MR signal contribution	64 ^a	36 ^a	this work
	Volume fraction	73–71	27–29	17
		65	35	17
		51–45	49–55	20
		75–55	25–45	19
Liver	MR signal contribution	ND	ND	this work
	Volume fraction	85	15	21
		83.4	16.6	17
Kidney	MR signal contribution	ND	ND	this work
	Volume fraction	85	15	23
Muscle	MR signal contribution	ND	ND	this work
	Volume fraction	91–81.4	9–18.6	18
		91.8–81.1	8.2–18.9	22

^aThese values were recalculated from the values reported in the text (45% and 25%) to account for the 30% SE which is lost in the first 2 h due to clearance of the probe.

ND, values not detectable by the method used in this work.

muscle is difficult to rationalize. In principle, one may forward two alternative explanations: (i) Mn-DO2A does not reach the extravascular space, i.e. the vessels' fenestration is not suitable for the leakage of the added metal complex whereas the passage of Mn²⁺ ions has occurred through other transport routes (e.g. calcium channels); (ii) Mn²⁺ ions do not accumulate in the extracellular regions of these healthy tissues as they are avidly taken up by the parenchyma cells. Option (i) has to be excluded as small paramagnetic complexes show a rapid extravasation (distribution half-lives of 5–15 min) into the extracellular space in most body organs with the exception of brain (24). Option (ii) remains a tentative explanation to account for the observed behavior. The chemical composition of the extracellular microenvironment in healthy tissue may be very different from that one present in tumors. The latter may contain large amounts of serum albumin that can temporarily "sequester" Mn²⁺ ions.

The observed MR SE%, compared with the effective amounts of Mn²⁺ found in the investigated organs (liver, kidneys and muscle) by ICP-MS analysis, turned out to be well correlated. In tumor, the intracellular Mn (about 5 µg/g tissue) yields a good SE% (45 ± 10.4%), suggesting an important contribution arising from the presence of high relaxivity species, likely represented by macromolecular Mn(II) complexes.

In summary, the method reported herein may represent a useful tool to differentiate the extracellular contribution from cellular uptake in a MEMRI experiment. This approach may further strengthen the MEMRI approach for early detection and characterization of tumors (4–7).

Acknowledgements

MIUR (Grant PRIN 2012SK7ASN), AIRC Investigator Grant IG 14565, CIRCMSB and Compagnia di San Paolo are gratefully acknowledged. E.D.G. acknowledges the support of Fondazione Veronesi for the assignment of her fellowship.

REFERENCES

- Mihai R, Stevens J, McKinney C, Ibrahim NBN. Expression of the calcium receptor in human breast cancer – a potential new marker predicting the risk of bone metastases. *Eur. J. Surg. Oncol.* 2006; 32: 511–515.
- Aydar E, Yeo S, Djamgoz M, Palmer C. Abnormal expression, localization and interaction of canonical transient receptor potential ion channels in human breast cancer cell lines and tissues: a potential target for breast cancer diagnosis and therapy. *Cancer Cell Int.* 2009; 18: 9–23.
- Baio G, Fabbi M, Emionite L, Cilli M, Salvi S, Ghedin P, Prato S, Carbotti G, Tagliafico A, Truini M, Neumaier CM. In vivo imaging of human breast cancer mouse model with high level expression of calcium sensing receptor at 3T. *Eur. Radiol.* 2012; 22: 551–558.
- Alhamami M, Mokhtari RB, Ganesh T, Nofiele JT, Yeger H, Cheng HLM. Manganese-enhanced magnetic resonance imaging for early detection and characterization of breast cancer. *Mol. Imaging* 2014; 13. DOI: 10.2310/7290.2014.00021
- Ganesh T, Mokhtari RB, Alhamami M, Yeger H, Cheng HLM. Manganese-enhanced MRI of minimally gadolinium enhancing breast tumors. *J. Magn. Reson. Imaging* 2014. DOI: 10.1002/jmri.24608
- Nofiele JT, Czarnota GJ, Cheng HLM. Noninvasive manganese-enhanced magnetic resonance imaging for early detection of breast cancer metastatic potential. *Mol. Imaging* 2014; 13: 1–10.
- Nofiele JT, Cheng HLM. Ultrashort echo time for improved positive contrast manganese enhanced MRI of cancer. *PLoS One* 2013; 8: e58617.
- Braun RD, Bissig D, North R, Vistisen KS, Berkowitz BA. Human tumor cell proliferation evaluated using manganese-enhanced MRI. *PLoS One* 2012; 7: e30572.
- May PM, Linder PW, Williams DR. Computer simulation of metal-ion equilibria in biofluids: models for the low-molecular-weight complex distribution of calcium(II), magnesium(II), manganese(II), iron(III), copper(II), zinc(II), and lead(II) ions in human blood plasma. *J. Chem. Soc. Dalton Trans.* 1977; 6: 588–595.
- Aime S, Canton S, Geninatti C, Terreno E. ¹H and ¹⁷O relaxometric investigations of the binding of Mn(II) ion to human serum albumin. *Magn. Reson. Chem.* 2002; 40: 41–48.
- Smith RM, Martell AE. *Critical Stability Constants*. Plenum: New York, 1989.
- Aime S, Anelli PL, Botta M, Brocchetta M, Canton S, Fedeli F, Gianolio E, Terreno E. Relaxometric evaluation of novel manganese(II) complexes for application as contrast agents in magnetic resonance imaging. *J. Biol. Inorg. Chem.* 2002; 7: 58–67.
- Koenig SH, Baglin C, Brown RD, Brewer CF. Magnetic field dependence of solvent proton relaxation induced by Gd³⁺ and Mn²⁺ complexes. *Magn. Reson. Med.* 1984; 1: 496–501.
- Bianchi A, Calabi L, Giorgi C, Losi P, Mariani P, Palano D, Paoli P, Rossi P, Valtancoli B. Thermodynamic and structural aspects of manganese (II) complexes with polyaminopolycarboxylic ligands based upon 1,4,7,10-tetraazacyclododecane (cyclen). Crystal structure of dimeric [Mn₂]22CH₃OH containing the new ligand 1,4,7,10-tetraazacyclododecane-1,4-diacetate. *J. Chem. Soc. Dalton Trans.* 2001; 6: 917–922.
- Chang CA, Chen YH, Chen HY, Shieh FK. Capillary electrophoresis, potentiometric and laser excited luminescence studies of lanthanide(III) complexes of 1,7-dicarboxymethyl-1,4,7,10-tetraazacyclododecane (DO2A). *J. Chem. Soc. Dalton Trans.* 1998; 19: 3243–3248.
- Failli P, Bani D, Bencini A, Cantore M, Mannelli LD, Ghelardini C, Giorgi C, Innocenti M, Rugi F, Spepi A, Udisti R, Valtancoli B. A novel manganese complex effective as superoxide anion scavenger and therapeutic agent against cell and tissue oxidative injury. *J. Med. Chem.* 2009; 52: 7273–7283.
- Bhujwala ZM, McCoy CL, Glickson JD, Gillies RJ, Stubbs M. Estimations of intra- and extra-cellular volume and pH by ³¹P magnetic resonance spectroscopy: effect of therapy on RIF-1 tumors. *Br. J. Cancer* 1998; 78: 606–611.
- Dedieu V, Finat-Duclos F, Renou JP, Joffre F, Vincensini D. In vivo tissue extracellular volume fraction measurement by dynamic spin-lattice MRI relaxometry: application to the characterization of muscle fiber types. *Invest. Radiol.* 1999; 34: 185–189.
- Zhang H, Verkman AS. Microfiber optic measurement of extracellular space volume in brain and tumor slices based on fluorescent dye partitioning. *Biophys. J.* 2010; 99: 1284–1291.
- Stubbs M, Bhujwala ZM, Tozer GM, Rodrigues LM, Maxwell RJ, Morgan R, Howe FA, Griffiths JR. An assessment of ³¹P MRS as a method of measuring pH in rat tumours. *NMR Biomed.* 1992; 5: 351–359.
- Campbell-Washburn AE, Price AN, Ellmerich S, Simons JP, Al-Shawi R, Kalber TL, Ghatrora R, Hawkins PN, Moon JC, Ordidge RJ, Pepys MB, Lythgoe MF. Monitoring systemic amyloidosis using MRI measurements of the extracellular volume fraction. *Amyloid J. Protein Folding Disord.* 2013; 20: 93–98.
- Vincensini D, Dedieu V, Renou JP, Otal P, Joffre F. Measurements of extracellular volume fraction and capillary permeability in tissues using dynamic spin-lattice relaxometry: studies in rabbit muscles. *Magn. Reson. Imaging* 2003; 21: 85–93.
- Fournier LR. *Basic Transport Phenomena in Biomedical Engineering*. Taylor and Francis: Philadelphia, PA, 1998.
- Lawaczek R, Jost G, Pietsch H. Pharmacokinetics of contrast media in humans: model with circulation, distribution, and renal excretion. *Invest. Radiol.* 2011; 46: 576–585.

SUPPORTING INFORMATION

Additional supporting information may be found in the online version of this article at the publisher's web site.

2.3 Exploring a new role of MEMRI to visualize Brown adipose tissue

2.3.1. Title of the abstract

- Rosa F, Basso L, Pace D, Secondini L, Boccardo S, Neumaier CE, **Baio G**. In vivo Non-invasive Detection of Brown Adipose Tissue through Manganese Enhanced Magnetic Resonance Imaging (MEMRI). WMIC 2015. P688.

2.3.2. Objective of the study

To demonstrate the feasibility of *in vivo* MEMRI to visualise and quantify brown adipose tissue (BAT) activity in healthy controls and cancer animal models.

2.3.3. What this study added to the literature

This study was a novel imaging approach to investigate brown adipose tissue in cancer animal models. The results of this study are not published yet; however, they were awarded during the World Molecular Imaging Conference in 2015 and highlighted by Prof. G Gore as high impact research during his plenary lecture.

2.3.4. In retrospect, what should have been done differently in this study?

Looking back at this work, it would have strengthened our results if we had distinguished adipose tissue manganese uptake from beige adipose tissue uptake, considering the significant biological role of beige adipose tissue and its activation. However, this will be part of a future research project.

2.3.5. Confirmation of authorship

This is shown at the end of Chapter 2.

2.3.6. External link to the paper on the journal website

http://www.wmis.org/wp-content/uploads/2015/09/WMIC2015_ProgramBook.pdf

CONTROL ID: 2244652

TITLE: In Vivo Non-invasive Detection of Brown Adipose Tissue through Manganese Enhanced Magnetic resonance Imaging (MEMRI)/b>

AUTHORS (FIRST NAME, LAST NAME): Francesca Rosa², Luca Basso³, Daniele Pace¹, Lucia Secondini³, Simona Boccardo⁵, Carlo Emanuele Neumaier⁶, Gabriella Baio⁴

INSTITUTIONS (ALL):

1. Radiology, IRCCS AZIENDA OSPEDALIERA UNIVERSITARIA SAN MARTINO IST - ISTITUTO NAZIONALE PER LA RICERCA SUL CANCRO, Genoa, Italy.
2. radiology, IRCCS IST- San Martino, Genova, Genova, Italy.
3. Radiology, IRCCS San Martino IST Hospital, Genova, Italia, Italy.
4. Aberdeen Biomedical Imaging Centre, University of Aberdeen, Aberdeen, United Kingdom.
5. anatomical pathology, AOU IRCCS IST San Martino, Genova, Genova, Italy.
6. Radiology, AOU IRCCS IIST San Martino, Genova, Genova, Italy.

CURRENT EMPHASIS: Technology & Software Developments

CURRENT CATEGORY: MRI

Abstract

ABSTRACT BODY:

Abstract Body: Introduction

Obesity is rapidly spreading across most developed countries . At a fundamental level, obesity is the result of an imbalance between energy intake and energy expenditure. The latter is very difficult to quantify and recent work suggests that it can be altered by the function of Brown Adipose Tissue (BAT).

The recent discovery of active BAT in adult humans has opened new avenues for obesity research and treatment, as reduced/increased BAT activity seems to be implicated in development of diabetes, hypertension and cancer cachexia.

However, clinical applications are currently limited by the lack of non-invasive tools for measuring mass and function of this tissue in humans. Here we show a new magnetic resonance imaging method based on biology of manganese and its accumulation in cells via calcium channels. With this method we can explore the characteristic cellular structure of BAT to selectively image it. We demonstrate and validate this method in mice using histology.

Objectives To demonstrate that Mn²⁺ can visualise BAT in human breast/prostate cancer murine model and healthy Adult Sprague-Dawley rats, as assessed by clinical 3T magnetic resonance (MR).

Methods

In vivo experiments were approved by the Institutional Review Committee of the National Cancer Institute (IST), and were performed in accordance to the National Regulation on Animal Research Resources (D.L. 116/92).

Human MDA-MB-231-Luc breast cancer cells (n=2) and PC3 prostate cancer cells (n=2) were orthotopically grown in NOD/SCID mice to a minimum mass of 5 mm. Mice and health Sprague-Dawley Male rats (n=2) were evaluated on T1- weighted sequences before and after intravenous injection of MnCl₂.

T1-3D-SPGR-weighted sequences before MnCl₂ i.v. inoculation and 20 minutes and 20 hours after, were performed. Both qualitative and quantitative analysis by using a clinical functool software 9.4.05a were performed.

Results 20 minutes and 20 hours after Mn²⁺ administration, on T1-3D-SPGRWI, we observed a significant increase in Signal Intensity (SI). Paired Student's t-test analysis of SNR values before and 20 hours after Mn²⁺ administration yielded a significant P value for BAT (P<0,05).

Conclusion

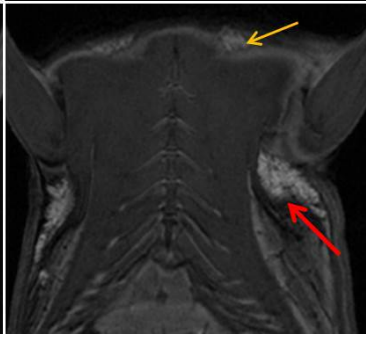
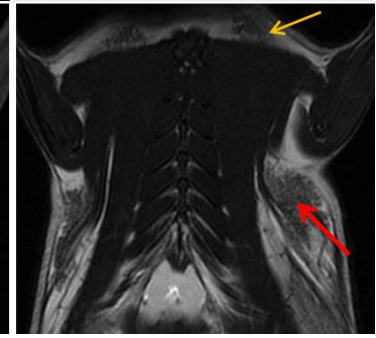
Many literature reports have investigated the BAT physiology in animals and humans. The activity of this tissue and its relation to metabolism has led to implications of BAT as a preventive mechanism against weight gain and obesity. On the other side, the activation of brown fat has been described in rodent models of cachexia and in certain cachectic patients.

Human breast cancer cell line MDA-MB-231 which give rise to tumours if transplanted in immunocompromised mice, secrete PTHrP upon stimulation which triggers adipose tissue browning and cancer cachexia.

Thus, neutralization of PTHrP might hold promise for ameliorating cancer cachexia and improving patient survival.

MEMRI can visualise BAT in both physiological and pathological condition, opening up possibilities for a new MRI

contrast agent able to evaluate BAT response to future target therapy and its activity in oncological animal models.
(no table selected)

T1 weighted imaging		
Before Manganese	After Manganese	T2 weigthd imaging
		

Abstract

Details

Copyright Affirmation: I agree.

Author Disclosure Affirmation: I agree.

Ownership of Work Affirmation: I agree.

Publications Affirmation: I agree.

Research Disclosures Affirmation: I agree.

Capture Content: I agree

Double Submission: I agree.

Interviews/Media Attention: Many literature reports have investigated the BAT physiology in animals and humans. The activity of this tissue and its relation to metabolism has led to implications of BAT as a preventive mechanism against weight gain and obesity.

On the other side, the activation of brown fat has been described in rodent models of cachexia and in certain cachectic patients.

MEMRI can visualise BAT in both physiological and pathological condition, opening up possibilities for a new MRI contrast agent able to evaluate BAT response to future target therapy and its activity in oncological animal models.

Pres Commitment: I agree.

Consent to T&A: I agree.

Disclosure Status

COI: Francesca Rosa: No COI to disclose. | Luca Basso: No COI to disclose. | Daniele Pace: No COI to disclose. | Lucia Secondini: No Answer. | Simona Boccardo: No Answer. | Carlo Emanuele Neumaier: No Answer. | Gabriella Baio: No COI to disclose.

2.4. Application of *in vivo* proton MR spectroscopy in breast cancer expressing different level of Calcium sensing receptors.

2.4.1. Title of papers

- **Baio G**, Rescinito G, Rosa F, Pace D, Boccardo S, Basso L, Salvi S, Calabrese M, Truini M, Neumaier CE. Correlation between Choline Peak at MR Spectroscopy and Calcium-Sensing Receptor Expression Level in Breast Cancer: A Preliminary Clinical Study. *Mol Imaging Biol.* 2015 Aug; 17(4):548-56.
- **Baio G**, Valdora F, Pace D, Salvi S, Villosio N, Truini M, Calabrese M and Neumaier CE. The key role of correlation between MR spectroscopy choline peak and calcium sensing receptor for breast cancer: Diagnosis by a 3T MR scanner. *Journal of Clinical Oncology*, ASCO 2013 Vol 31, No 15_suppl (May 20 Supplement).

2.4.2. Objective of the study

To explore the possible correlation between total choline peaks in breast cancer lesions as measured by *in vivo* proton magnetic resonance spectroscopy ((¹H-MRS) and CaSR expression levels in surgical specimens.

2.4.3. What this study added to the literature

In vivo proton magnetic resonance spectroscopy represents a useful technique for quantifying phosphocholine (P-Cho) concentration levels and for characterising tumour types (e.g., mass vs. diffuse) of breast cancer, but it may have limitations for small lesions. Our understanding of the molecular mechanisms that regulate the production of P-Cho compound is still

incomplete. This study explored a new approach to the interpretation of ¹H-MRS and proposed a novel role of CaSR in P-Cho production and interpretation of ¹H-MRS imaging of breast cancers. Part of the results of this study were also presented during the ASCO conference meeting in 2013. Following our publication, a review published by Bhujwalla ZM et al, one of the main experts in MRS, cited our paper as novel clinical imaging study on breast cancer MRS [144].

2.4.4. What changed as a result of the paper?

In vivo MRS is not routinely applied for breast cancer diagnosis because the results obtained by MRS are not easy to reproduce between imaging centres. However, following our investigation on CaSR in breast cancer there has been an increased number of publications supporting the important role this receptor has in cancer and response to treatment, also in other types of cancer, making this protein an interesting tumour target.

2.4.5. In retrospect, what should have been done differently in this study?

Looking back we might have increased the number of patients we prospectively analysed, especially for benign lesions. This would have improved the significance of our findings, as well as the correlation between P-Cho and CaSR. The opportunity to explore also the value of ¹H-MRS and CaSR before and after chemotherapy would have been beneficial for the understanding of CaSR in breast cancers during treatment.

2.4.6. Future work as a result of this publication

We have not performed further investigations on this topic but, as stated above, further investigation of the potential role of CaSRs in breast cancers and the opportunity to investigate by ¹H-MRS before and after chemotherapy might be an interesting future research work.

2.4.7. Confirmation of authorship

This is shown at the end of Chapter 2.

2.4.7. External link to the paper on the journal website

<https://www.ncbi.nlm.nih.gov/pubmed/25613673>

https://ascopubs.org/doi/abs/10.1200/jco.2013.31.15_suppl.e22132

RESEARCH ARTICLE

Correlation between Choline Peak at MR Spectroscopy and Calcium-Sensing Receptor Expression Level in Breast Cancer: A Preliminary Clinical Study

Gabriella Baio,^{1,2} Giuseppe Rescinito,¹ Francesca Rosa,¹ Daniele Pace,¹
Simona Boccardo,³ Luca Basso,¹ Sandra Salvi,³ Massimo Calabrese,¹ Mauro Truini,³
Carlo Emanuele Neumaier¹

¹*Diagnostic Imaging and Senology Unit, IRCCS Azienda Ospedaliera Universitaria (AOU) San Martino—IST—National Cancer Institute, 16132, Genoa, Italy*

²*Aberdeen Biomedical Imaging Centre, University of Aberdeen, Aberdeen, UK*

³*Department of Pathology, IRCCS Azienda Ospedaliera Universitaria (AOU) San Martino—IST—National Cancer Institute, 16132, Genoa, Italy*

Abstract

Purpose: The calcium-sensing receptor (CaSR) is overexpressed in many pathological states including breast cancer. Since choline kinase may be activated in breast cancer cells by CaSR resulting in increased phosphocholine production, we sought to correlate the total choline peak in breast lesions as measured by *in vivo* proton magnetic resonance spectroscopy (¹H-MRS) with the CaSR expression levels in surgical specimens.

Procedures: Thirty-six patients with breast lesions were MR scanned at 3T scanner. Tumour morphology and DCE-MR kinetics were evaluated. ¹H-MRS was applied for Cho detection and compared with the CaSR immunohistochemistry analysis (score 0–5) on surgical breast specimens.

Results: Thirty-four lesions demonstrated a DCE malignant kinetics curve (types 2 and 3), while two lesions showed a benign (type 1). Twenty of the 23 breast cancer lesions (87 %) with a consistent Cho peak expressed a CaSR score of 3–5, and ten of the 11 breast lesions negative for Cho (91 %) had a CaSR score of 1–2. The two benign lesions showed a non-uniform/weak intense expression of the CaSR (score 3) with a consistent Cho peak.

Conclusions: The presence or absence of choline peak evaluated by ¹H-MRS, well correlated with the expression of CaSR in patients with breast lesions ($p < 0.01$), supports the hypothesis that CaSR may play an important role in the production of choline in breast cancer.

Key words: Calcium-sensing receptor, MR spectroscopy, Breast cancer, Posphocholine, 3T MR, Magnetic resonance imaging, G protein-coupled receptor, Calcium channels, MRI breast, Molecular imaging cancer

Introduction

One important multimodal sensor to maintain systemic calcium homeostasis is the calcium-sensing receptor (CaSR), a member of the G protein-coupled receptor (GPCR) superfamily [1]. Calcium ions (Ca^{2+}) play an important role in the control of many important cellular functions such as proliferation, differentiation and secretion. It has been recently documented that CaSR is expressed in a variety of tissues in the body where it does not play an obvious role in calcium homeostasis, based on its ability to respond to a variety of ligands, including polyvalent cations and amino acids [2]. The different ligands may stabilise the CaSR in an activation state that allow stimulation of different pathways (the so called ligand-based signalling) [3]. Consequently, the alteration in the signalling is correlated with a number of pathophysiological states. In cancer, the role in the over or low expression of this receptor is still in discussion and could be related on the type of cancer, stage and grade. In particular, CaSR in breast cancer seems to have an important role in the development of bone metastasis as recently demonstrated [4]. Further studies might confirm the use of the CaSR expression as a prognostic marker for the risk of skeletal metastases in patients diagnosed with breast cancer.

At present, in the clinical setting, breast cancer prognosis is assessed by TNM (tumour, node and metastasis) staging, histologic type, histologic grade, mitotic figure count and hormone receptor status, by pathology examination. Breast magnetic resonance imaging (MRI) has been established as a powerful tool with a high sensitivity for breast cancer detection [5–7]. However, this technique has a low specificity, due to overlapping enhancement patterns that we obtain after gadolinium administration (quantitative analysis of the time-intensity curves in dynamic contrast-enhanced MRI). With the advances in technology and the faster sequences imaging, this limit can be overcome by measuring kinetic parameters, such as, for example, the transit of the contrast (transfer constant: K_{trans}) [8].

In addition, *in vivo* proton magnetic resonance spectroscopy ($^1\text{H-MRS}$) is increasingly being used in the clinical evaluation to characterise the cellular chemistry of breast cancer. The phosphocholine (PCho) compound evaluated by MRS may represent an imaging biomarker for cell proliferation thus allowing non-invasive molecular analysis of biologic tissue. Its value has been associated with the aggressiveness of the breast cancer phenotype [9]. Differences in its concentration between invasive and *in situ* breast lesions may reflect a different histological grade and receptor status [10].

However, the understanding of the molecular mechanisms that regulate the production of PCho compound is very limited. *In vitro* studies on breast cancer cells demonstrated the important role of the CaSR in the pathway

of choline kinase (ChoK) activity and PCho. Calcium ions induce a significant increase in extracellular PCho production in breast cancer cells primarily related to CaSR-induced ChoK activation and not from degradation of choline phospholipids [11]. Since a high level of CaSR expression induces a high concentration of calcium ions that activate ChoK in breast cancer cells, resulting in increased PCho production, we hypothesised that $^1\text{H-MRS}$ may detect elevated choline peak levels in breast cancer patients related with CaSR activity and expression levels demonstrated at the immunohistochemistry analysis.

In this study, we prospectively correlated the clinical results of breast MRI-MR spectroscopy obtained with a 3T MR scanner and CaSR-positive and negative breast specimens at the immunohistochemistry analysis.

The aim of this preliminary study is to evaluate a possible role of the CaSR in choline metabolism in breast lesion.

Material and Methods

Patient Selection

Thirty-six patients (range 34–70 years old; mean age 52 years) scanned with MRI/ $^1\text{H-MRS}$ protocol were included in this study. Patients with a suspicious findings at the clinical examination (such as, e.g., a lump in the breast) and/or at imaging evaluation (mammography or ultrasonography of the breast) were recruited from medical or surgical oncologists. All the suspicious lesions were biopsied and classified by the Breast Imaging Reporting and Data System (BI-RADS). Lesions greater than 1.5–2 cm were scanned with the $^1\text{H-MRS}$ protocol and included in this study, while lesion smaller than 1–1.5 cm or with the presence of a breast hematoma adjacent to the suspicious lesion were excluded. This study was approved by the institutional review board of our Institute. The informed consent was obtained from each patient prior to the study.

Dynamic Contrast Enhanced MR Imaging

The MR imaging protocol consisted of high-resolution imaging, dynamic contrast-enhanced MR imaging and single voxel MR spectroscopy was applied to all the patients recruited in the study. A clinical 3T whole body scanner (Signa EXCITE®HDxT, GE, Milwaukee, USA) with a dedicated software and channel phased-array breast coil (HD 8 Channels VIBRANT® Breast Array by GE, Milwaukee, USA) was used for both MR imaging and MR spectroscopy. All patients were examined in prone position with the breasts gently cushioned with rubber foam in order to reduce patient motion. After tri-plane calibration scans, axial pre-contrast T2-weighted images were acquired (see Table 1 for MR parameters details).

One set of images was acquired before contrast (2 ml/kg for 2 ml/s; ProHance® Bracco Imaging, Italy) and other five image stacks after bolus i.v. administration using an automatic injection system (Medrad Spectris Solaris EP) followed by a saline (30 cc) to flush the contrast medium. For quantitative analysis of contrast enhancement, the signal intensity was measured by a region of interest (ROI) selectively placed into the area of a lesion with the earliest contrast enhancement. Initial enhancement was quantified

Table 1. Parameters utilised for breast MRI and $^1\text{H-MRS}$ by a 3T MR scanner

	Sequence	Plane	TR (ms)	TE (ms)	FoV (cm)	Matrix	Spacing	PD	Thickness (mm)	Slices	AT (min)
T2 FSE	FSE XL	AXIAL	4020	120	34×34	512×384	0	R/L	4	45	1:50
VIBRANT	VIBRANT	AXIAL	5.3	2.4	32×32	320×320	0	R/L	1.2	144	1:35×7
$^1\text{H-MRS}$	GRE 3D BREASE	AXIAL	2000	155	24	–	–	A/P	20	–	5:00

TR Repetition time, TE Echo time, FoV Field of view, PD Phase direction, AT Acquisition time

by calculating the percent enhancement using the formula $[(\text{SI post} - \text{SI pre}) / \text{SI pre}] \times 100$, where SI post is the average SI within the ROI on the first post-contrast image and SI pre is the average SI within the ROI on the pre-contrast images. The time course of signal intensity was assessed visually using a graphic in which the x -axis represents the temporal resolution and the y -axis represents the signal intensity of the target area. For the post-processing analysis, the GE software application Functool 9.4.05a was used. The subtraction images were generated on the scanner console (Advantage Workstation Volume Share 2 GE (AW 4.4)), subtracting pre-contrast images from each post-contrast image, pixel by pixel.

MR Spectroscopy ($^1\text{H-MRS}$)

The subtraction images were used for placing the volume of interest (VOI) for the subsequent $^1\text{H-MRS}$. The VOI was a rectangular prism, which included the entire contrast enhanced lesion and adjusted to avoid the non-enhancing gland parenchyma or the surrounding fat. By this method, the theoretical filling factor was obtained comparing the lesion volume (calculated as an ellipsoid) with that of the VOI (calculated as a rectangular prism), ranged from 0.38 to 0.70. A radiologist with 2 years of experience in breast MRI/ $^1\text{H-MRS}$ was responsible of the VOI position and size.

For $^1\text{H-MRS}$, single-voxel water and fat suppressed point-resolved spectroscopy (BREASE) was acquired after contrast administration. The hypothesis was that the post-contrast localization of the lesion would yield a better consideration of its morphology including as much of the lesion as possible while avoiding surrounding adipose tissue.

The BREASE sequence was based on a PRESS single voxel acquisition, including a water suppression pulse and VSS sat bands. The acquisition is TE-averaged (4 to 8 echoes) to minimise the side bands effects from the lipid peak. The sensitive volume in PRESS localization was selected by applying a frequency-selective 90° pulse followed by two frequency-selective 180° pulses to generate a spin echo from the ROI.

Before $^1\text{H-MRS}$ was performed, the channel contralateral to the lesion site was automatically switched off. Automated parameter optimization was consisted of frequency and receiver gain adjustment and gradient tuning. An automatic shimming adjustment was also performed to reach a full width at half maximum (FWHM) of the unsuppressed water peak lower than 30 Hz (for voxel size $20 \times 20 \times 20$ mm). For values greater than 30 Hz, the automated shimming procedure was repeated. In the case of a value of FWHM greater than 30 Hz, the voxel was readjusted to the region of interest.

The $^1\text{H-MRS}$ sequence was acquired with the following parameters: TR/TE=2000/144 ms, number of excitations (NEX)=32 for voxel size 8 cm^3 ($2 \times 2 \times 2$ cm), NEX=56 for voxel size greater than 3.375 cm^3 and NEX=82 for voxel size 3.375 cm^3 ($1.5 \times 1.5 \times 1.5$ cm).

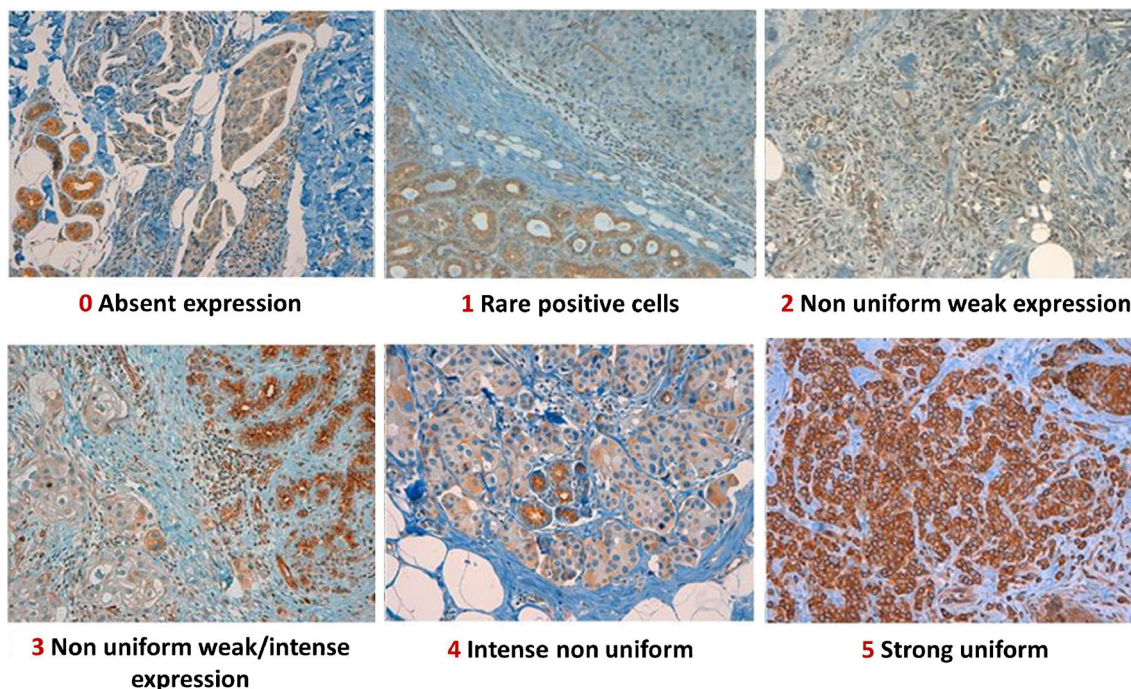


Fig. 1. Immunohistochemical analysis of CaSR expression in human breast cancers specimens (score 0–5).

This relatively long TE was chosen to increase the visibility of the Cho resonance because of the longer T2 of Cho (>350 ms) in comparison to that of lipids (~100 ms). Voxel size was chosen not less than 3.375 cm³ (1.5×1.5×1.5 cm) and not greater than 8 cm³ (2×2×2 cm), and it was carefully adjusted to the lesion.

The Cho resonance in breast spectra was qualitatively determined, and the criteria for determining the presence or absence of Cho were that a peak should be clearly identifiable at 3.2 ppm within the lesion (range 3.19–3.26 ppm). See Table 1 for MR parameters details.

BREASE is a specific spectroscopy sequence optimised to enhance breast choline concentration. It is a TE-averaged, PRESS spectroscopy acquisition compatible with a 4-, 7- or 8-channel breast coil.

Immunohistochemistry

Immunohistochemistry (IHC) was performed by staining formalin-fixed, paraffin-embedded 3-µm-thick tissue sections representative of the tumour. The sections were deparaffinised, rehydrated and treated using the automatic immunostainer Benchmark XT (Ventana Medical Systems, SA Strasbourg, France). Antigen retrieval was performed with citrate buffer high pH for 30 min. Then, the antibody was incubated for 1 h at 37 °C followed by addition of the polymeric detection system Ventana Medical System Ultraview Universal DAB Detection Kit. Finally, the sections were counter-stained (automatically) with Gill's modified haematoxylin and then coverslipped in Eukitt. The primary antibody, anti CaSR, was commercially available (PA1-934A, Affinity BioReagents, Inc., Thermo scientific INC Rockford, IL USA), polyclonal; dilution 1:200, visualisation: membrane/citoplasmic. As positive tissue control, parathyroid was used. Immunohistochemistry on adjacent sections in the absence of the primary antibody was performed for the negative control. The sections were analysed with an Olympus light microscope using 10× and 40× objectives. Two independent observers, blinded to clinical details of individual patients, evaluated the immunohistochemical analysis of CaSR reactivity, using a scoring system. Expression of CaSR (Fig. 1) was quantified using a visual grading system based on the extent of staining (percentage of tumour cells) graded on a scale of negative (score 0), weak (score 1), moderate (score 2), intense (score 3) and strong (score 4), as described in the literature [4].

Statistical Analysis

Demographic data are presented as means±standard deviation (range). Number of patients in different groups was compared using Fisher's exact test. For concern CaSR expression, we used two main categories: CaSR+ if score was 3–4 and CaSR– if the score was 0, 1 or 2.

Results

MR Dynamic Contrast enhancement and Spectroscopy analysis

Of all 36 patients, 25 showed one breast lesion as mass-nodule type morphology, nine patients showed a multifocal and multicentric morphology and two lesions appeared as ill-defined nodule type at MR imaging. No contralateral breast cancers were observed. A total of 34 of the 36 breast

demonstrated malignant type kinetics with rapid enhancements in the initial phase followed by washout or reaching a plateau in the late phase (types 2 and 3), while two lesions showed the benign enhancement kinetics with the persistent enhancement pattern (type 1). A total of 23 of the 34 malignant lesions (68 %) showed a positive choline peak at MRS, while in 11 of the 34 (32 %), the choline peak was absent or not consistent from a qualitative analysis. In the two lesions with benign enhancement kinetics, the choline peak was consistent.

Histological Results and Calcium Sensing Receptor Expression at Immunohistochemistry Analysis

At histological analysis, 25 lesions were invasive ductal carcinoma, eight lesions invasive lobular carcinoma, one

Table 2. Correlation breast cancer histotypes, hormone receptors, ki67, and CaSR-choline results

Histotype	Er	Pr	Ki67	Erb 2	CaSR	Cho
Invasive ductal carcinoma	98	99	66	2	4	+
Invasive ductal carcinoma	96	3	5	1	3	+
Invasive ductal carcinoma	99	5	10	1	4	+
Invasive ductal carcinoma	80	0	18	2	5	+
Invasive ductal carcinoma	99	46	10	1	3	+
Invasive ductal carcinoma	94	59	21	0	3	+
Invasive ductal carcinoma	90	93	12	0	5	+
Invasive ductal carcinoma	0	40	50	0	4	+
Invasive ductal carcinoma	66	0	20	3	4	+
Invasive ductal carcinoma	12	0	10	0	5	+
Invasive ductal carcinoma	34	0	8	0	3	+
Invasive ductal carcinoma	2	0	58	0	4	+
Invasive ductal carcinoma	61	9	32	0	3	+
Invasive ductal carcinoma	0	0	30	0	1	–
Invasive ductal carcinoma	93	96	0	1	2	+
Invasive ductal carcinoma	75	82	16	0	1	+
Invasive ductal carcinoma	57	83	10	0	3	–
Invasive ductal carcinoma	0	0	44	3	2	–
Invasive ductal carcinoma	2	0	92	0	1	–
Invasive ductal carcinoma	91	0	15	0	1	–
Invasive ductal carcinoma	0	0	15	3	3	+
Invasive ductal carcinoma	99	7	44	2	2	–
Invasive ductal carcinoma	99	98	11	0	1	–
Invasive ductal carcinoma	99	86	22	0	1	–
Invasive ductal carcinoma	0	0	56	3	2	–
Apocrin carcinoma	0	0	14	0	4	+
Invasive lobular carcinoma	98	0	24	2	3	+
Invasive lobular carcinoma	99	5	10	1	4	+
Invasive lobular carcinoma	95	10	43	3	3	+
Invasive lobular carcinoma	94	73	20	1	5	+
Invasive lobular carcinoma	99	38	22	0	5	+
Invasive lobular carcinoma	0	0	19	0	1	–
Invasive lobular carcinoma	97	97	12	0	2	–
Invasive lobular carcinoma	99	6	27	0	2	+
Papillary hyperplasia/ apocrine metaplasia	0	0	0	0	3	+
Papillary hyperplasia/ apocrine metaplasia	0	0	0	0	3	+

Er Estrogen receptor, Pr Progesterone receptor, Ki67 Antigen KI-67 cellular proliferation index, Erb2 Receptor tyrosine-protein kinase, CaSR Calcium-sensing receptor, Cho Choline peak at ¹H-MRS (+), no choline peak at ¹H-MRS (–), TR Repetition time, TE Echo time, FoV Field of view, PD Phase direction, AT Acquisition time

lesion apocrine carcinoma, two lesions with papillary hyperplasia/apocrine metaplasia (Table 2).

For the evaluation of CaSR, parathyroid was used as a gold standard, since its strong CaSR expression, while the negative control consisted of performing immunohistochemistry on adjacent sections in the absence of the primary antibody. The intense expression corresponds to the plasma membrane/citoplasmatic localisation of CaSR in parathyroid cells [4].

All breast lesions expressed the CaSR at the immunohistochemistry analysis, but at different levels. The predominant staining was membrane/citoplasmatic. The intensity of the CaSR expression was different between the malignant and benign lesions. Twenty-one of the 34 breast cancer lesions (62 %) showed a high level expression of CaSR with a score between 3 and 5 (five invasive lobular carcinoma, one apocrine carcinoma and 15 invasive ductal carcinoma). In 13 of the 34 malignant lesions (38 %), the CaSR patterns were between 1 and 2 (three lobular carcinoma and 10 invasive ductal carcinoma). The two benign lesions, with papillary hyperplasia/apocrin metaplasia, showed a score 3 for CaSR expression. For CaSR expression level interpretation, please see Fig. 1.

Choline peak and Calcium Sensing Receptor expression correlation

Twenty of the 23 breast lesions with a consistent choline peak at ^1H -MRS expressed a score of CaSR 3–5 (87 %) and ten of the 11 breast lesions negative at ^1H -MRS showed a score 1–2 of CaSR 91 % (Figs. 2, 3 and 4). No significant correlation was found between the different level expression of CaSR and hormone status (Er/Pr) of the different lesions ($p < 0.977$), nor between CaSR expression and morphology of the lesions at the DCE-MRI (mass-type cancers compared to non-mass-type cancers) ($p < 0.167$). An overview of the results is listed in the Table 2 and Figs. 5 and 6.

Discussion

Recently, a lot of interest has arisen in the activity of calcium-sensing receptor, in particular in tissues, such as breast cancer, that are not directly involved in the systemic mineral ion homeostasis, where the receptor probably acts in different kind of roles [12]. In patients with breast cancer, traditional anatomical imaging using size and morphological

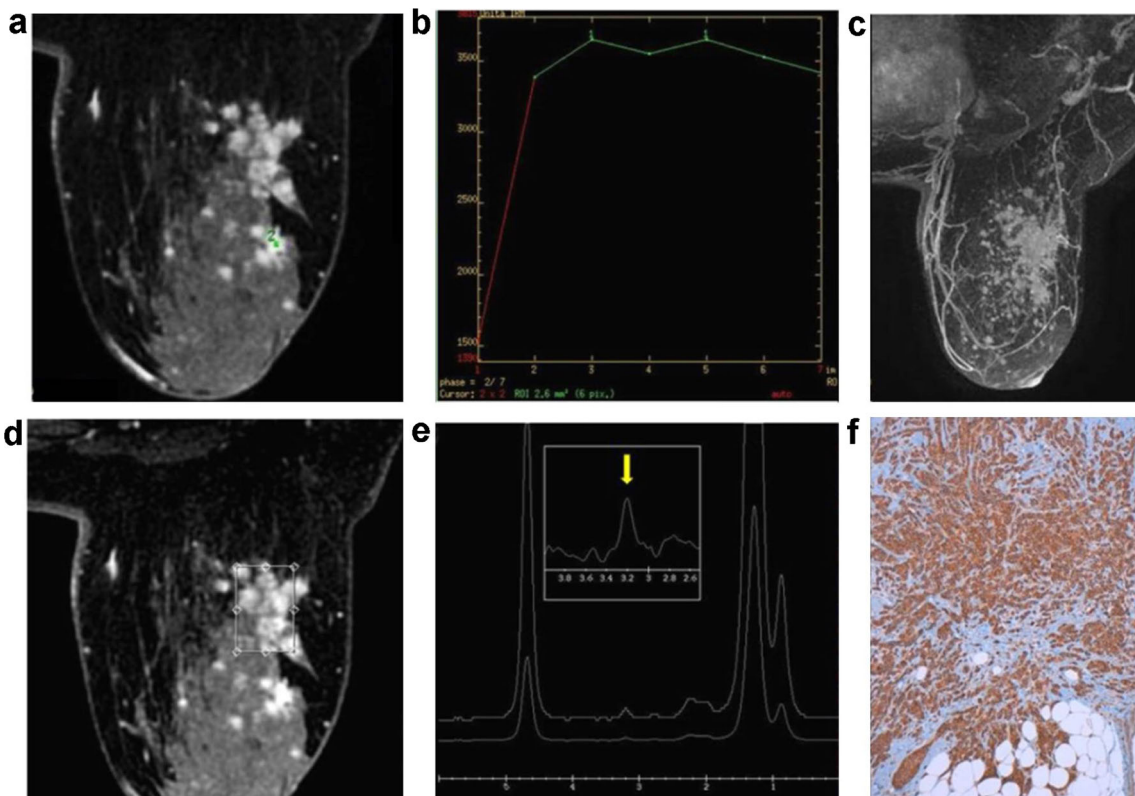


Fig. 2. Proton MR spectroscopy choline peak and calcium-sensing receptor (CaSR) correlation. A 58-year-old woman with an invasive lobular carcinoma. **a** Axial VIBRANT (Volume Imaging for BReast Assessment) contrast-enhanced magnetic resonance (MR) image (repetition time/echo time [TR/TE] 5.3/2.4 ms; 1.2 mm slice thickness) shows an enhancing irregularly multifocal and multicentric lesion in the right breast. **b** Malignant type kinetics intensity curve with rapid enhancements in the initial phase followed by a plateau in the late phase. **c** MIP reconstruction image of the lesion in the right breast. **d–e** Single-voxel MR spectroscopy (BREASE sequence): VOI localization on the axial VIBRANT contrast-enhanced magnetic resonance MR image and the resonance peak of total composite choline compounds (tCho) that was evident at 3.2 ppm. **f** Immunohistochemical analysis of CaSR expression in human breast cancer specimen (score 5).

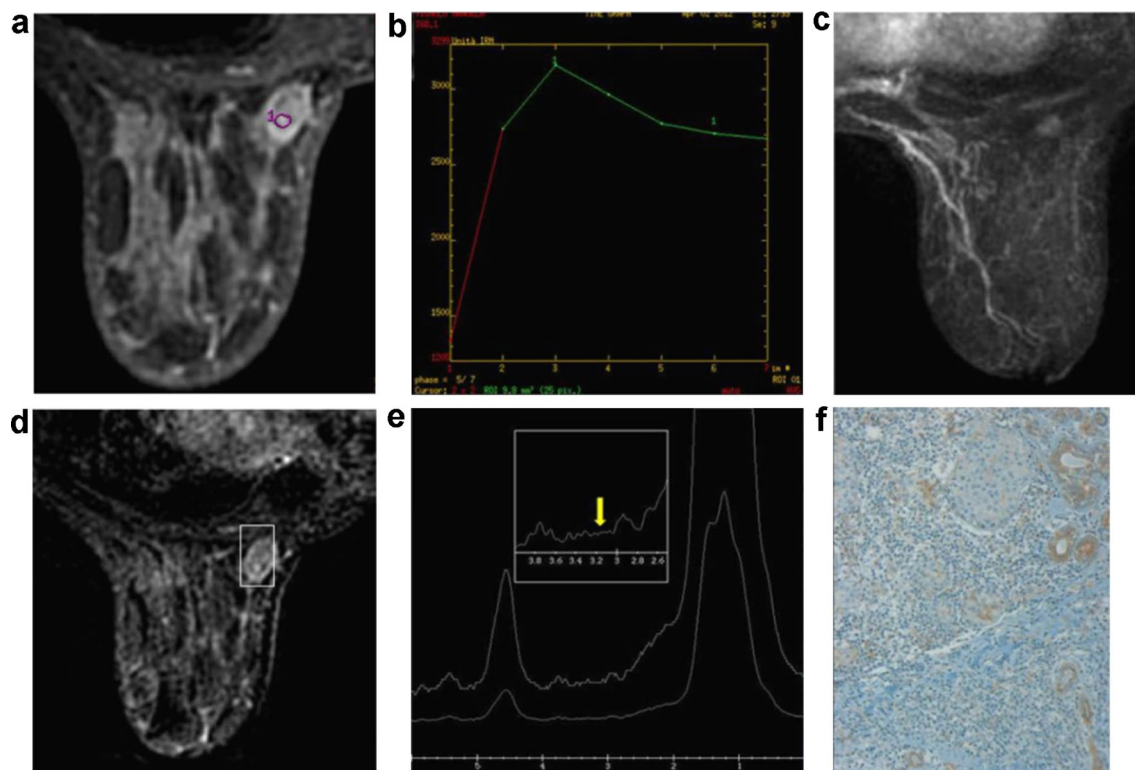


Fig. 3. Proton MR spectroscopy choline peak and calcium-sensing receptor (CaSR) correlation. A 62-year-old woman with an invasive lobular carcinoma. **a** Axial VIBRANT (Volume Imaging for BReast AssesseMNT) contrast-enhanced magnetic resonance (MR) image (repetition time/echo time [TR/TE] 5.3/2.4 ms; 1.2 mm slice thickness) shows an enhancing nodule in the left breast. **b** Malignant type kinetics intensity curve with rapid enhancements in the initial phase followed by washout. **c** MIP reconstruction image of the lesion in the left breast. **d–e** Single-voxel MR spectroscopy (BREASE sequence): VOI localization on the axial VIBRANT contrast-enhanced magnetic resonance MR image and the resonance peak of total composite choline compounds (tCho) that was not evident at 3.2 ppm. **f** Immunohistochemical analysis of CaSR expression in human breast cancer specimen (score 1).

criteria for diagnosis does not provide information on functional characteristics of the primitive tumours. The current challenge is to move towards a more molecular assessment of tumour for response evaluation that can be correlated with functional changes after neoadjuvant chemotherapy. Magnetic resonance imaging combines the morphological and functional assessment of breast tumours improving the diagnostic confidence and providing early surrogate markers of disease response [13]. Furthermore, *in vivo* ^1H -MRS represents a useful technique for quantifying Cho concentration levels and characterising tumour types (e.g., mass vs. diffuse) of breast cancer, but it may have limitations for characterising small lesions [14]. Understanding the molecular mechanisms that regulate the production of P-Cho compound is still incomplete. Recent studies on breast cancer cells demonstrated how CaSR could play an important role in the pathway of choline kinase (ChoK) activity and PCho production [11].

The extracellular calcium-sensing receptor (CaSR) is a cell surface receptor that binds calcium ions and mediates cellular responses to extracellular-free calcium. In the breast, the expression of the CaSR is localised in the ductal epithelial cells and during lactation it promotes Ca^{2+}

transport into milk [15]. We know that Ca^{2+} plays an important role in both normal physiological function and pathologic states in breast tissue. High level of CaSR expression induces a high concentration of calcium ions that activate ChoK in breast cancer cells, resulting in increased PCho production [11].

In our study, we prospectively correlated the presence or absence of choline peak at ^1H -MRS with the different expression levels of CaSR in breast lesions. A total of 34 of the 36 breast lesions demonstrated malignant type kinetics at DCE-MRI. A 68 % of these lesions showed positive choline peak (range of 3.19–3.26 ppm), while 32 % were negative. It is extensively showed that total choline concentration can be used as a marker of malignancy and, combined with DCE-MRI, increases the specificity up to 88 % (100 % after the inclusion of a single slice T2* perfusion measurement) [16], indeed, the tCho levels are significantly higher in mass-type cancers compared to non-mass-type cancers [14].

However, in our study, we had 32 % of breast cancers negative for total choline with MR spectroscopy, showing, in our opinion, an important limit of this technique, in the breast cancer detection. This “limit” maybe explained by other reasons beyond the technological aspects of the

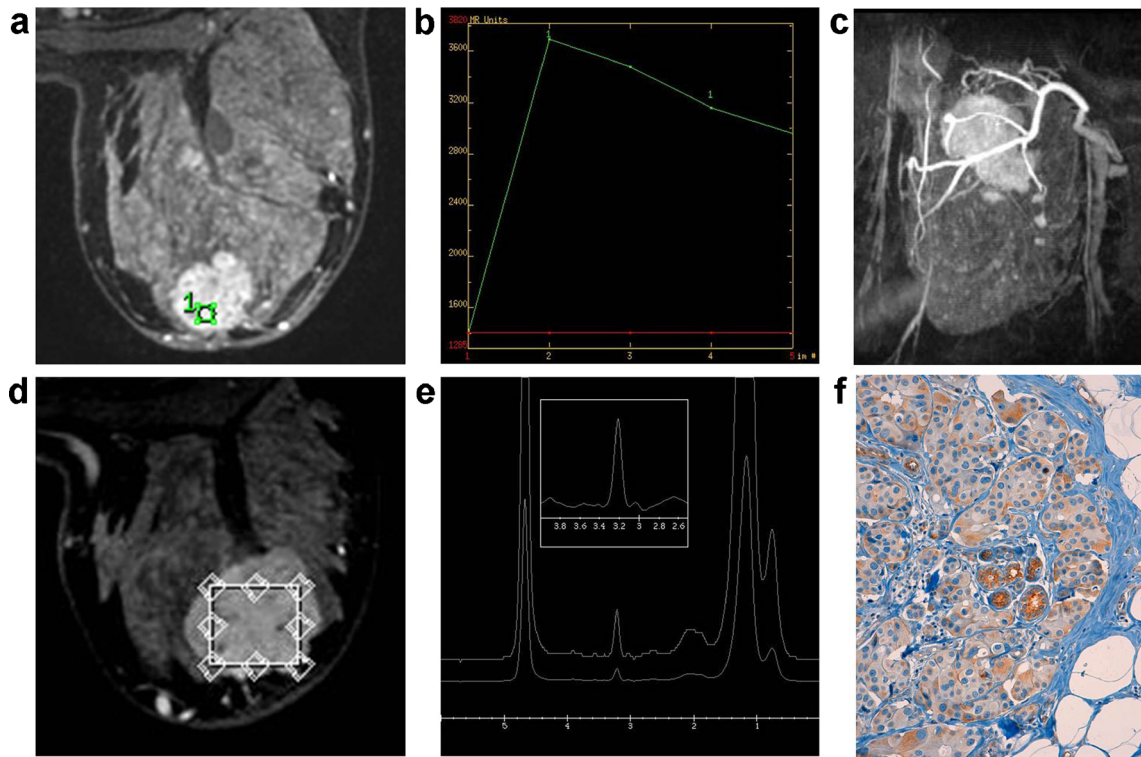


Fig. 4. Proton MR spectroscopy choline peak and calcium-sensing receptor (CaSR) correlation. A 54-year-old woman with an invasive ductal carcinoma. **a** Axial VIBRANT (Volume Imaging for BReast Assessment) contrast-enhanced magnetic resonance (MR) image (repetition time/echo time [TR/TE] 5.3/2.4 ms; 1.2 mm slice thickness) shows an enhancing polilobulated lesion in the right breast. **b** Malignant type kinetics intensity curve with rapid enhancements in the initial phase followed by washout. **c** MIP reconstruction image of the polilobulated lesion in the right breast, showing multifocal disease. **d–e** Single-voxel MR spectroscopy (BREASE sequence): VOI localization on the axial VIBRANT contrast-enhanced magnetic resonance MR image and the resonance peak of total composite choline compounds (tCho) that was evident at 3.2 ppm. **f** Immunohistochemical analysis of CaSR expression in human breast cancer specimen (score 4–5).

technique (such as, e.g., the quantity of fat included in the VOI or the dimension of the lesion) [14].

In our opinion, the results of this study, correlating MRI-MRS results and immunohistochemistry, could explain the negative results of choline in some breast cancer patients.

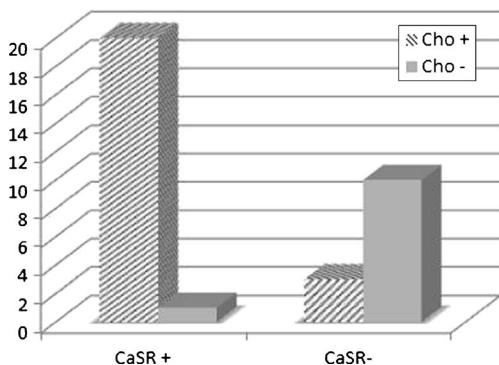


Fig. 5. Correlation between choline peak at ^1H -MRS and calcium-sensing receptor expression in breast lesions. *Cho+* Choline peak at ^1H -MRS, *Cho-* No choline peak at ^1H -MRS, *CaSR+* calcium-sensing receptor score 3–5, *CaSR-* calcium-sensing receptor score 1–2.

Indeed, 87 % of the breast lesions with choline peak at 3.2 ppm showed high level expression of CaSR (score 3–5). In 91 % of the lesions negative for choline, CaSR expression

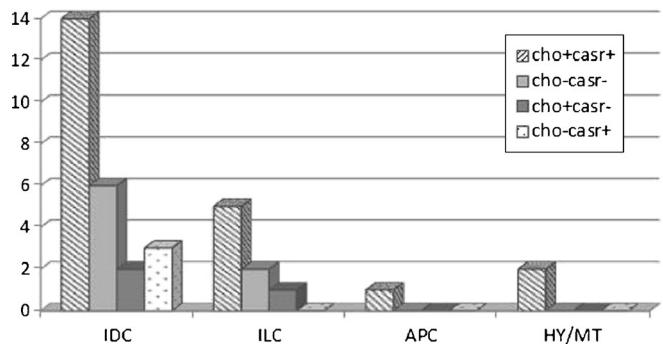


Fig. 6. Histopathology correlation between choline peak at ^1H -MRS and calcium-sensing receptor expression in breast lesions. *IDC* Invasive ductal carcinoma, *ILC* Invasive lobular carcinoma, *APC* Apocrine carcinoma, *HY/MT* Papillary hyperplasia/apocrine metaplasia, *Cho+* Choline peak at ^1H -MRS, *Cho-* No choline peak at ^1H -MRS, *CaSR+* Calcium-sensing receptor score 3–5, *CaSR-* Calcium-sensing receptor score 1–2.

was very low (score 1–2). The Fischer exact test statistic value was 0.001 with a significance limit at $p < 0.01$.

Our preliminary results could address a possible correlation between the expression of this receptor in breast lesions and how this expression is influencing the choline production within the tumour subsequently detected with $^1\text{H-MRS}$. We did not observe a correlation of hormone receptors and morphology of the lesions (mass-type cancers compared to non-mass-type cancers) with CaSR expression and choline peak (data not shown). From our results, we may deduce that the mechanism behind the production of choline is complex and influenced by other important factors, for example, as very recently described how Cho production and gene expression profiles are correlated and different, between cancers subtypes [17].

Furthermore, we also had two unexpected benign lesions at DCE-MR imaging, diagnosed as papillary hyperplasia/apocrine metaplasia, at the histology examination (“borderline benign lesion”). It is interesting that the MR spectroscopy examination of these two lesions showed a consistent choline peak and immunohistochemistry analysis confirmed the expression of CaSR with a score 3. Although the sample size is insufficient in this group for clear conclusions, this result is consistent with the idea that this receptor is expressed and probably differently regulated in both benign and malignant conditions [18], thus influencing the $^1\text{H-MRS}$ results. However, more examinations on benign lesion should be done in order to confirm this result (e.g., on breast fibroadenoma).

The physiological mechanism behind the CaSR-choline pathway confirms the importance of the role of this receptor in breast tumour. DCE-MRI plus $^1\text{H-MRS}$ could play together an important role in the study of breast cancer and CaSR, in particular, if this receptor has a special role in bone metastases development [4]. From a clinical point of view, it would be very important to perform a “molecular imaging diagnosis” of a group of patients with high risk to develop bone metastases, using a non-invasive imaging technique such as MRI- $^1\text{H-MRS}$.

Many clinical studies used $^1\text{H-MRS}$ to monitor the response of locally advanced breast cancer, showing that the change in tCho concentration can serve as an indicator for predicting clinical response to therapy [19, 20]. On the basis of our results and considering the link between CaSR and choline, we believe that it would be challenging to investigate more how the receptor expression changes under chemotherapy and how this relates to the choline peak changes. Recent investigation of BRCA1 and CaSR showed how these two factors together suppress the expression of survinine and promote sensitivity to paclitaxel in human breast cancer cell [21]: This is another example of how CaSR could influence not only the therapy effects (may promote aggressive behaviour and resistance to cytotoxic drugs?), but also the imaging results when using a technique such as $^1\text{H-MRS}$ (CaSR-choline production).

Furthermore, in our cohort of patients, five triple negative breast cancers were expressing different level of CaSR. We believe that this is another important point of our results, considering that actually the treatment of these patients is challenging and CaSR may represent an independent receptor suitable for a tumour targeting therapy of triple negative breast cancer.

The future in biomarkers research for the evaluation of treatment response will be the correlation of gene expression and MR imaging: Gene arrays and immunohistochemistry analysis of CaSR-Cho pathways could help to better understand which gene expression is related to specific changes in the aggressiveness of the disease, assessed by MRI.

A large cohort of patients is mandatory to confirm our preliminary results and to perform the next step in the analysis of CaSR-Cho during treatment. Furthermore, a larger sample of benign lesions would allow better understanding of CaSR in the “non-malignant” condition and its possible role in the progression to cancer.

The ongoing research and the development of new functional MR techniques applied into the routine of clinical care indicate that the prospects for substantial improvements in monitoring therapeutic response as well as for early detection of breast cancer are promising [13]. A key factor to success will depend in the rigorous reproducibility of the qualitative and quantitative measurements performed by an imaging technique, such as MRI- $^1\text{H-MRS}$.

Conclusions

Our findings suggest that $^1\text{H-MRS}$ presence or absence of choline peak correlates with different expression levels of CaSR in patients with breast lesions. These results support the hypothesis that CaSR plays an important role in the production of choline in breast cancer and that the CaSR-Cho signalling is important in breast cancer cell biology, suggesting the possibility that this pathway may represent a potential tumour imaging targeting strategy.

Acknowledgments. The authors thank Mrs Teresa Morris, Coordinator of Aberdeen Biomedical Imaging, University of Aberdeen, UK, for his helpful revision of the manuscript, in particular for English editing.

Conflict of Interests. The authors declare that they have no conflict of interests.

Ethical Approval. All procedures performed in studies involving human participants were in accordance with the ethical standards of the institutional and/or national research committee and with the 1964 Helsinki declaration and its later amendments or comparable ethical standards.

References

1. Ward DT, Riccardi D (2012) New concepts in calcium-sensing receptor pharmacology and signalling. *Br J Pharmacol* 165:35–48
2. Diez-Fraile A, Lammens T, Benoit Y et al (2013) The calcium-sensing receptor as a regulator of cellular fate in normal and pathological conditions. *Curr Mol Med* 13:282–295

3. Ward DT (2004) Calcium receptor-mediated intracellular signalling. *Cell Calcium* 35:217–228
4. Mihai R, Stevens J, McKinney C et al (2006) Expression of the calcium receptor in human breast cancer—a potential new marker predicting the risk of bone metastases. *Eur J Surg Oncol* 32:511–515
5. Warner E, Plewes DB, Shumak RS et al (2001) Comparison of breast magnetic resonance imaging, mammography, and ultrasound for surveillance of women at high risk for hereditary breast cancer. *J Clin Oncol* 19:3524–3531
6. Warner E, Messersmith H, Causer P et al (2008) Systematic review: using magnetic resonance imaging to screen women at high risk for breast cancer. *Intern Med* 148:671–679
7. Houssami N, Hayes DF (2009) Review of preoperative magnetic resonance imaging (MRI) in breast cancer: should MRI be performed on all women with newly diagnosed, early stage breast cancer? *Cancer J Clin* 59:290–302
8. Su MY, Yu HJ, Carpenter PM et al (2005) Pharmacokinetic parameters analyzed from MR contrast enhancement kinetics of multiple malignant and benign breast lesions detected in the same patients. *Technol Cancer Res Treat* 4:255–263
9. Aboagye EO, Bhujwall ZM (1999) Malignant transformation alters membrane choline phospholipid metabolism of human mammary epithelial cells. *Cancer Res* 59:80–84
10. Lean C, Doran S, Somorjai RL et al (2004) Determination of grade and receptor status from the primary breast lesion by magnetic resonance spectroscopy. *Technol Cancer Res Treat* 3:551–556
11. Huang C, Hydo LM, Liu S et al (2009) Activation of choline kinase by extracellular Ca^{2+} is Ca^{2+} -sensing receptor, Galpha12 and Rho-dependent in breast cancer cells. *Cell Signal* 21:1894–1900
12. Brown EM, MacLeod RJ (2001) Extracellular calcium sensing and extracellular calcium signaling. *Physiol Rev* 81:239–297
13. O'Flynn EA, DeSouza NM (2011) Functional magnetic resonance: Biomarkers of response in breast cancer. *Breast Cancer Res* 13:405
14. Baek HM, Lee YJ (2014) Feasibility of MR spectroscopy for characterizing malignant breast lesions using a clinical 3-T scanner. *Breast Cancer Jan* 4. [Epub ahead of print]
15. Cheng I, Klingensmith ME, Chattopadhyay N et al (1998) Identification and localization of the extracellular calcium-sensing receptor in human breast. *J Clin Endocrinol Metab* 83:703–707
16. Huang W, Fisher PR, Dulaimy K et al (2004) Detection of breast malignancy: Diagnostic MR protocol for improved specificity. *Radiology* 232:585–591
17. Grinde MT, Skrbo N, Moestue SA et al (2014) Interplay of choline metabolites and genes in patient-derived breast cancer xenografts. *Breast Cancer Res* 16:R5
18. Brennan SC, Thiem U, Roth S et al (2013) Calcium sensing receptor signalling in physiology and cancer. *Biochim Biophys Acta* 1833:1732–1744
19. Meisamy S, Bolan PJ, Baker EH et al (2004) Neoadjuvant chemotherapy of locally advanced breast cancer: predicting response with *in vivo* ^1H MR spectroscopy a pilot study at 4T. *Radiology* 233:424–431
20. Kumar M, Jagannathan NR, Seenu V et al (2006) Monitoring the therapeutic response of locally advanced breast cancer patients: Sequential *in vivo* proton MR spectroscopy study. *J Magn Reson Imaging* 24:325–332
21. Promkan M, Liu G, Patmasiriwat P et al (2011) BRCA1 suppresses the expression of survivin and promotes sensitivity to paclitaxel through the calcium sensing receptor (CaSR) in human breast cancer cells. *Cell Calcium* 49:79–88

Enter words / phrases / DOI / ISBN / authors / keywords / etc.

Search

Advanced Search

Newest Articles Issues Browse By Topic Special Content Authors Subscribers About ASCO Journals Career Center

TUMOR BIOLOGY

The key role of correlation between MR spectroscopy choline peak and calcium sensing receptor for breast cancer: Diagnosis by a 3T MR scanner.

Gabriella Baio, Francesca Valdora, Daniele Pace, Sandra Sahli, Nicolo Villosio, Mauro Truini, Massimo Calabrese, Carlo Emanuele Neumaier

Diagnostic Imaging and Senology Unit, Irccs Azienda Ospedaliera Universitaria SAN Martino, IST, National Cancer Institute, Genoa, Italy; Department of Pathology, National Institute for Cancer Research, Genoa, Italy; AUO San Martino IST, Genoa, Italy

Show Less

Abstract Disclosures

Abstract

e22132

Background: The Ca2+-sensing receptor (CaSR) regulates the Ca2+ signaling and its expression is present in both normal and malignant breast tissues. Recently, we demonstrated in a pre-clinical setting the CaSR expression in breast cancer mouse model by manganese enhanced MRI (Baio G et al. Eur Rad 2011). Alteration in choline phospholipid metabolism as detected by MRI, is a common feature of breast and many other cancer cells or tumors. Since CaSR-ChoK signaling plays an important role in breast cancer, we compared the MRS (MR spectroscopy) choline peak by a 3T MR scanner between calcium sensing receptor positive and negative breast cancers. **Methods:** Breast MRI of 16 consecutive patients with breast lesions were performed by a 3T MR and MRS findings were defined as positive by the visual inspection for the presence or the absence of choline peak. MRS imaging were compared with histologic findings and the pattern of CaSR by immunohistochemistry. The immunohistochemical results were qualitatively classified according to intensity and pattern of the staining, using a 6-point scale to score the intensity of the CaSR expression (0, absent; 5, intense, widespread expression). **Results:** A choline peak was present in 10 of 15 malignant lesions and the CaSR expression was between 3 to 5 score at immunohistochemistry analysis (p<.0006). In 4 of 15 malignant lesions the choline peak was absent or not consistent at the visual analysis with a CaSR patterns of 1-2. In one benign lesion (papillary hyperplasia), the choline peak was consistent and the CaSR pattern was with score 3. **Conclusions:** In this study we evaluated if MRS presence or absence of choline peak well correlated with CaSR positive and negative breast cancers. We observed a choline peak with an high level expression of CaSR (score 3-5) in 67% of the breast lesions, while in 27% of the lesions the choline peak was absent with a low CaSR expression (score 1-2). These preliminary results support the hypothesis that CaSR represents an important role in the production of choline in breast cancer, determining an increase of his production when CaSR is expressed at high level and implicating and absence of choline peak when CaSR is not expressed.

OPTIONS & TOOLS

- Export Citation
- Track Citation
- Add To Favorites
- Rights & Permissions



COMPANION ARTICLES

No companion articles

ARTICLE CITATION

DOI: 10.1200/jco.2013.31.15_suppl.e22132
Journal of Clinical Oncology 31, no. 15, suppl
Published online January 30, 2017.

WE RECOMMEND

Linitis Plastica of the Rectum As a Clinical Presentation of Metastatic Lobular Carcinoma of the Breast
Filippo Venturini et al., J Clin Oncol, 2016

Magnetic Resonance Imaging in Predicting Pathological Response of Triple Negative Breast Cancer Following Neoadjuvant Chemotherapy
Joon-Ho Chen et al., J Clin Oncol, 2007

Magnetic Resonance As a Cancer Imaging Biomarker
A Gregory Sorensen, J Clin Oncol, 2006

A pilot study to compare F18 expression in normal and malignant tissue in receptor-positive early-stage breast cancer
N. Kounalakis et al., J Clin Oncol, 2016

Multimodality Screening of High-Risk Women: A Prospective Cohort Study
Susan P. Weinstein et al., J Clin Oncol, 2009

3T MR Shows Clinical Strengths
Greg Frelherr, Medscape

RSNA: Italian study shows MR-guided ultrasound as noninvasive treatment for breast cancer
Uniwads (UK), 2013

MR Spectroscopy: Is it a Clinical Contender?
Greg Frelherr et al., Medscape

Value of the Central Vein Sign at 3T to Differentiate MS From Seropositive NMOSD
PracticeUpdate, 2018

Where We are Standing in the Choice of Most Effective Radiological Imaging for Patient's Benefits?
Hediye Pinar Gunbey, International Journal of Radiology and Radiation Oncology, 2015

Powered by TREND MD

I consent to the use of Google Analytics and related cookies across the TrendMD network (widget, website, blog). Learn more
Yes No

WHAT'S POPULAR

Most Read Most Cited

Management of Immune-Related Adverse Events in Patients Treated With Immune Checkpoint Inhibitor Therapy: American Society of Clinical Oncology Clinical Practice Guideline
Brahmer et al.

Outpatient Management of Fever and Neutropenia in Adults Treated for Malignancy: American Society of Clinical Oncology and Infectious Diseases Society of America Clinical Practice Guideline Update
Taplitz et al.

Minimal Residual Disease Assessed by Multiparameter Flow Cytometry in Multiple Myeloma: Impact on Outcome in the Medical Research Council Myeloma IX Study
Rawstron et al.

Comparison of an Oral Factor Xa Inhibitor With Low Molecular Weight Heparin in Patients With Cancer With Venous Thromboembolism: Results of a Randomized Trial (SELECT-D)
Young et al.

Antimetabites: American Society of Clinical Oncology Clinical Practice Guideline Update
Hesketh et al.

ASCO eLearning WEEKLY PODCAST
NEW EPISODES EVERY WEDNESDAY
FREE TO EVERYONE
Subscribe Now

FOR YOUR PATIENTS
CANCER.NET PODCASTS
A Trusted Resource For Patients From ASCO's Patient Education Website
www.cancer.net/podcasts
Cancer.Net
Doctor-Approved Patient Information from ASCO®

NEW JOB BLOG
Speak Up Now!

2.5. A non-invasive approach to investigate chronic lymphocytic Leukaemia by using iron oxide nanoparticles.

2.5.1. Title of papers

- Valdora F, Cutrona G, Matis S, Morabito F, Massucco C, Emionite L, Boccardo S, Basso L, Recchia AG, Salvi S, Rosa F, Gentile M, Ravina M, Pace D, Castronovo A, Cilli M, Truini M, Calabrese M, Neri A, Neumaier CE, Fais F, **Baio G**, Ferrarini M. A non-invasive approach to monitor chronic lymphocytic leukaemia engraftment in a xenograft mouse model using ultra-small superparamagnetic iron oxide-magnetic resonance imaging (USPIO-MRI). *Clin Immunol.* 2016 Jul 15.
- Cutrona G, Matis S, Colombo M, Massucco C, **Baio G**, Valdora F, Emionite L, Fabris S, Recchia AG, Gentile M, Neumaier CE, Reverberi D, Massara R, Boccardo S, Basso L, Salvi S, Rosa F, Cilli M, Zupo S, Truini M, Tassone P, Calabrese M, Negrini M, Neri A, Morabito F, Fais F, Ferrarini M. Effects of miRNA-15 and miRNA-16 expression replacement in chronic lymphocytic leukaemia: implication for therapy. *Leukaemia.* 2017 Sep; 31(9):1894-1904.

2.5.2. Objectives of the studies

- To demonstrate noninvasively that iron oxide nanoparticles can be applied in *in vivo* MR imaging to monitor chronic cell leukaemia (CLL) engraftment.
- To investigate in *in vivo* the effects of replacement of miR-15a and miR-16-1 into CLL cells by using USPIO-MRI.

2.5.3. What these studies added to the literature

The temporal window between early disease detection and the subsequent steps (either mouse death or CLL cell engraftment rejection) provides a tool to evaluate more precisely treatment efficacy and the possible emergence of therapy resistant clones. Examples of the potential use of the USPIO-MRI approach that we developed are provided by observations in which CLL-engrafted mice could, in part, be “cured” by the administration of the anti CD20 mAb rituximab. This MRI approach may be used for a more precise staging of patients with CLL and possibly other lymphoproliferative disorders.

2.5.4. What changed as a result of the papers?

A novel MR imaging approach was developed to investigate *in vivo* CLL engraftment and to evaluate response to treatment. This study included a scientific collaboration with Viscover™ Imaging Agents (<https://www.miltenyibiotec.com/GB-en/products/macs-imaging-and-microscopy/viscover-imaging.html>).

2.5.5. In retrospect, what should have been done differently in these studies?

Looking back we might have considered applying ¹⁸FDG-PET/CT to one of the CLL group of animal models in order to compare the sensitivity and specificity of our technique versus ¹⁸FDG-PET/CT, since this technique has been applied by other research groups. This may have further strengthened our method.

2.5.6. Future work as a result of these publications

The research here described was concluded after the paper was published. No further research was carried out on this topic by our research group.

miRNAs are a “hot topic” in both the field of haematological malignancies and autoimmunity, since these two conditions are often concomitant in patients because a causal bidirectional relationship exists between them. Considerable effort has been made to understand the proteins that have a relevant role in both processes; literature advances demonstrate that miRNAs surface as the epigenetic regulators of those proteins and control networks are linked to both autoimmunity and haematological malignancies. Furthermore, in solid malignancies, a different expression signature of miRNA has recently been validated in oral squamous cell carcinoma (OSCC).

2.5.7. Confirmation of authorship

This is shown at the end of Chapter 2.

2.5.8. External link to the paper on the journal website

<https://www.ncbi.nlm.nih.gov/pubmed/27430522>

<https://www.ncbi.nlm.nih.gov/pubmed/28053325>



A non-invasive approach to monitor chronic lymphocytic leukemia engraftment in a xenograft mouse model using ultra-small superparamagnetic iron oxide-magnetic resonance imaging (USPIO-MRI)



Francesca Valdora ^{a,1,2}, Giovanna Cutrona ^{a,1}, Serena Matis ^a, Fortunato Morabito ^{b,c}, Carlotta Massucco ^a, Laura Emionite ^d, Simona Boccardo ^e, Luca Basso ^f, Anna Grazia Recchia ^{b,c}, Sandra Salvi ^e, Francesca Rosa ^f, Massimo Gentile ^{b,c}, Marco Ravina ^g, Daniele Pace ^g, Angela Castronovo ^g, Michele Cilli ^d, Mauro Truini ^{e,3}, Massimo Calabrese ^g, Antonino Neri ^{h,i}, Carlo Emanuele Neumaier ^g, Franco Fais ^{a,j,1}, Gabriella Baio ^{g,1,4}, Manlio Ferrarini ^{k,*}

^a Molecular Pathology, IRCCS - A.O.U. San Martino – IST, Largo Rosanna Benzi 10, 16132 Genoa, Italy

^b Hematology Unit, Department of Onco-Hematology, A.O. of Cosenza, Cosenza, Italy

^c Biotechnology Research Unit, Aprigliano, A.O./ASP of Cosenza, Cosenza, Italy

^d Animal Facility, IRCCS - A.O.U. San Martino – IST, Largo Rosanna Benzi 10, 16132 Genoa, Italy

^e Division of Histopathology and Cytopathology, IRCCS - A.O.U. San Martino – IST, Largo Rosanna Benzi 10, 16132 Genoa, Italy

^f Department of Science of Health (DISSAL), University of Genoa, Via Antonio Pastore 1, 16132 Genoa, Italy

^g Diagnostic Imaging and Senology, IRCCS - A.O.U. San Martino – IST, Largo Rosanna Benzi 10, 16132 Genoa, Italy

^h Department of Oncology and Hemato-Oncology, University of Milano, Milan, Italy

ⁱ Hematology Unit, Fondazione IRCCS Ca' Granda, Ospedale Maggiore Policlinico, Milan, Italy

^j Department of Experimental Medicine, University of Genoa, Genoa, Italy

^k Scientific Direction, IRCCS - A.O.U. San Martino – IST, Genoa, Italy

ARTICLE INFO

Article history:

Received 8 July 2016

Accepted with revision 10 July 2016

Available online 16 July 2016

Keywords:

Chronic lymphocytic leukemia (CLL)

Magnetic resonance imaging (MRI)

Ultra-small superparamagnetic iron oxide (USPIO)

Xenograft NSG mice model

Disease monitoring

ABSTRACT

Chronic lymphocytic leukemia (CLL) is the most prevalent leukemia among adults. Despite its indolent nature, CLL remains an incurable disease. Herein we aimed to monitor CLL disease engraftment and, progression/regression in a xenograft CLL mouse model using ultra-small superparamagnetic iron oxide-magnetic resonance imaging (USPIO-MRI). Spleen contrast enhancement, quantified as percentage change in signal intensity upon USPIO administration, demonstrated a difference due to a reduced USPIO uptake, in the spleens of mice injected with CLL cells (NSG-CLL, n = 71) compared to controls (NSG-CTR, n = 17). These differences were statistically significant both after 2 and 4 weeks from CLL cells injection. In addition comparison of mice treated with rituximab with untreated controls for changes in spleen iron uptake confirmed that it is possible to monitor treatment efficacy in this mouse model of CLL using USPIO-enhanced MRI. Further applications could include the preclinical in vivo monitoring of new therapies and the clinical evaluation of CLL patients.

© 2016 Elsevier Inc. All rights reserved.

* Corresponding author at: IRCCS A.O.U. San Martino – IST, Largo Rosanna Benzi 10, 16132 Genoa, Italy.

E-mail addresses: valdorafrancesca@gmail.com (F. Valdora), giovanna.cutrona@hsanmartino.it (G. Cutrona), serena.matis@hsanmartino.it (S. Matis), fortunato_morabito@tiscali.it (F. Morabito), carlotta.massucco@libero.it (C. Massucco), laura.emionite@hsanmartino.it (L. Emionite), simona.boccardo@hsanmartino.it (S. Boccardo), lukabasso89@gmail.com (L. Basso), annarecchia@tin.it (A.G. Recchia), sandra.salvi@hsanmartino.it (S. Salvi), francescarosa892@gmail.com (F. Rosa), massim.gentile@tiscali.it (M. Gentile), marco.ravina@hsanmartino.it (M. Ravina), daniele.pace@hsanmartino.it (D. Pace), angela.castronovo@hsanmartino.it (A. Castronovo), michele.cilli@hsanmartino.it (M. Cilli), mauro.truini@ospedalenuiguarda.it (M. Truini), massimo.calabrese@hsanmartino.it (M. Calabrese), antonino.neri@unimi.it (A. Neri), carlo.neumaier@gmail.com (C.E. Neumaier), franco.fais@unige.it (F. Fais), gabriella.baio@abdn.ac.uk (G. Baio), manlio.ferrarini@hsanmartino.it (M. Ferrarini).

¹ These authors have contributed equally to the work.

² Present address: Department of Experimental Medicine, University of Genoa, Genoa, Italy.

³ Present address: Department of Hematology & Oncology, Niguarda Cancer Center, Ospedale Niguarda Ca' Granda, Milan, Italy.

⁴ Present address: Aberdeen Biomedical Imaging Centre, University of Aberdeen, Aberdeen, UK.

Abbreviations

MRI	magnetic resonance imaging
ROI	region of interest
CLL	chronic lymphocytic leukemia
USPIO	ultra-small superparamagnetic iron oxide
SNR	signal-to-noise ratio
CT	computed tomography
SD	standard deviation
sem	standard error of mean
SI	signal intensity
Δ SNR%	percentage signal-to-noise ratio change
i.v.	intravenous injection
i.p.	intraperitoneal injection
RES	reticulo-endothelial system
PBMC	peripheral blood mononuclear cells
FC	flow cytometry
MHz	megahertz
FIESTA	Fast Imaging Employing Steady State Acquisition
FA	Flip Angle
FoV	field of view
TR	repetition time
TE	echo time
T1	longitudinal relaxation time
T2	transverse relaxation time
ROC	receiver-operating characteristic
CI	confidence interval
IGHV	immunoglobulin heavy chain variable region
FISH	fluorescent in situ hybridization
<i>Units</i>	
mm	millimeter
g	gram
mg	milligram
kg	kilogram
μ L	microliter
μ mol	micromole
ms	millisecond
nm	nanometer
min	minute
$^{\circ}$ C	centigrade

1. Introduction

Chronic lymphocytic leukemia (CLL) is the most common form of adult leukemia in Western countries [1,2]. CLL is characterized by the clonal expansion of mature CD5+/CD23+ lymphocytes that can infiltrate multiple organs including lymph nodes, the bone marrow, spleen, and liver. CLL is highly heterogeneous in terms of therapy-free interval, response to treatment and overall survival, ranging from rapid disease progression requiring early and frequent treatment, to survival for decades with minimal or no treatment. Staging of CLL patients involves periodical evaluation of lymph nodes, spleen, and liver infiltration and is used to define risk and treatment. Follow-up generally includes a blood cell count and palpation of lymph nodes, liver, and spleen every 3–12 months [3,4]. In daily clinical practice, a common modality for evaluating changes in spleen size is to assess if the spleen is palpable, which means that the spleen generally requires an enlargement of at least two folds in order for changes to be detected. In addition, unlike superficial lymph nodes, deep nodes cannot be evaluated by simple palpation alone.

Several mouse models for the study of CLL development have been established [5]. These encompass transgenic models in which key

genes have been altered [6–9] or xenograft models that use immunodeficient mice that are engrafted with human leukemic cells [10–12]. In all instances, development of the CLL clone can be followed by monitoring peripheral blood for the presence of leukemic cells, but the evaluation of lymphoid tissues (i.e. the spleen, in immunodeficient mice as lymph nodes are mostly atrophic), where the leukemic cells have to seed to begin their proliferative phase, requires sacrificing the animals. Thus, sensitive and safe imaging techniques to monitor disease development may be useful in preclinical models and, more importantly also based on the above considerations, may find application in routine clinical practice.

Computer tomography (CT) is used as the first-line modality for imaging of lymphoid malignancies [13]. The role of CT has not been clearly defined in CLL patients, although CT routine disease monitoring for CLL has been largely discouraged [3,14,15]. CT scans are recommended for baseline and final assessment in clinical trials and is not the method of choice to be used in clinical staging [16,17]. Magnetic resonance imaging (MRI) has a high sensitivity in the diagnosis of the disease and also plays an important role in the assessment of disease activity without the need for exposure to ionizing radiation. The success of MRI in vivo highly depends on the molecular imaging agent used. With the help of efficient imaging agents, it is possible for MRI to precisely detect early-stage disease and to monitor the response to drug therapy.

Superparamagnetic iron oxide (SPIO) or ultra-small superparamagnetic iron oxide (USPIO) nanoparticles are now primarily used and are becoming increasingly attractive as the precursor for the development of a target-specific MRI contrast agent in molecular MRI. The efficacy of iron oxide nanoparticles used as specific contrast agent in MRI for liver, spleen, and lymph node has been demonstrated in experimental and clinical studies. Several studies have shown that these particles can significantly improve the detection and characterization of focal lesions within these organs [18–20]. Due to their size-dependent properties and their applicability in non-invasive imaging methods, these materials are promising candidates for research, diagnostic, and therapeutic applications in various fields such as cancer, neurodegenerative diseases (e.g. multiple sclerosis, [21–23], stroke [24, 25]), as well as in inflammatory diseases (e.g. rheumatoid arthritis [26] and atherosclerosis [27]). Iron oxide particles can be used as contrast medium in MRI because they are agents of high relaxivity able to enhance the contrast in T2/T2*-weighted MRI in tissues in which they accumulate. USPIO are taken up by the cells of the liver, spleen, bone marrow, and lymph nodes. Because of their small size (mean size 10–20 nm), they diffuse freely through capillaries and are phagocytized by tissue-resident inflammatory cells of the reticulo-endothelial system (RES), which predominantly consists of macrophages, although neutrophils may also take up USPIO [28–30].

In this study we aimed to establish a non-invasive specific MRI method to better visualize and to quantify the presence of CLL disease by USPIO within the spleen in a pre-clinical setting. In particular, we used a mouse xenogeneic transplantation model, NOD/Shi-scid, γ c^{null} (NSG) mice, a NOD/SCID-derived strain that lacks the IL-2 family common cytokine receptor gamma chain gene (γ c) [10,11]. A secondary goal was to monitor CLL disease evolution using imaging strategies in an attempt to reduce the overall number of mice necessary for the evaluation of CLL cell engraftment over several time points, limiting their sacrifice and suffering during experimental protocols.

2. Materials and methods

2.1. CLL patients

Newly diagnosed CLL patients from participating Institutions were enrolled within 12 months from diagnosis (O-CLL1 protocol clinicaltrials.gov identifier NCT00917540). Diagnosis was confirmed by flow cytometry (FC) analysis centralized at the National Institute of Cancer Laboratory in Genoa, Italy, together with the determination of CD38

and ZAP-70 expression and IGHV mutational status as previously described [31,32]. Cytogenetic abnormalities involving deletions at chromosomes (11)(q22.3), (13)(q14.3) and (17)(p13.1), and trisomy 12 were evaluated by fluorescent in situ hybridization (FISH) in purified CD19+ population as previously described [32] (Table 1).

PBMC from patients with CLL were isolated by Ficoll-Hypaque (Seromed, Biochrom) density gradient centrifugation.

2.2. Murine model

Six to eight week old female NOD/Shi-scid, γ c^{null} (NSG) mice (The Jackson Laboratory), a xenograft model for CLL growth in vivo [10,11], were housed in sterile enclosures under specific pathogen-free conditions. All procedures involving animals were performed respecting the current National and International regulations and were reviewed and approved by the licensing and Animal Welfare Body of the IRCCS-AOU San Martino-IST National Cancer Research Institute, Genoa, Italy.

NSG mice were infused by intravenous injection (i.v.) with $30\text{--}50 \times 10^6$ PMNCs/mouse from 18 CLL cases (see Table 1) and the presence of CD19+ CD5+ leukemic cells were checked after 2 and 4 weeks from the date of injection in blood samples taken from the retro-orbital vein.

2.3. Preparation of USPIO particles-contrast agent and dosage

The USPIO contrast agent (Feraspin XS, Miltenyi Biotech GmbH, Germany) used, consists of commercially available USPIO nanoparticles with a mean particle size of 10–20 nm, able to circulate in the bloodstream and be taken up by RES macrophages. All animal groups were imaged before, and 24 h after i.v. injection of 100 μ l/25 g mouse of USPIO, corresponding to a dose of 40 μ mol Fe/kg body weight.

2.4. In-vivo MRI experiments

The mice were anesthetized by intraperitoneal injection (i.p.) with a combination of xylazine (30 mg/kg) and ketamine (100 mg/kg) and were positioned in a prototype coil (birdcage linear coil, transmit/receive coil, 100 mm in length, 55 mm in diameter, tuned at 127.6 MHz, Flick Engineering Solutions BV, Milwaukee, USA). The room temperature during experiments was 23 °C and the mean acquisition time was limited to 20 min by the spontaneous

awakening of mice. In vivo MRI was performed on a 3T clinical system (Sigma® EXCITE® HDxT, GE Healthcare, Milwaukee, USA). The approved imaging protocol is described in Table S1. The saline solution was administered before and after MRI scanning in order to rehydrate the mice and to alleviate pain. After completion of the MRI, all mice were sacrificed in a saturated CO₂ chamber and autopsies were performed. The spleens were collected for IHC analysis and cytofluorimetric analysis.

2.5. MRI signal intensity analysis

All animal groups were imaged before and 24 h after USPIO administration as described above. Both qualitative and quantitative analyses were performed with FIESTA (Fast Imaging Employing Steady State Acquisition)-weighted sequences [33]. Quantitative analyses were expressed as signal intensity (SI) \pm standard deviation (SD) for each mouse, calculated 24 h after Feraspin XS administration, with SI being measured in the spleen, and the background noise was determined by drawing a region outside the anatomy of the mice, using an operator-defined region of interest (ROI). Circular ROIs were manually drawn and the size of the ROIs were measured by consistently acquiring the same size in the control group and in mice injected with CLL cells. After defining the ROIs, the SI in the spleen of each mouse was acquired. A circular ROI, positioned as indicated in Fig. 1, was used to calculate the signal-to-noise ratio (SNR) and Δ SNR% as follows [34,35]:

$$\text{SNR} = \text{SI}_{\text{tissue}} / \text{SI}_{\text{noise}}$$

$$\Delta\text{SNR}\% = [(\text{SNR}_{\text{afterUSPIO}}) - (\text{SNR}_{\text{beforeUSPIO}})] / \text{SNR}_{\text{beforeUSPIO}} * 100$$

2.6. Histopathological analysis

Formalin-fixed and paraffin-embedded spleen specimens were analyzed for the presence of human CLL infiltrates. The sections were deparaffinized and antigen-retrieval was performed with citrate buffer high pH for 8 min. Double staining with CD20 and Ki67 by IHC was performed by incubation (32 min at 37 °C) with a specific anti-human Ki67 antibody (MIB-1, DAKO Cytomation, dilution 1:25) and followed by addition of the polymeric detection system Ultraview Universal DAB Detection Kit (Roche, Ventana). Automatic dispensing of the second antibody (anti-CD20, L26-Roche Ventana Medical System) for 20 min at 37 °C, was followed by addition of the polymeric detection system (Ultraview Universal RED Detection Kit). An appropriate positive tissue control was used for each staining run; the negative control consisted of performing the entire IHC procedure on adjacent sections in the absence of the primary antibody. The sections were counter-stained (automatically using a user-defined protocol) with Gill's modified hematoxylin and then cover-slipped. All sections were quantitatively evaluated by two observers with an Olympus light microscope using 10 \times , 40 \times and 63 \times objectives. All the sections were analyzed under a Leica DM3000 DMLB optical microscope (Leica Microsystems, Germany) and microphotographs were collected using a Leica DFC320 DMD108 digital microimaging camera (Leica Microsystems, Germany). Perls' Prussian blue staining (Histological staining Kit, code 010236, Diapath) was performed to detect ferric (Fe³⁺) iron.

2.7. Treatment with rituximab

CLL engraftment was achieved as described above. The anti-CD20 MAb, Rituximab, was donated by the pharmacy of our Institution from remnants of the patients' sack therapy. Rituximab treatment was started using a dosage of 50 μ g/mouse/dose (four treatments every 3 days) in 200 μ l of saline solution by i.v. injection [36]. The control group was injected with an equal volume of saline solution. Basal MRI was performed after four weeks of PBMC CLL injection before starting

Table 1
Biologic and molecular characteristics of CLL patients included in the study.

Prognostic parameters	n (% of total)
CD38	
Negative	13 (72.2)
Positive	5 (27.8)
Total	18 (100)
ZAP-70	
Negative	6 (33.3)
Positive	12 (66.7)
Total	18 (100)
IGHV	
Mutated	13 (72.2)
Unmutated	5 (27.8)
Total	18 (100)
FISH	
Negative	3 (16.6)
del(13)(q14)	15 (83.3)
Trisomy 12	0 (0)
del(11)(q22.3)	0 (0)
del(17)(p13)	0 (0)
Total	18 (100)

therapy and thereafter, at therapy completion [treated mice ($n = 3$), control mice ($n = 3$)] treated with saline solution as detailed in Supplementary Fig. 1.

After three days of the last dose of antibody, animals were sacrificed in a saturated CO₂ chamber and autopsies were performed. Blood, and different samples of the spleens were evaluated by both FC and by IHC as described above. Fresh spleen tissue samples were mechanically resuspended with gentleMACS™ Dissociator (Miltenyi). The spleens were previously enzymatically digested using the Spleen Dissociation Kit (Miltenyi). The single-cell suspensions were evaluated by flow cytometry analysis with FACSCanto (BD Biosciences) and DIVA 6 (BD Biosciences) or FLOWJO V.9.8.3 software (Treestar Inc.) for: anti-human (hu) CD45 FITC, CD19 PEcy7, CD5 APC antibodies (BD Biosciences).

2.8. Statistical analysis

The Mann-Whitney U statistical test was used for testing statistical differences between more than two groups of samples and the Wilcoxon test for matched-pairs groups.

In order to identify the best cut-off value to be used in our experiments able to discriminate engrafted disease from engraftment failure, a diagnostic threshold of the relative enhancement measurements was sought by constructing receiver operating characteristic (ROC) curves. In an ROC curve, the true-positive rate (sensitivity) is plotted as a function of the false-positive rate (100 specificity) for different cut-off points. Each point on the ROC plot represents a sensitivity and specificity pair that corresponds to a particular decision threshold. The area under the ROC curve (AUROC) was analyzed to define the performance of the applied methods. The 95% confidence intervals (CI) were calculated (see Supplementary Fig. 2). A value of $P < 0.05$ was considered significant for all statistical calculations. Values are given as means \pm sem.

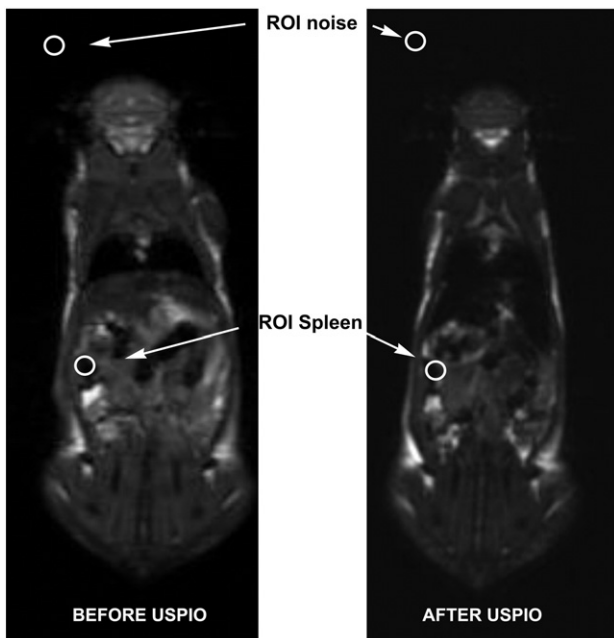


Fig. 1. Representative slices of the sequence protocol used to measure the signal intensity (SI) in tissues of interest. The regions of interest (ROIs, white circles) were drawn in the tissues of interest, spleen and in the region outside the anatomy of the mice (background noise) in order to measure the signal intensity (SI), as mean \pm standard deviation (SD) and to calculate the signal-to-noise ratio (SNR) as described in [Materials and methods](#) section.

3. Results

3.1. MRI signal measurements and histopathological correlations

NSG mice were inoculated with CLL cells and autologous T cells (defined as NSG-CLL) to favor the engraftment of the leukemic clones. USPIO-enhanced MRI was performed after two weeks and/or after four weeks in control mice (NSG-CTR, mice that did not receive any human cells), and in the NSG-CLL mice; results were expressed as Δ SNR%.

Overall, 24 h after USPIO administration we observed an increase in SI in the NSG-CLL at two weeks ($n = 41$) and at four weeks ($n = 28$) compared to the NSG-CTR mice. In Fig. 2 two representative experiments of mice analyzed at four weeks are shown. Fig. 2A and D show MRI images of NSG-CTR and NSG-CLL after 24 h of USPIO administration. Fig. 2B and E show spleen IHC analysis of the same mice displaying the absence of CD20+ cells in NSG-CTR mice and the presence of focal aggregates of CD20 positive cells in NSG-CLL spleen surrounded by CD3+ cells (not shown). In addition, Perls' Prussian blue staining (used to detect USPIO nanoparticles) indicated that ferric iron particles were excluded from the focal lesions (Fig. 2F) whereas a random distribution of USPIO nanoparticles was observed in the spleens of NSG-CTR mice (Fig. 2C).

Fig. 3 summarizes the data obtained from all NSG mice analyzed including those that did not achieve engraftment [defined as NSG non-engrafted mice (NSG-CLL-ne)] as demonstrated by the absence of CD20+ and CD3+ cells when sacrificed for IHC and FC examination of the spleen at four weeks (data not shown). In addition, at this time, their peripheral blood did not show presence of huCD45+ cells (data not shown). The Mann-Whitney U statistical test found a significant difference ($P < 0.0001$) comparing the group of NSG-CTR mice to NSG-CLL mice at four weeks. Interestingly, a significant difference was also observed when comparing the NSG-CLL mice at two weeks ($P < 0.0001$) (Fig. 3A). Significant differences were also observed comparing measurements of the same NSG-CLL mice at two and four weeks from PBMC CLL injection (Fig. 3B).

3.2. Cut-off determination

ROC analysis was utilized in order to identify the best cut-off for Δ SNR% to be used in our experiments for discriminating NSG-CLL mice from NSG-CTR. The best cut-off values were -4.8 (AUC = 0.97 [95% CI 0.92–1.0]) at 2 weeks and -6.0 (AUC = 0.99 [95% CI 0.97–1.0]) at 4 weeks (Supplementary Fig. 2).

3.3. Measurements of CLL disease regression in NSG engrafted mice

In order to investigate whether this technique would be useful for evaluating CLL disease regression upon therapy, NSG-CLL mice were treated with rituximab. Four mice were treated four times at three-day intervals using a dosage of 50 μ g/mouse, and compared with five mice injected with an identical volume of saline solution (mock-treated mice).

MRI was carried out in three mock-treated NSG-CLL mice and in three NSG-CLL treated with rituximab and the relative signal measurements obtained at therapy start were compared with those obtained at therapy completion (Fig. 4). The Δ SNR% values showed a clear reduction in animals treated with rituximab compared to mock-treated animals (Fig. 4C and D). Differences did not reach statistical significance likely due to the limited number of animals investigated. The general strategy of treatments and spleen evaluations is shown in Supplementary Fig. 1.

Spleen IHC analysis for expression of CD20, Ki67, CD3, and Perls' Prussian blue staining of mice treated with rituximab or with saline solution are shown in Fig. 5A and B. Spleen tissue IHC indicates that the decreased MRI signal observed in rituximab-treated mice correlates

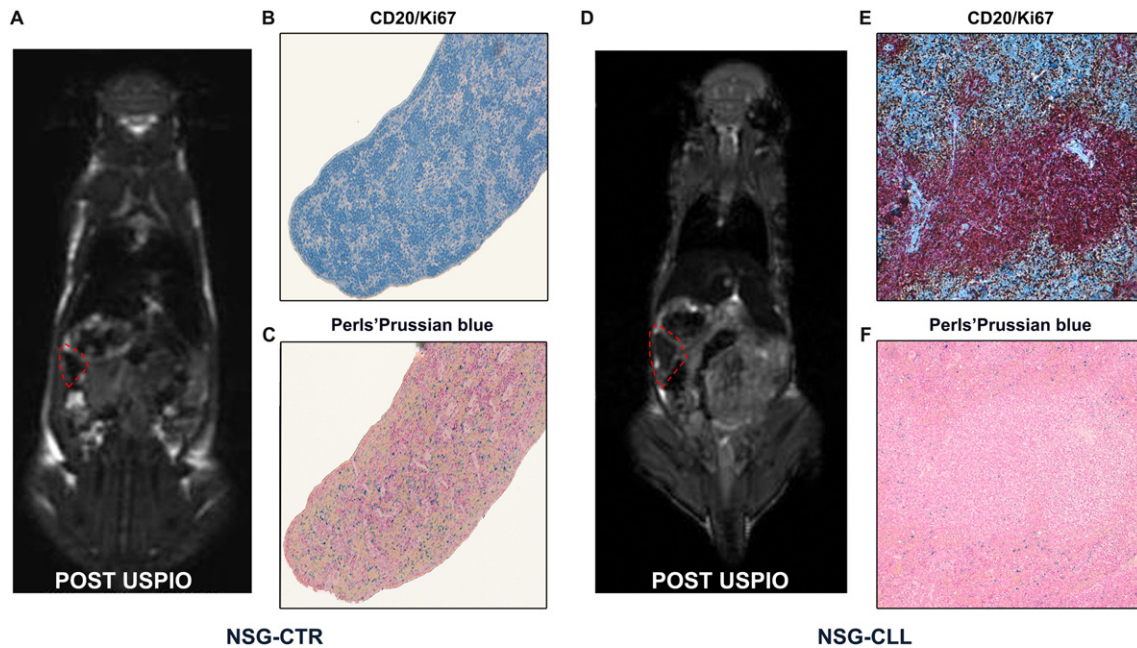


Fig. 2. Magnetic resonance image signal determination and histological analysis in control (NSG-CTR) compared to engrafted (NSG-CLL) mice. The figure shows representative in vivo USPIO magnetic resonance images (MRI) obtained after 24 h of USPIO administration in a NSG-CTR (A) and NSG-CLL mouse (D). The position of the spleen is indicated by the red outline. Matched histology sections (magnification, 100 \times) show the absence (B) or the presence (E) of CD20 (red) and Ki67 (brown) positive cells; Perls' Prussian blue ferric iron staining (C and F) allows the detection of USPIO nanoparticles.

with the loss of CD20 + cells organized in follicles (clearly observable in the spleen of mock-treated NSG-CLL mice). In addition, follicle residues are clearly infiltrated by T cells and USPIO nanoparticles (Fig. 5B). Spleen FC analysis showed that huCD45/CD19/CD5 + cells were significantly less represented in rituximab-treated mice compared to mock-treated mice. In contrast, the percentage of CD3-positive cells was significantly higher in mock-treated mice, compared to NSG-CLL mice treated with rituximab (Fig. 5C and D).

4. Discussion

MRI is a well-suited imaging modality for noninvasive cell tracking because of its tissue characterization, excellent image quality, and high spatial resolution, although currently nuclear imaging is a more sensitive technique. Furthermore, MRI advantages include lack of ionizing radiation, flexible image contrast, and the ability to assess localized function, perfusion, and necrosis. MRI offers the potential of tracking cells in vivo using innovative approaches and contrast media as well as cell labeling and image acquisition.

In this study, we used MRI to track CLL cell seeding in a xenograft mouse model. We first observed that changes in spleen organization could be identified four weeks after CLL cell inoculation and analyzed by means of a high field 3T clinical scanner and USPIO nanoparticles. We used FIESTA acquisition because our previous observations indicated that it was suitable and also high sensitive in conditions of very low iron oxide nanoparticle concentrations [37] rendering this sequence the best option for the study of single cell iron oxide nanoparticles [33]. Histologic examination of the same spleens confirmed the presence of CD20 + nodular structures (see Fig. 2) surrounded by CD3 + cells (not shown). In addition, Perls' Prussian blue staining demonstrated that iron particles were excluded from the nodular areas occupied by lymphoid cells, providing a rational explanation for the MRI signals observed. The combination of extracellular with intracellular iron oxide nanoparticles compartmentalization within the CLL spleen, affected iron oxide proton relaxivity, which sometimes resulted in an increase rather than in the usual and expected SI decrease. This high T2-USPIO effect has also been reported by Simon G.H. et al. [38].

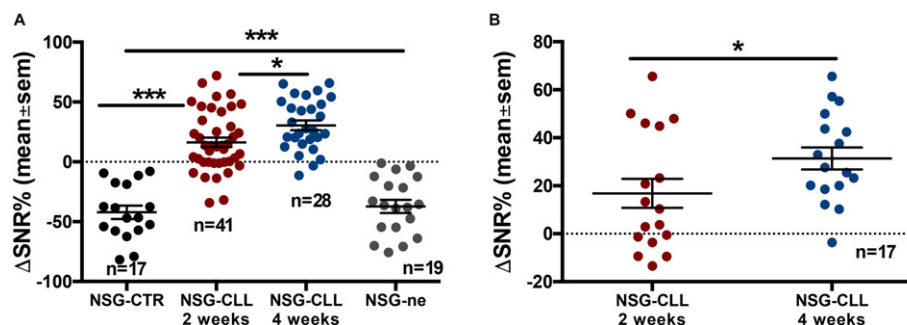


Fig. 3. Comparison of magnetic resonance image signal intensity change in the spleen of control (NSG-CTR), engrafted (NSG-CLL) at 2 and 4 weeks and non-engrafted (NSG-ne) mice. (A) The scatter dot plot represents percentage signal-to-noise ratio change (Δ SNR%) of the MRI acquisition analysis comparing NSG-CLL mice at 2 weeks (red dots) and 4 weeks (blue dots) from peripheral blood mononuclear cell (PBMC) CLL injection, NSG-CTR mice (black dots) and NSG-ne (grey dots, evaluated at 4 weeks from PBMC CLL injection). Values of Δ SNR% are expressed as mean \pm sem. NSG-CTR mice: -42.16 ± 5.6 ; NSG-CLL at 2 weeks: $+16.32 \pm 3.95$; NSG-CLL at 4 weeks: $+30.49 \pm 4.0$; NSG-CLL-ne mice: -37.21 ± 5.5 . Statistical comparisons were carried out using the Mann-Whitney *U* test. A P-value < 0.0001 is indicated by *** and P = 0.017 by *. (B) Comparison of MRI signals detected in the same mice 2 weeks (red dots) or 4 weeks (blue dots) from PBMC CLL injection (P = 0.02 Wilcoxon-matched pair test).

FC analyses of splenic cell suspensions showed that huCD45 + cells were comprised of CD19/CD5 + cells and a variable proportion of CD3 + cells (not shown). An analogous approach of using FC to measure circulating T and B cells can be employed to assess the take of CLL engraftment in NSG mice although this method may be misleading, as leukemic cells can be difficult to track due to their extremely low number in peripheral blood. In addition, when tracked, the leukemic cells may represent cells merely surviving after the injection. Indeed, 17/19 non engrafted mice showed the presence of huCD45/CD19/CD5 cells (representing the bona fide leukemic clone). In contrast USPIO enhanced MRI spleen analysis was able to consistently assess the engraftment of CLL cells two weeks after their injection (see Fig. 3), as could also be confirmed by IHC evaluation.

A reliable assessment of CLL engraftment two weeks after leukemic clone inoculation is most advantageous given that this animal model does not allow long term persistence/expansion of the inoculated leukemic cells beyond 6–8 weeks. Thereafter, mice can develop a graft-versus-host disease that may cause also the reduction and even disappearance of the leukemic cells [11]. In addition, leukemic cells

can mature into plasmablasts/plasma cells [39]. The above limitations might impair the experimental data, particularly when drug treatments are evaluated, because this time-frame may not be sufficient to provide information on the long term effect of drugs.

We also report the possibility of identifying a cut-off value for $\Delta\text{SNR}\%$ able of discriminating NSG-CLL from NSG-CTR or NSG-ne mice. A similar cut-off value was used to identify the different disease extension at two and four weeks after inoculum in NSG-CLL mice. The identification of a relatively precise cut-off value allows investigators to reliably define when a single mouse can be considered engrafted or not and make decisions regarding the subsequent experimental procedures. This analysis however requires standardization on the instrument(s) used for the image acquisition.

USPIO-enhanced MRI also was able to detect CLL disease regression after rituximab treatment of engrafted mice. MRI images, acquired before and following treatment, MRI images detected definite changes with an inversion of the $\Delta\text{SNR}\%$ value (see Fig. 4). IHC showed a radical change in the architecture of the spleen of treated animals compared to controls. Following treatment, lymphoid infiltrates were mainly represented by unorganized T lymphocytes with the loss of the typical

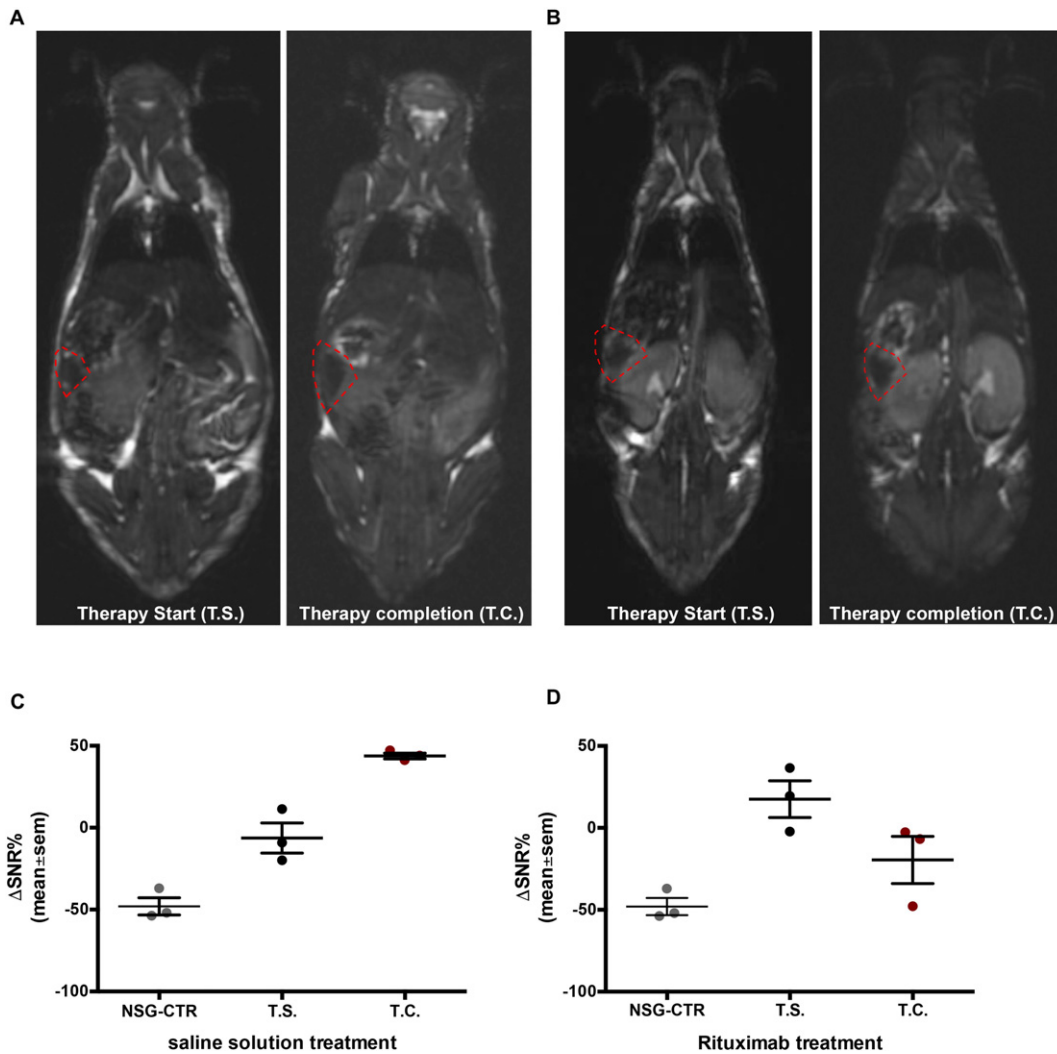


Fig. 4. Representative experiment of treatment with rituximab. The figure shows a representative in vivo USPIO magnetic resonance image (MRI) obtained 24 h after USPIO administration in a NSG-CLL mouse treated with saline solution (A) and a NSG-CLL mouse treated with rituximab (B). The position of the spleen is indicated by the red outline. MRI images show acquisition at therapy start (T.S.) and at therapy completion (T.C.). The scatter dot plots (C) and (D) display data for each mouse and percentage signal-to-noise ratio change ($\Delta\text{SNR}\%$) mean values are calculated for each treatment-mice group ($n = 3$) and the control NSG-CTR group.

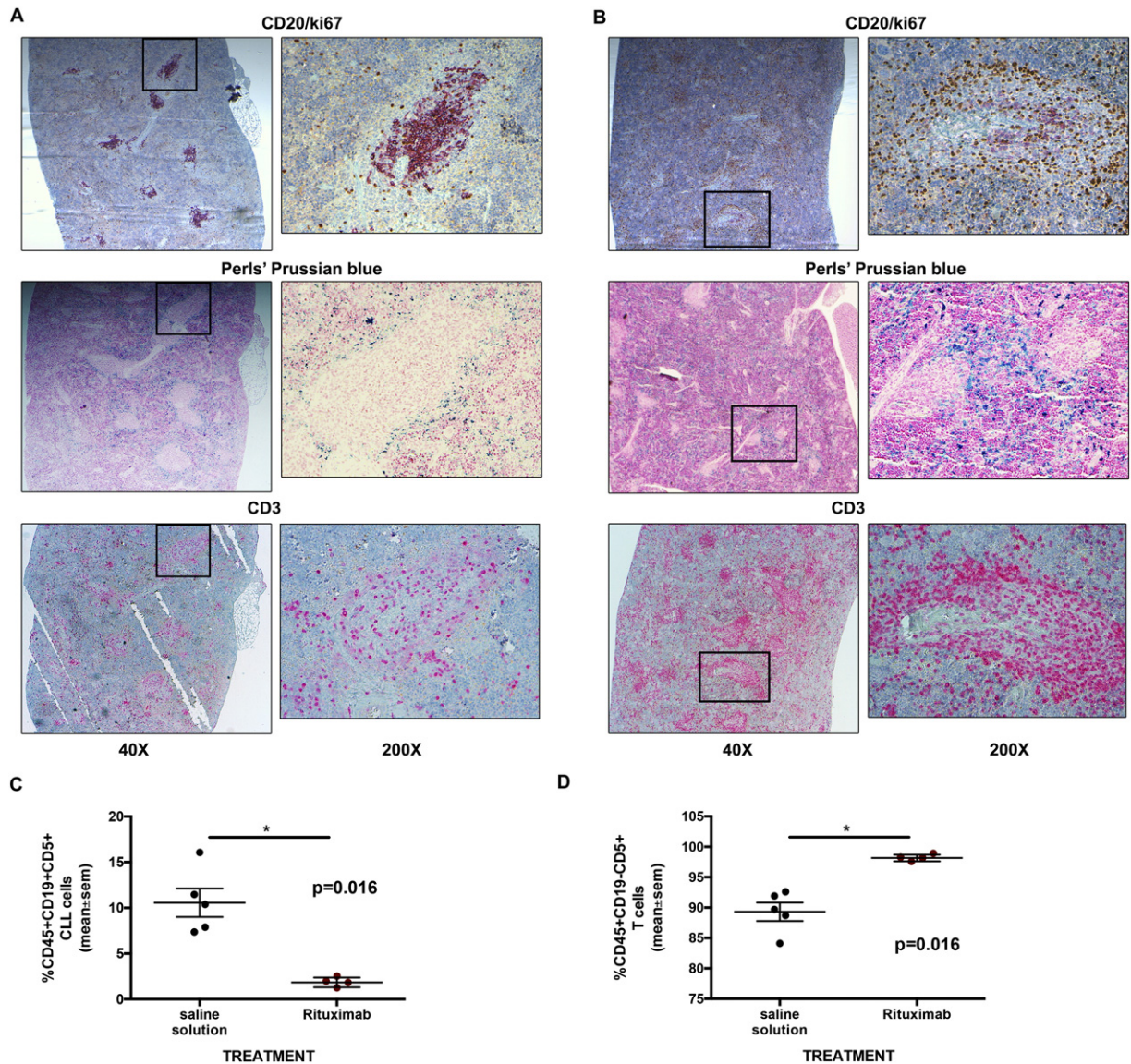


Fig. 5. Representative immunohistochemistry and flow cytometry analysis of mouse spleens from a rituximab experiment. The figure shows the histologic analysis carried out for the presence of CLL cells (CD20, red), proliferating cells (Ki67, brown), T cells (CD3, red) and USPIO nanoparticles (Perls' Prussian blue) in the NSG-CLL mice treated with saline solution (A) and in NSG-CLL mice treated with rituximab (B). Magnification 40× (left panels) and 200× (right panels). In panels C and D, the scatter-plots show the presence of CLL cells and autologous T-cells, respectively, evaluated by flow cytometry (CD45+/CD19+/CD5+ or CD45+/CD19-/CD5+), indicating a significant decrease of the percentage of CLL cells in the group of mice treated with rituximab (n = 4) compared to the control group treated with saline solution (n = 5). Statistical comparisons were carried out by Wilcoxon test.

CD20 + nodular areas. Tissue Perls' Prussian blue stain confirmed the diverse disposition of USPIO nanoparticles (Fig. 5). Thus, this technique clearly distinguishes between the different types of lymphoid infiltrates on the basis of their organization.

Another point that should be underlined is that the use of this technique limits the number of animals to be tested and sacrificed. This is important for several reasons: first, it requires fewer leukemic cells for injection thus sparing other cells for additional experimental procedures. Although a large number of CLL cells can generally be recovered from CLL patients, a typical experiment may require more than half a billion cells, a quantity often obtained from selected patients only. Second, this approach facilitates clearance of animal experimentation protocols by ethics committees. Currently, animal testing regulations pay increasingly more attention to the procedures and the experimental settings applied, encouraging the use of methods that limit animal sacrifice (and ultimately suffering of animals). A related point is the control of experimental variability, as only animals with evidence of disease are used to complete the experimental procedures with no additional trauma.

5. Conclusions

In summary, we present here an *in vivo* imaging approach for monitoring CLL disease evolution in a pre-clinical model of CLL using xenografted immunodeficient mice. MRI is a valuable, non-invasive modality to predict progression in our CLL-model. In addition, by anticipating the timing of CLL engraftment, applications of MRI may include *in vivo* monitoring of new therapies thus allowing a longer temporal window to evaluate treatment efficacy and the possible emergence of therapy resistant clones.

Finally, this method may have potential application in the clinical setting and may be used to evaluate organ involvement in CLL disease, allowing more accurate staging without exposing patients to additional radiation.

Conflicts of interest

The authors declared no conflict of interest.

Funding

This work was supported by: Associazione Italiana per la Ricerca sul Cancro (AIRC) [Grant 5 x mille n. 9980 (to M.F., F.M. and A.N.); AIRC I.G. [n. 14326 (to M.F.)], [n. 10136 and 16722 (A.N.)], [n. 15426 (to F.F.)]. AIRC and Fondazione CaRiCal co-financed Multi Unit Regional Grant 2014 [n. 16695 (to F.M.)]. Ministry of Health, Italy 5x1000 funds (to F.F.). A.G.R. was supported by Associazione Italiana contro le Leucemie-Linfomi-Mielomi (AIL) Cosenza - Fondazione Amelia Scorza (FAS). S.M., C.M., F.V., L.E., and S.B., were supported by AIRC.

Acknowledgements

In addition to the listed Authors, the following Investigators participated in this study as part of the GISL - Gruppo Italiano Studio Linfomi: Gianni Quintana, Divisione di Ematologia, Presidio Ospedaliero "A.Perrino", Brindisi; Giovanni Bertoldo, Dipartimento di Oncologia, Ospedale Civile, Noale, Venezia; Paolo Di Tonno, Dipartimento di Ematologia, Venere, Bari; Robin Foà and Francesca R Mauro, Divisione di Ematologia, Università La Sapienza, Roma; Nicola Di Renzo, Unità di Ematologia, Ospedale Vito Fazzi, Lecce; Maria Cristina Cox, Ematologia, A.O. Sant'Andrea, Università La Sapienza, Roma; Stefano Molica, Dipartimento di Oncologia ed Ematologia, Pugliese-Ciaccio Hospital, Catanzaro; Attilio Guarini, Unità di Ematologia e Trapianto di Cellule Staminali, Istituto di Oncologia "Giovanni Paolo II", Bari; Antonio Abbadessa, U.O.C. di Oncoematologia Ospedale "S. Anna e S. Sebastiano", Caserta; Francesco Iuliano, U.O.C. di Oncologia, Ospedale Giannettasio, Rossano Calabro, Cosenza; Omar Racchi, Ospedale Villa Scassi Sampierdarena, Genova; Mauro Spriano, Ematologia, A.O. San Martino, Genova; Felicetto Ferrara, Divisione di Ematologia, Ospedale Cardarelli, Napoli; Monica Crugnola, Ematologia, CTMO, Azienda Ospedaliera Universitaria di Parma; Alessandro Andriani, Dipartimento di Ematologia, Ospedale Nuovo Regina Margherita, Roma; Nicola Cascavilla, Unità di Ematologia e Trapianto di Cellule Staminali, IRCCS Ospedale Casa Sollievo della Sofferenza, San Giovanni Rotondo; Lucia Ciuffreda, Unità di Ematologia, Ospedale San Nicola Pellegrino, Trani; Graziella Pinotti, U.O. Oncologia Medica, Ospedale di Circolo Fondazione Macchi, Varese; Anna Pascarella, Unità Operativa di Ematologia, Ospedale dell'Angelo, Venezia-Mestre; Maria Grazia Lipari, Divisione di Ematologia, Ospedale Policlinico, Palermo, Francesco Merli, Unità Operativa di Ematologia, A.O.S. Maria Nuova, Reggio Emilia; Luca Baldini Istituto di Ricovero e Cura a Carattere Scientifico Cà Granda-Maggiore Policlinico, Milano; Caterina Musolino, Divisione di Ematologia, Università di Messina; Agostino Cortelezzi, Ematologia and CTMO, Foundation IRCCS Ca' Granda Ospedale Maggiore Policlinico, Milano; Francesco Angrilli, Dipartimento di Ematologia, Ospedale Santo Spirito, Pescara; Ugo Consoli, U.O.S. di Emato-Oncologia, Ospedale Garibaldi-Nesima, Catania; Gianluca Festini, Centro di Riferimento Ematologico-Seconda Medicina, Azienda Ospedaliero-Universitaria, Ospedali Riuniti, Trieste; Giuseppe Longo, Unità di Ematologia, Ospedale San Vincenzo, Taormina; Daniele Vallisa and Annalisa Arcari, Unità di Ematologia, Dipartimento di Onco-Ematologia, Guglielmo da Saliceto Hospital, Piacenza; Francesco Di Raimondo and Annalisa Chiarenza, Divisione di Ematologia, Università di Catania Ospedale Ferrarotto, Catania; Iolanda Vincelli, Unità di Ematologia, A.O. of Reggio Calabria; Donato Mannina, Divisione di Ematologia, Ospedale Papardo, Messina, Italy.

We would thank Gerolama Buconte for her very helpful technical support for the MRI acquisition and Dr. Marcella Bado, Dr. Barbara Rebesco for providing rituximab preparations.

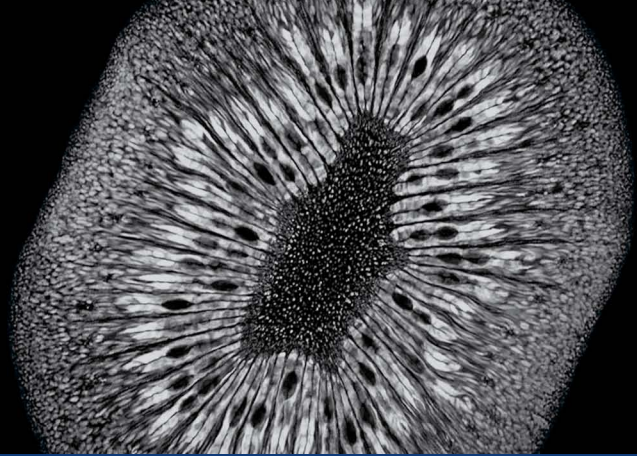
Appendix A. Supplementary data

Supplementary data to this article can be found online at <http://dx.doi.org/10.1016/j.clim.2016.07.013>.

References

- [1] N. Chiorazzi, K.R. Rai, M. Ferrarini, Chronic lymphocytic leukemia, *N. Engl. J. Med.* 352 (2005) 804–815.
- [2] M.J. Keating, Chronic lymphocytic leukemia, *Semin. Oncol.* 26 (1999) 107–114.
- [3] M. Hallek, B.D. Cheson, D. Catovsky, F. Caligaris-Cappio, G. Dighiero, H. Dohner, P. Hillmen, M.J. Keating, E. Montserrat, K.R. Rai, T.J. Kipps, L. International Workshop on Chronic Lymphocytic, Guidelines for the diagnosis and treatment of chronic lymphocytic leukemia: a report from the International Workshop on Chronic Lymphocytic Leukemia updating the National Cancer Institute-Working Group 1996 guidelines, *Blood* 111 (2008) 5446–5456.
- [4] S. Kempin, Update on chronic lymphocytic leukemia: overview of new agents and comparative analysis, *Curr. Treat. Options in Oncol.* 14 (2013) 144–155.
- [5] S.E. Herman, A. Wiestner, Preclinical modeling of novel therapeutics in chronic lymphocytic leukemia: the tools of the trade, *Semin. Oncol.* 43 (2016) 222–232.
- [6] R. Bichi, S.A. Shinton, E.S. Martin, A. Koval, G.A. Calin, R. Cesari, G. Russo, R.R. Hardy, C.M. Croce, Human chronic lymphocytic leukemia modeled in mouse by targeted TCL1 expression, *Proc. Natl. Acad. Sci. U. S. A.* 99 (2002) 6955–6960.
- [7] J.M. Zapata, M. Krajewska, H.C. Morse III, Y. Choi, J.C. Reed, TNF receptor-associated factor (TRAF) domain and Bcl-2 cooperate to induce small B cell lymphoma/chronic lymphocytic leukemia in transgenic mice, *Proc. Natl. Acad. Sci. U. S. A.* 101 (2004) 16600–16605.
- [8] U. Klein, M. Lia, M. Crespo, R. Siegel, Q. Shen, T. Mo, A. Ambesi-Impiombato, A. Califano, A. Migliazza, G. Bhagat, R. Dalla-Favera, The DLEU2/miR-15a/16-1 cluster controls B cell proliferation and its deletion leads to chronic lymphocytic leukemia, *Cancer Cell* 17 (2010) 28–40.
- [9] V. Shukla, S. Ma, R.R. Hardy, S.S. Joshi, R. Lu, A role for IRF4 in the development of CLL, *Blood* 122 (2013) 2848–2855.
- [10] J. Durig, P. Ebeling, F. Grabelius, U.R. Sorg, M. Mollmann, P. Schutt, J. Gothert, L. Sellmann, S. Seeber, M. Flasshove, U. Dührsen, T. Moritz, A novel nonobese diabetic/severe combined immunodeficient xenograft model for chronic lymphocytic leukemia reflects important clinical characteristics of the disease, *Cancer Res.* 67 (2007) 8653–8661.
- [11] D. Bagnara, M.S. Kaufman, C. Calissano, S. Marsilio, P.E. Patten, R. Simone, P. Chum, X.J. Yan, S.L. Allen, J.E. Kolitz, S. Baskar, C. Rader, H. Mellstedt, H. Rabbani, A. Lee, P.K. Gregersen, K.R. Rai, N. Chiorazzi, A novel adoptive transfer model of chronic lymphocytic leukemia suggests a key role for T lymphocytes in the disease, *Blood* 117 (2011) 5463–5472.
- [12] S.E. Herman, X. Sun, E.M. McAuley, M.M. Hsieh, S. Pittaluga, M. Raffeld, D. Liu, K. Keyvanfar, C.M. Chapman, J. Chen, J.J. Buggy, G. Aue, J.F. Tisdale, P. Perez-Galan, A. Wiestner, Modeling tumor-host interactions of chronic lymphocytic leukemia in xenografted mice to study tumor biology and evaluate targeted therapy, *Leukemia* 27 (2013) 2311–2321.
- [13] B.H. Mavromatis, B.D. Cheson, Pre- and post-treatment evaluation of non-Hodgkin's lymphoma, *Best Pract. Res. Clin. Haematol.* 15 (2002) 429–447.
- [14] B.D. Cheson, J.M. Bennett, M. Grever, N. Kay, M.J. Keating, S. O'Brien, K.R. Rai, National Cancer Institute-sponsored Working Group guidelines for chronic lymphocytic leukemia: revised guidelines for diagnosis and treatment, *Blood* 87 (1996) 4990–4997.
- [15] B.F. Eichhorst, K. Fischer, A.M. Fink, T. Elter, C.M. Wendtner, V. Goede, M. Bergmann, S. Stilgenbauer, G. Hopfinger, M. Ritgen, J. Bahlo, R. Busch, M. Hallek, C.L.L.S.G. German, Limited clinical relevance of imaging techniques in the follow-up of patients with advanced chronic lymphocytic leukemia: results of a meta-analysis, *Blood* 117 (2011) 1817–1821.
- [16] J.C. Byrd, J.M. Pagel, F.T. Awan, A. Forero, I.W. Flinn, D.P. Deauna-Limayo, S.E. Spurgeon, L.A. Andritsos, A.K. Gopal, J.P. Leonard, A.J. Eisenfeld, J.E. Bannink, S.C. Stromatt, R.R. Furman, A phase I study evaluating the safety and tolerability of otlertuzumab, an anti-CD37 mono-specific ADAPTIR therapeutic protein in chronic lymphocytic leukemia, *Blood* 123 (2014) 1302–1308.
- [17] M. Gentile, G. Cutrona, S. Molica, F. Ilariucci, F.R. Mauro, N. Di Renzo, F. Di Raimondo, I. Vincelli, K. Todorci, S. Matis, C. Musolino, S. Fabris, M. Lionetti, L. Levato, S. Zupo, F. Angrilli, U. Consoli, G. Festini, G. Longo, A. Cortelezzi, P. Musto, M. Federico, A. Neri, M. Ferrarini, F. Morabito, Prospective validation of predictive value of abdominal computed tomography scan on time to first treatment in Rai 0 chronic lymphocytic leukemia patients: results of the multicenter O-CLL1-GISL study, *Eur. J. Haematol.* 96 (2016) 36–45.
- [18] J.M. Froehlich, M. Triantafyllou, A. Fleischmann, P. Vermathen, G.N. Thalmann, H.C. Thoeny, Does quantification of USPIO uptake-related signal loss allow differentiation of benign and malignant normal-sized pelvic lymph nodes? *Contrast Media Mol. Imaging* 7 (2012) 346–355.
- [19] R. Weissleder, G. Elizondo, J. Wittenberg, C.A. Rabito, H.H. Bengel, L. Josephson, Ultrasound superparamagnetic iron oxide: characterization of a new class of contrast agents for MR imaging, *Radiology* 175 (1990) 489–493.
- [20] R. Weissleder, P.F. Hahn, D.D. Stark, G. Elizondo, S. Saini, L.E. Todd, J. Wittenberg, J.T. Ferrucci, Superparamagnetic iron oxide: enhanced detection of focal splenic tumors with MR imaging, *Radiology* 169 (1988) 399–403.
- [21] Y.Z. Wadghiri, J. Li, J. Wang, D.M. Hoang, Y. Sun, H. Xu, W. Tsui, Y. Li, A. Boutajangout, A. Wang, M. de Leon, T. Wisniewski, Detection of amyloid plaques targeted by bi-functional USPIO in Alzheimer's disease transgenic mice using magnetic resonance microimaging, *PLoS One* 8 (2013) e57097.
- [22] A. Crimi, O. Commowick, A. Maarouf, J.C. Ferre, E. Bannier, A. Tourbah, I. Berry, J.P. Ranjeva, G. Edan, C. Barillot, Predictive value of imaging markers at multiple sclerosis disease onset based on gadolinium- and USPIO-enhanced MRI and machine learning, *PLoS One* 9 (2014) e93024.
- [23] T. Tourdias, S. Roggerone, M. Filippi, M. Kanagaki, M. Rovaris, D.H. Miller, K.G. Petry, B. Brochet, J.P. Pruvo, E.W. Radue, V. Dousset, Assessment of disease activity in

- multiple sclerosis phenotypes with combined gadolinium- and superparamagnetic iron oxide-enhanced MR imaging, *Radiology* 264 (2012) 225–233.
- [24] M. Marinescu, F. Chauveau, A. Durand, A. Riou, T.H. Cho, A. Dencausse, S. Ballet, N. Nighoghossian, Y. Berthezene, M. Wiart, Monitoring therapeutic effects in experimental stroke by serial USPIO-enhanced MRI, *Eur. Radiol.* 23 (2013) 37–47.
- [25] Y.L. Wu, Q. Ye, K. Sato, L.M. Foley, T.K. Hitchens, C. Ho, Noninvasive evaluation of cardiac allograft rejection by cellular and functional cardiac magnetic resonance, *JACC Cardiovasc. Imaging* 2 (2009) 731–741.
- [26] A.M. Lutz, C. Seemayer, C. Corot, R.E. Gay, K. Goepfert, B.A. Michel, B. Marincek, S. Gay, D. Weishaupt, Detection of synovial macrophages in an experimental rabbit model of antigen-induced arthritis: ultrasmall superparamagnetic iron oxide-enhanced MR imaging, *Radiology* 233 (2004) 149–157.
- [27] K. Tsuchiya, N. Nitta, A. Sonoda, H. Otani, M. Takahashi, K. Murata, M. Shiomi, Y. Tabata, S. Nohara, Atherosclerotic imaging using 4 types of superparamagnetic iron oxides: new possibilities for mannan-coated particles, *Eur. J. Radiol.* 82 (2013) 1919–1925.
- [28] C. Bremer, T. Allkemper, J. Baermig, P. Reimer, RES-specific imaging of the liver and spleen with iron oxide particles designed for blood pool MR-angiography, *J. Magn. Reson. Imaging* 10 (1999) 461–467.
- [29] S. Metz, G. Bonaterre, M. Rudelius, M. Settles, E.J. Rummeny, H.E. Daldrup-Link, Capacity of human monocytes to phagocytose approved iron oxide MR contrast agents in vitro, *Eur. Radiol.* 14 (2004) 1851–1858.
- [30] J. Gellissen, C. Axmann, A. Prescher, K. Bohndorf, K.P. Lodemann, Extra- and intracellular accumulation of ultrasmall superparamagnetic iron oxides (USPIO) in experimentally induced abscesses of the peripheral soft tissues and their effects on magnetic resonance imaging, *Magn. Reson. Imaging* 17 (1999) 557–567.
- [31] F. Morabito, G. Cutrona, M. Gentile, S. Fabris, S. Matis, E. Vigna, K. Todoerti, M. Colombo, A.G. Recchia, S. Bossio, L. De Stefano, F. Ilariucci, A. Cortelezzi, U. Consoli, I. Vincelli, E.A. Pesce, C. Musolino, S. Molica, F. Di Raimondo, A. Neri, M. Ferrarini, Is ZAP70 still a key prognostic factor in early stage chronic lymphocytic leukaemia? Results of the analysis from a prospective multicentre observational study, *Br. J. Haematol.* 168 (2015) 455–459.
- [32] F. Morabito, L. Mosca, G. Cutrona, L. Agnelli, G. Tuana, M. Ferracin, B. Zagatti, M. Lionetti, S. Fabris, F. Maura, S. Matis, M. Gentile, E. Vigna, M. Colombo, C. Massucco, A.G. Recchia, S. Bossio, L. De Stefano, F. Ilariucci, C. Musolino, S. Molica, F. Di Raimondo, A. Cortelezzi, P. Tassone, M. Negrini, S. Monti, D. Rossi, G. Gaidano, M. Ferrarini, A. Neri, Clinical monoclonal B lymphocytosis versus Rai 0 chronic lymphocytic leukemia: a comparison of cellular, cytogenetic, molecular, and clinical features, *Clin. Cancer Res.* 19 (2013) 5890–5900.
- [33] P. Foster-Gareau, C. Heyn, A. Alejski, B.K. Rutt, Imaging single mammalian cells with a 1.5 T clinical MRI scanner, *Magn. Reson. Med.* 49 (2003) 968–971.
- [34] S.D. Wolff, R.S. Balaban, Assessing contrast on MR images, *Radiology* 202 (1997) 25–29.
- [35] H.E. Daldrup-Link, M. Rudelius, G. Piontek, S. Metz, R. Brauer, G. Debus, C. Corot, J. Schlegel, T.M. Link, C. Peschel, E.J. Rummeny, R.A. Oostendorp, Migration of iron oxide-labeled human hematopoietic progenitor cells in a mouse model: in vivo monitoring with 1.5-T MR imaging equipment, *Radiology* 234 (2005) 197–205.
- [36] K.K. Wong, F. Brennehan, A. Chesney, D.E. Spaner, R.M. Gorczynski, Soluble CD200 is critical to engraft chronic lymphocytic leukemia cells in immunocompromised mice, *Cancer Res.* 72 (2012) 4931–4943.
- [37] G. Baio, M. Fabbi, D. de Totero, S. Ferrini, M. Cilli, L.E. Derchi, C.E. Neumaier, Magnetic resonance imaging at 1.5 T with immunospecific contrast agent in vitro and in vivo in a xenotransplant model, *MAGMA* 19 (2006) 313–320.
- [38] G.H. Simon, J. Bauer, O. Saborovski, Y. Fu, C. Corot, M.F. Wendland, H.E. Daldrup-Link, T1 and T2 relaxivity of intracellular and extracellular USPIO at 1.5 T and 3 T clinical MR scanning, *Eur. Radiol.* 16 (2006) 738–745.
- [39] P.E. Patten, G. Ferrer, S.S. Chen, R. Simone, S. Marsilio, X.J. Yan, Z. Gitto, C. Yuan, J.E. Kolitz, J. Barrientos, S.L. Allen, K.R. Rai, T. MacCarthy, C.C. Chu, N. Chiorazzi, Chronic lymphocytic leukemia cells diversify and differentiate in vivo via a nonclassical Th1-dependent, Bcl-6-deficient process, *JCI Insight* 1 (2016).



Monitoring of leukemia using USPIO

Magnetic resonance imaging (MRI) of chronic lymphocytic leukemia (CLL) by ultrasmall superparamagnetic iron oxide (USPIO) nanoparticles

Gabriella Baio*, Giovanna Cutrona, Serena Matis, Carlotta Massucco, Simona Boccardo, Francesca Valdora, Laura Emionite, Michele Cilli, Sandra Salvi, Carlo Emanuele Neumaier, and Manlio Ferrarini
IRCCS University San Martino Hospital-National Cancer Institute-IST, Largo Rosanna Benzi 10, 16132 Genoa, Italy

*Corresponding author (gabriella.baio@hsanmartino.it)

Introduction

The efficacy of iron oxide nanoparticles as a macrophage-monocytic phagocytic system (MMPS)-specific contrast agent for liver, spleen, and lymph node MRI has been demonstrated in experimental and clinical studies. Several studies have shown that these particles can significantly improve the detection and characterization of focal lesions within these organs¹. Due to their size-dependent properties and their applicability in non-invasive imaging methods, these materials are promising candidates for research, diagnostic, and therapeutic applications in various fields such as cancer, neurodegenerative diseases (e.g. multiple sclerosis, stroke) as well as inflammatory diseases (e.g. rheumatoid arthritis, atherosclerosis)². In our study, we focused on a specific mouse xenogeneic transplantation model, NOD/LtSz-scid/scid (NOD/SCID), of chronic lymphocytic leukemia (CLL)³. CLL is a type of slow growing leukaemia, characterized by a gradual increase in the number of B lymphocytes, first in the blood and bone marrow and, as the disease progresses, in the lymph nodes, liver, and spleen. In particular, computed tomography (CT) is used as the first-line modality for imaging of lymphoid malignancies but, specifically for CLL, the role of CT has not yet been clearly defined⁴. In order to prevent the exposure of the CLL patient to irradiation, we aimed to establish a specific MRI method to better visualize the presence of the disease within the spleen using a pre-clinical setting.

Materials and methods

FeraSpin™ XS consisting of USPIO nanoparticles, with a mean particle size of 10–20 nm, was used as MRI contrast agent. Upon intravenous injection, FeraSpin XS nanoparticles circulate in the bloodstream and are taken up by macrophages, including those in the liver and spleen (reticulo-endothelial system, RES). Two groups of mice were injected with the contrast agent: one group of healthy NOD/LtSz-scid/scid (NOD/SCID) mice (NSG; n=2) and another group of NOD/SCID mice injected with chronic MG0248-CLL cells (NSG-CLL; n=4), which served as a xenogeneic mouse transplantation model³. Scanning was performed on a clinical 3T MR scanner (Signa® EXCITE® HDxT, GE Healthcare, Milwaukee, USA) and the mice were positioned in a prototype coil (linear birdcage transmit/receive coil, 100 mm length, 55 mm diameter, tuned at 127.6 MHz, Flick Engineering Solutions B.V., Netherlands; General Electric Company) placed on a warm plate to prevent animal hypothermia. Imaging was performed on both animal groups before and 24 hours after administration of 100 µL/25 g mouse of FeraSpin XS, corresponding to a dose of 40 µmol Fe/kg body weight. In the healthy animal group (NSG) imaging was also performed 6 days and 14 days after contrast agent injection. Both qualitative and quantitative analyses were performed with a FIESTA sequence (fast imaging employing steady state acquisition) as described in literature⁵. Regions of interest (ROI) were defined and the signal intensities in the liver and spleen of each mouse were calculated. Histological analysis was performed according to standard techniques on the NSG and NSG-CLL mice, 28 days and 6 days post injection (p.i.) of FeraSpin XS, respectively. Immunohistochemistry of the spleen using anti-human-CD20 antibody was performed to demonstrate the human CD20⁺ CLL cell aggregates. Perls' Prussian blue staining was conducted for the detection of iron. A quantitative assessment by estimation of iron-positive cells was performed using an Olympus BX41 microscope.

Results and discussion

NSG mice (control)

In the NSG mice, at 24 hours p.i. of FeraSpin XS, a strong decrease in signal intensity (SI) in the liver (80%) and spleen (50%) has been observed (figure 1A,B). In order to investigate the time-dependent SI in the healthy animal group, we repeated the imaging acquisition at 6 and 14 days after contrast agent administration. While the SI of the liver was found to increase and reach a baseline level at 14 days p.i., the SI of the spleen remained constant over the imaging time period. Additionally, we performed a histopathological analysis on the liver and spleen by Perl's Prussian blue staining at 28 days p.i. of FeraSpin XS. Only very few iron oxide nanoparticles were observed in both organs indicating that the nanoparticles are cleared from the liver and spleen in the healthy animal group within one month.

NSG-CLL mice (tumor)

In the NSG-CLL mice, at 24 hours p.i. of FeraSpin XS, a significant decrease in SI (60%) was observed in the liver but, in comparison, only a slight decrease in the SI (20%) was observed in the spleen (figure 2A, B).

Immunohistochemistry of the liver and spleen using the anti-human-CD20 antibody to reveal the focal aggregates of human CD20⁺ CLL showed that these aggregates were localized only in the white pulp of the spleen (figure 1C) and close to the vessels within the liver (data not shown). Interestingly, iron oxide nanoparticles were detectable only in the red pulp (healthy area) of the spleen and were found to be absent in the white pulp, where the CLL cells were localized.

Our findings demonstrate that after FeraSpin XS administration, a significant initial decrease in SI is observed in the healthy liver and spleen (NSG mice), which is attributed to phagocytosis of iron oxide nanoparticles by the reticulo-endothelial cells. In the NSG-CLL mice, however, a reduced uptake of FeraSpin XS by the spleen is observed and is due to the presence of the CLL foci within the white pulp. This report demonstrates the suitability of the MRI method to detect the presence of a non-solid tumor, such as chronic lymphocytic leukemia, within the spleen. The clearance of iron oxide nanoparticles within the spleen after 28 days p.i. in the healthy group of mice offers the potential to apply this technique for the MR imaging follow-up of CLL mouse models in order to evaluate the response to therapy.

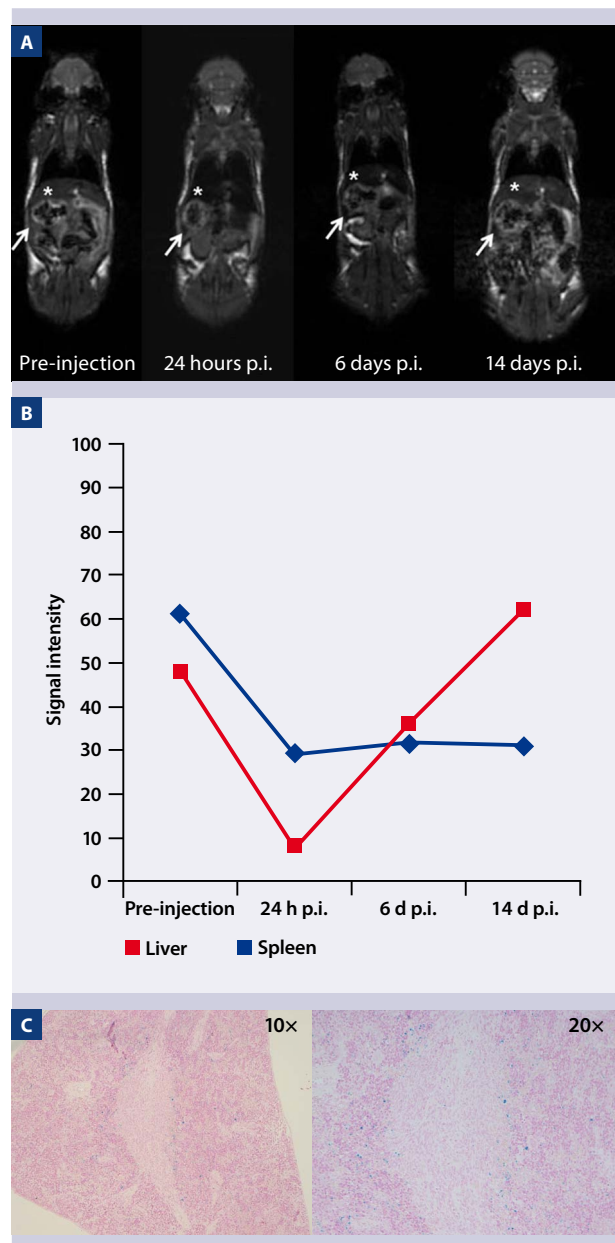


Figure 1: NSG mice

A) Coronal MR images before, 24 hours, 6 days, and 14 days after FeraSpin XS administration. Signal intensity changes are observed in the liver (asterisk) and spleen (arrow).

B) Time-dependence of SI in the liver and spleen before and after FeraSpin XS administration.

C) Histopathological analysis of the healthy spleen by Perl's Prussian blue staining 28 days after FeraSpin XS administration reveals only few nanoparticles present.

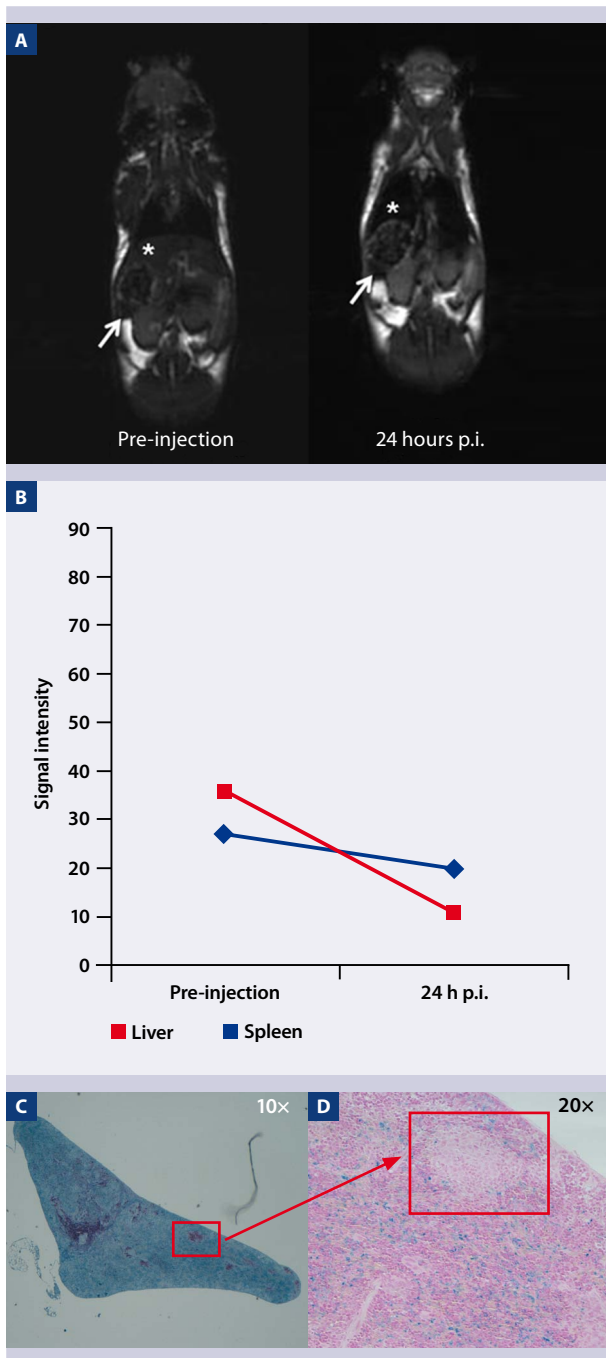


Figure 2: NSG-CLL mice

A) Coronal MR images before and 24 hours after FeraSpin XS administration. Signal intensity changes are observed in the liver (asterisk) and spleen (arrow).

B) Time-dependence of SI in the liver and spleen before and after FeraSpin XS administration.

C) Immunohistochemistry with anti-human-CD20 antibody reveals that CLL cells are localized in focal aggregates in the white pulp of the spleen.

D) Histopathological analysis of the spleen by Perls' Prussian blue staining 6 days after FeraSpin XS administration shows that iron oxide nanoparticles are present only in the red pulp of the spleen; no nanoparticles are present in the white pulp where the CLL cells are localized.

Acknowledgements

This work was supported by: Associazione Italiana Ricerca sul Cancro (AIRC) grant 5xmille no. 9980, 2010-15 to M.F., and AIRC IG10492 to M.F.

References

1. Weissleder, R. *et al.* (1988) Superparamagnetic iron oxide: enhanced detection of focal splenic tumors with MR imaging. *Radiology* 169 (2): 399–403.
2. Neumaier, C.E. *et al.* (2008) MR and iron magnetic nanoparticles. Imaging opportunities in preclinical and translational research. *Tumori*. 94(2): 226–233.
3. Bagnara, D. *et al.* (2011) A novel adoptive transfer model of chronic lymphocytic leukemia suggests a key role for T lymphocytes in the disease. *Blood* 117(20): 5463–5472.
4. Cheson, B.D. *et al.* (2007) Revised response criteria for malignant lymphoma. *J. Clin. Oncol.* 25(5): 579–586.
5. Baio, G. *et al.* (2010) Two-step *in vivo* tumor targeting by biotin-conjugated antibodies and superparamagnetic nanoparticles assessed by magnetic resonance imaging at 1.5 T. *Mol. Imaging Biol.* 12(3): 305–315.

Viscover™ Products	Order no.
FeraSpin XS, 5 injections	130-095-140
FeraSpin XS, 25 injections	130-095-141
FeraSpin L, 5 injections	130-095-170
FeraSpin L, 25 injections	130-095-171
FeraSpin M, 5 injections	130-095-168
FeraSpin M, 25 injections	130-095-169
FeraSpin R, 5 injections	130-095-138
FeraSpin R, 25 injections	130-095-139
FeraSpin S, 5 injections	130-095-166
FeraSpin S, 25 injections	130-095-167
FeraSpin XL, 5 injections	130-095-172
FeraSpin XL, 25 injections	130-095-173
FeraSpin XXL, 5 injections	130-095-174
FeraSpin XXL, 25 injections	130-095-175
FeraTrack™ MRI Contrast Agent Kit, 5 tracking experiments	130-096-498
FeraTrack MRI Contrast Agent Kit, 25 tracking experiments	130-096-499



Miltenyi Biotec

Germany/Austria/ Switzerland

Miltenyi Biotec GmbH
Friedrich-Ebert-Straße 68
51429 Bergisch Gladbach
Germany
Phone +49 2204 8306-0
Fax +49 2204 85197
macs@miltenyibiotec.de

USA/Canada

Miltenyi Biotec Inc.
2303 Lindbergh Street
Auburn, CA 95602, USA
Phone 800 FOR MACS
Phone +1 530 888 8871
Fax +1 530 888 8925
macs@miltenyibiotec.com

Australia

Miltenyi Biotec
Australia Pty. Ltd.
Unit 16A, 2 Eden Park Drive
Macquarie Park NSW 2113
Australia
Phone +61 2 8877 7400
Fax +61 2 9889 5044
macs@miltenyibiotec.com.au

Benelux

Miltenyi Biotec B.V.
Schipholweg 68 H
2316 XE Leiden
The Netherlands
macs@miltenyibiotec.nl

Customer service The Netherlands

Phone 0800 4020120
Fax 0800 4020100

Customer service Belgium

Phone 0800 94016
Fax 0800 99626

Customer service Luxembourg

Phone 800 24971
Fax 800 24984

China

Miltenyi Biotec GmbH
Shanghai Office
Rm. 2309
No. 319 Xianxia Rd.
Shanghai 200051, P.R. China
Phone +86 21 62351005
Fax +86 21 62350953
macs@miltenyibiotec.com.cn

France

Miltenyi Biotec SAS
10 rue Mercœur
75011 Paris, France
Phone +33 1 56 98 16 16
Fax +33 1 56 98 16 17
macs@miltenyibiotec.fr

Italy

Miltenyi Biotec S.r.l.
Via Persicetana, 2/D
40012 Calderara di Reno (BO)
Italy
Phone +39 051 6 460 411
Fax +39 051 6 460 499
macs@miltenyibiotec.it

Japan

Miltenyi Biotec K.K.
Nittsu-Eitai Building 5F
16-10 Fuyuki, Koto-ku,
Tokyo 135-0041, Japan
Phone +81 3 5646 8910
Fax +81 3 5646 8911
macs@miltenyibiotec.jp

Nordics and Baltics

Miltenyi Biotec Norden AB
Scheelevägen 17
223 70 Lund
Sweden
macs@miltenyibiotec.se

Customer service Sweden

Phone 0200-111 800
Fax 046-280 72 99

Customer service Denmark

Phone 80 20 30 10
Fax +46 46 280 72 99

Customer service Norway, Finland, Iceland, and Baltic countries

Phone +46 46 280 72 80
Fax +46 46 280 72 99

Singapore

Miltenyi Biotec Asia Pacific Pte Ltd.
100 Beach Road
#28-06 to 28-08 Shaw Tower
Singapore 189702
Phone +65 6238 8183
Fax +65 6238 0302
macs@miltenyibiotec.com.sg

South Korea

Miltenyi Biotec Korea
Petra building
659 Yeoksam-dong
Gangnam-gu
Seoul, South Korea
Phone +82 2 555 1988
Fax +82 2 555 8890
macs@miltenyibiotec.co.kr

Spain

Miltenyi Biotec S.L.
C/Luis Buñuel 2
Ciudad de la Imagen
28223 Pozuelo de Alarcón (Madrid)
Spain
Phone +34 91 512 12 90
Fax +34 91 512 12 91
macs@miltenyibiotec.es

United Kingdom

Miltenyi Biotec Ltd.
Almac House, Church Lane
Bisley, Surrey GU24 9DR, UK
Phone +44 1483 799 800
Fax +44 1483 799 811
macs@miltenyibiotec.co.uk

www.miltenyibiotec.com

Miltenyi Biotec provides products and services worldwide. Visit www.miltenyibiotec.com/local to find your nearest Miltenyi Biotec contact.

Unless otherwise specifically indicated, Miltenyi Biotec products and services are for research use only and not for therapeutic or diagnostic use. FeraSpin, FeraTrack, MACS, the MACS logo, and Viscover are either registered trademarks or trademarks of Miltenyi Biotec GmbH. Copyright © 2013 Miltenyi Biotec GmbH. All rights reserved.

ORIGINAL ARTICLE

Effects of miRNA-15 and miRNA-16 expression replacement in chronic lymphocytic leukemia: implication for therapy

G Cutrona¹, S Matis¹, M Colombo¹, C Massucco¹, G Baio^{2,15}, F Valdora^{1,3}, L Emionite⁴, S Fabris⁵, AG Recchia^{6,7}, M Gentile^{6,7}, CE Neumaier², D Reverberi¹, R Massara¹, S Boccardo⁸, L Basso⁹, S Salvi⁸, F Rosa⁹, M Cilli⁴, S Zupo¹⁰, M Truini^{8,16}, P Tassone¹¹, M Calabrese², M Negrini¹², A Neri^{5,13}, F Morabito^{6,7}, F Fais^{1,3} and M Ferrarini¹⁴

Chronic lymphocytic leukemia (CLL) clones are characterized by loss of a critical region in 13q14.3, (del(13)(q14)) involving the microRNA (miRNA) cluster miR-15a and miR-16-1. We have investigated the effects of replacement of miR-15a and miR-16-1. CLL cells transfected with these miRNA mimics exhibited a decrease in cell viability *in vitro* and impaired capacity for engraftment and growth in NOD/Shi-scid,γnull (NSG) mice. No synergistic effects were observed when the two miRNA mimics were combined. The phenomena were not restricted to CLL with the del(13)(q14) lesion. Similar effects induced by miRNA mimics were seen in cells with additional chromosomal abnormalities with the exception of certain CLL clones harboring *TP53* alterations. Administration of miRNA mimics to NSG mice previously engrafted with CLL clones resulted in substantial tumor regression. CLL cell transfection with miR-15a and miR-16-1-specific inhibitors resulted in increased cell viability *in vitro* and in an enhanced capacity of the engrafted cells to grow in NSG mice generating larger splenic nodules. These data demonstrate that the strong control by miR-15a and miR-16-1 on CLL clonal expansion is exerted also at the level of full-blown leukemia and provide indications for a miRNA-based therapeutic strategy.

Leukemia (2017) 31, 1894–1904; doi:10.1038/leu.2016.394

INTRODUCTION

Chronic lymphocytic leukemia (CLL) is characterized by the monoclonal expansion of B cells expressing CD19, CD5 and CD23 and low levels of surface immunoglobulin.¹ The mechanisms underlying the disease have only been partially elucidated. In CLL, well-defined chromosomal abnormalities, such as deletions at (17)(p13.1), (11)(q22.3) or trisomy 12 (+12) are infrequent at early stages and more common in patients with more advanced disease or at relapse. Therefore, these lesions are unlikely to contribute to the initial pathogenetic mechanisms, although they may be involved in both disease progression and resistance to therapy.^{2–8}

The 13q14.3 (del(13)(q14)) deletion represents a remarkable exception, as it is observed in approximately 50% of cases either in a mono- or biallelic form and is also present in the early disease stages,^{4,9} including monoclonal B cell lymphocytosis or MBL,^{10,11} suggesting a pathogenetic role. The deletion identified involves primarily the *DLEU2* gene which carries the locus of two microRNAs (miRNAs): miR-15a and miR-16-1 (miR-15 and miR-16, respectively).^{12–17} MiRNAs are single stranded, non-coding RNA, which are evolutionary conserved and capable of regulating the expression of several genes concomitantly.¹⁸ The regulation of gene expression occurs mainly through the specific binding of

miRNAs to the 3'-untranslated region (3'-UTR) of the messenger RNA of the target gene via a RNA-induced silencing complex,¹⁹ although additional mechanisms have been described.²⁰

Biallelic del(13)(q14) results in an incapacity of the cell to express miR-15 and miR-16^{14,15,17,21,22} (Supplementary Figure S1) and the deregulation of several target genes, including those involved in cell cycle progression and apoptosis.^{23–25} This confers an increased resistance to apoptosis and a propensity to leukemic cell proliferation. Low levels of miR-15 or miR-16 are observed in patients with monoallelic deletions and in many patients without del(13)(q14).^{15,21,22,26–28} Additional support for the role of the miR-15/miR-16 locus in CLL pathogenesis comes from the New Zealand Black (NZB) mice strain harboring a germ-line point mutation downstream of the miR-16 locus, which prevents normal expression of both miR-15 and miR-16 and facilitates leukemia onset and possibly autoimmune manifestations.²⁹ An analogous lesion, present in particular families, genetically predisposes humans to CLL and possibly to other neoplasias.³⁰ Finally, the selective deletion of the miR-15/miR-16 locus in mice predisposes the development of a CLL-like leukemia.^{16,31} Therefore, impairment of miR-15 and miR-16 function may be involved in promoting the initial phases of leukemogenesis; however, little is known

¹Department Integrated Oncological Therapies, Molecular Pathology Unit, IRCCS-A.O.U., San Martino-IST, Genoa, Italy; ²Diagnostic Imaging and Senology, IRCCS-A.O.U., San Martino-IST, Genoa, Italy; ³Department of Experimental Medicine, University of Genova, Genova, Italy; ⁴Animal Facility, IRCCS-A.O.U., San Martino-IST, Genoa, Italy; ⁵Hematology Unit, Fondazione IRCCS Ca' Granda, Ospedale Maggiore Policlinico, Milan, Italy; ⁶Hematology Unit, Department of Onco-Hematology, A.O. of Cosenza, Cosenza, Italy; ⁷Biotechnology Research Unit, Aprigliano, A.O./ASP of Cosenza, Cosenza, Italy; ⁸Division of Histopathology and Cytopathology, IRCCS-A.O.U., San Martino-IST, Genoa, Italy; ⁹Department of Science of Health (DISSAL), University of Genova, Genova, Italy; ¹⁰Molecular Diagnostic Unit, Division of Histopathology and Cytopathology, IRCCS-A.O.U., San Martino-IST, Genoa, Italy; ¹¹Department of Experimental and Clinical Medicine, Magna Graecia University, Salvatore Venuta University Campus, Catanzaro, Italy; ¹²Department of Morphology, Surgery and Experimental Medicine, University of Ferrara, Ferrara, Italy; ¹³Department of Oncology and Hemato-Oncology, University of Milano, Milan, Italy and ¹⁴Scientific Direction, IRCCS-A.O.U., San Martino-IST, Genoa, Italy. Correspondence: Professor F Fais, Department Integrated Oncological Therapies, Molecular Pathology Unit, IRCCS-A.O.U., San Martino-IST, Via Alberti 2, Lgo Rosanna Benzi, 10, Genoa 16132, Italy.

E-mail: franco.fais@unige.it

¹⁵Current address: Aberdeen Biomedical Imaging Centre, University of Aberdeen, Aberdeen, UK.

¹⁶Current address: A.O. Division of Histopathology and Cytogenetics, Ospedale Niguarda Ca'Granda, Milano, Italy.

Received 28 September 2016; revised 27 November 2016; accepted 6 December 2016; accepted article preview online 5 January 2017; advance online publication, 3 February 2017

regarding the role of these lesions in maintaining the transformed status and the clonal expansion of full-blown leukemia.³²

Here, we investigated the possibility of interfering with both miR-15 and miR-16 expression by CLL cells, both in *in vivo* and *in vitro*.

MATERIALS AND METHODS

Patients and CLL cell preparations

Newly diagnosed CLL patients from participating Institutions were enrolled within 12 months from diagnosis in the O-CLL1 protocol (clinicaltrial.gov identifier NCT00917540). All participants provided written informed consent in accordance with the declaration of Helsinki and the study was approved by the appropriate institutional review boards. Supplementary Table S1 summarizes the phenotype and the major cytogenetic features of CLL cases ($n=59$) selected for *in vitro* ($n=48$) and *in vivo* ($n=17$) experiments reported in this study.^{11,33,34}

PBMCs from patients with CLL were isolated by Ficoll-Hypaque (Seromed, Biochrom, Berlin, Germany) density gradient centrifugation. In selected experiments, CD19-positive CLL cells were enriched by negative selection with the EasySep-Human B-cell Enrichment Kit without CD43 depletion (STEMCELL Technologies, Voden Medical Instruments S.p.A, Milan, Italy).

Cell transfection

MirVana miRNA mimics or inhibitors (Ambion, Inc., Thermo Fisher Scientific, Grand Island, NY, USA) were delivered to CLL cells with a Neon Transfection System (Invitrogen, Thermo Fisher Scientific) at the final concentration of $50 \text{ nm}/2 \times 10^6$ CLL cells. Optimal transfection and survival of CLL cells was obtained by applying 1 pulse at 2150 pulse voltage and 20 pulse width, as indicated by the manufacturer for the primary blood-derived suspension cells protocol. After transfection, cell suspensions were seeded in 24-well plates containing 500 μl of culture medium without antibiotics (RPMI-1640 with L-glutamine and 10% FBS (Gibco, Thermo Fisher Scientific, Paisley, UK), Sodium piruvate 0.1% (Euroclone, Pero, Milan, Italy) at 37 °C and incubated at the final concentration of 2×10^6 CLL cells/ml/well in a 5% CO₂ atmosphere. The following miRNA mimics and inhibitors were employed: hsa-miR-15a-5p, hsa-miR-16-5p, and miRNA Negative Control (CTR)#1, miRNA Inhibitor Negative CTR #1.

Evaluation of miRNA expression

MiR-15 and miR-16 expression was evaluated with two methods: SmartFlare RNA Detection Probes (Merck Millipore, Guyancourt, France) in $n=13$ CLL cases and quantitative real time PCR (qRT-PCR; $n=38$ CLL cases; Supplementary materials and methods and Supplementary Figure S2).

SmartFlare technology is useful to study miRNA expression at the single-cell level. SmartFlare RNA Detection Probes, are constituted by tiny gold nanoparticles conjugated to oligonucleotides duplexed with reporter strands (oligo+fluorophore). When Smartflare probes bind to their complementary RNA sequences the fluorophore is released and can be detected by flow-cytometry (FC). The following Smartflare probes conjugated with the Cyanine 5 (Cy5) fluorophore were used: SF-430/ miR-15a-5p (miR-15 CY5); SF-178/ miR-16-5p (miR-16 CY5); SF-102/ Scramble CTR Cy5. The latter reagent does not bind to any RNA sequences within the cells and is used to measure the level of background fluorescence within CLL cells. Cells were incubated with Smartflare probes overnight, harvested and analyzed by FACSCanto (BD Biosciences, San José, CA, USA) and DIVA 6 (BD Biosciences) or FLOWJO V.9.8.3 software (Treestar, Inc., Ashland, OR, USA).

Counter staining with propidium iodide (PI; 50 mg/ml, Sigma-Aldrich, Milan, Italy) in isotonic solution was employed to evaluate cell viability.

Changes in miR-15/miR-16 expression following transfection with miRNA mimics or inhibitors were expressed as: % fold induction = (%smartflare positive cells transfected with miR-15/miR-16 mimic) / (%smartflare positive cells transfected with miR-CTR mimic) / (%smartflare positive cells transfected with miR-15/miR-16 mimic) $\times 100\%$ fold inhibition = (%smartflare positive cells transfected with miR-CTR inhibitor) / (%smartflare positive cells transfected with miR-15/miR-16 inhibitor) / (%smartflare positive cells transfected with miR-CTR inhibitor) $\times 100\%$.

Apoptosis assays

Cultured cells were double stained with Annexin-V-FITC conjugate (cat. 556419, BD Biosciences Pharmingen, San José, CA, USA), and PI in isotonic solution, and then analyzed by FC. Viable cells were defined as double negative cells.³⁵

Xenogeneic mouse transplantation

Six- to 8-week-old female NOD/Shi-scid,ycnull (NSG) mice (The Jackson Laboratory), a xenograft model for CLL growth *in vivo*^{36,37} were housed in sterile enclosures under specific pathogen-free conditions. All procedures involving animals were performed in the respect of the current National and International regulations and were reviewed and approved by the Licensing and Animal Welfare Body of the IRCCS-AOU San Martino-IST National Cancer Research Institute, Genoa, Italy.

Depending on the number of leukemic cells available for animal injection, groups of 2–3 NSG mice were employed for each test and treatment group. The number of animals used for each treatment is detailed in brackets in Table 1 and Supplementary Tables S3–S5. Full details are in Supplementary Material and Methods.

In miRNA pre-treatment experiments NSG mice ($n=38$) were inoculated with CLL cells ($n=6$) transfected with miRNA mimic/inhibitors and cultured for 6 h prior to injection. A total of 50×10^6 CLL cells per mouse were injected together with a proportion of autologous T cells (~5–10%).

After four weeks, mice were anesthetized by intraperitoneal injection of combination of xylazine (10 mg/kg) and ketamine (100 mg/kg) and analyzed by Magnetic Resonance Imaging (MRI) with USPIO contrast reagent.³⁸

On termination of the experiment (maximum 6 weeks from start), animals were sacrificed in a saturated CO₂ chamber and autopsies were performed. Spleens were evaluated by FC and by immunohistochemical (IHC) analysis. The Animal Welfare Body posed a time limit to the experimental protocol to prevent unneeded suffering.

Fresh spleen samples were enzymatically digested using the Spleen Dissociation Kit (Miltenyi Biotec) and mechanically resuspended with gentleMACS™ Dissociator (Miltenyi Biotec). The single-cell suspensions were stained with anti-human CD45-FITC (555482), CD19-PE-Cy7(557835), CD5-APC(555355), (BD Biosciences) and analyzed by FC. Apoptosis was evaluated using Annexin-V-FITC, CD19-PE-Cy7, CD5-PE (555353) (BD Biosciences), CD45-APC(130-091-230, Miltenyi Biotec,) cell staining.

Formalin-fixed and paraffin-embedded spleen specimens were analyzed for the presence of human CLL infiltrates and for the presence of co-injected bystander T-cells by IHC as detailed above.³⁸ The primary antibodies anti-CD20 Mouse monoclonal antibody (760-2531, clone L26-Ventana Medical System, Roche) and CD3 Rabbit Monoclonal Antibody (790-4341, clone 2GV6—Ventana Medical System, Roche) were incubated for 30 min at 37 °C and signals revealed using the polymeric detection system, Ultraview Universal Red Detection Kit (Ventana Medical System). An appropriate positive tissue control was used for each staining run; the negative control consisted of performing the entire IHC procedure on adjacent sections in the absence of the primary antibody; the sections were counter-stained (automatically) with Gill's modified hematoxylin and then cover-slipped. The sections were evaluated by two observers with an Olympus light microscope using 4, 10, 40 \times and objectives under a Leica DMD108 optical digital microscope (Leica Microsystems, Wetzlar, Germany).

To evaluate therapeutic effects of miRNA, CLL ($n=11$) engraftment in the spleen was determined by MRI following USPIO contrast reagent injection after 2–3 weeks from cell injection. At this stage, mice were treated intraperitoneally (every second day with mirVana miRNA mimic, (*In Vivo* Ready formulation, Ambion, Inc.) complexed with InvivoFectamine 2.0 (Thermo Fisher Scientific) at a final concentration of 0.7 mg/ml (200 μl /mouse). Overall three doses were administered. The following miRNA were used: hsa-miR-15a-5p, hsa-miR-16-5p, miRNA negative control#1. Three days from the last injection, mice ($n=74$) were analyzed again by MRI and then sacrificed in a saturated CO₂ chamber and autopsies were performed. Spleens were analyzed by FC and IHC. Apoptosis was evaluated by Annexin-V-FITC, CD19-PE-Cy7, CD5-PE, CD45-APC, and FC or by Cleaved Caspase-3 (Asp175) (5A1E) Rabbit mAb (9664, Cell Signaling Technology, Danvers, MA, USA) and IHC on spleen tissue sections.

Magnetic resonance imaging

All *in vivo* MRI experiments and MRI analyses, using USPIO nanoparticles, were carried out and acquired as previously described.³⁸ Details are reported in the Supplementary Information.

Definition of IHC index

The IHC index is a measure of the spread of leukemia based on the average diameters of the follicular lesions. We assigned a numerical value of 1 to the follicles with diameters \pm s.d. of $102(\pm 90) \times 42(\pm 7)$ μ m; a value of 3 to follicles with a diameter $195(\pm 80) \times 138(\pm 85)$ μ m; a value of 6 to follicles between $399(\pm 245) \times 300(\pm 39)$, and a value of 12 to follicles between $734(\pm 461) \times 540(\pm 167)$. The IHC index is given by the sum of the number of follicles multiplied by the value assigned according to size (Supplementary Figure S3).

Statistical analysis

The statistical package SPSS for Windows, v13.0, 2004 software (SPSS, London, UK) was used for all analyses of statistical significance from adequately powered sample sizes for two-tailed tests. Statistical comparisons between related samples were carried out by nonparametric Wilcoxon signed rank (paired data) or by Mann-Whitney *U*- (unpaired data) tests. A value of $P < 0.05$ was considered significant for all statistical calculations. Values are given as mean \pm s.e.m. or mean \pm s.d. as stated in figure legends, which was calculated invariably from *n* (the number of

patients or animals, biological replicates). All exact *P*-values are provided in the figure panels, in figure legends or in Results section.

RESULTS

Transfection of miR-15 and miR-16 mimics or inhibitors into CLL cells *in vitro*

Transfection of miRNAs mimics or inhibitors into purified CLL cells was verified by FC using Smartflare technology and qRT-PCR.

For the experiments with miRNA mimics, 7 CLL cases with biallelic del(13)(q14) deletions were selected (Supplementary Information and Supplementary Table S1 for case characteristics). At 24 h after transfection, a significantly larger number of cells were found to express miR-15 (%fold induction = 79 ± 5 , mean \pm s.e.m.) and miR-16 (%fold induction = 75 ± 5) compared with control preparations ($P = 0.015$; Figure 1a and Supplementary Figure S4a). Comparable data were obtained by qRT-PCR (Supplementary Figure S2a).

For experiments with miRNA inhibitors, we selected 6 CLL cases that did not display biallelic del(13)(q14) and expressed miR-15 and miR-16 to a variable extent. Transfection with specific miRNA inhibitors efficiently reduced miRNA expression in all CLL clones

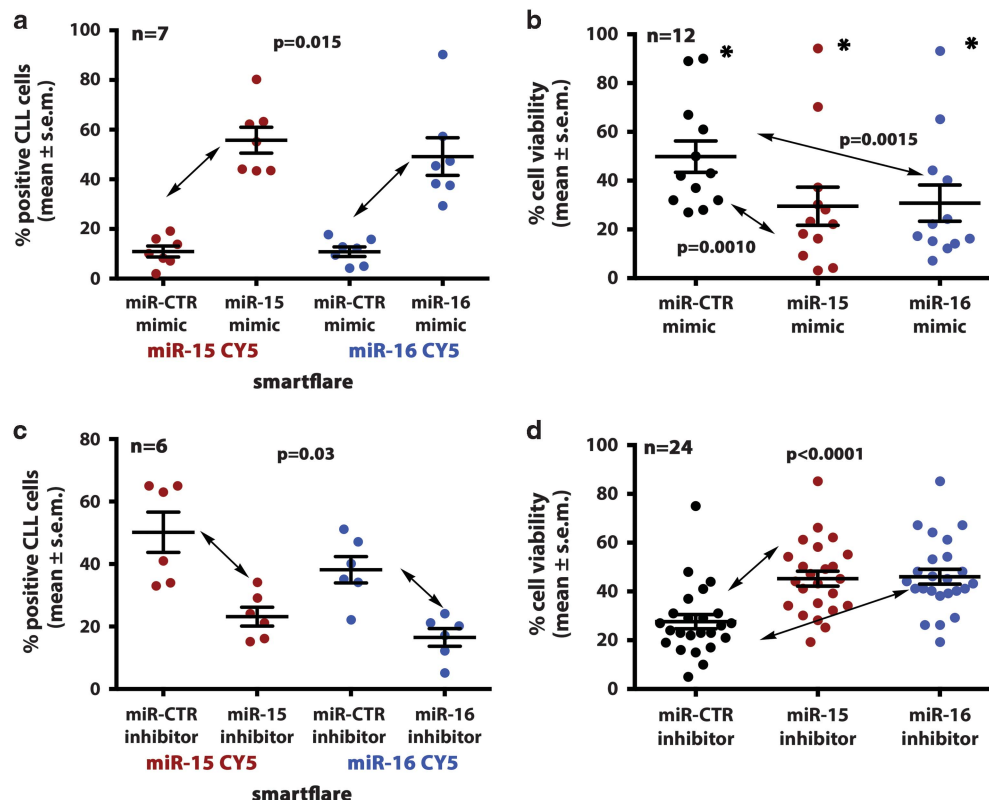


Figure 1. Transfection with miRNA mimics and inhibitors and variations in CLL cell viability *in vitro*. (a) Expression of miR-15 and miR-16 following transfection with miR-15 (% of positive CLL cells mean \pm s.e.m. = 55.7 ± 5.2) or miR-16 (49.1 ± 7.6) or miR-CTR mimics (10.9 ± 2.2 for miR-15; 10.8 ± 1.9 for miR-16) determined by smartflare technology. Summary of tests on 7 CLL cases with biallelic del(13)(q14) (MG0248, DT0300, MA0088, LD0062, GM0041, RD0296 and GD0051). (b) Summary of viability determinations obtained on cells from 12 different biallelic del(13)(q14) CLL cases after a 48-h culture following transfection of the indicated miRNA mimics (data for individual cases are reported in Supplementary Figure S6a). The asterisks indicate data from a CLL case (CG0620) harboring the TP53 mutation (Supplementary Table S1). (c) Expression of miR-15 and miR-16 following transfection with miR-15 (23.17 ± 3) or miR-16 (16.5 ± 2.8) or miR-CTR inhibitors (50.17 ± 6.4 for miR-15; 38.17 ± 4.2 for miR-16). Summary of tests on 6 CLL cases (CP0036, CR0203, PA0145, PM0608, CG0623, MA0342). (d) Summary of the viability results obtained on cells from 24 CLL cases transfected with miRNA inhibitors. In (a) and (c) purified CLL cells were transfected with the indicated miRNA mimics or inhibitors and cultured overnight in the presence of miR-15-CY5, miR-16-CY5 or scramble CY5 Smartflare probes. Counter staining with propidium iodide (PI) was employed to evaluate cell viability (see also Supplementary Figure S4). In b and d viable cells (%) are measured as Annexin-V/PI-double negative cells (Supplementary Figure S5). The *P*-values were obtained by Wilcoxon test in all panels.

compared with controls (%fold inhibition = 54 ± 4 , mean \pm s.e.m., for miR-15; and %fold inhibition = 59 ± 4 for miR-16) ($P=0.03$) (Figure 1c and Supplementary Figure S4b). Again, comparable data were obtained when miRNA expression was measured by qRT-PCR (Supplementary Figure S2b).

As miR-15 and miR-16 expression may impact on CLL cell survival *in vitro*, purified cells from 12 CLL cases with biallelic del(13)(q14) were transfected with miR-15 or miR-16 miRNA mimics and cultured for up to 72 h. Viable cells were measured at different time intervals (Supplementary Figure S5a shows the data of a

representative experiment). A significant decrease in cell viability (%fold reduction mean \pm s.e.m. = 53 ± 7 and 48 ± 6 for miR-15 and miR-16 mimics, respectively in 11/12 CLL samples) after 48 h ($P=0.001$ for miR-15 and $P=0.0015$ for miR-16) was observed. Figure 1b shows the pooled data from the tests performed while experiments on individual CLL cases are reported in Supplementary Figure S6a. Viability of cells from the CLL case CG0620, carrying a *TP53* mutation, did not change, but the cells from two other CLL cases (MG0248, PA0254), also displaying *TP53* mutations, showed a substantial drop in cell viability following

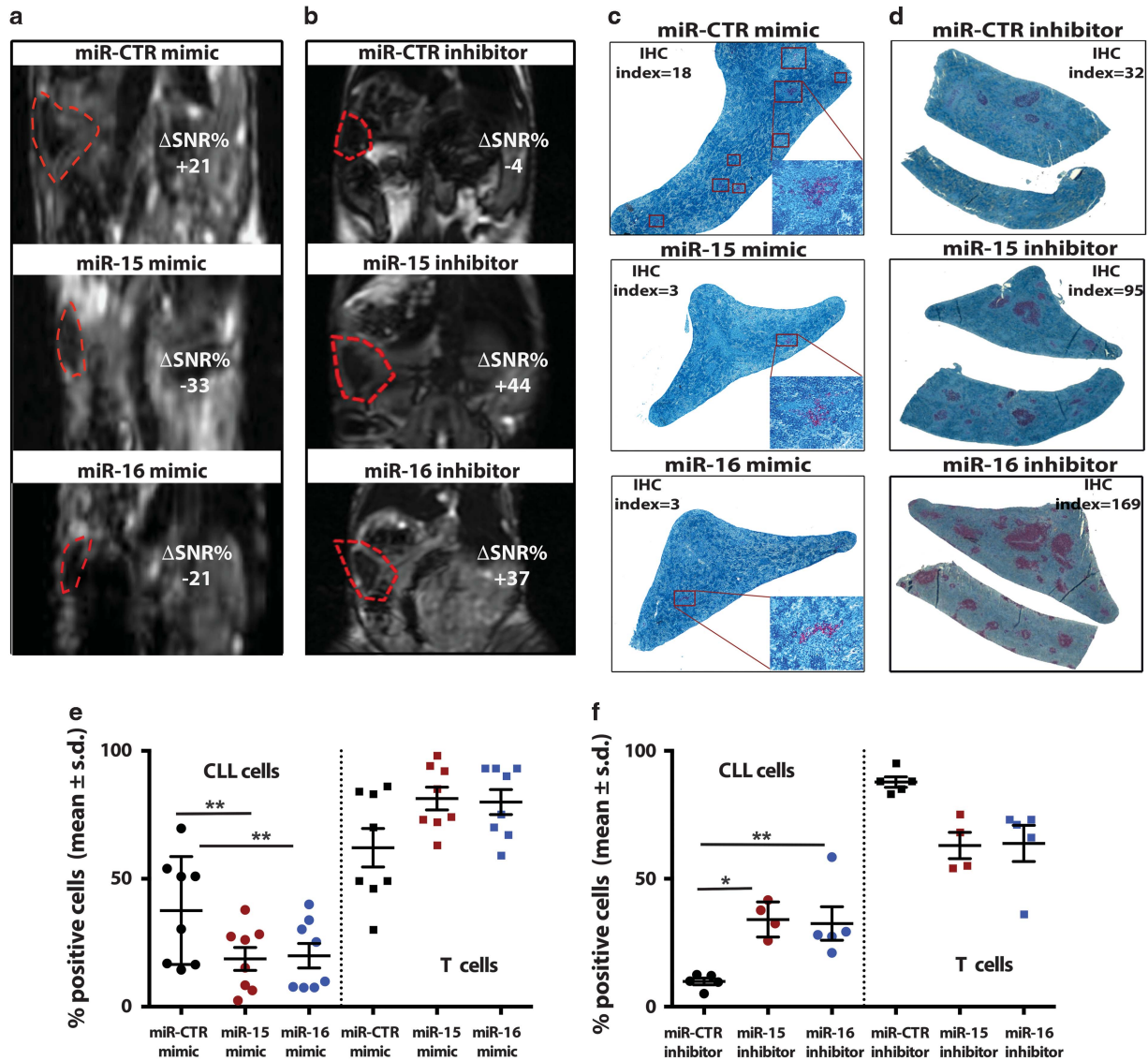


Figure 2. CLL cell engraftment in NSG mice following *in vitro* transfection with miRNA mimics or inhibitors. Representative tests on mice engrafted with CLL cells pre-treated *in vitro* with miRNA mimics (CLL CD0310), miRNA inhibitors (CLL PM0608), or miRNA-CTR. (a and b) The figure shows the MRI images 24 h after USPIO administration. The position of the spleen is indicated by the dotted red outline. Δ SNR% values also are indicated. The spleens with superior iron uptake and consequent lower Δ SNR% values, appear darker and less nodular. Conversely, spleens with lower iron uptake and higher Δ SNR% values are not so dark and show a nodular structure possibly related to the presence of follicles. Additional explanations are given in text. (c and d) α -CD20 Ab staining (red) of paraffin tissue embedded spleen samples following injection of CLL cells pre-treated with the indicated miRNA (d). The CD20+ follicle-like structures are highlighted by red squares in c (magnification $\times 40$). The $\times 400$ magnification of a representative follicle for each panel is shown. IHC index is indicated in each panel. (e and f) Flow-cytometry analysis of cells from of the same spleens used for the IHC analyses shown in (c) and (d). CLL cells (CD5+/CD19+) and T cells (CD5+/CD19-) were identified on gated huCD45-positive cells (Supplementary Figure S8). (e) Pooled flow-cytometry data obtained from 4 CLL cases with biallelic del(13)(q14) pre-treated with miRNA mimics *in vitro* before injection into mice ($n=8$ mice for each treatment group). The cells, harvested from mice at the end of tests, were stained and counted. Statistical comparisons were carried out using Wilcoxon-matched pair test. A P -value = 0.0078 is indicated by **. (f) Pooled flow-cytometry data on cells from 2 CLL cases with normal FISH pre-treated *in vitro* with miRNA inhibitors prior to injection into mice ($n=5$ mice for miR-CTR, $n=4$ for miR-15 and $n=5$ for miR-16 inhibitors). * $P=0.016$ and ** $P=0.007$, respectively (Mann-Whitney U -test). In e and f values are expressed as mean \pm s.d. and detailed in Supplementary Table S3.

transfection with either miR-15 or miR-16 (Supplementary Table S1 and Supplementary Figure S6a).

Co-transfection of biallelic del(13)(q14) CLL cells with both miR-15 and miR-16 miRNAs never resulted in an additive/synergistic effect (data not shown). Consistent with previous observations, transfection of miR-15 or miR-16 into del(13)(q14) CLL cells caused down-regulation of BCL-2 or MCL1 (antiapoptotic) and of Cyclin D1 or D2 (cell cycle induction) proteins encoded by target genes of these miRNAs.^{23,24} In contrast, Survivin, which is involved in an alternative apoptotic pathway, was not down-regulated (Supplementary Figure S6b–c).

Inhibition of miR-15 or miR-16 expression with specific miRNA inhibitors resulted in a substantial increase in CLL cell viability.

Supplementary Figure 5b reports the cell viability of a representative CLL case. A significant increase in cell viability was measured until 48-hours culture, whereas at 72 h, a drop in cell viability was observed both in the presence of miR-15/miR-16 inhibitors and in the presence of miR-CTR inhibitor, although there were still differences in the two conditions. Pooled viability data, measured after a 48-h culture from a group of 24 CLL cases displaying different cytogenetic features (Supplementary Table S2 and Supplementary Figure S7), are summarized in Figure 1d (%fold increase = 40 ± 3 and 42 ± 4 with miR-15 or miR-16 inhibitor, respectively; $P < 0.0001$) and show that miRNA inhibition expression resulted consistently in a better in vitro survival of CLL cells.

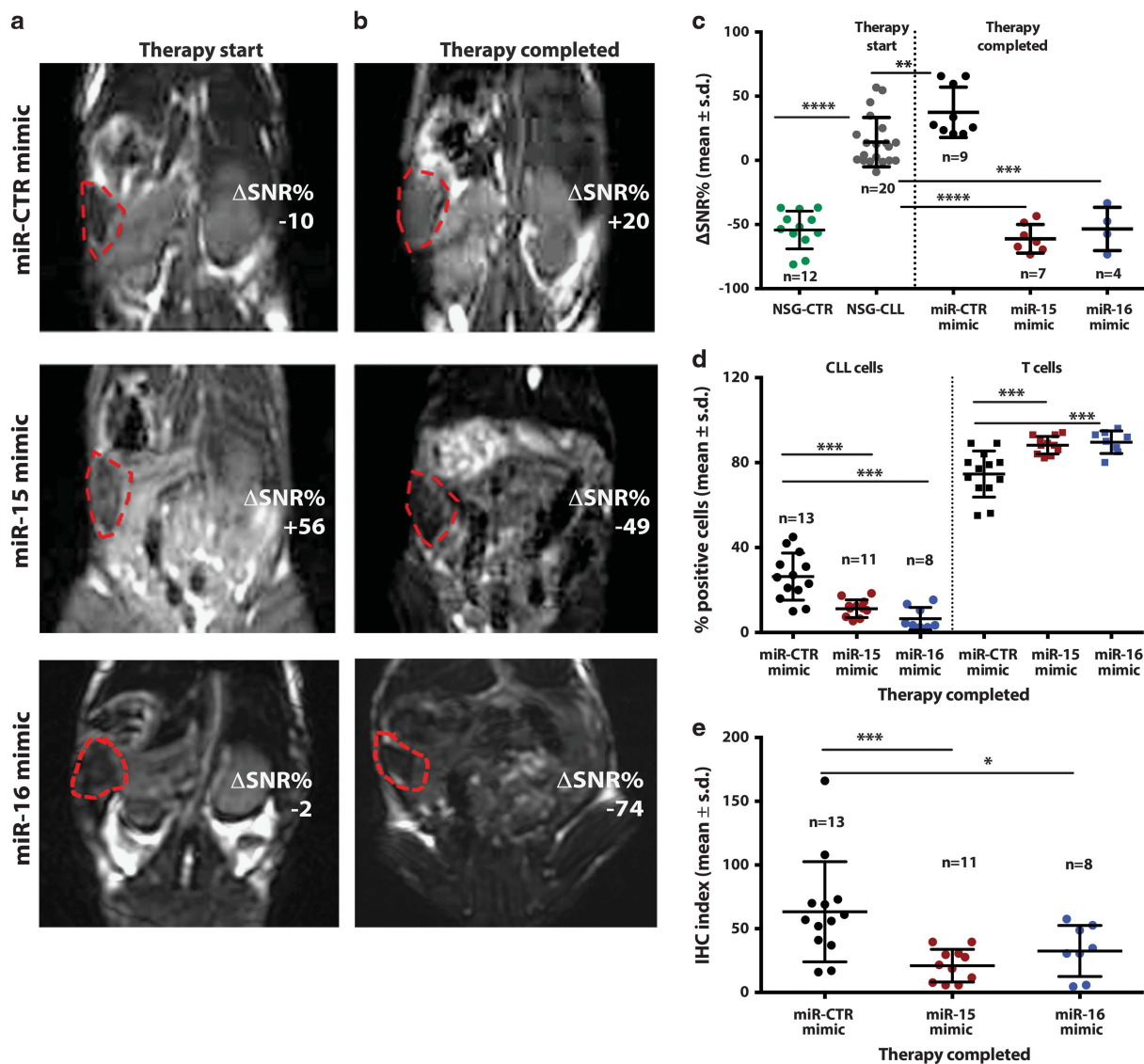


Figure 3. Effects of *in vivo* treatment with miRNA mimics on CLL cells engrafted in NSG mice. (a and b) MRI analysis of the spleen before and after the indicated treatment (representative experiment with cells from MP0456 CLL case). (MRI) images obtained 24 h after Spleens which are characterized by high USPIO uptake appear darker and less granular, a finding which correlates with a low presence of leukemic follicles. See text and legend to Figure 2 for additional details. (c) Summary of MRI results observed on cells from 6 CLL cases biallelic for del(13)(q14) treated with the indicated miRNA mimics. After 2 weeks from CLL cells injection (NSG-CLL, gray dots), mice displayed Δ SNR% values significantly higher compared with those not receiving CLL cells (NSG-CTR, green dots). NSG-CLL mice treated with miR-15 (red dots) or miR-16 (blue dots) mimics had significantly different MRI patterns from the same mice before therapy or after treatment with miR-CTR (black dots). (d) Summary of the flow-cytometry analysis of freshly isolated cells from the same spleens analyzed in (c). Percentages of CD19+CD5+ CLLs cells or CD19-CD5+ T cells detected by gating CD45+ cells are expressed as mean \pm s.d. (e) Summary of the IHC analysis of splenic tissue stained by α -CD20 mAb. In c–e each dot represents an individual mouse. Values also are expressed as mean \pm s.d. Statistical comparisons were carried out using Mann–Whitney *U*-test. All data are detailed in Supplementary Table S4.

Effects of in vitro transfection with miRNA-15 or miRNA-16 mimics/inhibitors on the growth of CLL cells in NSG mice

Purified cells from four CLL cases with biallelic del(13)(q14) were transfected with miR-15, miR-16 or miR-CTR mimics, cultured for 6-h and then injected intravenously (i.v.) into NSG mice together with autologous T cells (B/T cell ratio 5–10:1). Two/three mice were used for each treatment group. Disease engraftment was measured after 4 weeks by USPIO-MRI of the spleen.³⁸ Iron uptake is inversely correlated with the presence of CLL follicles-like structures which prevent iron uptake. Signal-to-Noise ratio change (Δ SNR%) values are higher when low iron levels enter the splenic tissue. Thus, higher uptake of the USPIO contrast reagent was

observed in the spleens of NSG mice receiving CLL cells transfected with miR-15 or miR-16 mimics which resulted into a lower Δ SNR% value compared with the spleens of mice receiving miR-CTR-transfected CLL cells (Figure 2a). The Δ SNR% of mice injected with miR-15 (mean \pm s.d. = -31.1 ± 25.1) or miR-16 (mean \pm s.d. = -18.2 ± 28.19) mimics pre-treated cells resembled that of NSG mice that had not received leukemic cells (mean \pm s.d. = -54.3 ± 15), whereas this value was higher ($+30.7 \pm 23.4$) in the mice receiving miR-CTR pre-treated cells. Δ SNR% values of mice groups pre-treated with miR-15 ($n=7$) or with miR-16 ($n=6$) were significantly lower compared with those pre-treated with miR-CTR ($n=8$; $P=0.001$ for miR-15; $P=0.01$ for miR-16). This MRI

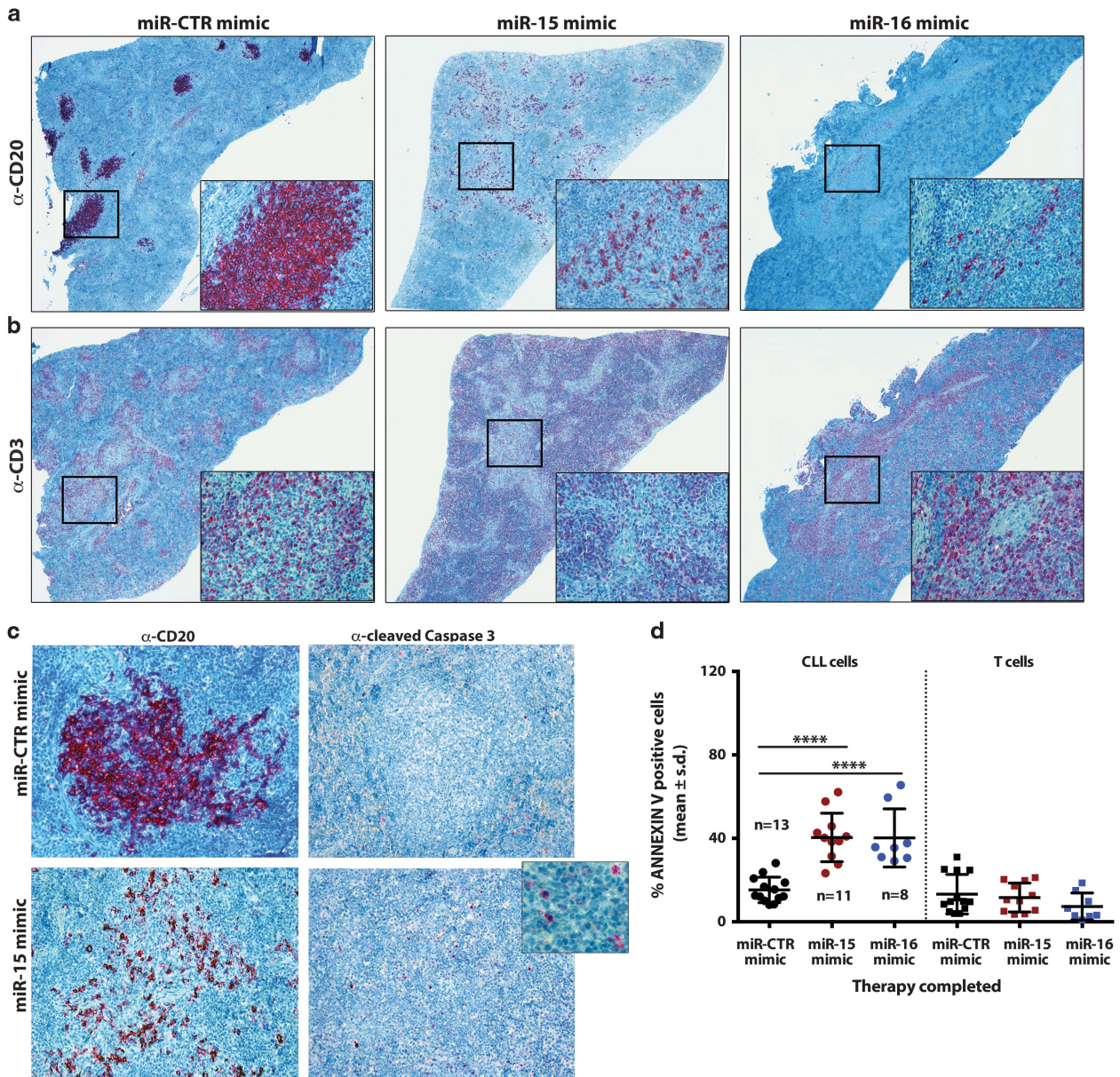


Figure 4. Effects of treatment with miR-15 or miR-16 mimics on the expansion of CLL clones in NSG mice. **(a and b)** IHC analysis of the spleen of a mouse a representative CLL case (MP0456). The typical CD20+ aggregates **(a)** surrounded by CD3+ T cells **(b)**, that are evident in the spleens of the mice treated with miR-CTR, virtually disappear following treatment with miR-15 or miR-16 mimics. $\times 40$ magnification view of splenic sagittal sections. The inset indicates the same areas at a higher magnification ($\times 400$). **(c)** Numerous cells were stained by α -Cleaved Caspase-3 mAb in the spleen of mice treated with miR-15. These were virtually absent in mice treated with miR-CTR (magnification $\times 200$ and $\times 400$ in the inset). **(d)** Summary of flow-cytometry results observed in mice injected with the cells from 6 CLL cases biallelic for del(13)(q14.3). Annexin-V positive cells were determined at the end of the experiment. Each dot represents an individual mouse. Values are expressed as mean \pm s.d. Statistical comparisons were carried out using Mann-Whitney *U*-test (**** $P < 0.0001$). All data are detailed in Supplementary Table S5.

pattern was likely related to the lower number of neoplastic foci within the splenic white pulp, a finding consistent with the observation of a lower number of follicle-like structures detected by IHC with anti-CD20 mAb in the spleen of mice receiving miR-15/16 treated cells compared with controls. Likewise, the IHC index (as detailed in Supplementary Figure S3) of mice receiving CLL cells treated with miR-15/16 mimics was decreased compared with that of mice receiving cells transfected with miR-CTR. The average \pm s.d. of the IHC index reduction was 68 ± 11 and 67 ± 11 following transfection of miR-15 and miR-16 mimics, respectively (Figure 2c) ($P=0.0078$ for both miRNAs compared with miR-CTR). FC showed a significantly lower proportion of CD19+CD5+ cells in the spleens of mice inoculated with miR-15/16-mimic-transfected CLL cells than in controls ($P=0.012$; Figure 2e and Supplementary Figure S8a). B cells recovered from NSG mice consistently shared the same BCR gene rearrangements as the leukemic clone used for injection, whereas T cells displayed oligoclonal TCR rearrangements (data not shown).

Cells from two CLL cases (PM0608, PA0145) lacking del(13)(q14) were pre-treated with miR-15 or miR-16 inhibitors *in vitro* and subsequently injected into NSG mice together with T cells according to the same schedule described above. This treatment resulted in a better splenic engraftment of the CLL cells as documented by the differences in the Δ SNR% (Figure 2b). In the spleen of mice injected with the cells from PM608 CLL case, these values were of $+49 \pm 8.4$

and $+33 \pm 19.3$ after pre-treatment of the cells with miR-15 and miR-16 inhibitors, respectively and of $+8 \pm 11.1$ after cell pre-treatment with miR-CTR inhibitors. This was paralleled by an average IHC index increase (mean \pm s.d.) of $69 \pm 6\%$ and $71 \pm 17\%$ respectively, in mice inoculated with miR-15 or miR-16 inhibitor pre-treated cells ($P=0.039$ for miR-15 and $P=0.05$ for miR-16 inhibitors compared with miR-CTR inhibitor, Figure 2d). Consistent with these data was the significant increase in the percentage of CD45+CD19+CD5+ cells observed by FC in the mice inoculated with miRNA inhibitor-treated cells ($71 \pm 3\%$ and $69 \pm 1\%$, mean \pm s.d., respectively) (Figure 2f, and Supplementary Figure S8b). All data are detailed in Supplementary Table S3. Again, the BCR and TCR gene rearrangement analyses confirmed that the engrafted B cells were mostly from the leukemic clones, whereas T cells were oligoclonal (not shown).

Inhibition of CLL cell expansion in NSG mice by treatment with miR-15 and miR-16 mimics

Next, we investigated whether administration of miRNA mimics could inhibit the expansion of a previously inoculated CLL clone in NSG mice. In preliminary tests, six NSG mice were injected with MG0248 CLL cells. After four weeks, a single potentially therapeutic dose of miR-15 miR-16 or miR-CTR complexed with InvivoFectamine was administered intraperitoneally. Mice were sacrificed 24-h after miRNA administration and CLL cells

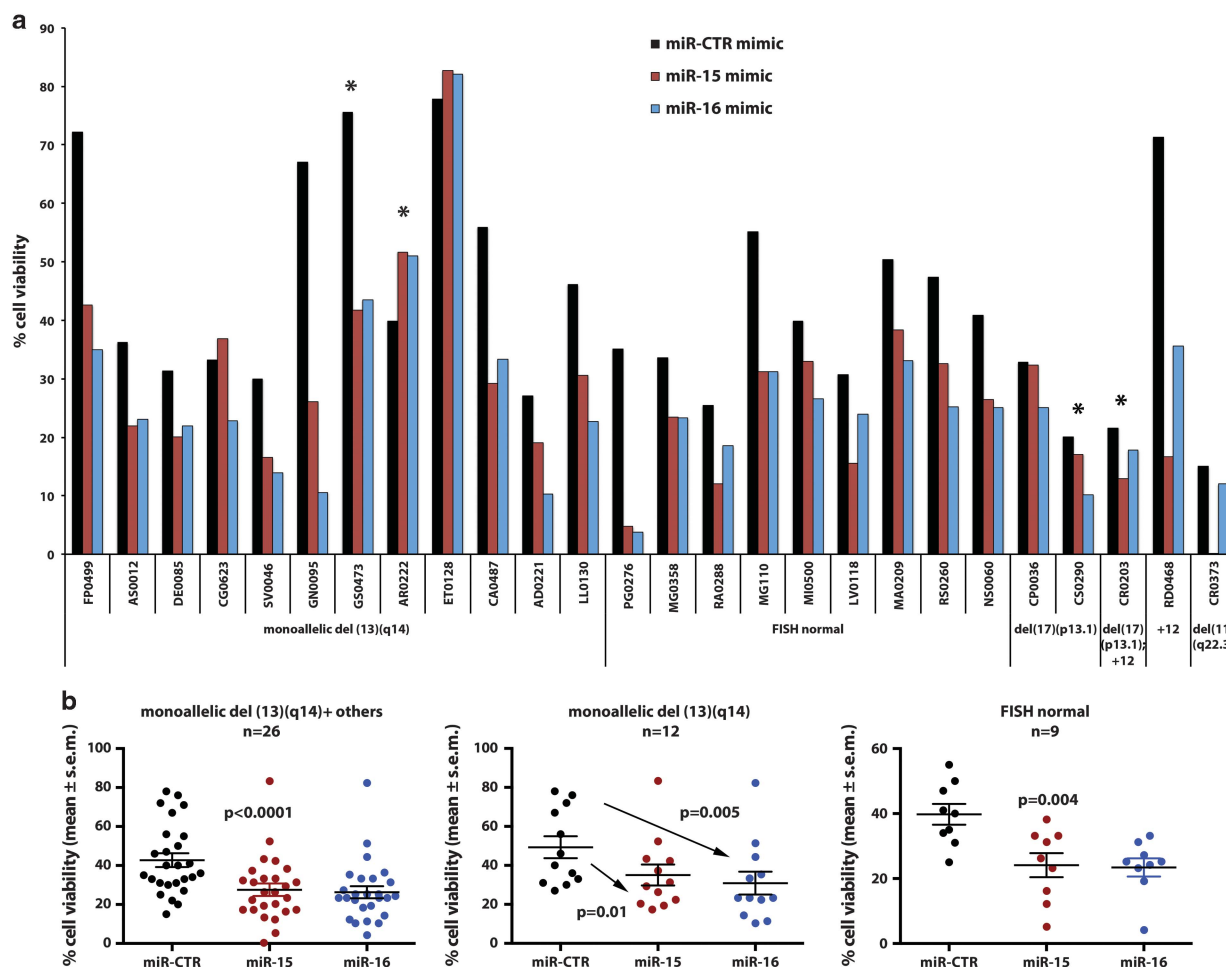


Figure 5. Effects of treatment with miRNA mimics on the growth of cells from CLL with non-biallelic del(13)(q14). **(a)** Determination of viable cells (measured as Annexin-V/PI- negative cells) in 26 CLL cases at 48-h culture following transfection of the indicated miRNA mimics. CLL cases were grouped according to their karyotype. The asterisks indicate CLL cases carrying TP53 alterations (Supplementary Table S1). **(b)** Summary of the results of the 26 CLLs cases (left panel) and subdivided in cases with monoallelic del(13)(q14) ($n=12$) (central panel) and with normal FISH ($n=9$; right panel). P -values shown were calculated by Wilcoxon test.

(CD45+, CD19+ and CD5+) were purified by FACS sorting from splenic cell suspensions (the resulting preparations contained >98% CLL cells). qRT-PCR analysis showed an increase of miR-15 (fold increase=407.80) and of miR-16 (fold increase 34.15) levels above control mice injected with miR-CTR (Supplementary Figure S9).

Next, CLL cells from six cases with biallelic del(13)(q14) were inoculated into NSG mice together with T cells (NSG-CLL) and CLL engraftment was verified in the spleen after approximately two weeks by MRI.³⁸ Mice found to have an above-average splenic Δ SNR%, compared with NSG mice that had not received leukemic cells (NSG-CTR, $n=12$, Δ SNR% -54.3 ± 15 , mean \pm s.d.), were placed on treatment with miR-15 or miR-16 mimics or miR-CTR (one injection on alternate days for a total of three injections). Three days after the final treatment, splenic infiltration by leukemic cells was evaluated (Figures 3 and 4). On MRI (exemplified in Figure 3a and b), miR-CTR treated mice displayed a splenic infiltration by leukemic cells with an 63 ± 14 average increase of Δ SNR% over that of mice not receiving leukemic cells ($P < 0.0001$). In contrast, mice treated with miR-15 or miR-16 mimics showed a significant Δ SNR% decrease ($P < 0.0001$ and $P = 0.0002$, respectively) compared with mice before therapy administration (Figure 3c). The values of the treated mice were similar to those of NSG-CTR mice not receiving CLL cell inocula. The Δ SNR% values of mice treated with miR-CTR following CLL cell inoculation were similar to or greater than those at therapy start time point ($P = 0.002$; Figure 3c). These results predicted a response to therapy, which was subsequently confirmed by FC analysis (average percentage CLL cells reduction of 61 ± 8 ($P = 0.0006$) and of 75 ± 12 ($P = 0.0001$) after miR-15 and miR-16 mimics treatment, respectively, vs. mice treated with miR-CTR; Figure 3d) and IHC. A significantly lower IHC index was observed in mice treated with miR-15 or miR-16 compared with mice treated with miR-CTR (average IHC index reduction 62 ± 15 ($P = 0.0007$) and 78 ± 22 ($P = 0.02$), respectively) (Figure 3e and Supplementary Table S4).

IHC analysis showed an almost complete disappearance of the typical aggregates of leukemic (CD20+) cells after treatment with miR-15 or miR-16 mimics (Figure 4a and Supplementary Figure S3b). However, autologous T cells (CD3+ cells), surrounding what was presumably the area of the previously existing CLL cell aggregates/nodules, were still present in a substantial number, possibly indicating that T cells were not affected by treatment

(Figure 4b). Cleaved CASP3 could be observed in the 'empty nodules' possibly indicating apoptotic leukemic cells (Figure 4c and Supplementary Figure S10) as also suggested by the observation of an increased percentage of Annexin-V-positive CLL cells ($P < 0.0001$) in the splenic cell suspension by FC (Figure 4d and Supplementary Table S5).

Decrease *in vitro* viability and growth ability of CLL cells with different cytogenetic features following transfection with miR-15 or miR-16 mimics

We extended our observations to a set of 26 CLL cases lacking biallelic del(13)(q14) (Figure 5 and Supplementary Table S1). The cells from these cases, which expressed different levels of miR-15 and miR-16 as evaluated by qRT-PCR (Supplementary Figure S1c and d), were purified and transfected with miR-15, miR-16 mimics or miR-CTR (Supplementary Figure S2c). Cell viability was significantly decreased following transfection in most cases ($P < 0.001$, Figures 5a and b). Decreased cell viability also was observed when the two major CLL groups were analyzed separately: ie, those with monoallelic del(13)(q14) (statistically significant differences in the miR-15-mimic ($P = 0.01$), miR-16-mimic ($P = 0.005$)-treated cells compared with controls) and the group with normal FISH ($P = 0.004$).

In addition, viability of the cells from other cases, including one with del(11)(q22.3), involving the *ATM* gene, and others with p53 mutations or del(17)(p13.1) was reduced following miR-15 and miR-16 mimic transfection.

Finally, NSG mice were engrafted with cells from two cases harboring monoallelic del(13)(q14) (FP0499, GN0095), one case with trisomy 12 (RD0468), one with a normal FISH pattern (VS0624) and one with del(17)(p13.1) and a *TP53* mutation on the remaining allele (RM0626), and were subsequently treated with miR-15 or miR-16 as above. A significant reduction of splenic disease was observed by FC ($P = 0.0001$ and $P = 0.006$ following miR-15 or miR-16 mimic treatment, respectively compared with miR-CTR; Table 1). A decrease in the IHC index of $72 \pm 18\%$ and $74 \pm 10\%$ following treatment with miR-15 and miR-16 mimics, respectively ($P = 0.001$) was observed in four of the CLL cases tested. Case RM0626 represented a remarkable exception, as treatment with the miRNA mimics consistently failed to significantly block the growth of CLL cells *in vivo*. Of note is the finding that this case had low miR-15 and medium to high miR-16 expression. Thus, the findings were unlikely related to the

Table 1. Inhibition of non-biallelic del(13q14) CLL cell growth in NSG mice by miR-15 or miR-16 mimic treatment

ID	miRNAs treatment (n of mice)	CD45+CD19+CD5+ CLL cells (FC) % (mean \pm s.d.)	CD45+CD19-CD5+ T cells (FC) % (mean \pm s.d.)	IHC index (mean \pm s.d.)
FP0499	miR-CTR mimic (3)	9 \pm 1.7	90 \pm 0.9	137 \pm 36.8
	miR-15 mimic (3)	4 \pm 0.7	87 \pm 2.1	72 \pm 10.8
	miR-16 mimic (2)	2 \pm 0.3	86 \pm 8	26 \pm 7.4
GN0095	miR-CTR mimic (2)	13 \pm 0.5	82 \pm 2.8	107 \pm 12.7
	miR-15 mimic (3)	8 \pm 1.8	86 \pm 2.9	12 \pm 10
	miR-16 mimic (3)	7 \pm 0.7	82 \pm 8.5	23 \pm 13.7
RD0468	miR-CTR mimic (4)	13 \pm 5.4	51 \pm 10.7	56 \pm 5.5
	miR-15 mimic (3)	4 \pm 1.4	60 \pm 2.8	12 \pm 5.8
	miR-16 mimic (3)	5 \pm 1.5	51 \pm 8.4	14 \pm 9.8
VS0624	miR-CTR mimic (3)	18 \pm 1.9	81 \pm 2.7	248 \pm 45.1
	miR-15 mimic (3)	8 \pm 3.6	87 \pm 7.6	68 \pm 7.5
	miR-16 mimic (3)	14 \pm 1.9	79 \pm 6.9	101 \pm 35.1
RM0626	miR-CTR mimic (3)	46 \pm 12.7	51 \pm 15.4	65 \pm 12.9
	miR-15 mimic (2)	58 \pm 2.5	36 \pm 1.4	53 \pm 3.5
	miR-16 mimic (2)	63 \pm 1.8	28 \pm 5.4	53 \pm 8.5

Abbreviations: CLL, chronic lymphocytic leukemia; FC, flow-cytometry; IHC index, immunohistochemical index; miR-15, micro RNA-15.

possibility that the miRNA values were already so high that could not be changed by the transfection. Rather, a completely dysfunctional *TP53* was the possible cause for the findings.

DISCUSSION

This study demonstrates that *in vitro* transfection of miR-15 and miR-16 mimics into CLL cells with del(13)(q14) results in a significant inhibition of their subsequent growth in NSG mice. Furthermore, administration of miR-15 or miR-16 mimics to NSG mice, in which these CLL cells were already engrafted and proliferating, caused significant tumor regression. Both observations are in line with the notion that miR-15 and miR-16 control the cell apoptotic apparatus and proliferative capacities.^{17,23,24} No additive/synergistic effects were noted when miR-15 and miR-16 mimics were co-transfected, suggesting that the regulatory controls of the two miRNAs on the expression of other genes largely overlap, a consideration consistent with the notion that miR-15 and miR-16 interact with the same 3'-UTR region of BCL-2 mRNA.²⁴

Selective inhibition of miR-15 and miR-16 expression in CLL cells resulted in improved *in vitro* survival and a more robust expansion in NSG mice.¹⁶ In contrast, enforced expression of miR-15 or miR-16 in cells retaining the capacity to express these miRNAs resulted in impaired *in vitro* survival or diminished expansion in NSG mice. Both findings provide further support for the regulatory role of intracellular miR-15/miR-16 concentrations in full-blown CLL^{14,23,24,32} (Figure 5). The experimental design utilized here was intended to obtain a specific and selective inhibition or replacement of miR-15 and miR-16 without further influence of other gene segments such as *Dleu2* or *Dleu7*,³⁹ the absence of which have been shown to synergize with that of miR-15 and miR-16 in CLL pathogenesis. Thus, the data demonstrate that low/absent expression of miR-15 and miR-16 plays a crucial pathogenetic role *per se*, in line with the observation that replacement of these miRNAs in NZB mice using suitable viral carriers blocks the expansion of CLL-like cells both *in vivo* and *in vitro*.⁴⁰

MiR-15 or miR-16 mimics did not apparently interfere with the function of T cells that are normally needed to support *in vivo* CLL cell growth. In the experiments where CLL cell growth in NSG mice was inhibited by pre-exposure to miR-15/miR-16 mimics *in vitro* (Figure 2), the T cells were added to the purified CLL cells following their *in vitro* exposure to these miRNAs. However, in experiments, where transfection was carried out *in vitro* on unfractionated cell suspensions, containing both T and CLL cells, before injection into mice, we observed an unaltered distribution pattern of T cells in the spleen of mice even in the presence a largely diminished proportion of B cells. Moreover, when mice were treated with miR-15 or miR-16 mimics *in vivo*, seemingly unaltered T cell proportions were observed surrounding the 'empty' areas, previously occupied by CLL cells (Figure 4). Thus, inhibition of CLL cell growth in NSG mice presumably occurred through interference of the transfected mimics with the CLL cell survival/proliferating apparatus, rather than through an indirect action on the T cells promoting CLL cell growth. Whether or not progressive CLL cell death, induced by the transfected miRNA mimics *in vivo*, may lead to T cell immune-priming capable of causing further CLL cell elimination is presently unknown.

A final issue concerns the potential use of miR-15 and miR-16 for therapy. MiRNA mimics are effective on CLL cells growing *in vivo* and on CLL cells with additional chromosomal alterations; however, some results from both *in vivo* and *in vitro* experiments showed that the presence of *TP53* gene mutations/deletions may render administration of the miR-15 and miR-16 mimics ineffective. This is expected, given the close interactions between miR-15 and miR-16, *TP53* and the cluster of miR-34 genes in the regulation of cell survival/apoptosis.^{41,42} Nevertheless, not all cases with *TP53*

defects failed to respond to miRNA mimics treatment suggesting heterogeneity of functional *TP53* alterations. These observations are being extended to additional cohorts of patients including more advanced stage/relapsed patients that more frequently harbor additional *TP53* alterations.^{43–46}

We provide proof of principle data supporting the potential use of miRNA mimics to block CLL clonal expansion. Additional miRNAs, other than miR-15 or miR-16, may become suitable therapeutic targets, as a number of studies have demonstrated anomalous expression of various miRNAs in CLL cells compared with normal cells.^{11,22,30} Moreover, when certain miRNA are overexpressed, they can be targeted by miRNA inhibitors.⁴⁷ Several anomalies in miRNA expression have prognostic/predictive value for disease course and outcome, indicating a potential mechanistic role in the disease pathogenesis/progression.^{22–24,30,48–52} Thus, the miRNA approach, especially if multiple miRNA mimics and inhibitors can be targeted, either alone or in combination with other drugs, may represent an additional therapeutic strategy. In connection with this, it should be noted that therapy with miR inhibition/replacement is being employed in a variety of experimental tumors. Moreover, there are many available studies on human tumors, some of which have reached the clinical stage I, with potentially promising results.⁵³ Thus, miR therapy may represent a 'real' tool in the future armamentarium of drugs usable in CLL, a disease that so far has escaped attempts toward a radical cure.

CONFLICT OF INTEREST

The authors declare no conflict of interest.

ACKNOWLEDGEMENTS

In addition to the authors listed, the following investigators participated in this study as part of the GISL—Gruppo Italiano Studio Linfomi: Gianni Quintana, Divisione di Ematologia, Presidio Ospedaliero 'A. Perrino', Brindisi; Giovanni Bertoldo, Dipartimento di Oncologia, Ospedale Civile, Noale, Venezia; Paolo Di Tonno, Dipartimento di Ematologia, Venere, Bari; Robin Foà and Francesca R Mauro, Divisione di Ematologia, Università La Sapienza, Roma; Nicola Di Renzo, Unità di Ematologia, Ospedale Vito Fazzi, Lecce; Maria Cristina Cox, Ematologia, A.O. Sant'Andrea, Università La Sapienza, Roma; Stefano Molica, Dipartimento di Oncologia ed Ematologia, Pugliese-Ciaccio Hospital, Catanzaro; Attilio Guarini, Unità di Ematologia e Trapianto di Cellule Staminali, Istituto di Oncologia 'Giovanni Paolo II', Bari; Antonio Abbadesse, U.O.C. di Oncoematologia Ospedale 'S. Anna e S. Sebastiano', Caserta; Francesco Iuliano, U.O.C. di Oncologia, Ospedale Giannettasio, Rossano Calabro, Cosenza; Omar Racchi, Ospedale Villa Scassi Sampierdarena, Genova; Mauro Spriano, Ematologia, A.O. San Martino, Genova; Felicetto Ferrara, Divisione di Ematologia, Ospedale Cardarelli, Napoli; Monica Crugnola, Ematologia, CTMO, Azienda Ospedaliera Universitaria di Parma; Alessandro Andriani, Dipartimento di Ematologia, Ospedale Nuovo Regina Margherita, Roma; Nicola Cascavilla, Unità di Ematologia e Trapianto di Cellule Staminali, IRCCS Ospedale Casa Sollievo della Sofferenza, San Giovanni Rotondo; Lucia Ciuffreda, Unità di Ematologia, Ospedale San Nicola Pellegrino, Trani; Graziella Pinotti, U.O. Oncologia Medica, Ospedale di Circolo Fondazione Macchi, Varese; Anna Pascarella, Unità Operativa di Ematologia, Ospedale dell'Angelo, Venezia-Mestre; Maria Grazia Lipari, Divisione di Ematologia, Ospedale Policlinico, Palermo; Francesco Merli, Unità Operativa di Ematologia, A.O.S. Maria Nuova, Reggio Emilia; Luca Baldini Istituto di Ricovero e Cura a Carattere Scientifico Cà Granda-Maggiore Policlinico, Milano; Caterina Musolino, Divisione di Ematologia, Università di Messina; Agostino Cortelezzi, Ematologia and CTMO, Fondazione IRCCS Ca' Granda Ospedale Maggiore Policlinico, Milano; Francesco Angrilli, Dipartimento di Ematologia, Ospedale Santo Spirito, Pescara; Ugo Consoli, U.O.S. di Emato-Oncologia, Ospedale Garibaldi-Nesima, Catania; Gianluca Festini, Centro di Riferimento Ematologico-Seconda Medicina, Azienda Ospedaliero-Universitaria, Ospedali Riuniti, Trieste; Giuseppe Longo, Unità di Ematologia, Ospedale San Vincenzo, Taormina; Daniele Vallisa and Annalisa Arcari, Unità di Ematologia, Dipartimento di Onco-Ematologia, Guglielmo da Saliceto Hospital, Piacenza; Francesco Di Raimondo and Annalisa Chiarenza, Divisione di Ematologia, Università di Catania Ospedale Ferrarotto, Catania; Iolanda Vincelli, Unità di Ematologia, A.O. of Reggio Calabria; Donato Mannina, Divisione di Ematologia, Ospedale Papardo, Messina, Italy. This work was supported by Associazione Italiana Ricerca sul Cancro (AIRC) Grant 5 x mille n.9980, (to MF, FM, AN, PT and MN); AIRC I.G. n.14326 (to MF), n.10136 and 16722 (AN), n.15426 (to FF). AIRC and Fondazione CaRiCal co-financed Multi Unit Regional Grant 2014 n.16695 (to FM). Italian Ministry

of Health 5x1000 funds (to SZ and FF). AGR was supported by Associazione Italiana contro le Leucemie-Linfomi-Mielomi (AIL) Cosenza—Fondazione Amelia Scorza (FAS). SM, CM, MC, LE and SB were supported by AIRC.

AUTHOR CONTRIBUTIONS

Conception and design: GC, GB, FF and MF; Development of methodology: GC, SM, CM, GB, MC, DR, RM, SS, SB, LE and SF; Acquisition of data: GC, SM, LE, MC, GB, MM, SF, SS, DR, RM, FV, SZ, FM and MN; Analysis and interpretation of data: GC, SM, GB, CM, AN, SS, MC, SF, CEN, MC, FR, LB, FF, SZ, MN, PT, MG, MT, MF and FM; Writing, review, and/or revision of the manuscript: GC, AGR, MN, PT, AN, FF and MF; Study supervision: GC, FF and MF. All authors reviewed and approved the manuscript.

REFERENCES

- Chiorazzi N, Rai KR, Ferrarini M. Chronic lymphocytic leukemia. *N Engl J Med* 2005; **352**: 804–815.
- Dohner H, Stilgenbauer S, James MR, Benner A, Weigl T, Bentz M et al. 11q deletions identify a new subset of B-cell chronic lymphocytic leukemia characterized by extensive nodal involvement and inferior prognosis. *Blood* 1997; **89**: 2516–2522.
- Neilson JR, Auer R, White D, Bienz N, Waters JJ, Whittaker JA et al. Deletions at 11q identify a subset of patients with typical CLL who show consistent disease progression and reduced survival. *Leukemia* 1997; **11**: 1929–1932.
- Dohner H, Stilgenbauer S, Benner A, Leupolt E, Krober A, Bullinger L et al. Genomic aberrations and survival in chronic lymphocytic leukemia. *N Engl J Med* 2000; **343**: 1910–1916.
- Grever MR, Lucas DM, Dewald GW, Neuberg DS, Reed JC, Kitada S et al. Comprehensive assessment of genetic and molecular features predicting outcome in patients with chronic lymphocytic leukemia: results from the US Intergroup Phase III Trial E2997. *J Clin Oncol* 2007; **25**: 799–804.
- Stilgenbauer S, Zenz T, Winkler D, Buhler A, Schlenk RF, Groner S et al. Subcutaneous alemtuzumab in fludarabine-refractory chronic lymphocytic leukemia: clinical results and prognostic marker analyses from the CLL2H study of the German Chronic Lymphocytic Leukemia Study Group. *J Clin Oncol* 2009; **27**: 3994–4001.
- Fischer K, Cramer P, Busch R, Bottcher S, Bahlo J, Schubert J et al. Bendamustine in combination with rituximab for previously untreated patients with chronic lymphocytic leukemia: a multicenter phase II trial of the German Chronic Lymphocytic Leukemia Study Group. *J Clin Oncol* 2012; **30**: 3209–3216.
- Zenz T, Habe S, Denzel T, Mohr J, Winkler D, Buhler A et al. Detailed analysis of p53 pathway defects in fludarabine-refractory chronic lymphocytic leukemia (CLL): dissecting the contribution of 17p deletion, TP53 mutation, p53-p21 dysfunction, and miR34a in a prospective clinical trial. *Blood* 2009; **114**: 2589–2597.
- Kalachikov S, Migliazza A, Cayanis E, Fracchiolla NS, Bonaldo MF, Lawton L et al. Cloning and gene mapping of the chromosome 13q14 region deleted in chronic lymphocytic leukemia. *Genomics* 1997; **42**: 369–377.
- Rawstron AC, Bennett FL, O'Connor SJ, Kwok M, Fenton JA, Plummer M et al. Monoclonal B-cell lymphocytosis and chronic lymphocytic leukemia. *N Engl J Med* 2008; **359**: 575–583.
- Morabito F, Mosca L, Cutrona G, Agnelli L, Tuana G, Ferracin M et al. Clinical monoclonal B lymphocytosis versus Rai 0 chronic lymphocytic leukemia: A comparison of cellular, cytogenetic, molecular, and clinical features. *Clin Cancer Res* 2013; **19**: 5890–5900.
- Liu Y, Corcoran M, Rasool O, Ivanova G, Ibbotson R, Grandt D et al. Cloning of two candidate tumor suppressor genes within a 10 kb region on chromosome 13q14, frequently deleted in chronic lymphocytic leukemia. *Oncogene* 1997; **15**: 2463–2473.
- Migliazza A, Bosch F, Komatsu H, Cayanis E, Martinotti S, Toniato E et al. Nucleotide sequence, transcription map, and mutation analysis of the 13q14 chromosomal region deleted in B-cell chronic lymphocytic leukemia. *Blood* 2001; **97**: 2098–2104.
- Calin GA, Dumitru CD, Shimizu M, Bichi R, Zupo S, Noch E et al. Frequent deletions and down-regulation of micro-RNA genes miR15 and miR16 at 13q14 in chronic lymphocytic leukemia. *Proc Natl Acad Sci USA* 2002; **99**: 15524–15529.
- Mosca L, Fabris S, Lionetti M, Todoerti K, Agnelli L, Morabito F et al. Integrative genomics analyses reveal molecularly distinct subgroups of B-cell chronic lymphocytic leukemia patients with 13q14 deletion. *Clin Cancer Res* 2010; **16**: 5641–5653.
- Klein U, Lia M, Crespo M, Siegel R, Shen Q, Mo T et al. The DLEU2/miR-15a/16-1 cluster controls B cell proliferation and its deletion leads to chronic lymphocytic leukemia. *Cancer Cell* 2010; **17**: 28–40.
- Sellmann L, Scholtysik R, Kreuz M, Cyrrill S, Tiacci E, Stanelle J et al. Gene dosage effects in chronic lymphocytic leukemia. *Cancer Genet Cytogenet* 2010; **203**: 149–160.
- Lagos-Quintana M, Rauhut R, Lendeckel W, Tuschl T. Identification of novel genes coding for small expressed RNAs. *Science* 2001; **294**: 853–858.
- Ghildiyal M, Zamore PD. Small silencing RNAs: an expanding universe. *Nat Rev Genet* 2009; **10**: 94–108.
- Hausser J, Zavolan M. Identification and consequences of miRNA-target interactions—beyond repression of gene expression. *Nat Rev Genet* 2014; **15**: 599–612.
- Ouillette P, Erba H, Kujawski L, Kaminski M, Shedden K, Malek SN. Integrated genomic profiling of chronic lymphocytic leukemia identifies subtypes of deletion 13q14. *Cancer Res* 2008; **68**: 1012–1021.
- Negrini M, Cutrona G, Bassi C, Fabris S, Zagatti B, Colombo M et al. microRNAome expression in chronic lymphocytic leukemia: comparison with normal B-cell subsets and correlations with prognostic and clinical parameters. *Clin Cancer Res* 2014; **20**: 4141–4153.
- Calin GA, Cimmino A, Fabbri M, Ferracin M, Wojcik SE, Shimizu M et al. MiR-15a and miR-16-1 cluster functions in human leukemia. *Proc Natl Acad Sci USA* 2008; **105**: 5166–5171.
- Cimmino A, Calin GA, Fabbri M, Iorio MV, Ferracin M, Shimizu M et al. miR-15 and miR-16 induce apoptosis by targeting BCL2. *Proc Natl Acad Sci USA* 2005; **102**: 13944–13949.
- Linsley PS, Schelter J, Burchard J, Kibukawa M, Martin MM, Bartz SR et al. Transcripts targeted by the microRNA-16 family cooperatively regulate cell cycle progression. *Mol Cell Biol* 2007; **27**: 2240–2252.
- Allegra D, Bilan V, Garding A, Dohner H, Stilgenbauer S, Kuchenbauer F et al. Defective DROSHA processing contributes to downregulation of miR-15/16 in chronic lymphocytic leukemia. *Leukemia* 2014; **28**: 98–107.
- Veronese A, Pepe F, Chiacchia J, Pagotto S, Lanuti P, Veschi S et al. Allele-specific loss and transcription of the miR-15a/16-1 cluster in chronic lymphocytic leukemia. *Leukemia* 2015; **29**: 86–95.
- Mertens D, Wolf S, Tschuch C, Mund C, Kienle D, Ohl S et al. Allelic silencing at the tumor-suppressor locus 13q14.3 suggests an epigenetic tumor-suppressor mechanism. *Proc Natl Acad Sci USA* 2006; **103**: 7741–7746.
- Raveche ES, Salerno E, Scaglione BJ, Manohar V, Abbasi F, Lin YC et al. Abnormal microRNA-16 locus with synteny to human 13q14 linked to CLL in NZB mice. *Blood* 2007; **109**: 5079–5086.
- Calin GA, Ferracin M, Cimmino A, Di Leva G, Shimizu M, Wojcik SE et al. A MicroRNA signature associated with prognosis and progression in chronic lymphocytic leukemia. *N Engl J Med* 2005; **353**: 1793–1801.
- Underbayev C, Kasar S, Ruezinsky W, Degheidy H, Schneider JS, Marti G et al. Role of miR-15a/16-1 in early B cell development in a mouse model of chronic lymphocytic leukemia. *Oncotarget* 2016; **7**: 60986–60999.
- Pekarsky Y, Croce CM. Role of miR-15/16 in CLL. *Cell Death Differ* 2015; **22**: 6–11.
- Morabito F, Cutrona G, Gentile M, Fabris S, Matis S, Vigna E et al. Is ZAP70 still a key prognostic factor in early stage chronic lymphocytic leukaemia? Results of the analysis from a prospective multicentre observational study. *Br J Haematol* 2015; **168**: 455–459.
- Lionetti M, Fabris S, Cutrona G, Agnelli L, Ciardullo C, Matis S et al. High-throughput sequencing for the identification of NOTCH1 mutations in early stage chronic lymphocytic leukaemia: biological and clinical implications. *Br J Haematol* 2014; **165**: 629–639.
- Cutrona G, Colombo M, Matis S, Fabbi M, Spriano M, Callea V et al. Clonal heterogeneity in chronic lymphocytic leukemia cells: superior response to surface IgM cross-linking in CD38, ZAP-70-positive cells. *Haematologica* 2008; **93**: 413–422.
- Durig J, Ebeling P, Grabellus F, Sorg UR, Mollmann M, Schutt P et al. A novel nonobese diabetic/severe combined immunodeficient xenograft model for chronic lymphocytic leukemia reflects important clinical characteristics of the disease. *Cancer Res* 2007; **67**: 8653–8661.
- Bagnara D, Kaufman MS, Calissano C, Marsilio S, Patten PE, Simone R et al. A novel adoptive transfer model of chronic lymphocytic leukemia suggests a key role for T lymphocytes in the disease. *Blood* 2011; **117**: 5463–5472.
- Valdora F, Cutrona G, Matis S, Morabito F, Massucco C, Emionite L et al. A non-invasive approach to monitor chronic lymphocytic leukemia engraftment in a xenograft mouse model using ultra-small superparamagnetic iron oxide-magnetic resonance imaging (USPIO-MRI). *Clin Immunol* 2016; **172**: 52–60.
- Palamarchuk A, Efanov A, Nazaryan N, Santanam U, Alder H, Rassenti L et al. 13q14 deletions in CLL involve cooperating tumor suppressors. *Blood* 2010; **115**: 3916–3922.
- Kasar S, Salerno E, Yuan Y, Underbayev C, Vollenweider D, Laurindo MF et al. Systemic in vivo lentiviral delivery of miR-15a/16 reduces malignancy in the NZB

- de novo mouse model of chronic lymphocytic leukemia. *Genes Immun* 2012; **13**: 109–119.
- 41 Fabbri M, Bottoni A, Shimizu M, Spizzo R, Nicoloso MS, Rossi S *et al*. Association of a microRNA/TP53 feedback circuitry with pathogenesis and outcome of B-cell chronic lymphocytic leukemia. *JAMA* 2011; **305**: 59–67.
- 42 Lin K, Farahani M, Yang Y, Johnson GG, Oates M, Atherton M *et al*. Loss of MIR15A and MIR16-1 at 13q14 is associated with increased TP53 mRNA, de-repression of BCL2 and adverse outcome in chronic lymphocytic leukaemia. *Br J Haematol* 2014; **167**: 346–355.
- 43 Herling CD, Klaumunzer M, Rocha CK, Altmuller J, Thiele H, Bahlo J *et al*. Complex karyotypes and KRAS and POT1 mutations impact outcome in CLL after chlorambucil-based chemotherapy or chemoimmunotherapy. *Blood* 2016; **128**: 395–404.
- 44 Rossi D, Rasi S, Spina V, Bruscazzin A, Monti S, Ciardullo C *et al*. Integrated mutational and cytogenetic analysis identifies new prognostic subgroups in chronic lymphocytic leukemia. *Blood* 2013; **121**: 1403–1412.
- 45 Landau DA, Carter SL, Stojanov P, McKenna A, Stevenson K, Lawrence MS *et al*. Evolution and impact of subclonal mutations in chronic lymphocytic leukemia. *Cell* 2013; **152**: 714–726.
- 46 Guieze R, Robbe P, Clifford R, de Guibert S, Pereira B, Timbs A *et al*. Presence of multiple recurrent mutations confers poor trial outcome of relapsed/refractory CLL. *Blood* 2015; **126**: 2110–2117.
- 47 Saleh LM, Wang W, Herman SE, Saba NS, Anastas V, Barber E *et al*. Ibrutinib downregulates a subset of miRNA leading to upregulation of tumor suppressors and inhibition of cell proliferation in chronic lymphocytic leukemia. *Leukemia* 2017; **31**: 340–349.
- 48 Calin GA, Liu CG, Sevignani C, Ferracin M, Felli N, Dumitru CD *et al*. MicroRNA profiling reveals distinct signatures in B cell chronic lymphocytic leukemias. *Proc Natl Acad Sci USA* 2004; **101**: 11755–11760.
- 49 Visone R, Rassenti LZ, Veronese A, Taccioli C, Costinean S, Aguda BD *et al*. Karyotype-specific microRNA signature in chronic lymphocytic leukemia. *Blood* 2009; **114**: 3872–3879.
- 50 Pekarsky Y, Santanam U, Cimmino A, Palamarchuk A, Efanov A, Maximov V *et al*. Tcl1 expression in chronic lymphocytic leukemia is regulated by miR-29 and miR-181. *Cancer Res* 2006; **66**: 11590–11593.
- 51 Bresin A, Callegari E, D'Abundo L, Cattani C, Bassi C, Zagatti B *et al*. miR-181b as a therapeutic agent for chronic lymphocytic leukemia in the Emicro-TCL1 mouse model. *Oncotarget* 2015; **6**: 19807–19818.
- 52 Visone R, Veronese A, Rassenti LZ, Balatti V, Pearl DK, Acunzo M *et al*. miR-181b is a biomarker of disease progression in chronic lymphocytic leukemia. *Blood* 2011; **118**: 3072–3079.
- 53 Shah MY, Ferrajoli A, Sood AK, Lopez-Berestein G, Calin GA. microRNA therapeutics in cancer—an emerging concept. *EBioMedicine* 2016; **12**: 34–42.

Supplementary Information accompanies this paper on the Leukemia website (<http://www.nature.com/leu>)

Genova, 04th June 2019

To whom it may concern

This is to confirm that Dr Gabriella Baio had the contribution stated below for each of the following publications:

Role: Principal investigator, conception and design, development of methodology, acquisition of data, analysis and interpretation of data, writing, review, and/or revision of the manuscript, study supervision.

- **Baio G**, Fabbi M, de Toterò D, Ferrini S, Cilli M, Derchi LE, Neumaier CE. Magnetic resonance imaging at 1.5 T with immunospecific contrast agent in vitro and in vivo in a xenotransplant model. *MAGMA* 2006 Dec; 19:313-20.
- Neumaier CE, **Baio G**, Ferrini S, Corte G, Daga A. MR and iron magnetic nanoparticles. Imaging opportunities in preclinical and translational research. *Review Tumori* 2008 Mar-Apr; 94:226-33.
- **Baio G**, Fabbi M, Salvi S, de Toterò D, Truini M, Ferrini S, Neumaier CE. Two-step in vivo tumor targeting by biotin-conjugated antibodies and superparamagnetic nanoparticles assessed by magnetic resonance imaging at 1.5T. *Mol Imaging and Biol*, 2010 Jun; 12(3):305-15.
- **Baio G**, Fabbi M, Emionite L, Cilli M, Salvi S, Ghedin P, Prato S, Carbotti G, Tagliafico A, Truini M, Neumaier CE. In vivo imaging of human breast cancer mouse model with high level expression of calcium sensing receptor at 3T. *Eur Radiol*. 2012 Mar; 22(3):551-8.
- **Baio G**, Valdora F, Pace D, Salvi S, Villosio N, Truini M, Calabrese M and Neumaier CE. The key role of correlation between MR spectroscopy choline peak and calcium sensing receptor for breast cancer: Diagnosis by a 3T MR scanner. *Journal of Clinical Oncology, ASCO 2013 Vol 31, No 15_suppl (May 20 Supplement)*.
- **Baio G**, Rescinito G, Rosa F, Pace D, Boccardo S, Basso L, Salvi S, Calabrese M, Truini M, Neumaier CE. Correlation between Choline Peak at MR Spectroscopy and Calcium-Sensing Receptor Expression Level in Breast Cancer: A Preliminary Clinical Study. *Mol Imaging Biol*. 2015 Aug; 17(4):548-56.
- Valdora F, Cutrona G, Matis S, Morabito F, Massucco C, Emionite L, Boccardo S, Basso L, Recchia AG, Salvi S, Rosa F, Gentile M, Ravina M, Pace D, Castronovo A, Cilli M, Truini M, Calabrese M, Neri A, Neumaier CE, Fais F, **Baio G**, Ferrarini M. A non-invasive approach to monitor chronic lymphocytic leukemia engraftment in a xenograft mouse model using ultra-small superparamagnetic iron oxide-magnetic resonance imaging (USPIO-MRI). *Clin Immunol*. 2016 Jul 15.



- Rosa F, Basso L, Pace D, Secondini L, Boccardo S, Neumaier CE, **Baio G**. In Vivo Non-invasive Detection of Brown Adipose Tissue through Manganese Enhanced Magnetic Resonance Imaging (MEMRI). WMIC 2015. P688.

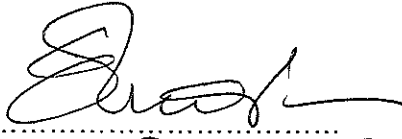
Role: Conception and design, analysis and interpretation of data, writing, review, and/or revision of the chapter.

- **Baio G**, Neumaier CE. "T2 weighted MR contrast agents for cancer research. Chapter 22. Molecular Imaging Probes for Cancer Research, Editor Xiaoyuan Chen, Publisher: World Scientific Sept. 2012.

Role: Conception and design of the imaging methodology, development of imaging methodology, acquisition of data, analysis and interpretation of data, writing, review, and/or revision of the manuscript, imaging study supervision.

- Cutrona G, Matis S, Colombo M, Massucco C, **Baio G**, Valdora F, Emionite L, Fabris S, Recchia AG, Gentile M, Neumaier CE, Reverberi D, Massara R, Boccardo S, Basso L, Salvi S, Rosa F, Cilli M, Zupo S, Truini M, Tassone P, Calabrese M, Negrini M, Neri A, Morabito F, Fais F, Ferrarini M. Effects of miRNA-15 and miRNA-16 expression replacement in chronic lymphocytic leukemia: implication for therapy. Leukemia. 2017 Feb 3.

I can confirm that Dr Gabriella Baio was involved in the all the aspects stated above of this research.

Signed 
Date 05 06 2019

Dr Carlo Emanuele Neumaier
Senior Research Supervisor
Policlinico San Martino, Genova, Italy

Torino, 04th June 2019

To whom it may concern

This is to confirm that Dr Gabriella Baio had the contribution stated below for each of the following publications:

Gianolio E, Arena F, Di Gregorio E, Pagliarin R, Delbianco M, **Baio G**, Aime S. MEMRI and Tumors: A method for the evaluation of the contribution of Mn(II) ions in the extra- cellular compartment. NMR in Biomedicine 2015 Jul 14. Doi: 10.1002/nbm.3349.

Role: Co-investigator, conception and design, development of methodology, acquisition of data, analysis and interpretation of data, writing, review, and/or revision of the manuscript, study supervision.

I can confirm that Dr Gabriella Baio was involved in the all the aspects stated above of this research.



Signed.....

Date...04-06-19.....

Prof Silvio Aime

Professor of General and Inorganic Chemistry

Chair, Department of Molecular Biotechnology and Health Science

Vice-dean, University of Torino, Italy

Discussion and Conclusion

Where are we now? Where are we going?

Despite many recent advances in non-invasive imaging technologies, such as MRI, we are still limited in our ability to detect, monitor, and assess tumour response to treatment at molecular levels. The advent of “molecular imaging” with specific molecular probes was set to radically change this situation, and to revolutionise our approach to the detection and treatment of cancer [15,16,147,148].

To better understand the impact of the “molecular revolution” in medicine, we must look at the astonishing developments in other specialties that we have witnessed over the past ten years. The most striking examples have been the introduction of more specific drugs and inhibitors, the ability to genetically engineer and repair cells and tissues, and the commercialisation of a multitude of diagnostic tools and kits (such as DNA and protein assays). These tools have led to dramatic advancements in the understanding of the molecular pathways of cancer. The knowledge of these new targets and pathways can now be translated into new drugs and many of them are now commercially available. We expect that these developments will ultimately allow the earlier detection of disease, resulting in improved patient care.

The question regarding the role of imaging in this “molecular revolution” is how we, as radiologists, can be actively engaged in molecular medical research, and how this can help the translation of molecular discoveries clinically facilitated by early imaging diagnosis.

One of the key topics of radiology’s engagement in molecular imaging is more efficient involvement of biologists and chemists in our specialty. Basic

scientists and imaging specialties have long been in separate worlds. Bridging these two worlds is still difficult, but it is necessary to build bridges in order to advance the field. This can be achieved by attracting and training new Radiology trainees eager to learn more about molecular developments and stimulating their interest by engaging them more in basic science research, in order to successfully translate the new discoveries into clinical imaging applications.

As I initially stated in this thesis, the first research that we developed in 2005 was part of a pioneering Italian work. We were one of only two research groups in Italy working in the field of new molecular imaging probes for MRI, and we were the only radiologists, since the other group, led by Silvio Aime in Turin, were chemists.

For myself, first as a radiology trainee and later as a consultant radiologist, it has been a great experience working and collaborating with people with such a variety of expertise: immunologists, biologists, bioengineers, chemists, and physicists. I had the opportunity not only to gain more knowledge in basic science, but also to “open my mind” as a clinician to something more adventurous, representing an important part of the future of radiology.

Over these ten years of research, I had the opportunity to attend most of the European and International Molecular Imaging conferences, providing my active contribution either as attendee or as a scientific reviewer. The well-known “translation from the bench to the bedside” has been, over these years, the main “leitmotif” of our MI scientific community and, especially

for MR molecular imaging probes, we are still far from applying these in our daily clinical routine.

Magnetic resonance imaging has had a great development in biomedical engineering and computing science. MR scanners are now markedly improved in terms of resolution and speed as compared with those of only a few years ago, allowing concomitant acquisition of functional and physiological information. However, when we think about translating a preclinical MR imaging study into clinical practice, we need to consider that there are both technical and biological challenges that can impede immediate translation. Preclinical scanners often have technical advantages over clinical scanners, with increased field strength (from 4.7 to 9.4T, but can be as high as 22T) and high-performance gradients that allow for higher temporal and spatial resolution compared with the clinical setting [149]. However, preclinical systems often lack the wide selection of clinically available coils optimised for target geometry or image acceleration (e.g. multichannel), requiring the development of lab-specific coils. Finally, while the higher field strengths of preclinical systems are attractive from a signal-to-noise perspective, the tissue contrast can be significantly reduced, especially for T1-weighted imaging, confounding translation to typical clinical field strengths of 1.5T and 3.0T. For this reason, one of the novelties of our MI research was the application of a clinical MR scanner to a preclinical imaging study to facilitate the translation of the results obtained preclinically into the clinical setting. This study led to the development of a new prototype birdcage coil for a clinical MR scanner in collaboration with a well-known imaging healthcare company.

In addition to the technical considerations mentioned above, the translation of a novel imaging study depends also on the selection of an appropriate animal model. Cancer animal models are developed to recapitulate the imaging and pathophysiological features of human cancers; however, we learned by the recent introduction of the models based on patient-derived xenografts, that the knowledge gained from certain type of cancer animal models may be of limited value for optimising an imaging approach (for example, the rodent models of C6 and 9L glioblastoma tumour, which grow in different patterns compared with a human brain tumour) [149].

The development of an MR contrast agent is a very complex field which requires a long experimental phase, from the proof of concept until the clinical application of the new agent. Sometimes this leads to a very unsuccessful clinical application: an example has been the clinical application of USPIO (Sinerem[®], Guerbet, Paris) to visualise metastatic prostate or urinary bladder lymph nodes. After a long phase 3, this contrast never reached the imaging market and it is not routinely used in the clinic. One of the main reasons that MR contrast agents are very difficult to get into clinical environment is the potential toxicity of the compounds, which necessitates strict safety regulations.

On the other side, with the advent of PET/CT in Nuclear Medicine, we have seen the development of a large number of new PET tracers over the years. These new tracers are applied not only preclinically but also clinically, as diagnostic as well as therapeutic tools, in keeping with the concept of “theragnostic imaging”.

One of the most striking examples has been shown in detection of metastatic prostate cancer in initial and recurrent staging prostate cancer: novel functional and targeted imaging agents, exhibiting both high sensitivity and specificity for detecting metastatic prostate cancer, have been developed, including radiolabelled choline, prostate specific membrane antigen (PSMA), and anti-¹⁸F-fluorocyclobutane-1-carboxylic acid (¹⁸F-FACBC) that are among some of the most promising novel PET agents [150]. The combination of specific PET tracer, such as ⁶⁸Ga-PSMA-PET/CT and MRI, in guiding intra-prostatic biopsy, has been successfully shown in several studies [151, 152]. Furthermore, PET tracer avidity correlates well with gross tumour volume as detected by multiparametric MRI, and voxel based determinants directly match to histopathological specimens. This correlation supports another important concept of “multimodality imaging”, where the utilisation of the data provided by the combination of the two techniques is partially reducing sampling error and improving diagnostic accuracy of targeted biopsy. Attempts at improving surgical detection by probe techniques, similar to those described with sentinel node biopsy, have also been attempted, to improve lymphadenectomy both in the primary and salvage settings of prostate cancer. Although data are limited, the use of a gamma probe to detect the ¹¹¹In-PSMA injected pre-operatively appears promising in detecting PSMA-avid occult small volume/micro-metastatic nodal disease [153-155].

All these studies are demonstrating the potential theragnostic implications of PET tracers and their applications that are increasingly at the forefront of oncology [156-159]. The power of this theragnostic paradigm, prior to that of prostate cancer, has been well demonstrated in gastroenteropancreatic neuroendocrine tumors (GEP-NETs) over many years [160-167] and recently confirmed in the randomized controlled NETTER-1 trial

showing a five-fold improvement in response with ^{177}Lu -DOTATATE (Lutathera™) compared with conventional treatment [168].

The theragnostic principle is simply allowing us “to see what we treat and treat what we see” [167]. In this optic, the use of molecular imaging agents to target specific therapy is directly analogous to the use of Herceptin in patients with breast cancer that we have discussed in Chapter 1 [14] where treatment is only given following the demonstration of specific HER-2 receptor expression on tumor cells [169] or for example, as we demonstrated in our early experiments, by applying a specific UPSIO conjugates antibody anti-CD20 (rituximab) directed to high CD20 lymphoma tumours [17]. PET/CT imaging by using ^{68}Ga -PSMA performs the same gate keeping function by in vivo demonstration of the upregulation of the PSMA receptor in prostate cancer.

In the course of using these novel agents we need to consider that a manifold of pitfalls has also been discovered and in this regard, a great deal of progress has been made by the introduction of several framework systems for theragnostic PET radiotracers (such as for example, the PROstate cancer Molecular Imaging Standardization Evaluation (PROMISE), the European Association of Nuclear Medicine and Molecular Imaging and Society of Nuclear Medicine and Molecular Imaging joint procedure guideline for PSMA-targeted PET (EANM), and the NeuroEndocrine Tumor Positron Emission Tomography (NETPET) grading system for NETs) [170-172].

Both, PET/CT with novel PET tracer and MR with specific MRI probes, are clearly demonstrating that MI is not the exclusive domain of a single imaging technology or field. In fact, the success of this field is in the integrated application of a broad range of technologies for producing image

signals [173]. The information gained through multimodality imaging permits more complete delineation and characterisation of the biological process than by using only one modality. Thus, while we cannot state that Molecular Magnetic Resonance probes are easily translatable into the clinical setting, we can certainly state that a multimodality imaging approach has now been brought to the bedside, as is evident from the increasing use of hybrid imaging such as PET/CT, SPECT/CT, and recently the application of clinical PET/MR imaging. The concept of integrated multimodality imaging in clinical practice will certainly improve accuracy for detecting and quantifying diseases, permit monitoring responses to treatment, and provide a means for improved targeting and outcome prediction.

The progress, made in medical imaging techniques, and the development of high-throughput algorithms to extract quantitative features from medical images has led to the development of another approach to perform molecular imaging, called “radiomics” [174]. In clinical research, radiomics is becoming a meaningful tool and might be considered as an additional and complementary source of the so called “omic information” (such as genomics, transcriptomics, or epigenomics), not achievable in a multi-omics biological environment. In this scenario, the growing impact of non-invasive imaging techniques for disease definition, in parallel with the evolution of next-generation sequencing tools, provides powerful methods for investigating tissue phenotype through the combination of imaging characteristics (radiomic features) into a multi-omics biological framework. Indeed, the correlation of radiomic features with genomic features, has given rise to a field of study defined as “radiogenomics” [175]. The increasing scale and availability of a high volume of health data certainly requires new and efficient strategies for data management, data linkage and data

integration. These types of datasets are defined as “multimodal” [176]. In this context, there are many challenges to overcome such as: i) identifying relationships between the data produced by different imaging modalities, ii) joining multimodal information for prediction, iii) learning information to help understand limited data of another modality and iiiii) representing, integrating and summarizing multimodal data [174]. Thus, in order to optimise data management and analysis, it is necessary to reshape the existing information systems into innovative multi-layer data systems by combining statistical and computational methods. So far, no tools integrating genomic and radiomic data have been designed; therefore, consolidating single-omic datasets from different domains in a meaningful manner is the next ambitious undertaking of this “new approach of radiology analysis”.

To conclude, this thesis, and the publications collected herein, is not meant to demonstrate the impact of each single topic within the scientific community but, in a broader, more general view, it is intended to demonstrate how the improvement of knowledge gained either by preclinical or clinical studies is of great support for cancer detection and diagnosis. Furthermore, I propose that radiology has its own important place in basic science supporting the identification of cancer targets for therapeutic strategies and therapy response monitoring.



ISMRM Molecular and Cellular Imaging Study Group Workshop: Cruising Into Molecular and Cellular Imaging. Western Caribbean Cruise from Galveston, Texas, USA to Cozumel, Mexico, February 2007.

References

- [1] Krestin GP, Bernsen MR. Molecular imaging in radiology: the latest fad or the new frontier? *Eur Radiol* 2006; **16**(11):2383-2385
- [2] Pressman D, Keighley G. The zone of activity of antibodies as determined by the use of radioactive tracers. *Fed Proc*; 1948; **7**(1 Pt 1):308.
- [3] Pressman D, Korngold L. The in vivo localization of anti-Wagner-osteogenic-sarcoma antibodies. *Cancer*; 1953; **6**(3):619-23.
- [4] Goldenberg DM, DeLand F, Kim E *et al.* Use of radiolabelled antibodies to carcinoembryonic antigen for the detection and localization of diverse cancers by external photoscanning. *N Engl J Med*; 1978; **298**(25):1384-6.
- [5] Goldenberg DM, Preston DF, Primus FJ, Hansen HJ. Photoscan localization of GW-39 tumours in hamsters using radiolabelled anticarcinoembryonic antigen immunoglobulin G. *Cancer Res*; 1974; **34**(1):1-9.
- [6] Goldenberg DM, Gaffar SA, Bennett SJ, Beach JL. Experimental radioimmunotherapy of a xenografted human colonic tumour (GW-39) producing carcinoembryonic antigen. *Cancer Res*; 1981; **41**(11 Pt 1):4354-4360.
- [7] Hnatowich DJ, Virzi F, Rusckowski M. Investigations of avidin and biotin for imaging applications. *J Nucl Med*; 1987; **28**(8):1294-1302.
- [8] Reimer P, Weissleder R, Lee AS, Wittenberg J, Brady TJ. Receptor imaging: application to MR imaging of liver cancer. *Radiology*; 1990; **177**(3):729-34.
- [9] Reimer P, Weissleder R, Wittenberg J, Brady TJ. Receptor-directed contrast agents for MR imaging: preclinical evaluation with affinity assays; *Radiology*; 1992; **182**(2):565-569.
- [10] Artemov D. Molecular magnetic resonance imaging with targeted contrast agents. *J Cell Biochem*; 2003; **90**(3):518-524.

- [11] Burtea C, Laurent S, Vander Elst L, Muller RN. Contrast agents: magnetic resonance. *Handb Exp Pharmacol*; 2008; **185**(Pt 1):135-165.
- [12] Tanimoto A, Oshio K, Suematsu M, Pouliquen D, Stark DD. Relaxation effects of clustered particles. *J Magn Reson Imaging*; 2001; **14**(1):72-77.
- [13] Ferrucci JT, Stark DD. Iron oxide-enhanced MR imaging of the liver and spleen: review of the first 5 years. *AJR Am J Roentgenol*; 1990; **155**(5):943-950.
- [14] Artemov D, Mori N, Okollie B, Bhujwalla ZM. MR molecular imaging of the Her-2/neu receptor in breast cancer cells using targeted iron oxide nanoparticles. *Magn Reson Med*; 2003; **49**(3):403-408.
- [15] Weissleder R. Scaling down imaging: molecular mapping of cancer in mice. *Nat Rev Cancer*; 2002; **2**(1):11-18.
- [16] Massoud TF, Gambhir SS. Molecular imaging in living subjects: seeing fundamental biological processes in a new light. *Genes Dev*; 2003; **17**(5):545-580.
- [17] Baio G, Fabbi M, de Toter D *et al*. Magnetic resonance imaging at 1.5 T with immunospecific contrast agent in vitro and in vivo in a xenotransplant model. *MAGMA*; 2006; **19**(6):313-320.
- [18] Molecular Imaging probes for cancer research”, edited by Professor Xiaoyuan Chen, Laboratory of Molecular Imaging and Nanomedicine (LOMIN), at NIH Bethesda, USA).
- [19] Ludwig DL, Pereira DS, Zhu Z, Hicklin DJ, Bohlen P. Monoclonal antibody therapeutics and apoptosis. *Oncogene*; 2003; **22**(56):9097-9106.
- [20] Tazzari PL, de Toter D, Bolognesi A *et al*. An Epstein-Barr virus-infected lymphoblastoid cell line (D430B) that grows in SCID-mice with the morphologic features of a CD30+ anaplastic large cell lymphoma, and is sensitive to anti-CD30 immunotoxins. *Haematologica*; 1999; **84**(11):988-995.

- [21] Ferrini S, Cantoni C, Ciccone E *et al.* A novel surface molecule expressed by long-term cultured T and natural killer cells is involved in cell activation. *Eur J Immunol*; 1991; **21**(9):1981-1987.
- [22] Orengo AM, Cantoni C, Neglia F, Biassoni R, Ferrini S. Reciprocal expression of CD70 and of its receptor, CD27, in human long term-activated T and natural killer (NK) cells: inverse regulation by cytokines and role in induction of cytotoxicity. *Clin Exp Immunol*; 1997; **107**(3):608-613.
- [23] Israel BF, Gulley M, Elmore S *et al.* Anti-CD70 antibodies: a potential treatment for EBV+ CD70-expressing lymphomas. *Mol Cancer Ther*; 2005; **4**(12):2037-2044.
- [24] Baio G, Fabbi M, Salvi S *et al.* Two-step in vivo tumour targeting by biotin-conjugated antibodies and superparamagnetic nanoparticles assessed by magnetic resonance imaging at 1.5 T. *Mol Imaging Biol*; 2010;**12**(3):305-315.
- [25] Pirko I, Johnson A, Ciric B *et al.* In vivo magnetic resonance imaging of immune cells in the central nervous system with superparamagnetic antibodies. *FASEB J*; 2004; **18**(1):179-182.
- [26] Pirko I, Ciric B, Gamez J *et al.* A human antibody that promotes remyelination enters the CNS and decreases lesion load as detected by T2-weighted spinal cord MRI in a virus-induced murine model of MS. *FASEB J*; 2004;**18**(13):1577-1579.
- [27] Cheng KT. Ultrasmall superparamagnetic iron oxide-anti-CD20 monoclonal antibody. *Molecular Imaging and Contrast Agent Database (MICAD)*; 2007; 21 May.
- [28] Mankoff DA. A definition of molecular imaging. *J Nucl Med*; 2007; **48**(6):18N, 21N.
- [29] Srivastava S, Lundqvist A, Childs RW. Natural killer cell immunotherapy for cancer: a new hope. *Cytotherapy*; 2008;**10**(8):775-

- 783.[30] Slezak SE, Muirhead KA. Radioactive cell membrane labelling. *Nature*; 1991; **352**(6332):261-262.
- [31] Blomberg K, Granberg C, Hemmilä I, Lövgren T. Europium-labelled target cells in an assay of natural killer cell activity. I. A novel non-radioactive method based on time-resolved fluorescence. *J Immunol Methods*; 1986; **86**(2):225-229.
- [32] Basso L, Rosa F, Pace D, Cilli M, Neumaier CE, Baio G. Mn-enhanced Magnetic Resonance (MEMRI) of rat salivary glands using a clinical 3T MR scanner. ECR. 2014. C-1228. <http://dx.doi.org/10.1594/ecr2014/C-1228>.
- [33] Rosa F, Basso L, Valdora F, Neumaier CE, Baio G. Normal mouse anatomy on 3 T MRI. ECR 2014. C-1198. <http://dx.doi.org/10.1594/ecr2014/C-1198>.
- [34] Baio G, Fabbi M, Emionite L *et al.* In vivo imaging of human breast cancer mouse model with high level expression of calcium sensing receptor at 3T. *Eur Radiol*; 2012; **22**(3):551-558.
- [35] Barrett PQ, Kojima I, Kojima K *et al.* Short term memory in the calcium messenger system. Evidence for a sustained activation of protein kinase C in adrenal glomerulosa cells. *Biochem J*; 1986; **238**(3):905-912.
- [36] Rasmussen H. The calcium messenger system (1). *N Engl J Med*; 1986; **314**(17):1094-1101.
- [37] Capiod T, Shuba Y, Skryma R, Prevarskaya N. Calcium signalling and cancer cell growth. *Subcell Biochem*; 2007; **45**:405-427.
- [38] Brown EM, MacLeod RJ. Extracellular calcium sensing and extracellular calcium signalling. *Physiol Rev*; 2001; **81**(1):239-297.
- [39] Bikle DD, Oda Y, Xie Z. Calcium and 1, 25(OH)₂D: interacting drivers of epidermal differentiation. *J Steroid Biochem Mol Biol*; 2004; **89-90**(1-5):355-360.

- [40] Drapeau P, Nachshen DA. Manganese fluxes and manganese-dependent neurotransmitter release in presynaptic nerve endings isolated from rat brain. *J Physiol*; 1984; **348**:493-510.
- [41] Narita K, Kawasaki F, Kita H. Mn and Mg influxes through Ca channels of motor nerve terminals are prevented by verapamil in frogs. *Brain Res*; 1990; **510**(2):289-295.
- [42] Lin YJ, Koretsky AP. Manganese ion enhances T1-weighted MRI during brain activation: an approach to direct imaging of brain function. *Magn Reson Med*; 1997; **38**(3):378-388.
- [43] Duong TQ, Silva AC, Lee SP, Kim SG. Functional MRI of calcium-dependent synaptic activity: cross correlation with CBF and BOLD measurements. *Magn Reson Med*; 2000; **43**(3):383-392.
- [44] Hu TC, Pautler RG, MacGowan GA, Koretsky AP. Manganese-enhanced MRI of mouse heart during changes in inotropy. *Magn Reson Med*; 2001; **46**(5):884-890.
- [45] Krombach GA, Saeed M, Higgins CB, Novikov V, Wendland MF. Contrast-enhanced MR delineation of stunned myocardium with administration of MnCl₂ in rats. *Radiology*; 2004; **230**(1):183-190.
- [46] Pautler RG, Silva AC, Koretsky AP. In vivo neuronal tract tracing using manganese-enhanced magnetic resonance imaging. *Magn Reson Med*; 1998; **40**(5):740-748.
- [47] Watanabe T, Michaelis T, Frahm J. Mapping of retinal projections in the living rat using high-resolution 3D gradient-echo MRI with Mn²⁺-induced contrast. *Magn Reson Med*; 2001; **46**(3):424-429.
- [48] Lin CP, Tseng WY, Cheng HC, Chen JH. Validation of diffusion tensor magnetic resonance axonal fiber imaging with registered manganese-enhanced optic tracts. *Neuroimage*; 2001; **14**(5):1035-1047.

- [49] Allegrini PR, Wiessner C. Three-dimensional MRI of cerebral projections in rat brain in vivo after intracortical injection of MnCl₂. *NMR Biomed*; 2003; **16**(5):252-256.
- [50] Lin Y. MRI of the rat and mouse brain after systemic administration of MnCl₂. Thesis, Carnegie Mellon University, Pittsburgh, PA; 1997.
- [51] Watanabe T, Natt O, Boretius S, Frahm J, Michaelis T. In vivo 3D MRI staining of mouse brain after subcutaneous application of MnCl₂. *Magn Reson Med*; 2002; **48**(5):852-859.
- [52] Ogan MD, Revel D, Brasch RC. Metalloporphyrin contrast enhancement of tumours in magnetic resonance imaging. A study of human carcinoma, lymphoma, and fibrosarcoma in mice. *Invest Radiol*; 1987; **22**(10):822-828.
- [53] van Zijl PC, Place DA, Cohen JS *et al*. Metalloporphyrin magnetic resonance contrast agents. Feasibility of tumour-specific magnetic resonance imaging. *Acta Radiol Suppl*; 1990; **374**:375-379.
- [54] Brown EM. G protein-coupled, extracellular Ca²⁺ (Ca²⁺(o))-sensing receptor enables Ca²⁺(o) to function as a versatile extracellular first messenger. *Cell Biochem Biophys*; 2000; **33**(1):63-95.
- [55] Garrett JE, Capuano IV, Hammerland LG *et al*. Molecular cloning and functional expression of human parathyroid calcium receptor cDNAs. *J Biol Chem*; 1995; **270**(21):12919-12925.
- [56] Fukumoto S. Basic and clinical aspects of calcimimetics. Structure and function of calcium-sensing receptor. *Clin Calcium*; 2008; **18**(1):32-36.
- [57] Cheng I, Klingensmith ME, Chattopadhyay N *et al*. Identification and localization of the extracellular calcium-sensing receptor in human breast. *J Clin Endocrinol Metab*; 1998; **83**(2):703-707.
- [58] McGrath CM, Soule HD. Calcium regulation of normal human mammary epithelial cell growth in culture. *In Vitro*; 1984; **20**(8):652-662.

- [59] Percival RC, Yates AJ, Gray RE *et al.* Mechanism of malignant hypercalcaemia in carcinoma of the breast. *Br Med J (Clin Res Ed)*; 1985; **291**(6498):776-779.
- [60] House MG, Kohlmeier L, Chattopadhyay N *et al.* Expression of an extracellular calcium-sensing receptor in human and mouse bone marrow cells. *J Bone Miner Res*; 1997; **12**(12):1959-1970.
- [61] Silver IA, Murrills RJ, Etherington DJ. Microelectrode studies on the acid microenvironment beneath adherent macrophages and osteoclasts. *Exp Cell Res*; 1988; **175**(2):266-276.
- [62] Sanders JL, Chattopadhyay N, Kifor O *et al.* Extracellular calcium-sensing receptor expression and its potential role in regulating parathyroid hormone-related peptide secretion in human breast cancer cell lines. *Endocrinology*; 2000; **141**(12):4357-4364.
- [63] Coleman RE. Skeletal complications of malignancy. *Cancer*; 1997; **80**(8 Suppl):1588-1594.
- [64] Guise TA, Mundy GR. Cancer and bone. *Endocr Rev*; 1998; **19**(1):18-54.
- [65] Guise TA, Yin JJ, Taylor SD *et al.* Evidence for a causal role of parathyroid hormone-related protein in the pathogenesis of human breast cancer-mediated osteolysis. *J Clin Invest*; 1996; **98**(7):1544-1549.
- [66] Nemeth EF, Fox J, Delmar EG *et al.* Stimulation of parathyroid hormone secretion by a small molecule antagonist of the calcium receptor (Abstract). *J Bone Miner Res*; 1998; **23**:S156.
- [67] Mihai R, Stevens J, McKinney C, Ibrahim NB. Expression of the calcium receptor in human breast cancer--a potential new marker predicting the risk of bone metastases. *Eur J Surg Oncol*; 2006; **32**(5):511-515.

- [68] Remy C, Kirchhoff P, Hafner P *et al.* Stimulatory pathways of the Calcium-sensing receptor on acid secretion in freshly isolated human gastric glands. *Cell Physiol Biochem*; 2007; **19**(1-4):33-42.
- [69] Günzel D, Amasheh S, Pfaffenbach S *et al.* Claudin-16 affects transcellular Cl⁻ secretion in MDCK cells. *J Physiol*; 2009; **587**(Pt 15):3777-3793.
- [70] Ye C, Rogers K, Bai M *et al.* Agonists of the Ca(2+)-sensing receptor (CaR) activate nonselective cation channels in HEK293 cells stably transfected with the human CaR. *Biochem Biophys Res Commun*; 1996; **226**(2):572-579.
- [71] Tsien RW, Hess P, McCleskey EW, Rosenberg RL. Calcium channels: mechanisms of selectivity, permeation, and block. *Annu Rev Biophys Chem*; 1987; **16**:265-290.
- [72] VanHouten J, Dann P, McGeoch G *et al.* The calcium-sensing receptor regulates mammary gland parathyroid hormone-related protein production and calcium transport. *J Clin Invest*; 2004; **113**(4):598-608.
- [73] Grünecker B, Kaltwasser SF, Peterse Y *et al.* Fractionated manganese injections: effects on MRI contrast enhancement and physiological measures in C57BL/6 mice. *NMR Biomed*; 2010; **23**(8):913-921.
- [74] Gianolio E, Arena F, Di Gregorio E *et al.* MEMRI and tumours: a method for the evaluation of the contribution of Mn(II) ions in the extracellular compartment. *NMR Biomed*; 2015; **28**(9):1104-1110.
- [75] Chen KY, Cypess AM, Laughlin MR *et al.* Brown Adipose Reporting Criteria in Imaging Studies (BARCIST 1.0): Recommendations for Standardized FDG-PET/CT Experiments in Humans. *Cell Metab*; 2016; **24**(2):210-222.

- [76] Lee P, Greenfield JR, Ho KK, Fulham MJ. A critical appraisal of the prevalence and metabolic significance of brown adipose tissue in adult humans. *Am J Physiol Endocrinol Metab*; 2010; **299**(4):E601-6.
- [77] Schrauwen-Hinderling VB, Carpentier AC. Molecular imaging of postprandial metabolism. *J Appl Physiol (1985)*; 2018; **124**(2):504-511.
- [78] Rosa F, Basso L, Pace D, Secondini L, Boccardo S, Neumaier CE, Baio G. In vivo Non-invasive Detection of Brown Adipose Tissue through Manganese Enhanced Magnetic Resonance Imaging (MEMRI). World Molecular Imaging Conference (WMIC) 2015. P688.
- [79] Clarke KJ, Porter RK. The Importance of Calcium Ions for Determining Mitochondrial Glycerol-3-Phosphate Dehydrogenase Activity When Measuring Uncoupling Protein 1 (UCP1) Function in Mitochondria Isolated from Brown Adipose Tissue. *Methods Mol Biol*; 2018; 1782:325-336.
- [80] de Meis L, Arruda AP, da Costa RM, Benchimol M. Identification of a Ca²⁺-ATPase in brown adipose tissue mitochondria: regulation of thermogenesis by ATP and Ca²⁺. *J Biol Chem*; 2006; **281**(24):16384-16390.
- [81] Baio G, Rescinito G, Rosa F *et al.* Correlation between Choline Peak at MR Spectroscopy and Calcium-Sensing Receptor Expression Level in Breast Cancer: A Preliminary Clinical Study. *Mol Imaging Biol*; 2015; **17**(4):548-556.
- [82] Hanahan D, Weinberg RA. Hallmarks of cancer: the next generation. *Cell*; 2011; **144**(5):646-74.
- [83] Griffiths JR, Stevens AN, Iles RA, Gordon RE, Shaw D. ³¹P-NMR investigation of solid tumours in the living rat. *Biosci Rep*; 1981; **1**(4):319-325.
- [84] Griffiths JR, Cady E, Edwards RH *et al.* ³¹P-NMR studies of a human tumour in situ. *Lancet*; 1983; **1**(8339):1435-1436.

- [85] Daly PF, Lyon RC, Faustino PJ, Cohen JS. Phospholipid metabolism in cancer cells monitored by ³¹P NMR spectroscopy. *J Biol Chem*; 1987; **262**(31):14875-14878.
- [86] Aboagye EO, Bhujwala ZM. Malignant transformation alters membrane choline phospholipid metabolism of human mammary epithelial cells. *Cancer Res*; 1999; **59**(1):80-84.
- [87] Podo F, Canevari S, Canese R *et al.* MR evaluation of response to targeted treatment in cancer cells. *NMR Biomed*; 2011; **24**(6):648-672.
- [88] Lean CL, Newland RC, Ende DA *et al.* Assessment of human colorectal biopsies by ¹H MRS: correlation with histopathology. *Magn Reson Med*; 1993; **30**(5):525-533.
- [89] Cheng LL, Chang IW, Smith BL, Gonzalez RG. Evaluating human breast ductal carcinomas with high-resolution magic-angle spinning proton magnetic resonance spectroscopy. *J Magn Reson*; 1998; **135**(1):194-202.
- [90] Negendank W. Studies of human tumours by MRS: a review. *NMR Biomed*; 1992; **5**(5):303-324.
- [91] Mountford CE, Wright LC. Organization of lipids in the plasma membranes of malignant and stimulated cells: a new model. *Trends Biochem Sci*; 1988; **13**(5):172-177.
- [92] Kennedy EP, Weiss SB. The function of cytidine coenzymes in the biosynthesis of phospholipides. *J Biol Chem*; 1956; **222**(1):193-214.
- [93] Cuadrado A, Carnero A, Dolfi F, Jiménez B, Lacal JC. Phosphorylcholine: a novel second messenger essential for mitogenic activity of growth factors. *Oncogene*; 1993; **8**(11):2959-2968.
- [94] Price BD, Morris JD, Marshall CJ, Hall A. Stimulation of phosphatidylcholine hydrolysis, diacylglycerol release, and arachidonic acid production by oncogenic ras is a consequence of protein kinase C activation. *J Biol Chem*; 1989; **264**(28):16638-16643.

- [95] Besterman JM, Duronio V, Cuatrecasas P. Rapid formation of diacylglycerol from phosphatidylcholine: a pathway for generation of a second messenger. *Proc Natl Acad Sci U S A*; 1986; **83**(18):6785-6789.
- [96] Bogin L, Papa MZ, Polak-Charcon S, Degani H. TNF-induced modulations of phospholipid metabolism in human breast cancer cells. *Biochim Biophys Acta*; 1998; **1392**(2-3):217-232.
- [97] Huang C, Hydo LM, Liu S, Miller RT. Activation of choline kinase by extracellular Ca²⁺ is Ca(2+)-sensing receptor, Galph12 and Rho-dependent in breast cancer cells. *Cell Signal*; 2009; **21**(12):1894-1900.
- [98] Huang W, Fisher PR, Dulaimy K *et al.* Detection of breast malignancy: diagnostic MR protocol for improved specificity. *Radiology*; 2004; **232**(2):585-591.
- [99] Baek HM, Lee YJ. Feasibility of MR spectroscopy for characterizing malignant breast lesions using a clinical 3-T scanner. *Breast Cancer*; 2015; **22**(5):510-9.
- [100] Brennan SC, Thiem U, Roth S *et al.* Calcium sensing receptor signalling in physiology and cancer. *Biochim Biophys Acta*; 2013; **1833**(7):1732-1744.
- [101] Meisamy S, Bolan PJ, Baker EH *et al.* Neoadjuvant chemotherapy of locally advanced breast cancer: predicting response with in vivo (1)H MR spectroscopy--a pilot study at 4 T. *Radiology*; 2004;**233**(2):424-431.
- [102] Kumar M, Jagannathan NR, Seenu V *et al.* Monitoring the therapeutic response of locally advanced breast cancer patients: sequential in vivo proton MR spectroscopy study. *J Magn Reson Imaging*; 2006; **24**(2):325-332.
- [103] Promkan M, Liu G, Patmasiriwat P, Chakrabarty S. BRCA1 suppresses the expression of survivin and promotes sensitivity to paclitaxel through the calcium sensing receptor (CaSR) in human breast cancer cells. *Cell Calcium*; 2011; **49**(2):79-88.

- [104] O'Flynn EA, DeSouza NM. Functional magnetic resonance: biomarkers of response in breast cancer. *Breast Cancer Res*; 2011; **13**(1):204.
- [105] Mavromatis BH, Cheson BD. Pre- and post-treatment evaluation of non-Hodgkin's lymphoma. *Best Pract Res Clin Haematol*; 2002; **15**(3):429-447.
- [106] Hallek M, Cheson BD, Catovsky D *et al*. Guidelines for the diagnosis and treatment of chronic lymphocytic leukemia: a report from the International Workshop on Chronic Lymphocytic Leukemia updating the National Cancer Institute-Working Group 1996 guidelines. *Blood*; 2008; **111**(12):5446-5456.
- [107] Cheson BD, Bennett JM, Grever M *et al*. National Cancer Institute-sponsored Working Group guidelines for chronic lymphocytic leukemia: revised guidelines for diagnosis and treatment. *Blood*; 1996; **87**(12):4990-4997.
- [108] Eichhorst BF, Fischer K, Fink AM *et al*. Limited clinical relevance of imaging techniques in the follow-up of patients with advanced chronic lymphocytic leukemia: results of a meta-analysis. *Blood*; 2011; **117**(6):1817-1821.
- [109] Byrd JC, Pagel JM, Awan FT *et al*. A phase 1 study evaluating the safety and tolerability of otlertuzumab, an anti-CD37 mono-specific ADAPTIR therapeutic protein in chronic lymphocytic leukemia. *Blood*; 2014; **123**(9):1302-1308.
- [110] Gentile M, Cutrona G, Molica S *et al*. Prospective validation of predictive value of abdominal computed tomography scan on time to first treatment in Rai 0 chronic lymphocytic leukemia patients: results of the multicenter O-CLL1-GISL study. *Eur J Haematol*; 2016; **96**(1):36-45.

- [111] Bruzzi JF, Macapinlac H, Tsimberidou AM *et al.* Detection of Richter's transformation of chronic lymphocytic leukemia by PET/CT. *J Nucl Med*; 2006; **47**(8):1267-1273.
- [112] Conte MJ, Bowen DA, Wiseman GA *et al.* Use of positron emission tomography-computed tomography in the management of patients with chronic lymphocytic leukemia/small lymphocytic lymphoma. *Leuk Lymphoma*; 2014; **55**(9):2079-2084.
- [113] Papajík T, Mysliveček M, Urbanová R *et al.* 2-[18F]fluoro-2-deoxy-D-glucose positron emission tomography/computed tomography examination in patients with chronic lymphocytic leukemia may reveal Richter transformation. *Leuk Lymphoma*; 2014; **55**(2):314-319.
- [114] Parikh SA, Kay NE, Shanafelt TD. How we treat Richter syndrome. *Blood*; 2014; **123**(11):1647-1657.
- [115] Rossi C, Brisou G, Baseggio L *et al.* Central nervous system involvement in chronic lymphocytic leukemia: uncommon manifestation with undefined therapeutic management. *Leuk Lymphoma*; 2014; **55**(8):1939-1941.
- [116] Tardivon AA, Vanel D, Munck JN, Bosq J. Magnetic resonance imaging of the bone marrow in lymphomas and leukemias. *Leuk Lymphoma*; 1997; **25**(1-2):55-68.
- [117] Lecouvet FE, Vande Berg BC, Michaux L *et al.* Early chronic lymphocytic leukemia: prognostic value of quantitative bone marrow MR imaging findings and correlation with hematologic variables. *Radiology*; 1997; **204**(3):813-818.
- [118] Froehlich JM, Triantafyllou M, Fleischmann A *et al.* Does quantification of USPIO uptake-related signal loss allow differentiation of benign and malignant normal-sized pelvic lymph nodes? *Contrast Media Mol Imaging*; 2012; **7**(3):346-355.

- [119] Weissleder R, Elizondo G, Wittenberg J *et al.* Ultrasmall superparamagnetic iron oxide: characterization of a new class of contrast agents for MR imaging. *Radiology*; 1990; **175**(2):489-493.
- [120] Weissleder R, Hahn PF, Stark DD *et al.* Superparamagnetic iron oxide: enhanced detection of focal splenic tumours with MR imaging. *Radiology*; 1988; **169**(2):399-403.
- [121] Weissleder R, Stark DD, Compton CC, Wittenberg J, Ferrucci JT. Ferrite-enhanced MR imaging of hepatic lymphoma: an experimental study in rats. *AJR Am J Roentgenol*; 1987; **149**(6):1161-1165.
- [122] Valdora F, Cutrona G, Matis S *et al.* A non-invasive approach to monitor chronic lymphocytic leukemia engraftment in a xenograft mouse model using ultra-small superparamagnetic iron oxide-magnetic resonance imaging (USPIO-MRI). *Clin Immunol*; 2016; **172**:52-60.
- [123] Dürig J, Ebeling P, Grabellus F *et al.* A novel nonobese diabetic/severe combined immunodeficient xenograft model for chronic lymphocytic leukemia reflects important clinical characteristics of the disease. *Cancer Res*; 2007; **67**(18):8653-8661.
- [124] Bagnara D, Kaufman MS, Calissano C *et al.* A novel adoptive transfer model of chronic lymphocytic leukemia suggests a key role for T lymphocytes in the disease. *Blood*; 2011; **117**(20):5463-5472.
- [125] Simon GH, Bauer J, Saborovski O *et al.* T1 and T2 relaxivity of intracellular and extracellular USPIO at 1.5T and 3T clinical MR scanning. *Eur Radiol*; 2006; **16**(3):738-745.
- [126] Patten PE, Ferrer G, Chen SS *et al.* Chronic lymphocytic leukemia cells diversify and differentiate in vivo via a nonclassical Th1-dependent, Bcl-6-deficient process. *JCI Insight*; 2016; **1**(4).
- [127] Special Issue: Dr. Henry G. Kunkel. Edited by Shu Man Fu, Robert Winchester. *Clinical Immunology*; 2016; 172:1-122.

- [128] Cutrona G, Matis S, Colombo M *et al.* Effects of miRNA-15 and miRNA-16 expression replacement in chronic lymphocytic leukemia: implication for therapy. *Leukemia*; 2017; **31**(9):1894-1904.
- [129] Küppers R, Dalla-Favera R. Mechanisms of chromosomal translocations in B cell lymphomas. *Oncogene*. 2001; **20**(40):5580-5594.
- [128] Döhner H, Stilgenbauer S, Benner A *et al.* Genomic aberrations and survival in chronic lymphocytic leukemia. *N Engl J Med*; 2000; **343**(26):1910-1916.
- [130] Kalachikov S, Migliazza A, Cayanis E *et al.* Cloning and gene mapping of the chromosome 13q14 region deleted in chronic lymphocytic leukemia. *Genomics*; 1997; **42**(3):369-377.
- [131] Rawstron AC, Bennett FL, O'Connor SJ *et al.* Monoclonal B-cell lymphocytosis and chronic lymphocytic leukemia. *N Engl J Med*; 2008; **359**(6):575-583.
- [132] Morabito F, Mosca L, Cutrona G *et al.* Clinical monoclonal B lymphocytosis versus Rai 0 chronic lymphocytic leukemia: A comparison of cellular, cytogenetic, molecular, and clinical features. *Clin Cancer Res*; 2013; **19**(21):5890-5900.
- [133] Liu Y, Corcoran M, Rasool O *et al.* Cloning of two candidate tumor suppressor genes within a 10 kb region on chromosome 13q14, frequently deleted in chronic lymphocytic leukemia. *Oncogene*; 1997; **15**(20):2463-2473.
- [134] Migliazza A, Bosch F, Komatsu H *et al.* Nucleotide sequence, transcription map, and mutation analysis of the 13q14 chromosomal region deleted in B-cell chronic lymphocytic leukemia. *Blood*; 2001; **97**(7):2098-2104.
- [135] Calin GA, Dumitru CD, Shimizu M *et al.* Frequent deletions and down-regulation of micro- RNA genes miR15 and miR16 at 13q14 in

chronic lymphocytic leukemia. *Proc Natl Acad Sci U S A*; 2002; **99**(24):15524-15529.

[136] Mosca L, Fabris S, Lionetti M *et al.* Integrative genomics analyses reveal molecularly distinct subgroups of B-cell chronic lymphocytic leukemia patients with 13q14 deletion. *Clin Cancer Res*; 2010; **16**(23):5641-5653.

[137] Klein U, Lia M, Crespo M *et al.* The DLEU2/miR-15a/16-1 cluster controls B cell proliferation and its deletion leads to chronic lymphocytic leukemia. *Cancer Cell*; 2010; **17**(1):28-40.

[138] Sellmann L, Scholtysik R, Kreuz M *et al.* Gene dosage effects in chronic lymphocytic leukemia. *Cancer Genet Cytogenet*; 2010; **203**(2):149-160.

[139] Lagos-Quintana M, Rauhut R, Lendeckel W, Tuschl T. Identification of novel genes coding for small expressed RNAs. *Science*; 2001; **294**(5543):853-858.

[140] Ghildiyal M, Zamore PD. Small silencing RNAs: an expanding universe. *Nat Rev Genet*; 2009; **10**(2):94-108.

[141] Hausser J, Zavolan M. Identification and consequences of miRNA-target interactions--beyond repression of gene expression. *Nat Rev Genet*; 2014; **15**(9):599-612.

[142] Mertens D, Wolf S, Tschuch C *et al.* Allelic silencing at the tumor-suppressor locus 13q14.3 suggests an epigenetic tumor-suppressor mechanism. *Proc Natl Acad Sci U S A*; 2006; **103**(20):7741-7746.

[143] Fabbri M, Bottoni A, Shimizu M *et al.* Association of a microRNA/TP53 feedback circuitry with pathogenesis and outcome of B-cell chronic lymphocytic leukemia. *JAMA*; 2011; **305**(1):59-67.

- [144] Calin GA, Cimmino A, Fabbri M *et al.* MiR-15a and miR-16-1 cluster functions in human leukemia. *Proc Natl Acad Sci U S A*; 2008; **105**(13):5166-5171.
- [145] Glunde K, Penet MF, Jiang L, Jacobs MA, Bhujwalla ZM. Choline metabolism-based molecular diagnosis of cancer: an update. *Expert Rev Mol Diagn*; 2015; **15**(6):735-747).
- [146] van den Bos EJ, Wagner A, Mahrholdt H, *et al.* Improved efficacy of stem cell labeling for magnetic resonance imaging studies by the use of cationic liposomes. *Cell Transplant*; 2003; **12**(7):743–756.
- [147] Bogdanov A Jr, Weissleder R. The development of in vivo imaging systems to study gene expression. *Trends Biotechnol*; 1998; **16**(1):5-10.
- [148] Weissleder R. Molecular imaging: exploring the next frontier. *Radiology*; 1999; **212**(3):609-614.
- [149] Hormuth DA, Sorace AG, Virostko J, *et al.* Translating preclinical MRI methods to clinical oncology. *J Magn Reson Imaging*; 2019; Mar 29.
- [150] Smith CP, Laucis A, Harmon S, *et al.* Novel Imaging in Detection of Metastatic Prostate Cancer. *Curr Oncol Rep*; 2019; **21**(4):31.
- [151] Zamboglou C, Drendel V, Jilg CA, *et al.* Comparison of 68Ga-HBED-CC PSMA-PET/CT and multiparametric MRI for gross tumour volume detection in patients with primary prostate cancer based on slice by slice comparison with histopathology. *Theragnostics*; 2017; **7**(1):228-237.
- [152] Zamboglou C, Schiller F, Fechter T, *et al.* (68)Ga-HBED-CC-PSMA PET/CT Versus Histopathology in Primary Localized Prostate Cancer: A Voxel-Wise Comparison. *Theragnostics*; 2016; **6**(10):1619-28.
- [153] Siriwardana A, Thompson J, van Leeuwen PJ, *et al.* Initial multicentre experience of 68 gallium-PSMA PET/CT guided robot-assisted salvage lymphadenectomy: acceptable safety profile but oncological benefit appears limited. *BJU Int*; 2017; **120**(5):673-681.

- [154] Maurer T, Weirich G, Schottelius M, *et al.* Prostate-specific membrane antigen-radioguided surgery for metastatic lymph nodes in prostate cancer. *Eur Urol*; 2015; **68**(3):530-534.
- [155] Schottelius M, Wirtz M, Eiber M, Maurer T, Wester HJ. [(111)In]PSMA-I&T: expanding the spectrum of PSMA-I&T applications towards SPECT and radioguided surgery. *EJNMMI Res*; 2015; **5**(1):68.
- [156] Rauscher I, Düwel C, Wirtz M, *et al.* Value of 111 In-prostate-specific membrane antigen (PSMA)-radioguided surgery for salvage lymphadenectomy in recurrent prostate cancer: correlation with histopathology and clinical follow-up. *BJU Int*; 2017;**120**(1):40-47.
- [157] Kulkarni HR, Baum RP. Theragnostics with Ga-68 somatostatin receptor PET/CT: monitoring response to peptide receptor radionuclide therapy. *PET Clin*; 2014; **9**(1):91–97.
- [158] Werner RA, Bluemel C, Allen-Auerbach MS, Higuchi T, Herrmann K. 68Gallium- and 90Yttrium-/177Lutetium: “theragnostic twins” for diagnosis and treatment of NETs. *Ann Nucl Med*. 2015; **29**(1):1–7.
- [159] Rahbar K, Ahmadzadehfar H, Kratochwil C, *et al.* German Multicenter Study Investigating 177Lu-PSMA-617 radioligand therapy in advanced prostate cancer patients. *J Nucl Med*; 2017; **58**(1):85–90.
- [160] Werner RA, Weich A, Higuchi T, *et al.* Imaging of chemokine receptor 4 expression in neuroendocrine tumors—a triple tracer comparative approach. *Theragnostics*; 2017; **7**(6):1489–1498.
- [161] Claringbold PG1, Brayshaw PA, Price RA, Turner JH. Phase II study of radiopeptide 177Lu-octreotate and capecitabine therapy of progressive disseminated neuroendocrine tumours. *Eur J Nucl Med Mol Imaging*; 2011; **38**(2):302-311.
- [162] Claringbold PG, Price RA, Turner JH. Phase I-II study of radiopeptide 177Lu-octreotate in combination with capecitabine and temozolomide in

advanced low-grade neuroendocrine tumors. *Cancer Biother Radiopharm*; 2012; **27**(9):561-569.

[163] Claringbold PG, Turner JH. Pancreatic Neuroendocrine Tumor Control: Durable Objective Response to Combination ¹⁷⁷Lu-Octreotate-Capecitabine-Temozolomide Radiopeptide Chemotherapy. *Neuroendocrinology*; 2016; **103**(5):432-439.

[164] Claringbold PG, Turner JH. NeuroEndocrine Tumor Therapy with Lutetium-177-octreotate and Everolimus (NETTLE): A Phase I Study. *Cancer Biother. Radiopharm*; 2015; **30**:261–269.

[165] Baum RP, Kluge AW, Kulkarni H, *et al.* [(¹⁷⁷)Lu-DOTA](0)-D-Phe(1)-Tyr(3)-Octreotide ((¹⁷⁷)Lu-DOTATOC) For Peptide Receptor Radiotherapy in Patients with Advanced Neuroendocrine Tumours: A Phase-II Study. *Theragnostics*; 2016; **6**, 501–510.

[166] Van Vliet EI, van Eijck CH, de Krijger RR, *et al.* Neoadjuvant Treatment of Nonfunctioning Pancreatic Neuroendocrine Tumors with [¹⁷⁷Lu-DOTA⁰,Tyr³]Octreotate. *J Nucl Med*; 2015; **56**, 1647–1653.

[167] Strosberg J, El-Haddad G, Wolin E, *et al.* Phase 3 Trial of ¹⁷⁷Lu-Dotatate for Midgut Neuroendocrine Tumors. *N Engl J Med*; 2017; **376**(2):125-135.

[168] Turner JH. Recent advances in Theragnostics and challenges for the future. *Br J Radiol*; 2018; **91**(1091):20170893.

[169] Duffy MJ, Harbeck N, Nap M, *et al.* Clinical use of biomarkers in breast cancer: Updated guidelines from the European Group on Tumor Markers (EGTM). *Eur J Cancer*; 2017; **75**, 284–298.

[170] Eiber M, Herrmann K, Calais J, *et al.* Prostate cancer molecular imaging standardized evaluation (PROMISE): proposed miTNM classification for the interpretation of PSMA-ligand PET/CT. *J Nucl Med*; 2018; **59**(3):469–478.

- [171] Fanti S, Minozzi S, Morigi JJ, *et al.* Development of standardized image interpretation for 68 Ga-PSMA PET/CT to detect prostate cancer recurrent lesions. *Eur J Nucl Med Mol Imaging*; 2017; **44**(10):1622–35.
- [172] Chan DL, Pavlakis N, Schembri GP, *et al.* Dual somatostatin receptor/FDG PET/CT imaging in metastatic neuroendocrine tumours: proposal for a novel grading scheme with prognostic significance. *Theragnostics*; 2017; **7**(5):1149–1158.
- [173] Schelbert HR. Focus on Molecular Imaging. *J Nucl Med*; 2007; **48**(12):1915.
- [174] Zanfardino M, Franzese M, Pane K, *et al.* Bringing radiomics into a multi-omics framework for a comprehensive genotype-phenotype characterization of oncological diseases. *J Transl Med*; 2019; **17**(1):337.
- [175] Hariri AR, Weinberger DR. Imaging genomics. *Br Med Bull*; 2003; **65**:259–270.
- [176] Baltrušaitis T, Ahuja C, Morency LP. Multimodal machine learning: a survey and taxonomy. *IEEE Trans Pattern Anal Mach Intell*; 2018;